

Surface area and dispersant chemistry changes of milled titania pigment probed by relaxation NMR

Laura Nicola Elliott

Submitted in accordance with the requirements for the degree of Doctor of
Philosophy and Master of Science

The University of Leeds
School of Chemical and Process Engineering

October 2019

© 2019 The University of Leeds and Laura Nicola Elliott

Intellectual Property and Publication Declaration

I, the candidate confirm that the work submitted is my own, except where work which has formed part of jointly authored publications has been included. The contribution of the candidate and the other authors to this work has been explicitly indicated below. I confirm that appropriate credit has been given within the thesis where reference has been made to the work of others.

The work in chapter 4 of this thesis has been published as follows:

1. Elliott, L. N., Behra, J. S., Hondow, N., Bourne, R. A., Hassanpour, A., Edwards, J. L., Sutcliffe, S. & Hunter, T. N. 2019. Characterisation of polyphosphate coated aluminium-doped titania nanoparticles during milling. *Journal of Colloid and Interface Science*, 548, 110-122.

The work in chapter 5 of this thesis has been published as follows:

2. Elliott, L. N., Bourne, R. A., Hassanpour, A., Edwards, J. L., Sutcliffe, S. & Hunter, T. N. 2018. Salt enhanced solvent relaxation and particle surface area determination via rapid spin-lattice NMR. *Powder Technology*, 333, 458-467.

The preliminary work for chapters 5 and 6 of this thesis has been published as a conference proceeding as follows:

3. Elliott, L. N., Bourne, R. A., Hassanpour, A., Edwards, J. L., Sutcliffe, S. & Hunter, T. N. 2019. Characterisation and degradation of polyphosphate dispersant interactions with aluminium-doped titania nanoparticles during milling. *16th European Symposium on Comminution & Classification (ESCC 2019)*, 2-4 September 2019, Leeds, UK.

The work in chapter 6 of this thesis is in preparation for publication as follows:

4. Elliott, L. N., Austin, D., Bourne, R. A., Hassanpour, A., Edwards, J. L., Sutcliffe, S. & Hunter, T. N. Degradation of polyphosphate dispersant interactions with aluminium-doped TiO₂ during high shear-milling. In preparation.

Within this thesis Chapter 1, 2 and 3 contain some relevant introductory based material from papers 1, 2 and 4. For all the publications and conference proceedings, I was responsible for designing and performing the experiments, analysing the data and writing the publications. The contribution of co-authors to publications has predominately been advisory, consistent with their role as academic supervisors and industrial supervisors of this PhD.


The exception to this is that paper 2, author Juliette S. Behra, has assisted with the interpretation of dynamic light scattering results performed on the zetasizer and further she performed light scattering measurements which are detailed in the supplementary appendix to Chapter 5. Furthermore, Nicole Hondow assisted with TEM and EDS image acquisition which were used in paper 2 and Chapter 5.

David Austin assisted in experimental collection of results detailed in Chapter 6 which include the characterisation of unmilled aluminium doped TiO₂ surface charge and the SHMP adsorption isotherm by ICP-OES. David Austin also milled particles where no dispersant was present and the surface area and particle size results were used to understand changes in relaxation NMR. David Austin also helped obtain milled samples, where the dispersant was added to alumina-doped TiO₂ which were used to understand dispersant degradation.

Finally, David Morgan helped with XPS data collection (shown in Chapter 5 and paper 4) which he performed at the EPSRC National Facility for XPS ('HarwellXPS'), operated by Cardiff University and UCL, under contract No. PR16195. I, the candidate, confirm that the experimental data acquisition, analysis and written work within this thesis has been my own and that any contributions from colleagues are explicitly referenced in the text.

This copy has been supplied on the understanding that it is copyright material and that no quotation from my thesis may be published without proper acknowledgement. The right of Laura Nicola Elliott to be identified as Author of this work has been asserted by her in accordance with the Copyright, Designs and Patents Act 1988.

Signed



Laura Elliott

201

Acknowledgements

My first acknowledgement is to my supervisor, Tim Hunter, thank you for your continuous support through this journey. You always believed in my scientific abilities, pushed me to achieve more when I needed it most, and gave me freedom to explore my thoughts. I cannot express in words how grateful I am to have you as my supervisor. Many thanks to my other supervisors, Richard and Ali, you have been a pleasure to work with and have supported me with my publication writing throughout my PhD. I would like to thank Venator for having co-founded this project, Stephen Sutcliffe and John Edwards, for their scientific advice, numerous site visits and their patience throughout the project, it has been a pleasure working with you.

To the technicians who have helped along the way, this would not have been possible without you! Ben Douglas, thank you for all your help in the particles lab and stopping me from going insane with the numerous corridor chats, always putting a smile on my face! A massive thanks goes to the CP3 CDT manager, Anoushka Kulikowski who has signed endless forms and booked many of my conference trips – I will forgive you for the 11-hour stopover in Abu Dhabi after my Australia conference!

To my colleagues at the University of Leeds, the Colloids and Polymer Group and the Complex Particulate Products Doctoral Training Centre, too numerous to name you all, but thank you for your continued support and scientific input over the years. My office friends who have endured scientific debates, helped solve numerous problems and been there to distract me from my work – I would not have got through this without you! A special thanks goes to David Austin, who has helped me with the adsorption and milling experiments presented in this work. Thank you, David, for your scientific input and many lifts to Weetwood and Venator – without your help this work would not have been possible either.

To my two close friends that I have made whilst at Leeds, Jess Shiels and Juliette Bebra, you have both made this journey memorable but for very different reasons! Juliette thank you for all you help with scientific discussions, proof reading and especially with dynamic light scattering! Thank you for putting up with my rugby talk every lunchtime! Jess, I still remember when we first started talking in the particles lab at Leeds! Thank you for making my time at Leeds so memorable, from our nights and other adventures!

To those I met at conferences and whilst teaching at the Brilliant Club, thank you for keeping my passion for science alive and questioning the purpose of my work. A special thanks goes to Nicole Hondow and Andy Brown, who over the years have both helped me become a better scientist and taught me how to question and defend my work. Thank you, Nicole, for all your help on the TEM and support throughout my PhD – I still remember all your post-it notes on my transfer report for agglomerates and aggregates!

To my family in Devon; mum, dad, sister and brothers, thank you for always believing in me and listening to me, even when you did not have a clue about what I was talking about! To my family in Bingley, Carol Anne and Karim, thank you for looking after me throughout this PhD. Karim, thank you for the endless Malaysian food especially during my write-up! Carol Anne, thank you for all your emotional support throughout the years and listening to me rant! A massive shout out to my friends outside of University, the Gilstead Crew who have got me through the last few years by distracting me from my PhD worries. A particulate tribute to my tag rugby team, Velococity, thank you for helping me achieve my dreams of playing for Great Britain, even during the most stressful time of my PhD, you have all made me laugh and helped me so much over the past few years.

Finally, I am most grateful for Hafiz Karim, you have never stopped believing in me and have always supported my decisions throughout my PhD. Thank you for putting up with my scientific rants and

proofreading my publications! You have always been there to distract me from this scientific journey, we have made many memories over the last few years and been on so many adventures to Europe, Malaysia and Australia! Thank you for helping me with the numerous job applications, a truly stressful time, but you were always there to pick me back up again when something went wrong. I am now looking forward to my next learning adventure!

“We cannot solve our problems with the same thinking we used when we created them” - Albert Einstein

Abstract

Synthesised particle products are often formed as agglomerates of finer single crystallites. Understanding the internal clustering and structure, as well as overall size and chemical nature is extremely important, as the performance of these systems (e.g. optical properties) may be dominated by these primary forms. For instance, inorganic agglomerates can be formed in high temperature flame reactors, as with the production of titanium dioxide. The structure of these species is a complex mix of source crystals and final aggregated or sintered particles. High quality manufacturing often demands tight control of the surface area, size, distribution and other properties (e.g. chemical homogeneity) for end user performance. Standard measurement techniques to analyse physical and chemical properties do not always discern the raw crystal properties present in final products and are often very time consuming (e.g. BET surface area measurements). Due to these limitations, manufacturing knowledge is often limited to ex situ characterisation of extracted samples, where access to fast parameter analysis would greatly enhance process monitoring and control capabilities.

The focus of this thesis was to investigate the limitations of using relaxation NMR to probe changes in TiO_2 particle size during milling. Furthermore, dispersants such as sodium hexametaphosphate (SHMP) are adsorbed onto the TiO_2 particles during milling, to reduce particle-particle interactions allowing the suspensions to be handled more easily. The influence that changes in surface chemistry may have on relaxation NMR results during milling has not previously been explored. Therefore, a further focus of this thesis was to understand changes in titania surface chemistry with milling and relate this to any changes observed in the NMR relaxation data.

Initially, dispersions of titania, calcite and silica with and without 1 M KCl were investigated by relaxation NMR. The surface area of two commercial titanium dioxide powders were measured with the use of a standard colloidal silica reference material. There was excellent agreement between the NMR and BET surface area measurements. The addition of salt showed no significant change to relaxation measurements for titanium dioxide; however, for suspensions of calcite and silica, a relaxation rate enhancement was observed. Differences were correlated to the surface charge state of the dispersions, with titania being uncharged while the calcite and silica were positively and negatively charged respectively. It is proposed that the NMR relaxation enhancement is due to counterions at the monolayer surface of charged particles. The implication of

these results is that the monitoring of suspensions for particles which are charged stabilised (e.g. not at their i.e.p) where electrolyte concentration may change overtime is extremely challenging, even more so when competitive effects such as changes in available surface area occur.

The use of relaxation NMR to measure the specific surface area of milled Al doped TiO₂ prior to SHMP adsorption was explored. After calibrating the relaxation NMR results for an Al rich particle surface (which was found to vary with milling time) there was then excellent agreement with the BET surface area measurements. Furthermore, relaxation NMR was used to generate a pseudo-isotherm for the adsorption of SHMP to Al doped TiO₂. The addition of SHMP caused a decrease in the specific relaxation rate enhancement (R_{2sp}), compared to that of the pure particle surface. This was due to the blocking of the Al-rich TiO₂ surface by SHMP extending into the solvent. The effect of milling time on the interaction between aluminium doped titania pigment particles and polyphosphate (SHMP) dispersant was studied. TEM highlighted the presence of ~20 nm titania fractured fines. To the author's knowledge fines have not previously been reported for the harder rutile morphology. Relaxation NMR data as a function of milling time showed a linear increase and no plateau was detected. The lack of this plateau was due to either an increase in surface area from fractured fines in samples milled for longer times, or an increase in SHMP concentration and/or dispersant restructuring at the particle surface; both leading to an overestimation of bulk surface area.

Elemental analysis by X-Ray fluorescence (XRF) showed (unwashed) samples milled for longer contained more phosphorus element, however, this additionally adsorbed polyphosphate was found to be weakly bound, as centrifugal washing showed it could be removed. Washed SHMP adsorbed aluminium doped TiO₂ was found to have faster relaxation rates, most likely due to the removal of SHMP exposing Al rich sites. The influence of milling time upon polyphosphate (SHMP) degradation and dispersion efficiency when adsorbed onto Al doped TiO₂ was investigated by X-ray photoelectron spectroscopy (XPS). A decrease in the P_{2p} concentration with increased milling time was observed for washed samples after allowing SHMP to completely absorb, thus indicating hydrolysis of SHMP occurs. Overall this thesis demonstrates the difficulties of characterising shear-dependent milled aggregates and the need for multiple characterisation techniques, alongside the potential of NMR relaxometry as an online-process control tool for not only detecting changes in surface area but also surface chemistry.

Table of Contents

Intellectual Property and Publication Declaration	iii
Acknowledgements	v
Abstract.....	vii
Table of Tables	xxi
Chapter 1 : Introduction	1
1.1 Research background and scope	1
1.2 Research question.....	3
1.3 Thesis delivery	4
Chapter 2 Literature review	6
2.1 Titanium dioxide production process and milling.....	6
2.1.1 Polymorphs, properties and uses	6
2.1.2 Feedstock for manufacturing TiO ₂	10
2.1.3 Chloride process	11
2.1.4 Sulphate process	12
2.1.5 Size reduction.....	13
2.1.6 Venator size analysis protocol	21
2.1.7 Venator business cycle.....	22
2.1.8 Surface treatment and properties	23
2.2 Polyphosphate interactions with titanium dioxide and clay surfaces	26
2.2.1 Adsorption mechanism.....	26
2.2.2 Stability.....	30
2.3 Relaxation NMR to probe colloidal particles.....	38
2.3.1 Introduction	38
2.3.2 Surface area determination and porosity.....	40
2.3.3 Specific ion effects.....	47
2.3.4 Frequency.....	50
2.3.5 Probing polymers, surfactants and surface chemistry	51

2.4 Summary.....	57
2.5 Research objectives.....	58
Chapter 3 Relaxation NMR theory and method.....	62
3.1 Relaxation NMR theory.....	62
3.2 NMR surface area theory.....	66
3.3 Expression of relaxation data to calculate porosity.....	68
3.4 NMR Experiments Materials and Methods.....	69
Chapter 4 Salt enhanced solvent relaxation and particle surface area determination via rapid spin-lattice NMR.....	71
4.1 Introduction.....	71
4.2 Materials and Methods.....	72
4.2.1 Materials.....	72
4.2.2 Sonication.....	73
4.2.3 Particle size and morphology.....	73
4.2.4 Settling measurements.....	74
4.2.5 Surface charge.....	74
4.2.6 Crystal structure.....	75
4.2.7 Surface characterisation.....	75
4.2.8 Relaxation NMR measurements.....	75
4.3 Results and Discussion.....	76
4.3.1 Particle characterisation.....	76
4.3.2 NMR relaxation calibration.....	82
4.3.3 Enhancement of specific solvent relaxation in high electrolyte conditions ...	83
4.3.4 Comparison of BET and NMR surface area determination.....	87
4.4 Summary.....	90
Chapter 5 Characterisation of polyphosphate dispersant interactions with aluminium-doped titania nanoparticles during milling.....	92
5.1 Introduction.....	92

5.2 Materials and Methods	93
5.2.1 Transmission electron microscopy (TEM)	94
5.2.2 X-ray diffraction (XRD)	95
5.2.3 Zeta potential characterisation.....	96
5.2.4 Dynamic light scattering (DLS).....	96
5.2.5 X-ray disc centrifugation (XDC)	97
5.2.6 Brunauer–Emmett–Teller (BET)	97
5.2.7 NMR relaxometry.....	98
5.2.8 X-ray fluorescence (XRF).....	98
5.3 Results and Discussion.....	98
5.3.1 Microscopy, elemental characterisation and crystal structure	98
5.3.2 Particulate surface charge and size changes through milling and washing ..	104
5.3.3 Surface area determination and NMR relaxometry of milled samples	111
5.4 Summary	116
Chapter 6 Degradation of polyphosphate dispersant interactions with aluminium-doped TiO ₂ during high shear-milling.....	118
6.1 Introduction	118
6.2 Materials and Methods	120
6.2.1 Materials	120
6.2.2 Purification of TiO ₂	120
6.2.3 Polyphosphate adsorption isotherm	120
6.2.4 Polyphosphate degradation experiments post-adsorption	122
6.2.5 Milling procedure.....	123
6.2.6 Zeta potential	123
6.2.7 Particle size	124
6.2.8 Surface area by BET.....	124
6.2.9 NMR relaxometry.....	124

6.2.10 X-ray photoelectron spectroscopy (XPS).....	124
6.3 Results and Discussion.....	125
6.3.1 Adsorption of polyphosphate onto Al doped TiO ₂	125
6.3.2 Al doped TiO ₂ surface area determination by BET and adsorption density comparison	130
6.3.3 Al doped TiO ₂ surface area determination BET and NMR comparison.....	132
6.3.4 Al doped TiO ₂ polyphosphate degradation after milling - probed by XPS.	134
6.3.5 Al doped TiO ₂ polyphosphate degradation after exposure to Ca ²⁺ and heat treatment - probed by XPS	142
6.3.6 Dispersion stability.....	147
6.4 Summary.....	153
Chapter 7 Conclusions and future perspectives	155
References	161
Research bibliography	175
Scientific journal and conference papers	175
Oral and poster presentations associated with this thesis	175
Scholarships and grants associated with this thesis	176
Appendix 1 Supplementary information to Chapter 4.....	177
Appendix 2 Supplementary information to Chapter 5.....	179
A2.1 Dynamic light scattering methodology.....	179
A2.1.1 Equations and fitting	179
A2.1.2 Details about the light scattering device used to check for multiple scattering and to check the diffusive nature of the fast mode relaxation time.....	181
A2.1.3 Checking the diffusive nature of the fast relaxation mode	181
A2.1.4 Dilution, filtration and reproducibility trials.....	183
A2.1.5 Checking the method to disperse TiO ₂ particles	184
A2.2 Characterisation of unmilled TiO ₂	186
A2.3 Additional data related to TiO ₂ particle size by TEM.....	187
A2.4 Additional EDS maps of TiO ₂	187
A2.5 Additional data comparing washed and unwashed TiO ₂ samples.....	189
Appendix 3 Supplementary information to Chapter 6.....	192
A3.1 Lab milling SHMP coverage calculations	192

A3.2 Venator calculations for polyphosphate adsorption.....	193
A3.3 XPS survey scans	195

Table of Figures

Figure 1-1: Schematic to show the organisation of this thesis.	5
Figure 2-1: Composite phase diagram for TiO ₂ (Nie et al. (2009)). The filled point shows the 0 K anatase-to-brookite transition pressure.	7
Figure 2-2: Market segments for TiO ₂ re-drawn from McNulty (2008).	8
Figure 2-3: The scattering power of Rutile titanium dioxide vs. particle size.	8
Figure 2-4: TEM micrographs of four commercial nanopowders of TiO ₂ (a) anatase and (b) rutile both supplied from Nanostructured & Amorphous (N&A). (c) TiO ₂ anatase from Degussa and (d) 90% anatase 10% rutile from TAL materials Inc (Mandzy et al. (2005)). Scale bars (a) 10 nm, (b) and (c) 50 nm, and (d) 200 nm.	9
Figure 2-5: TEM image of pigment-TiO ₂ composed of elongated particles in the range from 100 to 300 nm. Scale bar 100 nm.	10
Figure 2-6: Approximation of the milling rate parameter, here denoted K _p for different particle fractions of microcrystalline cellulose (MCC) (Kwan et al. (2005)).	14
Figure 2-7: Schematics to show particle size nomenclature Pilarska et al. (2014).	16
Figure 2-8: Milling curve schematic to show the breakage of TiO ₂ aggregates over time towards primary particle size (Lindberg et al. (2017)).	16
Figure 2-9: TEM micrographs of anatase powder ground with steel balls with various milling times (a) 0 mins, (b) 5 mins, (c) 15 mins and (d) 30 mins (Bégin-Colin et al. (2000)).	17
Figure 2-10: TEM of TiO ₂ scale bar 100 nm, (a) unmilled sample anatase type TiO ₂ with high energy ball milling for (b) 1 hour with powder to ball weight ratio (R) 1:50 and (c) milled for 10 hours with R 1:10 Gajović et al. (2001).	18
Figure 2-11: Slurry stability compared to zeta potential (Vallar et al. (1999)).	19
Figure 2-12: Titanium dioxide slurry (30 vol %) effect of changing pH on suspension rheology (Mikulášek et al. (1997)).	20
Figure 2-13: Schematic showing steric stabilisation of particles after adsorption of polymeric dispersant (He et al. (2004), Klimpel (1999)).	20
Figure 2-14: Influence of dispersant in aiding the grinding of dolomite by a stirred bead mill (Wang and Forssberg (1995), He et al. (2004)).	21

Figure 2-15: Zeta potential as a function of pH for pure Al doped TiO ₂ (solid) and pure SiO ₂ (dashed).....	24
Figure 2-16: TEM images of Si-coated Al doped TiO ₂ at high (a, b) and low (c) mixing intensities, as well as (d) Co-oxidised (Teleki et al. (2008))......	25
Figure 2-17: TEM images of silica and alumina coated rutile TiO ₂ after various pre-dispersant treatment (Dong et al. (2018)). Scale bar 50 nm.....	26
Figure 2-18: SHMP chemisorption to TiO ₂ resulting in bidentate complexation through Ti-O-P bonds at the terminal group ends of SHMP.	27
Figure 2-19: Adsorption isotherm for polyphosphate adsorbed onto Al doped TiO ₂ pigment with two different Al surface concentrations (Taylor et al. (2001)).	27
Figure 2-20: Michelmore et al. (2000), adsorption isotherms for polyphosphate adsorbing onto TiO ₂ at (a) pH 4 and (b) pH 9.1	28
Figure 2-21: Zeta potential of Al doped TiO ₂ pigment nanoparticles after Calgon adsorption reported by Taylor et al. (2001).....	29
Figure 2-22: Comparison of streaming potential (open symbols) with the AFM measured diffuse layer potentials (filled symbols), as a function of increasing polyphosphate concentration in a background electrolyte (Feiler et al. (2000)).	30
Figure 2-23: Rulliere et al. (2012) report the composition of sodium hexametaphosphate 0.5% in aqueous solution (pH 5.6) after heat treatment for 10 minutes at 100 and 120 °C	31
Figure 2-24: Thilo (1965), degradation of polyphosphates proceeding by mono-phosphate units removal.	33
Figure 2-25: Thilo (1965), degradation of polyphosphates leading to the formation of trimetaphosphates and shorter anion chain.	33
Figure 2-26: Thilo (1965), chelation of polyphosphates to cation resulting in more positive phosphorus atom which can further promote hydrolytic degradation.	33
Figure 2-27: TiO ₂ suspension (50 wt.%) yield stress with polyphosphate (Calgon T) concentration.	34
Figure 2-28: TiO ₂ suspension (50 wt.%) yield stress with polyphosphate (Calgon T) as a function of pre-treatment time. (a) 25 °C and (b) 90 °C (Farrokhpay et al. (2012)).....	35

Figure 2-29: Andreola et al. (2006), molar concentration of SHMP (measured by inductively coupled plasma spectroscopy) remaining in solution after adsorption onto kaolin as a function of aging time (left) and apparent viscosity (right).....	36
Figure 2-30: Isotherms for adsorption of SHMP onto kaolinite at two different kaolinite volume fractions at neutral pH and 20 °C, reported by Castellini et al. (2005).....	37
Figure 2-31: 13 MHz benchtop spectrometer (Xigo (2019)).....	39
Figure 2-32: Relaxation rates for various fumed silica powders, Davis et al. (1987) (left)	41
Figure 2-33: (a) Fairhurst et al. (2016), nanocarbon blacks with vary primary particle sizes dispersed in tetrahydrofuran with surface area calculated from T_2 relaxation data compared to TEM surface area	42
Figure 2-34: Zhang et al. (2017) R_{2sp} of differently sized original and hydroxylated silica in different solvents, namely, Milli-Q water (a) and n-hexane (b), as a function of the volume ratio between the particle and liquid (ψ) in each system.	44
Figure 2-35: R_{sp} against silica concentration in the presence of salts: (x) No salt, (Δ) 1.25 mM $MgCl_2$, (\square) 5 mM $MgCl_2$, (\diamond) 5 mM $CaCl_2$, and (O) 5 mM $LaCl_3$ by Flood et al. (2006) (left). NMR relaxation study of negatively charged sulphate-stabilised polystyrene latex nanoparticles (466 nm) in the presence of 0.25 M NaCl (open) and in water (closed) by Schwarz and Schönhoff (2002) (right).....	48
Figure 2-36: Van der Beek et al. (1991) spin-lattice relaxation rates of silica (circle) at 5.15 w/w% with varying pH and pure water (square) (Cooper et al. (2013(a)).....	49
Figure 2-37: Variation of T_1 with surface area, concentration and frequency for water with controlled pore glass samples by Glaves et al. (1988).	51
Figure 2-38: Adsorption isotherm of PVP onto colloidal silica (Δ) and alumina-modified silica (\blacktriangle) by Cooper et al. (2012). Pseudoisotherm generated from NMR data for silica (\circ) and alumina-modified silica (\bullet). The R_{2sp} is the measured R_2 scaled to an equivalent sample of bare particle to remove the effect of increasing surface area.	52
Figure 2-39: ΔR_{2sp} of the adsorption of a 1st layer to polystyrene latex particles. Filled symbols: PAH in H_2O , open symbols: PAH in 0.25 M NaCl. Reported by Schwarz and Schönhoff (2002).	53

Figure 2-40: Specific relaxation rate enhancement (R_{2sp}) as a function of macroinitiator to particle ratio for 5 wt. % dispersions of 120 nm diameter silica in water Cheesman et al. (2013).	54
Figure 2-41: Surfactant concentration (prior to adsorption on kaolin) versus water T_1 values for solutions of the three surfactants SDS, TTAB, and DTAB adsorbed on unwashed kaolin by Totland et al. (2011).	55
Figure 2-42: Nelson et al. (2002), show the displacement of preadsorbed PEO on silica particles by PVP.	56
Figure 3-1: Energy levels for nucleus with spin number equal to $\frac{1}{2}$ (Hore (2015)).....	63
Figure 3-2: The adsorption of radiation by a nucleus in a magnetic field.....	64
Figure 3-3: T_1 relaxation mechanism (Tadanki (2018)).	64
Figure 3-4: Illustration of the inversion recovery method by Currie et al. (2013).....	65
Figure 3-5: T_2 relaxation mechanism redrawn from Ridgway (2010).	66
Figure 3-6: Exchange of bound and bulk solvent, due to fast exchange only an average relaxation rate is measured by NMR (R_{av}).	67
Figure 4-1: SEM images of (a) calcite, scale bar 10 μm and inset scale bar 5 μm . SEM images of (b) titanium dioxide (TiO_2^a) scale bar 1 μm and inset scale bar 300 nm.	77
Figure 4-2: Zeta potentials for TiO_2^a (triangle), calcite (circle), and silica ^b (square) in background electrolyte (1×10^{-4} M KCl).....	77
Figure 4-3: Particle size distributions from laser diffraction for sonicated calcite (circle), and TiO_2^a (triangle) dispersions without salt.	78
Figure 4-4: Particle size distribution from dynamic image analysis (a) TiO_2^a (triangle), and (b) calcite (circle), both in the presence of 0 M KCl (closed) and 1 M KCl (open).	79
Figure 4-5: Dynamic light scattering particle size distribution for silica ^b particles after 24 hours of mixing on carousel at 1 wt%, in the presence of 0 M KCl (closed) and 1 M KCl (open).	79
Figure 4-6: TEM images of silica ^b nanoparticles, scale bar 250 nm and inset scale bar 100 nm.....	80

Figure 4-7: Average Lumisizer interface versus time measurements at 300 rpm for 1 vol% dispersions undergoing sedimentation, of TiO_2^a (a) and calcite (b) in 0 M (black closed), 0.1 M (red open) and 1 M (black open) KCl.	81
Figure 4-8: TEM images of Ludox AS-40 silica ^a nanoparticles, scale bar 100 nm and inset silica ^a scale bar 20 nm.	81
Figure 4-9: Calibration measurements for silica ^a (Ludox standard) particles (a) relaxation time vs particle volume ratio and (b) average relaxation rates with the product of increasing particle volume ratio and known silica ^a surface area ($137 \text{ m}^2/\text{g}$).	82
Figure 4-10: (a) shows average relaxation times for TiO_2^a with increasing particle concentration. (b) Relative relaxation rate enhancement (R_{sp}) for TiO_2^a with increasing particle concentration in 0 M KCl (closed triangle) and 1 M KCl (open triangle).	84
Figure 4-11: Relative relaxation rate enhancement (R_{sp}) for (a) calcite and (b) 100 nm silica with increasing particle concentration in 0 M KCl (closed circle) and 1 M KCl (opencircle).	85
Figure 4-12: Schematic to show the difference in relaxation times for TiO_2 and Calcite in water and high electrolyte concentration.	87
Figure 5-1: (a) TEM image of TiO_2 particles after milling for 1 minute. (b) High magnification image of a TiO_2 nanoparticle after 1 minute of milling to show the lattice fringes.	99
Figure 5-2: (a) & (b) TEM images of TiO_2 particles after milling for 32 minutes (particle fines electrostatically aggregated highlighted by the arrow in (b)). (c)	100
Figure 5-3: (a) STEM image of TiO_2 milled for 32 minutes with EDS maps showing spatial distribution of relative elements.	101
Figure 5-4: (a) X-ray diffraction (XRD) pattern of 1 (black) and 32 minute (red) milled TiO_2 samples compared to anatase (Horn (1972)) and rutile (Okrusch (2003)) crystal structures.	102
Figure 5-5: (a) Zeta potential of aluminium doped TiO_2 particles in the presence of sodium hexametaphosphate (SHMP) for 1 and 32 minutes of milling.	105
Figure 5-6: X-Ray fluorescence data showing the relative difference in phosphorus content for 1, 16 and 32 minute milled TiO_2 particles, before and after centrifugal washing.	107

Figure 5-7: Intensity auto-correlation data from DLS measurements of TiO ₂ suspensions prepared from 1 (a) and 32 (b) minute milled samples.....	109
Figure 5-8: Particle diameter of unmilled and milled TiO ₂ particles measured using dynamic light scattering (DLS). Also shown is the particle size measured by x-ray disc centrifugation (XDC) and transmission electron microscopy (TEM) with associated standard error.....	110
Figure 5-9: Brunauer–Emmett–Teller (BET) surface area for milled TiO ₂ particles (left-hand side) with polynomial fit to guide the eye, and the calculated particle size based on a spherical shape (right-hand side) as a function of milling time.....	112
Figure 5-10: (a) T ₁ relaxation rate enhancement (R _{sp}) for unmilled and milled TiO ₂ particles compared to bulk water (T _{1, water} ~ 2,600 ms), with error bars representing the maximum standard deviation for washed and unwashed samples.	113
Figure 6-1: Linear plot of SHMP adsorption used to calculate the Langmuir isotherm parameters (at room temperature).	121
Figure 6-2: Zeta potential for unmilled Al doped TiO ₂ in 1 mM NaCl background electrolyte.....	125
Figure 6-3: Adsorption isotherm of SHMP on unmilled Al doped TiO ₂ at pH 4 in 1 mM NaCl by ICP-OES (black, closed).	126
Figure 6-4: Al doped TiO ₂ pigment particle surface charge with increasing polyphosphate (SHMP) concentration with the standard error shown.....	128
Figure 6-5: Al doped TiO ₂ pigment particle sedimentation velocity (measured using the Lumisizer) with increasing polyphosphate (SHMP) concentration.....	129
Figure 6-6: (a) Surface area for Al doped TiO ₂ reactor discharge with milling measured by BET and T ₂ relaxation NMR.	133
Figure 6-7: Elemental quantification of milled samples (washed) and un-milled (washed and un-washed*) obtained from XPS analysis, shown as a relative concentration to Ti (%) (Ti = 100 %) for the P _{2p} and Al _{2p} compositions.....	135
Figure 6-8: P _{2p} band for milled samples (washed) and un-milled (washed and un-washed*), fitted to a gaussian distribution shown in red.	136
Figure 6-9: O1s peak with fitted components for (a) Al doped TiO ₂ (unmilled), (b) SHMP and (c) Al doped TiO ₂ unmilled with adsorbed SHMP.....	139

Figure 6-10: O1s peak with fitted components bridging oxygen (BO) and non-bridging oxygen (NBO) for Al doped TiO ₂ with adsorbed SHMP after milling for (a) 0 min, (b) 2 min, (c) 30 min and (d) 60 min.	139
Figure 6-11: Elemental quantification from XPS data, shown as a relative concentration to Ti (%) for 0 min milled Al doped TiO ₂ with adsorbed SHMP (grey) which has been subjected to different processing conditions after SHMP adsorption, Ca ²⁺ at room temperature (green), Ca ²⁺ at 100°C (blue) and 100°C (pink).....	142
Figure 6-12: Surface charge of SHMP adsorbed onto Al doped TiO ₂ under different processing conditions.....	148
Figure 6-13: Size of Al doped TiO ₂ with SHMP adsorbed as a function of milling time after dispersing at pH 9. Also shown is an unmilled sample without SHMP.....	150
Figure 6-14: Relaxation NMR (a) T ₁ and (b) T ₂ for Al doped TiO ₂ particles with SHMP and without under different pH conditions. The error bars show the maximum standard error recorded under the different pH conditions.....	151

Table of Tables

Table 2-1: Thoma et al. (1993), NMR static slurry particle surface area measurements for TiO ₂ samples, aluminosilicate coated rutile R900 and 902dd, and uncoated 101dd. An additional silica measurement was made F2849 for material comparison. The materials were prepared at various weight concentrations and compared to classical BET surface area measurements (all values in m ² /g).....	45
Table 2-2 Summary of parameters effecting NMR relaxation signal.	60
Table 4-1: Summary of NMR constants, gradients of the R _{sp} /Ψ _p plots with and without KCl, where the ratio of this change in gradient has been calculated, and ratio of the gradient between salt and no salt.	85
Table 4-2: Comparison of the calculated NMR surface area (SA), BET and calculated spherical surface area obtained from the particle size distribution for silica ^b , TiO ₂ ^a , TiO ₂ ^b and calcite.	87
Table 5-1: Crystallite sizes calculated from Gaussian fitting of the (110) and (121) XRD peaks for 1 and 32 minutes milled TiO ₂	103
Table 6-1: Calculated parameters using the linearized form of the Langmuir equation and standard error shown.....	122
Table 6-2: The maximum adsorbed amount of polyphosphate onto Al doped TiO ₂ pigment using the Langmuir equation.....	130
Table 6-3: Comparison of BET surface area and size for (a) lab milled Al doped TiO ₂ without polyphosphate after 30 minutes of milling. (b) milled Al doped TiO ₂ with polyphosphate supplied by Venator (as characterised in Chapter 5).....	131
Table 6-4: Al concentration (%) determined by XPS for milling Al doped titania pigment in the presence of SHMP.....	135
Table 6-5: P _{2p} band fitted peak width (FWHM) and position as a function of milling time for washed and un-washed* TiO ₂	137
Table 6-6: P 2 _{p3/2} binding energy values reported in the literature for different phosphate compounds (Moulder and Chastain (1992), Naumkin et al. (2000)).	138
Table 6-7: O1s components for the bridging oxygen (BO) (P-O-P bonds) and the non-bridging oxygen (NBO) (Ti-O-P and P=O bonds) as a function of milling time.....	140

Table 6-8: XPS P2p and Ca2p bands peak position and FWHM shown for 0 min milled TiO₂ with different processing conditions. Also shown is the quantification (%) relative to the Ti element..... 145

Table 6-9: O1s components for the bridging oxygen (BO) (P-O-P bonds) and the non-bridging oxygen (NBO) (Ti-O-P and P=O bonds) for 0 min milled TiO₂ with different processing conditions..... 146

Chapter 1 : Introduction

1.1 Research background and scope

This project stems from the need of numerous industries to characterise and monitor particulate dispersions online and *in situ*. Titanium dioxide, is a pigment used across a wide range of consumer products, from paints and cosmetics to pharmaceutical, and more still in plastics (Zhao et al. (2014b), Xiong et al. (2013), Zhang et al. (2011), McNulty (2008)). The size of titanium dioxide is one key physical parameter used to provide whiteness and brightness to consumer goods (Manuel Jesús Gázquez (2014), McNulty (2008), Braun et al. (1992)). The TiO₂ particle size is controlled during synthesis and after the reaction by ball milling. Currently, TiO₂ is manufactured in a continuous process with concentrations up to 500 g/L and the monitoring of particle size is obtained by dynamic light scattering (DLS) (Sutcliffe (2016)). Inherently, DLS requires dilute dispersions and spherical shaped particles in order to obtain accurate results. Thus, to monitor the size of TiO₂ during the production process, aliquots must be removed and diluted in water, not only is this time consuming but these measurements can also be misrepresentative of the bulk system.

The estimated TiO₂ market in 2014 was 6 million tonnes worth approximately \$13.5 billion globally (Zion (2016)). Despite this large demand for TiO₂, there is some stagnation in the technology used to monitor particle size, with measurements taking in excess of 75 minutes (Sutcliffe (2016)). It is thought that, the online monitoring of TiO₂ particle size could lead to a better understanding of the milling process and a reduction in the energy required to produce the pigment through more efficient milling control.

Nuclear magnetic resonance relaxometry (commonly called NMR relaxometry or more simply relaxometry), can be used to obtain particle specific surface area, even for highly concentrated slurries (Fairhurst et al. (2016)). In complete contrast to DLS, the calculations to obtain surface area from relaxometry data are not dependent on particle size or shape (Catherine L. Cooper (2013), Fairhurst et al. (2016)). Thus, making relaxometry an ideal candidate for an online process control tool, and thus the possibility of continuously monitoring particle surface area whilst milling. This research aims to explore the use of relaxometry to understand the TiO₂ milling process and its use for online monitoring. Furthermore, the development of an online size control tool whilst milling to understand particle size, is useful across a vast number of other segments, for example, the production of pharmaceutical excipients.

The NMR technique allows particles to be measured in the wetted state and hence avoids aggregation which is commonly encountered upon drying, which is required for many surface area techniques (Fairhurst et al. (2016)). Studying industrially relevant processes are often not straight forward as the dispersions are commonly highly concentrated, opaque and have a variety of inorganic contaminants (Fairhurst et al. (2016)). The current technological advancement of low field NMR spectrometers means they are small enough in size to fit onto benchtops, relatively inexpensive and are portable, thus allowing for the potential adaption to flow lines to monitor particle surface area and infer size. From an industrial perspective, this technique is innovative as it could allow particle characterisation without the need for dilution and measurements could be obtained within 1-15 minutes, (compared to current analysis of 75 minutes). This NMR technique has not been implemented within industry to understand particle size or structure as far as the author is aware, however, the technique of NMR relaxometry has been employed by the oil and gas industry to study rock formation porosity (Grunewald and Knight (2009)).

Extensive literature has been published using relaxation NMR for example, to determine porosity (Terenzi et al. (2015), Li et al. (2015)) and polymer adsorption events (Cooper et al. (2013(a)), Cooper et al. (2013(b))), however, it is limited for surface area measurements (Thoma et al. (1993), Davis et al. (1987), Glaves et al. (1988)). Regardless of the number of previous studies encountered in the literature, which span over a wide research area, there are still significant questions which hinder the application of NMR relaxometry for the measurement of colloidal surface areas. One area which remains relatively unexplored is the effect of electrolyte conditions on relaxation NMR (Flood et al. (2006), Schwarz and Schönhoff (2002), Katika et al. (2014)), this is of importance since industrial processes often contain background electrolytes, dopants and dispersants. It is unknown whether specific ion effects from bound counterion monolayers may enhance or reduce the relaxation rate for titania dispersions?

To reduce particle-particle interactions during milling, polyphosphate dispersants are adsorbed onto the aluminium doped TiO₂ nanoparticles to increase both electrostatic repulsion and stop agglomeration through increased steric hinderance. The adsorption density of polyphosphates onto TiO₂ and dispersion performance has previously been studied (Connor and McQuillan (1999), Farrokhpay et al. (2010), Farrokhpay et al. (2012), Michelmore et al. (2000), Taylor et al. (2001)). However, some studies have shown polyphosphate hydrolysis under extreme pH conditions, temperature and in the presence

of metal ions (Thilo (1965), Rulliere et al. (2012), Cini and Ball (2014), Rashchi and Finch (2000)). Despite this body of literature, there appears to be no studies relating to the influence of polyphosphate dispersant density and stability with mineral milling. It is unknown whether milling leads to structural changes in the dispersant through hydrolysis? Furthermore, does milling cause any changes in dispersant density due to localised thermodynamic events resulting from particle breakage events? It remains unclear to what extent dispersant chemistry changes during milling may influence relaxation NMR data interpretation.

Alumina (^{27}Al) is a quadrupolar nucleus and can cause an enhancement in the relaxation rate of bound solvent molecules at the colloid surface (Cooper et al. (2013(a))). Cosgrove et al. (1992) studied relative relaxation rates for alumina. They showed that the time bound water spends at the surface of a particle is not entirely determined by the surface charge of the particle. They showed that alumina had a faster relaxation rate than polystyrene latex, indicating a faster relaxation of bound water at the alumina particle surface due to surface hydroxyl groups which causes the motional restriction of water through specific interactions. Cooper et al. (2012) observed alumina-modified silica particles had a faster relaxation than those without alumina. Dopants are regularly added during the TiO_2 production process, for example, AlCl_3 is added to the reactor feed to control pigment aggregation and favour the rutile phase (Hartmann (1996), Braun et al. (1992), Wang et al. (2010)). Therefore, it is unknown to what extent aluminium doping may have on the NMR relaxation rates and if it is possible to accurately calculate changes in surface area with milling? Can such relaxation enhancements from Al at the particle surface mask surface area changes during milling? Furthermore, could the presence of Al complicate relaxation data especially if the concentrations of Al at the particle surface are not constant throughout the manufacturing process or during milling?

1.2 Research question

The main research question is to conclude if NMR relaxometry can be used to determine changes in particle surface area for complex agglomerated materials. This can be framed in a broad overarching research question such as, can NMR relaxometry be used as an online process control tool for monitoring such agglomerated materials, for example titanium dioxide, during a high energy intensive milling process? More academically challenging problems arise when interpreting data for the NMR technique which simultaneously probes interfacial chemistry and surface area. Such questions include the

uncertainties in NMR measurement reliability in the presence of additives, such as dopants, salts and dispersants.

1.3 Thesis delivery

The current knowledge has been assessed around the use of relaxation NMR to determine particle surface area and its wider uses to understand colloidal dispersions. These findings are detailed in the literature review presented in Chapter 2. Then, more specifically the relaxation NMR methods and theory have been detailed in Chapter 3. In order to answer the research questions previously discussed, the use of solvent relaxometry to determine particle surface area has first been explored for commonly encountered particles, such as, calcium carbonate, silica and titanium dioxide, these results are shown in Chapter 4. Furthermore, Chapter 4 also explores the influence of electrolyte on relaxation NMR. Chapter 5 details the characterisation of Venators milled pigment particles which are aluminium doped and contain adsorbed polyphosphate dispersant. Chapter 5 continues to demonstrate the relaxation NMR technique in the presence of aluminium and discusses the challenges of interpreting relaxation data. Chapter 6 explores the potential degradation of polyphosphate interactions after milling pigment particles by using X-ray photoelectron spectroscopy (XPS). Finally, Chapter 7 summarises the key conclusions from each Chapter and suggests further work that is required to allow the full implementation of the relaxation technique to an online production process.

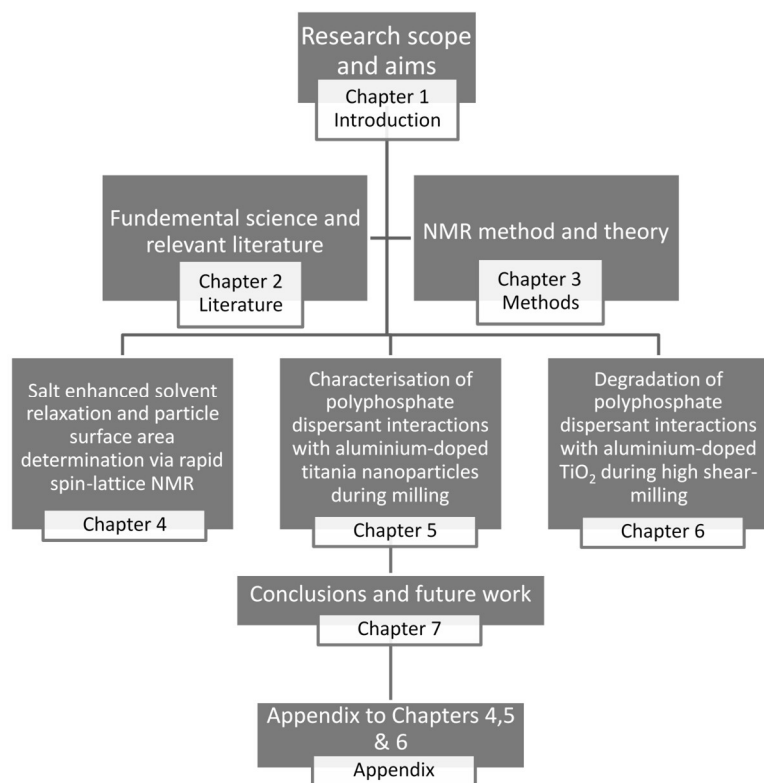


Figure 1-1: Schematic to show the organisation of this thesis.

Chapter 2 Literature review

This chapter has been broken down into three main sections. The first part provides information on the manufacturing of TiO_2 alongside the properties and application of the material. It is critical to know how TiO_2 is manufactured in order to understand what impact an online monitoring tool for particle size may have on the industrial process and how such a tool might be integrated into the production line. In addition, a literature review regarding the milling of TiO_2 and other ceramic materials has been included. A critical understanding of particle size and changes in surface area, that may occur during milling, is background knowledge that is required to aid the interpretation of relaxation NMR results for the milling of TiO_2 slurries. Furthermore, it is important to understand any chemical changes that may occur as a result of high milling energies, as any chemical changes may have a dramatic influence on relaxation signals. The second section explores literature regarding polyphosphate interactions with TiO_2 and other clay surfaces, which is essential to the understanding of relaxation rate changes and understanding how these interactions may be altered with milling. The chapter concludes with a literature review on NMR relaxometry and its uses within colloidal processing. This chapter aims to provide a deeper understanding on how relaxation signals can be used to understand complex colloidal systems, from basic surface area measurements to competitive polymer adsorption events.

2.1 Titanium dioxide production process and milling

2.1.1 Polymorphs, properties and uses

Titanium dioxide (TiO_2), also commonly called titanium (IV) oxide or titania, is an agglomerated inorganic particle which occurs in three abundant crystallographic forms; rutile (tetragonal), anatase (tetragonal) and brookite (rhombohedral) (M. Gardon and Guilemany (2014), Wang et al. (2010), Nie et al. (2009)). The phase diagram for these polymorphs is shown in Figure 2-1, where anatase occurs at lower temperatures and pressures, whereas, rutile is the high-temperature high-pressure phase (Nie et al. (2009)). The importance of the TiO_2 -II phase will be discussed in relation to phase transformations that can occur when grinding TiO_2 . The reason for introducing these polymorphs and phase diagram is to illustrate that different manufacturing routes are required. The two manufacturing routes to TiO_2 are the Chloride and Sulphate process.

Moreover, it is important to note that different polymorphs lend themselves to different uses due to their altered refractive index.

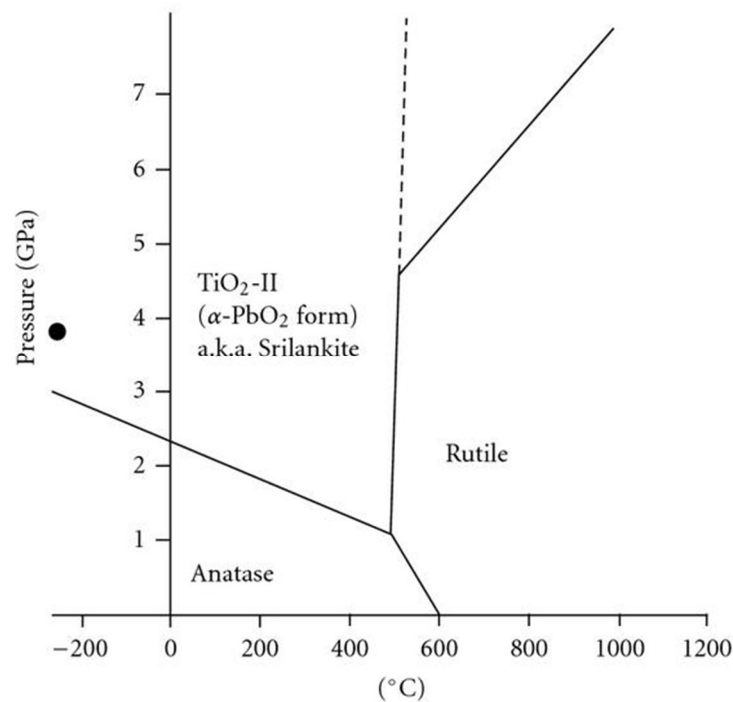


Figure 2-1: Composite phase diagram for TiO₂ (Nie et al. (2009)). The filled point shows the 0 K anatase-to-brookite transition pressure.

Titanium dioxide is a pigment used in paints, plastics, cosmetics, food and printing inks, providing whiteness and opacity to products (Zhao et al. (2014b), Xiong et al. (2013), Zhang et al. (2011), McNulty (2008)). Figure 2-2, shows the market segments for TiO₂ in 2007. The estimated market in 2014 was 6 million tonnes, worth approximately US\$ 13.5 billion globally (Zion (2016)). Functional TiO₂ (rutile type) is commonly used in emulsion paints and is made by the chloride or sulphate process (Sutcliffe (2016)). Whereas, ink and cosmetics customers require speciality pigment which is synthesised by the sulphate process (Manuel Jesús Gázquez (2014)). Speciality TiO₂'s are more expensive, as they are differentiated on performance (rather than price). This performance may derive from crystal form, crystal size or surface treatment. The use of surface coatings on TiO₂ will be expanded on later in this Chapter. Rutile pigments scatter light more effectively than anatase and thus are more commonly encountered in the paints, coatings and plastic

applications (Manuel Jesús Gázquez (2014)). Titanium dioxide is incorporated into plastic materials, where un-pigmented plastic remains translucent, this can be deemed unaesthetically pleasing, hence TiO_2 is added to create opacity, and also provide photo-durability (Braun et al. (1992)).

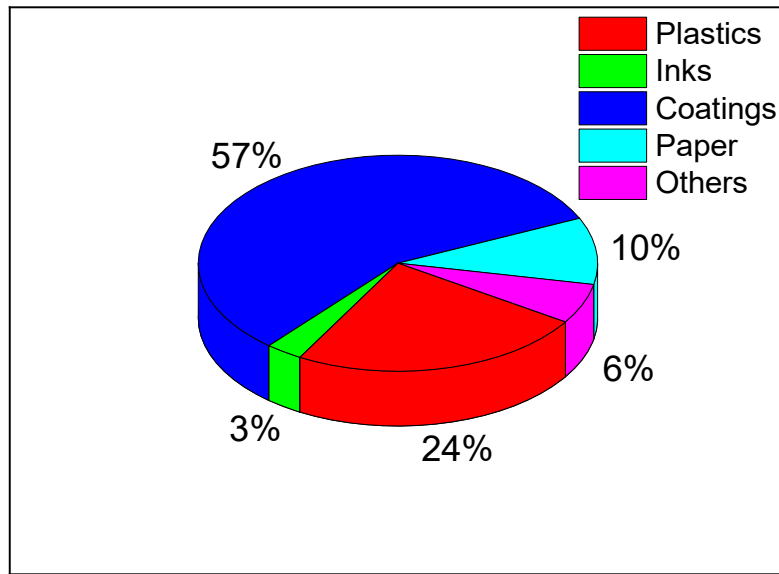


Figure 2-2: Market segments for TiO_2 re-drawn from McNulty (2008).

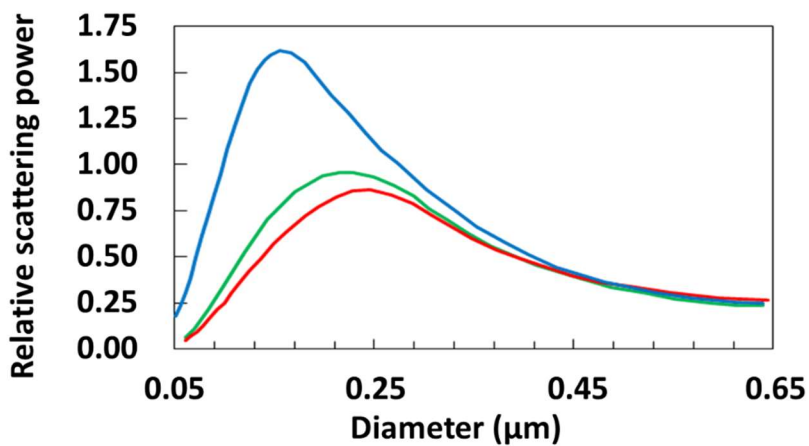


Figure 2-3: The scattering power of Rutile titanium dioxide vs. particle size. Where the optimum size is 200 nm, as the sum of the light scattered by all wavelengths is greatest (Sutcliffe (2016), Braun et al. (1992)).

The opacity and tinting strength of TiO_2 is dependent on the ability of the pigment to scatter light, which is governed by physical parameters such as, refractive index and particle size, but also by the TiO_2 content and dispersibility within a polymer matrix (Whiter than white (2002)). Tinting strength refers to the ability of TiO_2 to colour a product, for example, a plastic mould (Whiter than white (2002)). The higher the difference between the refractive index of a pigment and its surrounding medium (for example, the polymer matrix), the greater the light scattering ability (Whiter than white (2002)). TiO_2 has a high refractive index (RI) of 2.7 compared to other common white pigments for example, zinc oxide RI 2.0 and china clay RI 1.6, the high RI of TiO_2 gives the material high opacity and greater hiding power (ability to cover surfaces) (Manuel Jesús Gázquez (2014), McNulty (2008), Grubb and Bakshi (2011)).

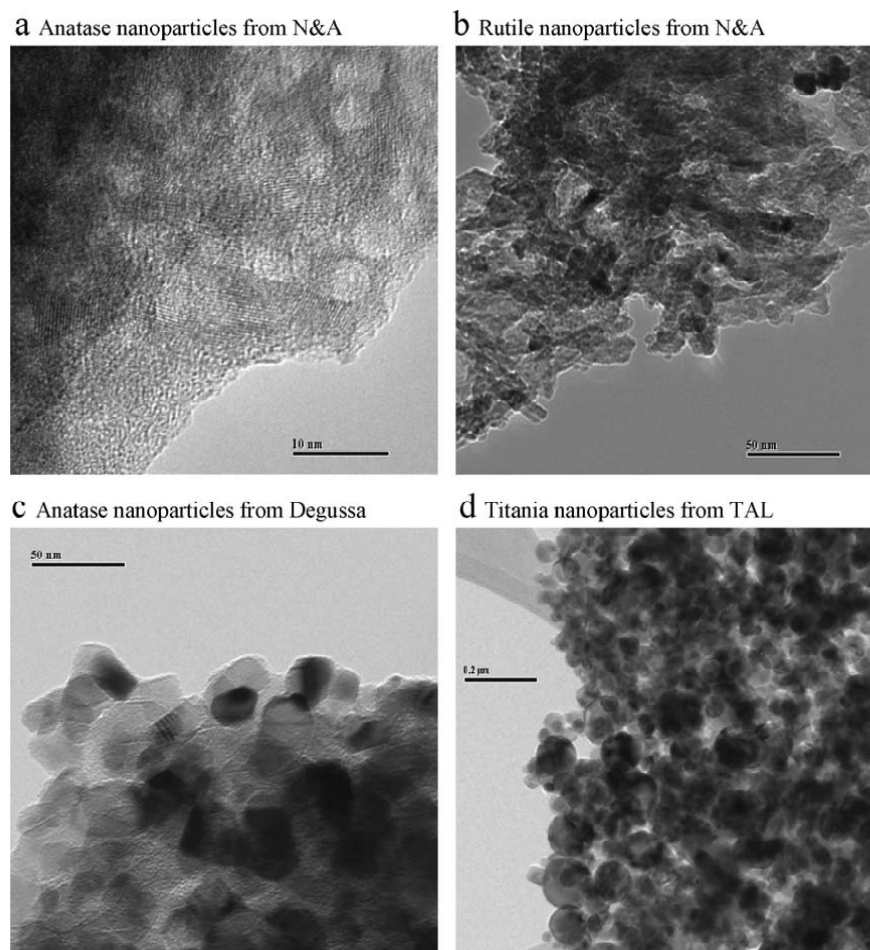


Figure 2-4: TEM micrographs of four commercial nanopowders of TiO_2 (a) anatase and (b) rutile both supplied from Nanostructured & Amorphous (N&A). (c) TiO_2 anatase from Degussa and (d) 90% anatase 10% rutile from TAL materials Inc (Mandzy et al. (2005)). Scale bars (a) 10 nm, (b) and (c) 50 nm, and (d) 200 nm.

TiO₂ particle size is important, as this controls the amount of scattered light (Figure 2-3). The optimum mean size is around 200 nm because the sum of the light scattered at each wavelength reaches its maximum (Manuel Jesús Gázquez (2014), McNulty (2008), Braun et al. (1992)). Examples of commercial TiO₂ nanopowders are shown in Figure 2-4, ranging in primary particle diameter between 5 and 100 nm (Mandzy et al. (2005)), due to the size of these nanoparticles, applications are most likely in thin nanocomposite films for the optical industry. The high surface energy of these particles causes aggregation and the formation of complex networks (Mandzy et al. (2005)). An example of pigmentary TiO₂ nanoparticles which are typically used in paints and plastics can be observed in Figure 2-5, here the nanoparticles range from 100 to 300 nm.

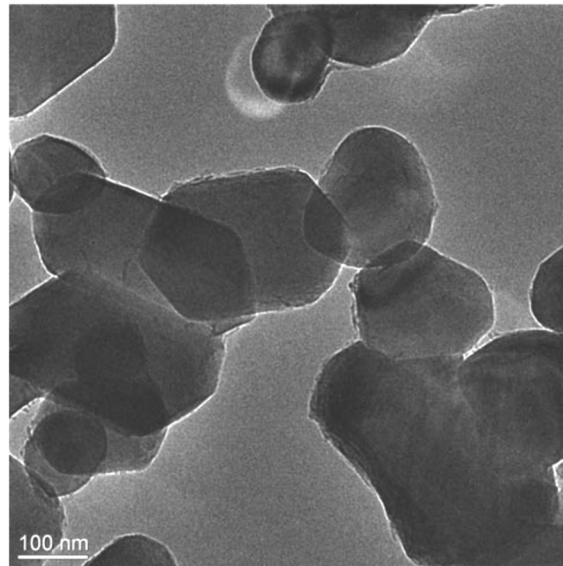


Figure 2-5: TEM image of pigment-TiO₂ composed of elongated particles in the range from 100 to 300 nm. Scale bar 100 nm.

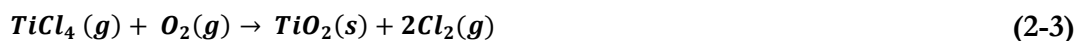
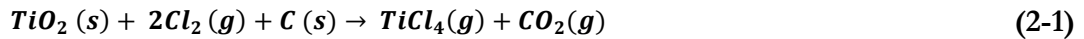
2.1.2 Feedstock for manufacturing TiO₂

The term feedstock refers to the numerous variety of natural and industrial titanium resources that are available to be used as a feed into the TiO₂ pigment manufacturing processes (Filippou and Hudon (2009)). Titanium ores are naturally occurring, the most commonly encountered being ilmenite (FeTiO₃), containing around 40-65 % TiO₂, due to its black colour the front end of the TiO₂ production process is commonly referred to as black sand (Manuel Jesús Gázquez (2014), Filippou and Hudon (2009)). Titania can

also be found as natural rutile, which has a TiO₂ content of 95 % and can be used as a raw TiO₂ material feed directly, compared to synthetic rutile which contains approximately 92 % TiO₂ (Zhang et al. (2011)). High titanium slag is obtained from smelting ilmenite ore, this feedstock contains around 85 - 90 % TiO₂ (Zhang et al. (2011), Filippou and Hudon (2009)). Higher grade TiO₂ feedstocks are mainly used in the chloride process and lower grades can be used for the sulphate process (McNulty (2008)).

2.1.3 Chloride process

The chloride process was commercialised by Du Pont in the 1950's, in the chloride process titanium dioxide present in the ilmenite ore, is reduced with carbon coke and then oxidised with chlorine in a fluidised bed reactor Eq. (2-1) (McNulty (2008), Braun et al. (1992)). This results in a gas stream, Eq. (2-1), containing impure TiCl₄, CO₂ and various other metals from the feedstock present as metal chlorides (McNulty (2008)). The TiCl₄ (g) is cooled using the recycled TiCl₄ (liquid feed), causing metal chlorides to separate out as solids, the TiCl₄ can then be condensed as a liquid, Eq. (2-2) (McNulty (2008)). TiO₂ rutile crystals are formed when titanium tetrachloride (TiCl₄) is oxidised in pure oxygen plasma or a flame, this occurs at high temperatures 1200-1700 °C and pressure (300 kPa) (Eq. (2-3)) (Braun et al. (1992), Wang et al. (2010)).



Dopants are regularly added during the chloride process for example; small quantities of AlCl₃ are added to the reactor feed to control pigment aggregation and favour the rutile phase (Hartmann (1996), Braun et al. (1992), Wang et al. (2010)). Quantities of aluminium containing dopants vary between 0.01 to 10 % and lead to the formation of the rutile phase (Mehdilo and Irannajad (2012)). It has been proposed that some Al dissolves into the titania lattice which enhances the phase transformation rate (Akhtar (1994)). Akhtar et al. (1991) studied the effect of process variables on titania using gas phase oxidation of titanium tetrachloride in a tubular flow reactor, concluding that increasing the temperature, reactant concentration and residence time led to the formation of larger titania particles Akhtar (1994). At higher reactor temperatures, particle collision frequency

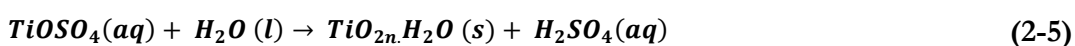
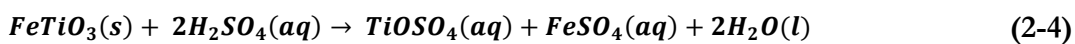
increases which results in larger aggregate sizes Akhtar (1994). Akhtar *et al.* (Akhtar et al. (1991), Akhtar (1994)) observed little change in the polydispersity index for titania particle growth suggesting that growth occurs by coagulation (Akhtar et al. (1991), Akhtar (1994)). The anatase to rutile conversion can be retarded by doping the TiCl₄ oxidation reactor with silicon, phosphorus and boron halides (Akhtar (1994)). Contradictions in reported literature results, can arise when studying doped TiO₂ systems, due to differences in sample preparation conditions.

2.1.4 Sulphate process

The sulphate process was the first commercialised technology used to obtain the titanium dioxide pigment, the process requires an ilmenite ore (FeTiO₃), which typically contains 40-60 % TiO₂ or titania-rich slag (Mehdilo and Irannajad (2012)). The ore or slag is digested in concentrated sulphuric acid, resulting in a liquor containing titanyl sulphate (TiOSO₄) and dissolved impurities, iron sulphate (FeSO₄) (Eq. (2-4)) (Zhao et al. (2014a)).

The by-product, iron sulphate is less soluble at low temperatures, and upon cooling crystallises, and is removed through filtration, thus, yielding the titanium salt (TiOSO₄), in the digest solution (Zhao et al. (2014b), Xiong et al. (2013)). The remaining aqueous digest is heated and water is added to hydrolyse the titanium salt, producing sulphuric acid and a precipitate containing hydrous TiO₂ (Zhao et al. (2014b), Xiong et al. (2013)) (Eq. (2-5)).

Water is removed in large rotary kilns and TiO₂ is calcined (a thermal treatment process), at 800–850 °C to produce anatase, or rutile alternatively, can be formed with the aid of seed crystals and calcination at 900–930 °C (Croce and Mousavi (2013), Heimann (2010)), (Eq. (2-6)). The acid that is released under hydrolysis in Eq. (2-5) is not strong enough to be directly used in the primary digestion step, thus it is either concentrated by heating and filtration cycles, or neutralised to produce gypsum which has industrial uses such as in plasterboard manufacture, agriculture and cement (McNulty (2008)).



The sulphate process can lead to more impurities due to co-precipitated Cr, Fe, and V which can lead to a reduction in pigment whiteness (Manuel Jesús Gázquez (2014), Sutcliffe (2016)). Crystal growth can be inhibited by the addition of phosphorus, which is not incorporated into the crystal structure but remains on the particle surface (creating an effective particle charge) (Braun et al. (1992)). The titana particle size can be optimised for the required light scattering, by controlling secondary growth regulators sodium and potassium sulphate (Braun et al. (1992)). The chloride process however, offers several advantages over the sulphate route such as; easier waste disposal with less environmental impact, as the chlorine is recycled (McNulty (2008), Braun et al. (1992)). Further to this, the chloride process yields a higher pigment quality with narrower size distributions (Braun et al. (1992)).

2.1.5 Size reduction

Milling is a process which causes the disintegration of solid particles by application of external forces, resulting in particle size reduction, and is used to obtain particles of a required size and shape (Baláž (2008)). The final quality of TiO₂ in consumer products is dependent on a number of factors however one key physical parameter that dictates overall whiteness and brightness is the crystallite size (Manuel Jesús Gázquez (2014), McNulty (2008), Braun et al. (1992)). After the synthesis of titanium dioxide, it is then wet-ball milled, dried, coated and finally supplied as a dried powder. Ultrafine grinding equipment is required to produce particles <1 µm, and ball mills (cylindrical type vessel), are widely used, here the milling energy is transferred through ball milling media (e.g. balls) (Salman et al. (2007)).

Ball milling is not a modern idea, in the 1870's it was used for the grinding of flint (Lynch and Rowland (2005)), some advantages are ball milling can be used both for wet and dry systems, and further batch or continuous processes (Salman et al. (2007), Bernotat and Schönert (2000)). Rotation of the cylindrical vessel results in a centrifugal force, causing balls to rise along the sides of the mill and down onto the material sample, thus causing impact and particle breakage. Milling rotational speeds are set to 80 % of the critical speed (N_c (rpm)) which can be calculated using Eq. (2-7), here, d_m and d_b are the mill and ball diameter respectively, in meters (Salman et al. (2007)).

$$N_c = \frac{42.3}{\sqrt{d_m - d_b}} \quad (2-7)$$

The performance of mills is affected by many different parameters, some suggest up to 44 parameters may affect grinding overall performance (Jayasundara et al. (2010)). The ball milling media is imperative, as the wrong choice can result in cross contamination of a sample, especially for repetitive milling processes and prolonged milling times (Becker and Schwedes (1999)). Examples of commonly used ball materials include steels, tungsten carbide, zirconia, alumina and silicon nitride (Baláž (2008), Wachtman (2009)). The density of the balls are required to be more dense than the material being milled, further to this, higher density, larger balls result in higher impact forces, giving better attrition results (Baláž (2008), Wachtman (2009)). Zirconium oxide, has very good abrasion resistance, high density (5.7 g/cm^3) (Baláž (2008)), and is used for the milling of titanium dioxide on an industrial scale. For optimum milling results, it is generally required 70-80% of the vessels volume should be filled with milling material and balls, thus leaving enough space for free movement and attrition to occur (Kwade (1999)).

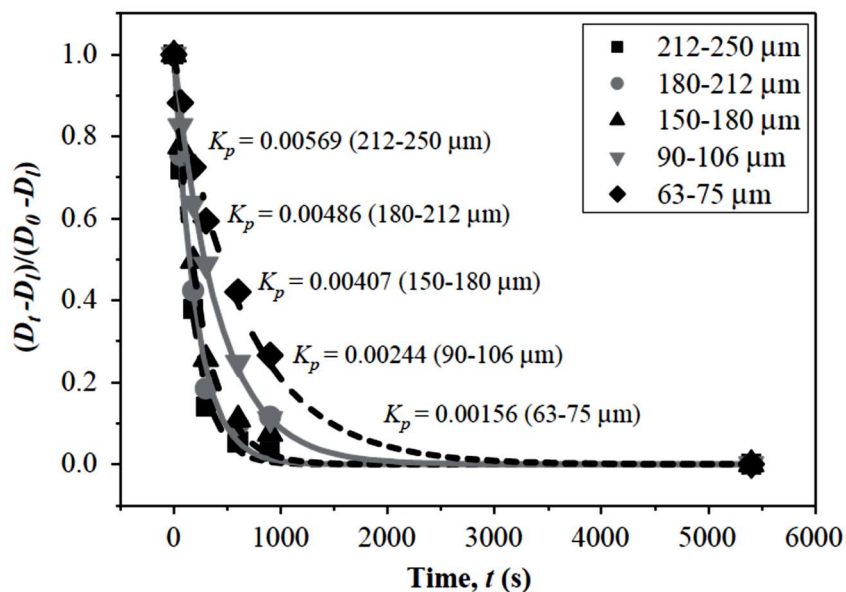


Figure 2-6: Approximation of the milling rate parameter, here denoted K_p for different particle fractions of microcrystalline cellulose (MCC) (Kwan et al. (2005)).

Milling time varies for each sample, and it should be noted that prolonged milling can lead to the contamination of ball milling media, and material phase transformations can occur (Baláž (2008), Gorrasi and Sorrentino (2015)). Significant reduction in particle size occurs during the first stage of milling following an exponential decay (Gorrasi and

Sorrentino (2015)), as milling time becomes less important once a critical size is reached and particle properties dominate over size reduction (Baláž (2008)).

Rittinger proposed a simple requirement of milling energy based on particle size reduction proportional to the surface area created, however, this is clearly a simplistic approach ignoring energy absorbed from elastic deformation (Baláž (2008), Duroudier (2016), Wills and Finch (2016)). The first order milling rate constant (k), can be given by Eq. (2-8), here, D_0 is equal to the d_{50} of the starting material. D_t is equal to the d_{50} of the material at time, t and D_l is the d_{50} of the sample at the milling limit (Kwan et al. (2005)). Figure 2-6 (Kwan et al. (2005)) shows how the rate constant can be determined thus allowing a numerical estimation of milling surface area with time. However, Figure 2-6, shows K_p can be approximated for large particle feed fractions, the mechanism of size reduction will occur through breakage of solid particles rather than in the case of TiO_2 breakage of aggregates, further to this primary particles are in the order of 250 nm for TiO_2 , which is not representative of particles shown in Figure 2-6. Therefore, the ability to calculate the milling rate constant using this method requires further investigation, for it to be used to approximate the surface area of TiO_2 primary particles numerically with increased milling time.

$$\frac{D_t - D_l}{D_0 - D_l} = \exp(-kt) \quad (2-8)$$

In order to control the size of the pigment a milling stage is required, (Story et al. (1994) US Patent 5,332,433) outline one process route to the production of the pigmentary TiO_2 through wet milling (Herkimer (1998)). Initially, the TiO_2 is dispersed in an aqueous medium to form a slurry, the material is then thoroughly milled, and hydrous oxides of alumina and silica are precipitated onto the titania surface, further followed by washing, drying and re-milling (Story et al. (1994), Herkimer (1998)). Hinley and Porter (1976), US Patent 3,942,999 and Berstein and G (1965), US Patent 3,212,911, also state the pigment is wet milled and coated with hydrous oxides. These hydrous oxides are used to alter the surface properties of the pigment and cause a reduction of titania dispersibility into plastics (Story et al. (1994)). In order to avoid the use of such inorganic oxides, polymeric flocculants can be used as an alternative, however, these result in undesirable impurities which drastically effect the quality of the final process product (Story et al. (1994)).

Despite the terms “agglomerate” and “aggregate” being widely used by powder technologists to describe a collection of particles found in dry powders, there is still confusion around the specific terminology (Nichols et al. (2002)). A powder will generally consist of a mixture of primary particles, agglomerates and aggregates, as shown in Figure 2-7 (Pilarska et al. (2014)). Primary particles are defined as well formed single crystals, or as a crystal composed of crystallites, but these can fracture when subjected to large mechanical stresses to give irregular shapes and sizes (Nichols et al. (2002)). It should be noted that throughout this discussion the term ‘aggregate’ is referred to as an assembly of primary particles which are sufficiently strongly bound that they require bead milling to break the particle-particle bonds. This contrasts to the term ‘agglomerate’ which is referred to as a collection of aggregated particles which has formed upon drying, these are softly bound and as later discussed can be broken by sonicating the suspension.



Figure 2-7: Schematics to show particle size nomenclature Pilarska et al. (2014).

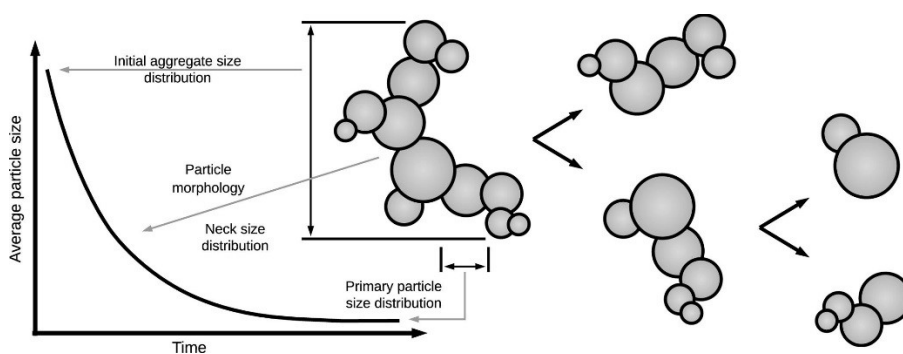


Figure 2-8: Milling curve schematic to show the breakage of TiO_2 aggregates over time towards primary particle size (Lindberg et al. (2017)).

It is important to differentiate that the milling of TiO_2 is based upon aggregate breakage rather than single particle breakage events, which would be encountered for example,

when milling the ore, Figure 2-8, shows a sketch of a milling curve for TiO_2 aggregates and how these reach the primary particle size with increased milling time (Lindberg et al. (2017)).

A vast number of studies have been conducted on the milling of TiO_2 aiming to determine the optimum milling control parameters for example, speed of agitation, ball size, filling ratio and suspension concentration (Lindberg et al. (2017)). Ohenoja et al. (2013) investigated milling surface un-modified TiO_2 in the rutile form with several different milling balls used (Glass, Zirconium oxide (ZrO_2) and yttria (Y_2O_3)-stabilized Zirconium oxide (YSZ)) using a stirred media mill which is representative of classically encountered tumbling ball mill. They found that the narrowest size distributions for a pigment target of 300 nm was achieved when the operational parameters had the lowest stress and specific energy consumption. They concluded that these parameters were Zirconium oxide milling media of 255 μm , tip speed 9.2 m/s with a solid concentration of 52 wt.% and fill ratio of 70 vol. %.

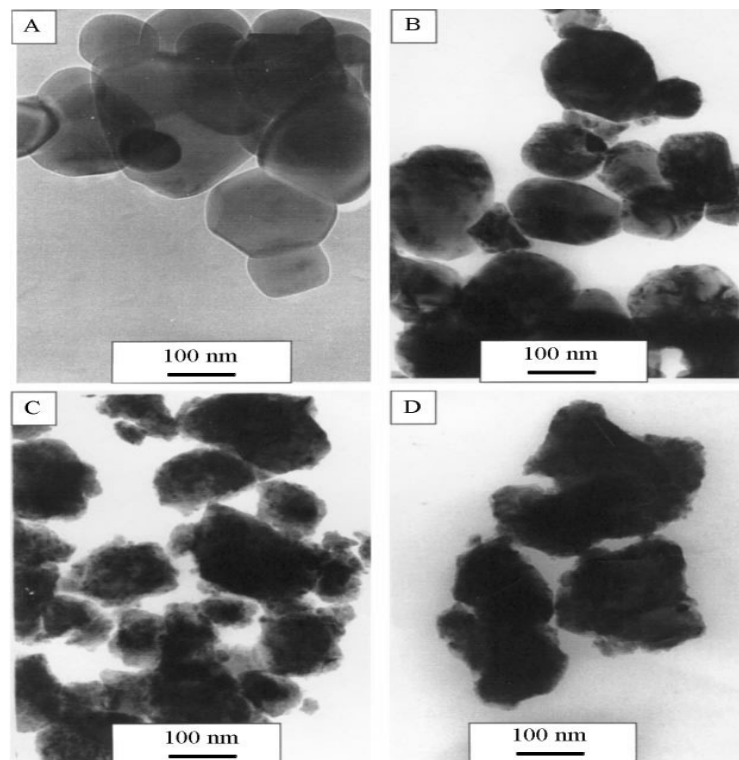


Figure 2-9: TEM micrographs of anatase powder ground with steel balls with various milling times (a) 0 mins, (b) 5 mins, (c) 15 mins and (d) 30 mins (Bégin-Colin et al. (2000)).

Similar studies have also been carried out by Bel Fadhel et al. (1999) and Inkyo et al. (2006). Interestingly, Inkyo et al. (2006) found that larger beads (50 and 100 μm) did not effectively break up nanoparticle agglomerates counter to the previously mentioned study, however, observed were altered structure and morphology of the nanoparticles, moving from rod shaped to more spherical with 100 μm beads. The structure and mechanical properties of titania have also been researched, Gesenhues (1999) monitored surface area using Brauner-Teller-Emmett (BET) obtaining surface areas for a 99% rutile TiO_2 between 6-8 m^2/g with 0 to 65 minutes milling.

Jeon et al. (2015) compare the wet milling of titania with alumina, which also involves the breakage of aggregates over time, they report with increased milling time alumina aggregates become more worm like whereas titania remains fairly spherical. More complicated phase transformations have been reported for the high energy ball milling of anatase, with prolonged milling times the rutile formation is observed through an intermediate TiO_2 II (Bégin-Colin et al. (2000)). Bégin-Colin et al. (2000) showed through TEM, polycrystalline particles with TiO_2 II grains at the surface of the anatase particles, after as little as 15 mins grinding the appearance of these fines are clearly present (Figure 2-9).

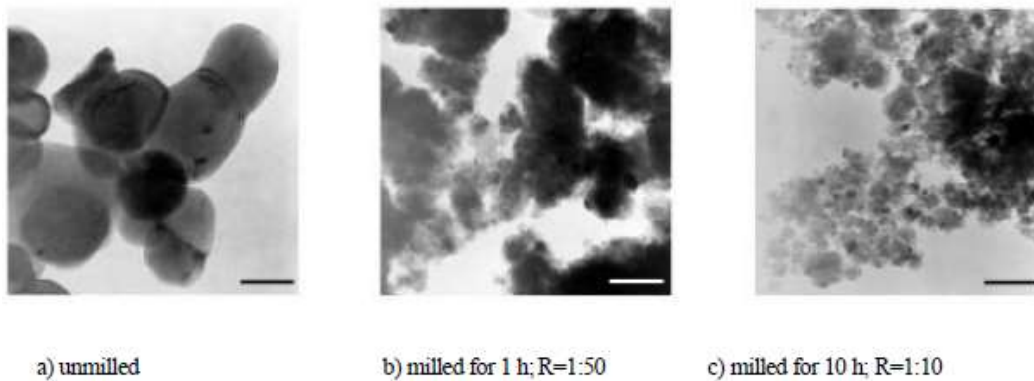


Figure 2-10: TEM of TiO_2 scale bar 100 nm, (a) unmilled sample anatase type TiO_2 with high energy ball milling for (b) 1 hour with powder to ball weight ratio (R) 1:50 and (c) milled for 10 hours with R 1:10 Gajović et al. (2001).

Gajović et al. (2001) also reported phase transformation from the anatase TiO_2 to the TiO_2 II phase which could be produced only at high pressure, and have investigated this change through Raman spectroscopy and TEM. Further work by Gajović et al. (2001) has shown the phase transformation with different powder to ball weight ratio (Figure

2-10). Sen et al. (2011) observed particle fines 40-50 nm in size after ball milling samples for 32 hours, and further milling for 100 hours caused disintegration of nanoparticles to sizes of ~13 nm. Both anatase and rutile can be transformed into TiO₂II with shear (Sepelak et al. (2012)). For example, Sepelak et al. (2012) observed TiO₂-II crystallites of 10 nm in diameter on the surface of anatase particles using high resolution TEM.

The vast amount of studies regarding the milling of TiO₂ suggests this process is clearly rather complicated, complementary to the milling of many materials phase transformations often occur. These studies become important and relevant to the research using NMR relaxometry, as the change in TiO₂ phase will have a profound effect on the relaxation signal due to a complete change in particle surface chemistry and this needs to be considered when interpreting NMR studies herein.

Interparticle forces that occur in an aqueous suspension are van der Waals, electrostatic forces and steric forces (if polymeric dispersants are present) (Leong and Ong (2015)). Since the zeta potential of a suspension is an indication of the magnitude of particle-particle repulsions it allows the inference of slurry rheology (Vallar et al. (1999)). This higher the zeta potential the more stable the suspension is likely to be due to electrostatic repulsion between particles, however, at the isoelectric point (when the zeta potential is zero) the particles will tend to agglomerate, as shown by Figure 2-11 (Vallar et al. (1999)). For oxides the potential determining ions are H⁺ and OH⁻ thus changing the pH of the liquid gives rise to a change in the particles surface charge and thus the slurry rheology can be altered, as shown by Figure 2-12 (Klimpel (1999)).

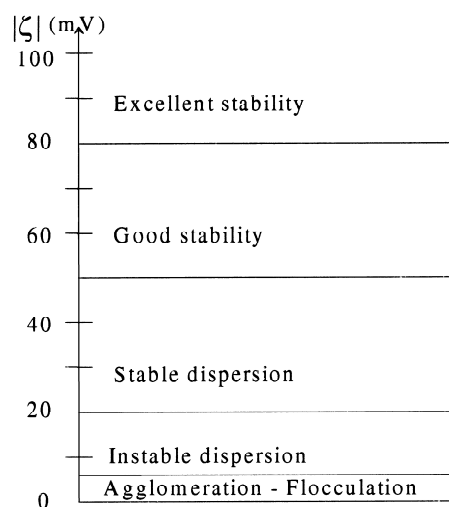


Figure 2-11: Slurry stability compared to zeta potential (Vallar et al. (1999)).

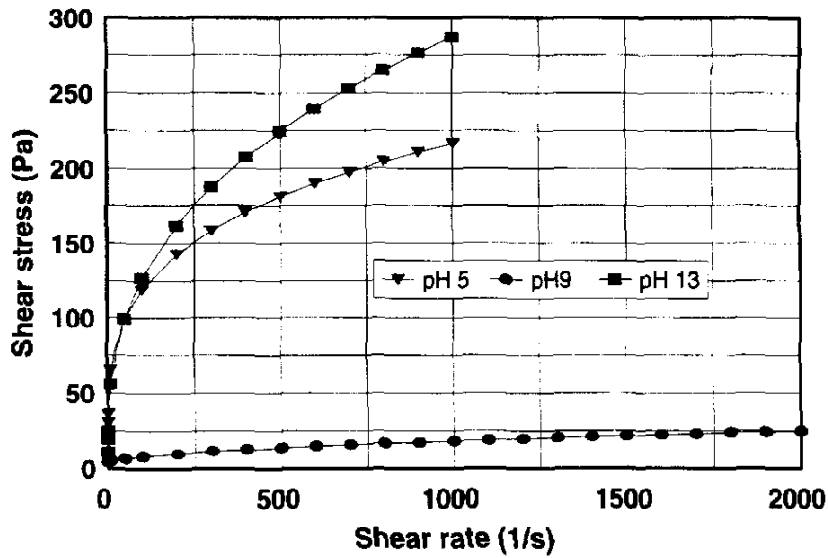


Figure 2-12: Titanium dioxide slurry (30 vol %) effect of changing pH on suspension rheology (Mikulášek et al. (1997)).

Fine grinding can cause aggregation and agglomeration of minerals, often to counteract this a dispersant is added, allowing milling to occur at much higher slurry concentrations (up to 80 wt.%) (He et al. (2004)). A steric force can be introduced from the adsorption of polymer molecules causing repulsive forces between particles at short distances, shown by Figure 2-13 (Klimpel (1999)). Importantly, for suspensions that are stabilized by polyelectrolytes (e.g. polyphosphates), the slurry behaviour can be described qualitatively as a collective effect of electrostatic and steric interactions (Velamakanni and Fuerstenau (1993), He et al. (2004)).

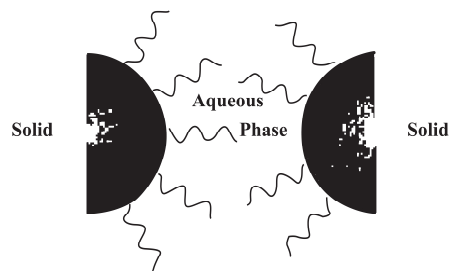


Figure 2-13: Schematic showing steric stabilisation of particles after adsorption of polymeric dispersant (He et al. (2004), Klimpel (1999)).

Wang and Forssberg (1995) studied the influence of dispersants including Dispex, Calgon (sodium hexametaphosphate (SHMP)), and tetrasodiumpyrophosphate (TSPOP), in aiding the grinding of dolomite by a stirred bead mill, of which they found Dispex gave superior dispersant performance in grinding energy efficiency (Figure 2-14). Dispersant type is one obvious key factor in determining the optimum dispersant for a milling process, however other important factors include the quantity of dispersant and solubility. Insufficient dispersant concentration can lead to particle aggregation as a result of patchy electrostatic charges and bridging flocculation, causing an increase in the suspension viscosity (He et al. (2004)).

Polyphosphate salts are widely used as dispersants in mineral and material processing industries, due to their ability to adsorb onto metal-oxides and clay-particle surfaces (Castellini et al. (2013), Castellini et al. (2005), Han et al. (2016), Wang and Forssberg (1995)). They are often added to the titania pigment suspension during processes such as milling, in order to improve the dispersion properties and reduce suspension viscosity (Taylor et al. (2001)), therefore for this reason a literature review will focus on this type of dispersant (see section 2.2). One commonly used polyphosphate reagent is Calgon, also known as sodium hexametaphosphate (SHMP).

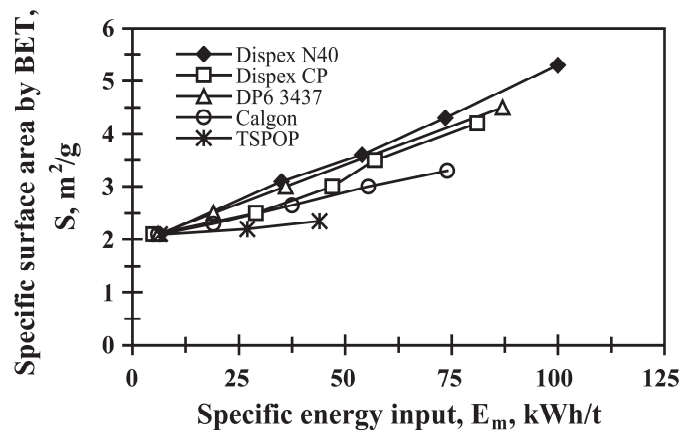


Figure 2-14: Influence of dispersant in aiding the grinding of dolomite by a stirred bead mill (Wang and Forssberg (1995), He et al. (2004)).

2.1.6 Venator size analysis protocol

As aforementioned, a small change in the size of TiO_2 leads to a significant change in the scattering ability of the pigment, further this can result in a change in the product

application. It is therefore extremely important to control the size of TiO₂ for the customers required needs, and typically the size is controlled during the milling stage of the production process as previously stated. Venator's current method (Sutcliffe (2016)) for the sizing of TiO₂ is obtained by removing aliquots of milled TiO₂ and diluting in water, and the size is calculated based on the scattering of different wavelengths of light (mie theory) (Braun et al. (1992)). The time taken to obtain the particle size distribution for the TiO₂ is approximately 75 minutes, from the moment the TiO₂ is made during synthesis (Sutcliffe (2016)). During this 75 minutes, a mill on the production plant might have failed, thus leading to a detrimental effect on the size distribution of TiO₂. When a problem comparable to this occurs, the TiO₂ is re-milled to the required size, wasting resources such as energy and time (Sutcliffe (2016)). This type of control process can be denoted as feed backwards, it would however, be desirable to have a method of continuously monitoring the size of the TiO₂, before and during the milling stage. This type of monitoring is known as online monitoring and would lead to a feed forward process.

2.1.7 Venator business cycle

In 2011, it was estimated the global demand for TiO₂ was expected to increase over the decade by 3% annually (Manuel Jesús Gázquez (2014)). Despite this, in 2013, global TiO₂ industrial production suffered stagnation with worldwide capacity at 6.56 million tonnes, whilst new capacity was mainly concentrated in China (Global and China Titanium Dioxide Industry Report (2014)). In 2013, China's production, stood at 2.94 million tonnes, accommodating 45% of the global production in 2013 compared to 30% in 2010 (Global and China Titanium Dioxide Industry Report (2014)). Venator's Pigments and Additives segment achieved sales of \$1.55 billion in 2014 and have 80 years of titanium dioxide pigment manufacturing experience, this is of significance as the partial sponsors of this PhD studentship (in conjunction with the EPSRC) (Sutcliffe (2016)). China produce lots of TiO₂ from the sulphate process (Xiong et al. (2013), Zhang et al. (2011), Sutcliffe (2016)).

Venator produced 770,000 tonnes per year (2015) of TiO₂ across eight global sites. The quality of the product is important as narrow size distributions and additional coatings add value (Sutcliffe (2016)). The sulphate and chloride process patents have expired, thus are widely available, and competition arises for either cheaper TiO₂ or higher quality pigment with added value. Venator's major competitors are Kronos, Chemours, Henan

Billions, Cristal, Tronox and Ishihara Sangyo Kaisha (ISK) (Sutcliffe (2016)). If competitors develop proprietary technology which could enable them to produce TiO_2 at a significantly lower cost, Venator's technology would need to catch up, hence the importance of developing new technologies that can increase the manufacturing efficiency of TiO_2 (Sutcliffe (2016)).

2.1.8 Surface treatment and properties

Nanoparticles have a large surface area compared to micro-sized powders, thus have a tendency to agglomerate (Jalili et al. (2016)), this is particularly undesirable for the application of TiO_2 as it leads to pigment crowding and a reduction in hiding ability or surface coverage. For TiO_2 end use, the structure and morphology of the coated film are important as they determine the final properties of the resultant material. Surface treatment of TiO_2 , for example with organic acid, is required to give dispersion properties in hydrophobic polymer matrices in plastics (Jalili et al. (2016)).

TiO_2 can also be inorganically surface coated in water by precipitation or adsorption, the most common coating additives include silica and alumina, however, others are reported such as zirconium, tin and boron, to name just a few (Braun et al. (1992)). Surface coating improves pigment performance in end-use applications, for example in paint, which requires the pigment to be durable, however optical properties must not be significantly impacted. Pigments must also be protected from UV degradation. Hydrous aluminium oxide particles coated onto the pigment result in a reduction in particle-particle interactions, and improved pigment dispersibility (Cole (1974)).

The zeta potential can be drastically altered after surface coating which can be useful if the pigment is required to interact with oppositely charged dispersants, as shown in Figure 2-15. Al doped TiO_2 nanoparticles have an isoelectric point (i.e.p) around $\sim\text{pH } 8$ dependent on Al surface concentration and this varies due to the presence of both AlOH and TiOH surface groups (Teleki et al. (2008)). The i.e.p of pure SiO_2 is $\text{pH } \sim 2$, surface treatment with SiO_2 causes the Al doped TiO_2 nanoparticles i.e.p to shift to between $\text{pH } 3-5$ dependent on SiO_2 concentration (Teleki et al. (2008)).

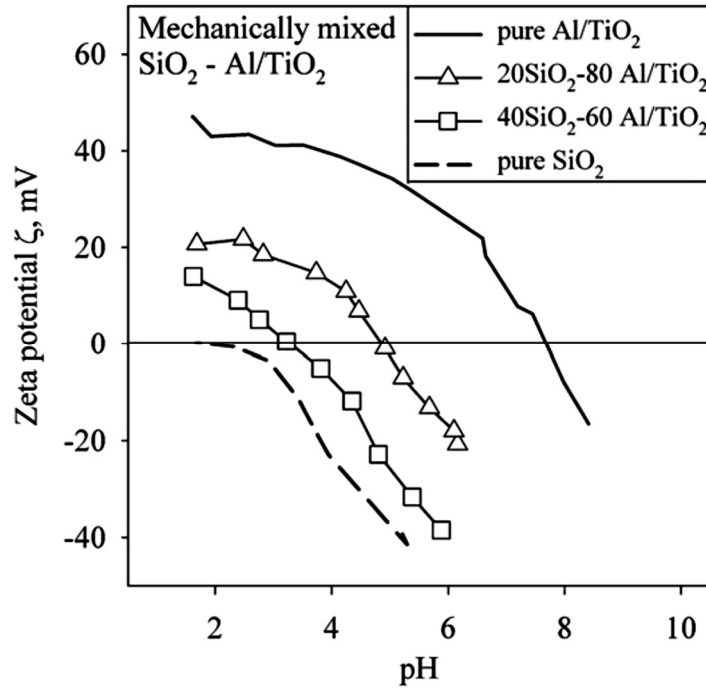


Figure 2-15: Zeta potential as a function of pH for pure Al doped TiO₂ (solid) and pure SiO₂ (dashed). Also shown are SiO₂ coated Al doped TiO₂ for different SiO₂ concentrations 20 % and 40 % Teleki et al. (2008).

Coherent and homogenous coatings on TiO₂ particles are required for optimal performance, however, characterisation of these nanoparticle surfaces especially during industrial manufacturing can be challenging, as TEM is required and gaining 1000 representative particles to analyse is time consuming and expensive (Teleki et al. (2008)). Thus, instead there has been extensive research around the quality of the coating from and academic research point, for example optimization of coating thickness. Several types of surface treatment methods exist and these include, deposition from the gas phase by hydrolysis, addition of oxides adsorbed during grinding and precipitation reactions (Nika (2018)). Figure 2-16 shows TEM images of SiO₂ coated Al doped TiO₂ nanoparticles. These coating appear homogenous in Figure 2-16 (a) and have thicknesses of 2 – 4 nm, although not shown in the TEM the coating thickness decreases with decreases SiO₂ concentration (Teleki et al. (2008)).

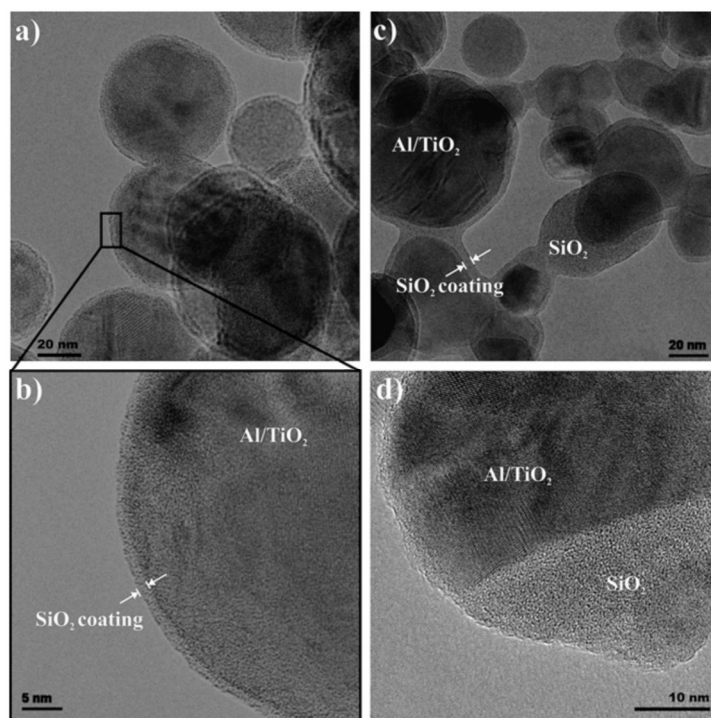


Figure 2-16: TEM images of Si-coated Al doped TiO_2 at high (a, b) and low (c) mixing intensities, as well as (d) Co-oxidised (Teleki et al. (2008)). Scale bars (a) 20 nm, (b) 5 nm, (c) 20 nm and (d) 10 nm.

The effect of using different pre-dispersants before the coating application has also been studied. This is important as during size reduction dispersants are adsorbed onto TiO_2 to reduce particle aggregation during milling which precede final particle coating application. Figure 2-17, Dong et al. (2018), shows silica and alumina coated TiO_2 nanoparticles with different pre-dispersants, from left to right the dispersants used were sodium silicate nonahydrate (SSNH), sodium hexametaphosphate (SHP), sodium dodecylbenzene sulfonate (SDBS) and polyethyleneglycol- 1000 (PEG).

Interestingly when the sodium hexametaphosphate was used, the silica layer detected was discontinuous, and silica particles appear agglomerated on the surface. In contrast when SSNH, SDBS and PEG were used the silica layers were more compact and continuous. In contrast, the surface morphologies of alumina coated rutile pigment after dispersing in SSNH, SDBS and SHP caused alumina aggregation on the surface of TiO_2 which would result in poor dispersion properties of the pigment despite a continuous coating being observed. When PEG was used as a pre-dispersant the hydrous alumina film had a fibrous structure, this would result in increased steric hindrance and electrostatic repulsion of the pigment particle which would therefore hinder particle agglomeration.

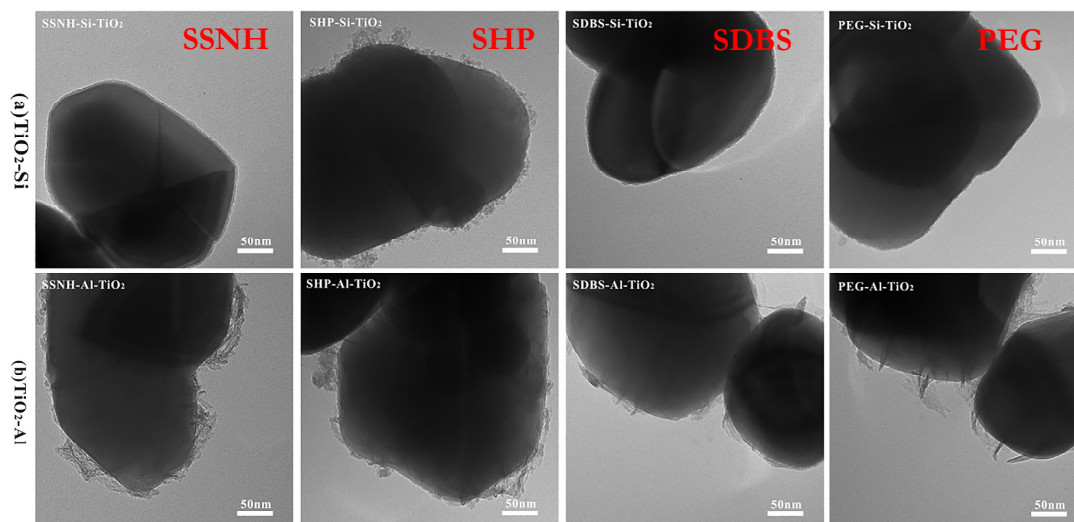


Figure 2-17: TEM images of silica and alumina coated rutile TiO_2 after various pre-dispersant treatment (Dong et al. (2018)). Scale bar 50 nm.

2.2 Polyphosphate interactions with titanium dioxide and clay surfaces

2.2.1 Adsorption mechanism

The adsorption of SHMP is known to occur to metal oxide surfaces, for example titanium dioxide (Taylor et al. (2001)) and clay particle surface including illite, montmorillonite, kaolinite and dolomite (Andreola et al. (2006), Castellini et al. (2005), Han et al. (2016), Castellini et al. (2013)). However, the adsorption chemistry is not trivial with both electrostatic and/or chemisorption possible. For titanium dioxide, the chemisorption mechanism of SHMP adsorption is dominant at pH 9 and complexation occurs through bidentate bridging thus forming Ti-O-P bonds (Figure 2-18) (Taylor et al. (2001)). Connor and McQuillan (1999) studied phosphate adsorption onto titanium dioxide films by *in situ* infrared spectroscopy and adsorption kinetics and suggested that phosphate strongly binds as a bidentate surface species as shown in (Figure 2-18).

At pH 4 both chemisorption and electrostatic adsorption occurs through the negative phosphate groups and positive MOH^{2+} particle surface (AlOH_2^+ , TiOH_2^+ and neutral TiOH surface groups). Upon adsorption of SHMP to aluminium doped TiO_2 the zeta potential is drastically altered (becomes increasingly more negative even at low SHMP concentration) and the isoelectric point shifts to between pH 3 to 4 dependent on polyphosphate surface concentration (Taylor et al. (2001)).

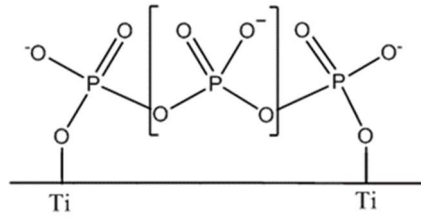


Figure 2-18: SHMP chemisorption to TiO_2 resulting in bidentate complexation through Ti-O-P bonds at the terminal group ends of SHMP.

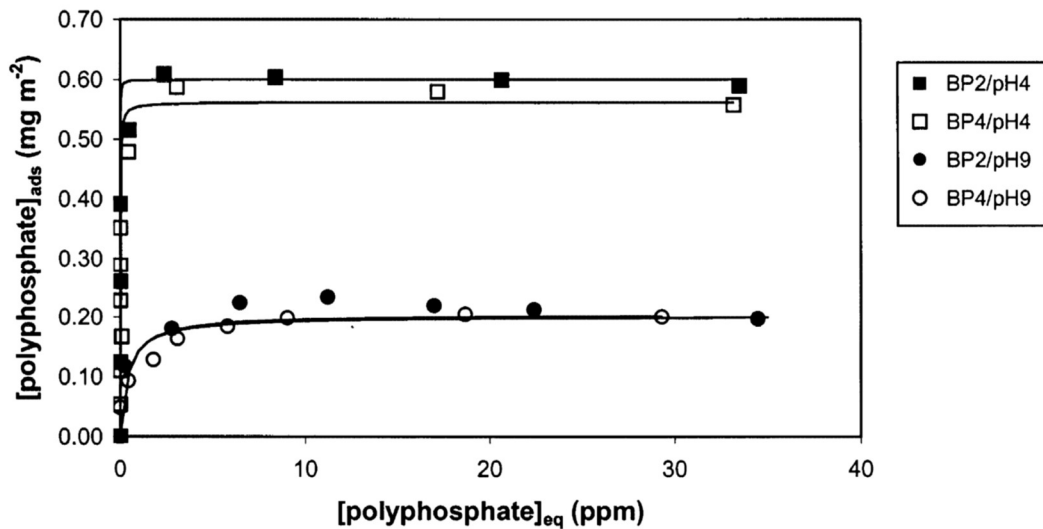


Figure 2-19: Adsorption isotherm for polyphosphate adsorbed onto Al doped TiO_2 pigment with two different Al surface concentrations (Taylor et al. (2001)).

The adsorption isotherm is shown in Figure 2-19, for polyphosphate adsorbed onto alumina doped TiO_2 nanoparticles for two different alumina surface concentrations, at pH 4 and pH 9 as reported by (Taylor et al. (2001)). The pH clearly has an influence on the adsorption density of polyphosphate, where three times more is adsorbed at pH 4 compared to pH 9. There is insignificant difference in polyphosphate density with changes in Al surface concentrations at pH 9, however a slight change is observed at pH 4. The reason for increased adsorption at pH 4 is due to the ability for both chemisorption and electrostatic adsorption to occur.

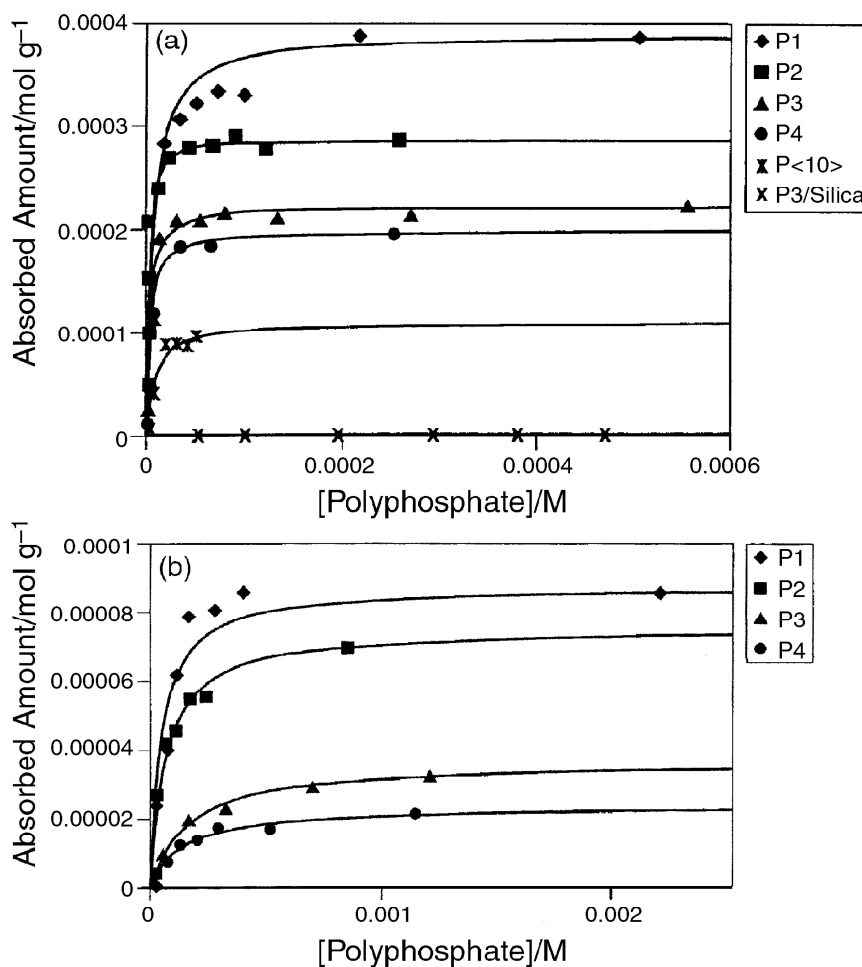


Figure 2-20: Michelmore et al. (2000), adsorption isotherms for polyphosphate adsorbing onto TiO_2 at (a) pH 4 and (b) pH 9.1 .

Michelmore et al. (2000) investigated the influence of phosphate chain length on the interaction with titanium dioxide surfaces. The phosphates that were studied included P_1 , P_2 , P_3 , P_4 and $\text{P}_{<10>}$ and these were adsorbed onto colloidal silica and titanium dioxide particles. After which, the structure was probed by ATR-FTIR, adsorption isotherms were obtained, and dispersion stability investigated by surface charge and rheology measurements. Figure 2-20, shows that increased adsorption occurs at pH 4 regardless of polyphosphate chain length, in agreement with the findings by Taylor et al. (2001), where the maximum adsorbed amount is almost 5 times greater at pH 4 for orthophosphates P_1 and P_2 (Michelmore et al. (2000)).

As previously conversed at pH 4 the TiO_2 is highly positively charged allowing both electrostatic adsorption and chemisorption to occur. The adsorbed amount decreases with increasing polyphosphate chain length, at both pH 4 and pH 9, suggesting that larger

molecules occupy a greater surface area on the particle surface, in other words the polyphosphate chains lie in a “flat” conformation rather than extending out into the solvent (Michelmore et al. (2000)). The FTIR spectra, showed a peak at 1260 cm^{-1} for $P_{<10>}$ which was assigned to the antisymmetric vibration of PO_2 groups within the polyphosphate chain. This peak did not shift upon adsorption of polyphosphate onto the TiO_2 surface, suggesting that it is not bound chemically to the surface (Michelmore et al. (2000)).

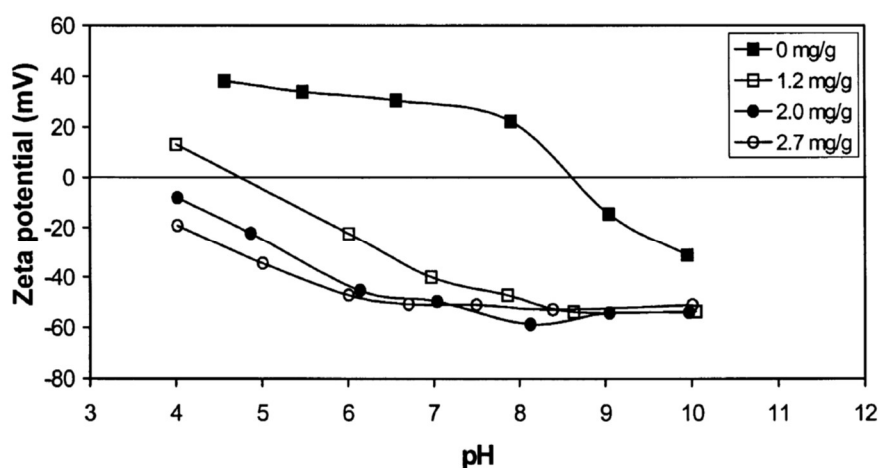


Figure 2-21: Zeta potential of Al doped TiO_2 pigment nanoparticles after Calgon adsorption reported by Taylor et al. (2001).

The adsorption of polyphosphate even at low concentrations causes a significant alteration to the surface charge of alumina doped pigment TiO_2 as observed by Taylor et al. (2001) as shown in Figure 2-21. Across the entire pH range studied, the adsorption of polyphosphate causes the zeta potential to become more negative and the magnitude increases with an increase in polyphosphate concentration, at least under acidic conditions. Above pH 9 the zeta potential remains unchanged, regardless of polyphosphate concentrations which indicates the maximum adsorption capacity has been reached. The isoelectric point (i.e.p) for Al doped TiO_2 is \sim pH 9 and upon adsorption of polyphosphate this shifts to between pH 2.5 – 5.5, with the i.e.p shifting to lower values with an increase in polyphosphate concentration.

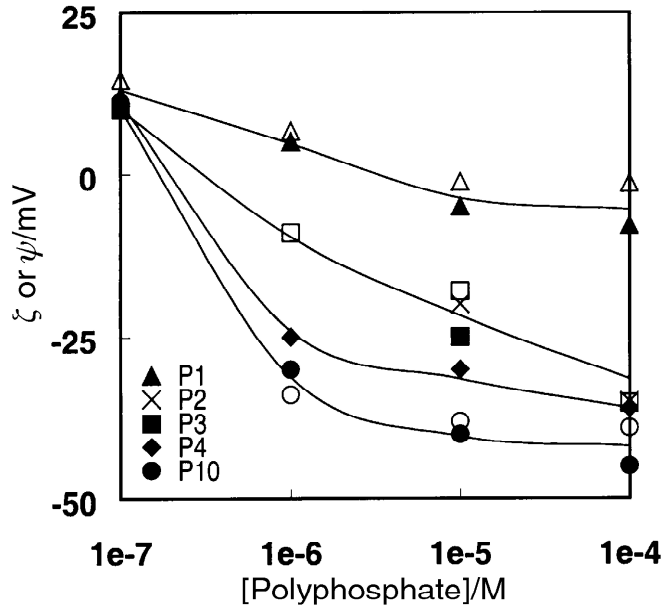


Figure 2-22: Comparison of streaming potential (open symbols) with the AFM measured diffuse layer potentials (filled symbols), as a function of increasing polyphosphate concentration in a background electrolyte (Feiler et al. (2000)).

Feiler et al. (2000) and Michelmore et al. (2000) both studied the adsorption of polyphosphates onto the surface of TiO_2 and SiO_2 particles. For TiO_2 it has been shown that increasing the concentration of polyphosphate and/or increasing the chain length of the linear polyphosphate lead to a decrease in the magnitude of the zeta potential at pH 4, but no interactions were observed for SiO_2 . Feiler et al. (2000) investigated the interactions of linear polyphosphates of varying chain length on metal oxide surfaces. They concluded with three main points which can be observed in Figure 2-22, (i) linear polyphosphates cause charge reversal of the TiO_2 surface, (ii) the molar polyphosphate concentration at which the i.e.p for the TiO_2 occurs decreases with increasing chain length and (iii) the surface potential of TiO_2 becomes more negative with increasing chain length for a fixed polyphosphate concentration.

2.2.2 Stability

Although there are a few studies that show the adsorption behaviour of polyphosphates onto TiO_2 and other clay particle surfaces (Michelmore et al. (2000), Taylor et al. (2001), Feiler et al. (2000), Andreola et al. (2006), Castellini et al. (2013), Castellini et al. (2005)), there is limited literature investigating the stability of these dispersions under static conditions (Farrokhpay et al. (2012)). Furthermore, the degradation of polymeric dispersants is known to occur during milling for ammonium salts of poly(acrylic acid)

(Chartier et al. (1996), Hotta et al. (2008)), thus, questions remain regarding the stability of polyphosphate dispersants during high energy milling.

As relaxation NMR is sensitive to changes in particle size and also surface chemistry (D. Fairhurst (2011)), it is important to understand, (i) the adsorption density of polyphosphates and (ii) the stability of polyphosphates, both under static conditions and shear. The adsorption behaviour of polyphosphates under static conditions has already been touched upon (see section 2.2.1), it was observed that for TiO_2 much higher adsorption densities occur at pH 9 compared to pH 4. This section will focus upon the stability of polyphosphate dispersants prior to adsorption and after adsorption onto clay particle surfaces.

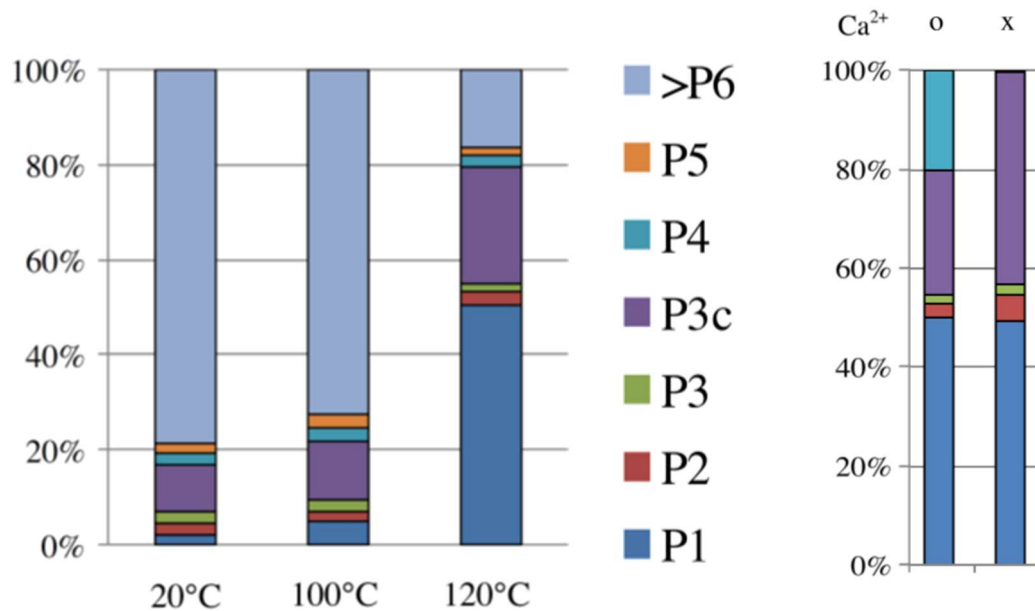


Figure 2-23: Rulliere et al. (2012) report the composition of sodium hexametaphosphate 0.5% in aqueous solution (pH 5.6) after heat treatment for 10 minutes at 100 and 120 °C (left). Composition in the presence (x) or absence (o) of CaCl_2 (0.1% w/w) after heat treatment at 120 °C (Right). The composition (% w/w), is presented for each species: P1 = orthophosphate, P2 = pyrophosphate, P3 = triphosphate, P3c = trimetaphosphate, P4, P5 and > P6 = polyphosphates with four, five and more than six phosphorus atoms.

It has been stated that aqueous polyphosphate solutions are not stable under high temperature (above 120 °C), acidic pH, or in the presence of some metal ions (Rulliere et al. (2012)), as covered in recent reviews by Cini and Ball (2014) and Rashchi and Finch (2000). Since industrial milling waters usually contain some degree of soluble salts for

example Ca^{2+} and milling can cause an increase in temperature to at least to a few tens of $^{\circ}\text{C}$ (Andreola et al. (2006)), this could have a significant impact on polyphosphate dispersant hydrolysis, which may ultimately lead to poor pigment dispersion properties. Furthermore, hydrolysed products of the polyphosphate salt may have significantly different relaxation rates which could lead to the incorrect interpretation of particle size changes during milling.

Rulliere et al. (2012), Figure 2-23, showed under acidic conditions SHMP treated at 100°C for as little as 10 minutes leads to the transformation of approximately 5% of long chain polyphosphates into trimetaphosphates (P3c) and orthophosphates (P1). Increasing the temperature to 120°C caused most of the long chain polyphosphates ($>\text{P6}$) present in SHMP to transform predominately into orthophosphates and trimetaphosphates. The increase in trimetaphosphates at 120°C suggests these species are stable to hydrolytic degradation, which agrees with other experiments by Rulliere et al., 2012, where only 3% of orthophosphate appeared in trimetaphosphate solutions after 120°C temperature treatment.

Three mechanisms have been proposed for the hydrolytic degradation of polyphosphates which may occur simultaneously (Rulliere et al. (2012), McCullough et al. (1956), Thilo (1965)), (i) splitting off end groups (Figure 2-24), (ii) random scission along the chain and (iii) ring formation. It has been suggested by Rulliere et al., 2012, that orthophosphates result from polyphosphate degradation by mechanisms (i) and (ii), in contrast to the trimetaphosphates that occur due to mechanism (iii) as shown by Figure 2-25. The addition of CaCl_2 to SHMP with 120°C heat treatment caused further degradation of the long chain polyphosphates (Figure 2-23), it is thought that this occurred due Ca^{2+} interacting with phosphorous atoms causing it to become less negatively charged, which may intern increase hydrolytic degradation (Rulliere et al. (2012), Thilo et al. (1962)) as shown by Figure 2-26.

It has become apparent that a variety of different processing conditions such as, temperature, pH and cation exposure, could result in polyphosphate degradation and thus care should be taken when handling such aqueous solutions. However, it is not clear from reviewing aqueous polyphosphate literature alone, what impact this degradation may have on titania dispersion properties. Furthermore, it is not clear if degradation of the polyphosphate will occur after adsorption to the particle surface, therefore, the following discussion will expand on these areas.

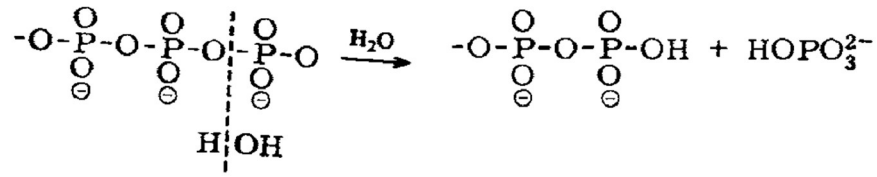


Figure 2-24: Thilo (1965), degradation of polyphosphates proceeding by mono-phosphate units removal.

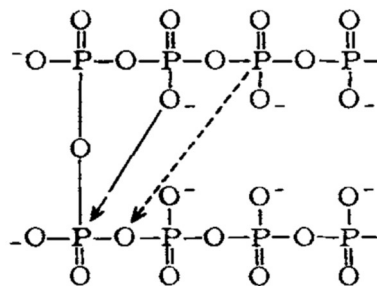


Figure 2-25: Thilo (1965), degradation of polyphosphates leading to the formation of trimetaphosphates and shorter anion chain.

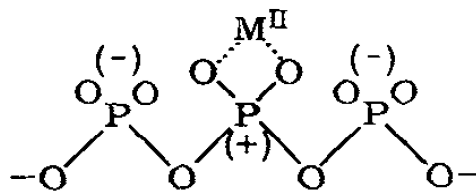


Figure 2-26: Thilo (1965), chelation of polyphosphates to cation resulting in more positive phosphorus atom which can further promote hydrolytic degradation.

Farrokhpay et al. (2005), Farrokhpay et al. (2010), Farrokhpay et al. (2012), have investigated the stability and the influence of polymeric and polyphosphate dispersants on titania pigment particles. They found that acidic conditions (pH 3.5 – 5.5), high calcium ion concentrations and elevated temperatures all decreased the polyphosphate dispersion properties of titanium pigment particles (Farrokhpay et al. (2012)). Figure 2-27 shows the yield stress of the suspension with and without polyphosphate pre-treatment, which decreases more rapidly when the polyphosphate solution is not pre-treated (pH 3.5 for 24 h). The high yield stress (27-30 Pa) when no polyphosphate is present is due to

inter-particle attraction and agglomeration, which is reduced with increasing polyphosphate concentration.

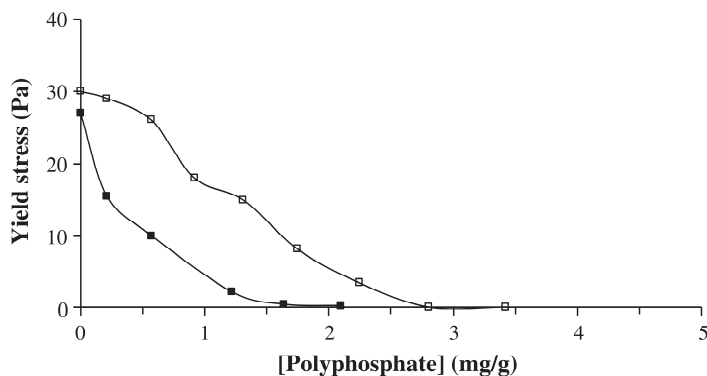


Figure 2-27: TiO₂ suspension (50 wt.%) yield stress with polyphosphate (Calgon T) concentration. Without polyphosphate pre-treatment (neutral pH and room temperature, closed squares) and polyphosphate pre-treatment for 24 h at pH 3.5 and 90 °C (open squares) (Farrokhpay et al. (2012)).

Figure 2-27 shows that after polyphosphate pre-treatment nearly twice as much polyphosphate is required to reach the minimum suspension yield stress, this is likely due to the degradation of polyphosphate chains into smaller phosphate molecules leading to reduced steric stabilisation. However, from Figure 2-27, it is not clear to what extent pH or temperature effects the dispersion properties of the suspension, hence Figure 2-28 shows a more detailed study of the individual process variables. Figure 2-28, shows that higher temperature has the greatest effect on increased suspension yield stress, compared to changes in pH alone, despite this the suspension yield stress is not dependent on temperature under alkaline conditions. Farrokhpay et al. (2012) showed by ATR-FTIR that the increase in suspension yield stress was due to an increase in the concentration of orthophosphate in the polyphosphate solution, leading to a reduction in steric stabilisation of titania.

Farrokhpay et al. (2012) and Andreola et al. (2006) both studied the effect of adsorbed SHMP onto mineral surfaces with pre-treatment of Ca²⁺ ions. Farrokhpay et al. (2012) showed that when the concentration of Ca(NO₃)₂ was greater than 0.025 M the yield stress reduction was reduced and at a concentration of 0.1 M no yield stress reduction was observed for the suspension. Furthermore, at higher Ca²⁺ concentrations, Farrokhpay et al. (2012) observed precipitation, which was most likely a calcium-phosphate insoluble

complex. The addition of Ca^{2+} caused either phosphate neutralisation, chain coiling and/or bridging to occur which reduced the ability for the polyphosphate to provide electrostatic and steric stabilisation of TiO_2 , Farrokhpay et al. (2012) did not report on the occurrence of chain scission which contrast to the findings by Rulliere et al. (2012).

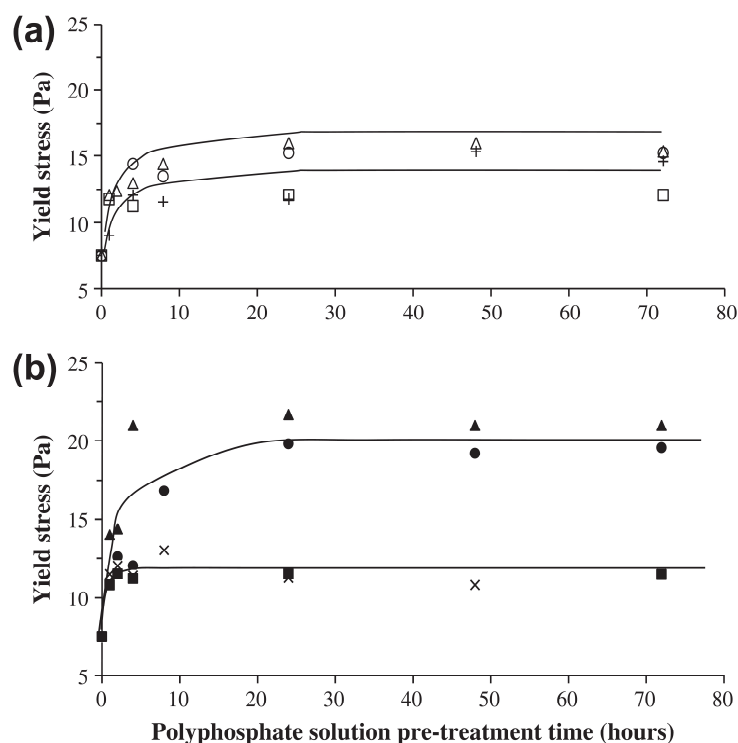


Figure 2-28: TiO_2 suspension (50 wt.%) yield stress with polyphosphate (Calgon T) as a function of pre-treatment time. (a) 25 °C and (b) 90 °C and suspension pH ▲(pH 3.5), ●(pH 5.5), +(pH 9.0) and ■(pH 11.0) (Farrokhpay et al. (2012)).

Andreola et al. (2006) showed the electrophoretic mobility of Kaolin in the presence of SHMP and electrolyte $\text{Ca}(\text{NO}_3)_2$, even at high Ca^{2+} concentrations the addition of SHMP increased the electrophoretic mobility confirming it was chemisorbed. Ma (2012) also investigated the dispersive effect of SHMP on kaolinite in saline water and it was found in very dilute solution of $\text{CaCl}_2 \leq 2 \times 10^{-3} \text{ M}$, kaolinite can form a stable dispersion. Andreola et al. (2006) observed high apparent viscosity for kaolin dispersed in SHMP at 60 °C despite, inductively coupled plasma spectroscopy (ICP) analysis indicating increased adsorbance of SHMP (Figure 2-29), with the apparent viscosity increasing with increased ageing time. Andreola et al. (2006) state that the disappearance of SHMP from

solution at higher temperature could be due to increased adsorption at the particle surface or degradation by hydrolysis, despite this claim it is not examined further in the study.

These results do correlate to the those found by (Farrokhpay et al., 2012) who observed an increase in suspension yield stress of titania in SHMP at 90 °C and this was due to an increase in the concentration of orthophosphate in the polyphosphate solution caused by SHMP hydrolysis. Figure 2-29 shows the amount of SHMP remaining in solution when Ca^{2+} is present is only slightly lower than distilled water at 30 °C, Andreola et al. (2006) suggest this is due to the adsorption of the Ca-SHMP complex to the particle surface. The suspensions apparent viscosity in the presence of Ca^{2+} ions shows an increase, most likely due to the increased screening effect of the surface charge by adsorbed Ca^{2+} ions leading to an increase in particle-particle interactions, although this was not explicitly stated.

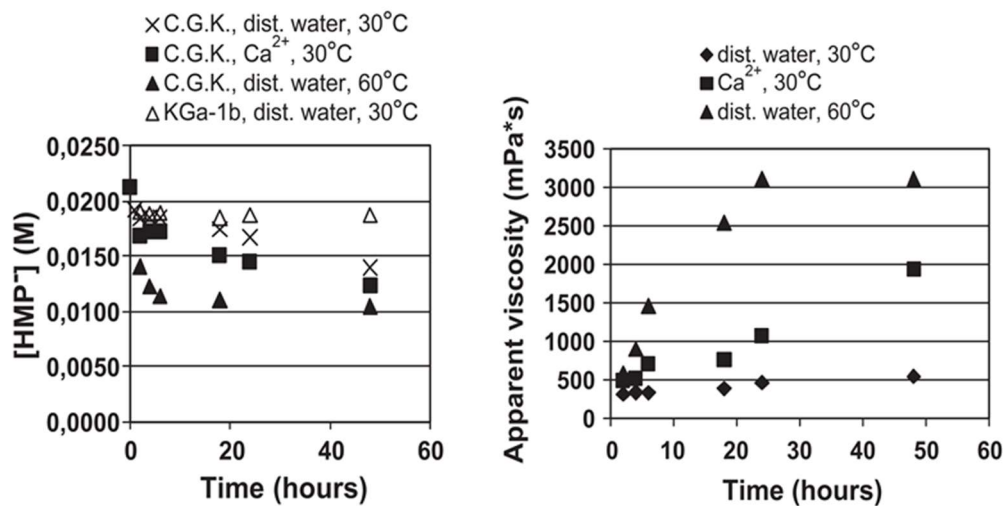


Figure 2-29: Andreola et al. (2006), molar concentration of SHMP (measured by inductively coupled plasma spectroscopy) remaining in solution after adsorption onto kaolin as a function of aging time (left) and apparent viscosity (right).

The thermodynamic aspects of SHMP adsorption onto kaolinite (8% volume fraction) have been explored by Castellini et al. (2005) who found a decrease in the adsorption ability of SHMP with increasing temperature which contradicts the ICP results reported by Andreola et al. (2006) shown in Figure 2-29. Castellini et al. (2005) also reported isotherms for adsorption of SHMP onto kaolinite at two different volume fractions (8 and 35 %) and observed very different behaviours as shown in Figure 2-30. The

differences reported could therefore be due to several factors including; (i) mineral processing and surface Al groups, since SHMP chemisorbs through these sites adsorption could be promoted at the particle surface containing more Al, (ii) localised changes in adsorption pH leading to hydrolysis of SHMP, (ii) differences in adsorption time (iii) different solid volume fractions and (iv) hydrolysis of SHMP occurring into smaller polyphosphate molecules.

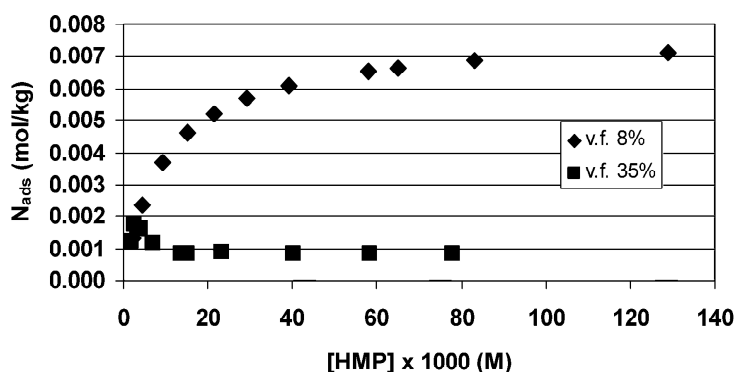


Figure 2-30: Isotherms for adsorption of SHMP onto kaolinite at two different kaolinite volume fractions at neutral pH and 20 °C, reported by Castellini et al. (2005).

It has become apparent from the literature that the structure of polyphosphates is a complex matter (Brow (2000), Thilo (1965), McCullough et al. (1956)) with several studies indicating hydrolysis under extreme pH conditions, temperature and in the presence of metal ions (Thilo (1965), Rulliere et al. (2012), Cini and Ball (2014), Rashchi and Finch (2000)). Some attempts have been made to understand the adsorption density of polyphosphates onto TiO₂ and the impact this has on dispersion performance (Connor and McQuillan (1999), Farrokhpay et al. (2010), Farrokhpay et al. (2012), Michelmor et al. (2000)). Less relevant but noteworthy are the studies that have used polyphosphates adsorbed onto calcium bentonite for the use of trench cutoff walls (Yang et al. (2017), Du et al. (2016)).

Even more relevant is the work by Taylor et al. (2001), who studied the influence of alumina surface concentration and changes in pH on polyphosphate adsorption onto TiO₂ pigment particles. Others have investigated the thermodynamics aspects of SHMP adsorption onto inorganic clays and investigated how temperature impacts dispersion performance (Andreola et al. (2006), Castellini et al. (2013), Castellini et al. (2005)).

Furthermore, some have researched how the presence of metal ions influence polyphosphate adsorption and dispersion properties (Ma (2012), Farrokhpay et al. (2012), Andreola et al. (2006)).

A few studies (Wang and Forsberg (1995), Zhao et al. (2013)) have shown the use of SHMP to aid milling and compared the effect to other commonly used dispersants, as previously discussed in Section 2.1.5. However, within these studies there is no analysis on dispersant density or structure, not even the acknowledgement of the potential for changes in either to occur.

There appears to be a deficit in the literature relating to the influence of SHMP dispersant density and stability with mineral milling. It could be that milling may lead to structural changes in the dispersant through hydrolysis or changes in dispersant density due to localised thermodynamic events resulting from particle breakage events. Therefore, it remains unclear if dispersant chemistry is likely to change as a result of milling and this is an important question to understand in relation to the use of relaxation NMR which can be used to detect both chemical and particle size changes which will be discussed in the following section.

2.3 Relaxation NMR to probe colloidal particles

2.3.1 Introduction

NMR involves the interaction of nuclei (e.g. hydrogen) with electromagnetic radiation in the radio frequency range (Kirtil et al. (2017)) and this theory is explained in greater detail in section 3.1. Undergraduate chemistry students are often taught the spectroscopic technique to aid with chemical identification and would be familiar with the cumbersome 400-600 MHz spectrometers found in most chemistry departs. This is because typically acquiring NMR signals requires a magnetic field which is generated by large liquid helium-cooled superconducting magnet (Kirtil et al. (2017), Meyer et al. (2016)). These characteristics have made the use of NMR to monitor processes significantly challenging, however, recent advancements in magnet technology (small light cryogenic free superconducting systems) allow for the reduction in equipment size (Kirtil et al. (2017), Meyer et al. (2016)).

These permanent magnets have enabled a new generation of devices to emerge called benchtop NMR spectrometers, that are small, affordable and operate at lower fields (Riegel and Leskowitz (2016)). Bruker introduced a low field NMR instrument in the

1970's (Blümich and Singh (2018)) and since then the technique of NMR relaxometry has been used in NMR well logging (Mitchell et al. (2014)), however, one of the most prevalent industrial applications is within the food industry (see reviews by (Capitani et al. (2017), Kirtil et al. (2017))). Relaxation NMR is used as a characterisation and quality control tool for a wide range of products e.g. potatoes (Thybo et al. (2003)) and emulsion droplet size (van Duynhoven et al. (2007)). Examples of low field benchtop NMR spectrometers include, 40-80 MHz Spinsolve Magritek (Magritek (2019)) which is capable of chemical identification making real time relaxation monitoring possible (Silva Elipe and Milburn (2016), Blümich and Singh (2018)). NMR measurements of emulsion droplets size distributions have been shown to be effective with a by-line measurement set up using a 40 MHz benchtop spectrometer capable of differentiating the chemical shift of oil and water signals (Ling et al. (2017)). However, low field instruments solely for the purpose of relaxation measurements can operate at lower frequencies of ~ 13 MHz, such examples includes the Xigo Nanotools Area (Xigo (2019)) shown in Figure 2-31.



Figure 2-31: 13 MHz benchtop spectrometer (Xigo (2019)).

Relaxation NMR can also be used as a rapid non-invasive and non-destructive method to study the behaviour of liquids in porous and non-porous media (Fairhurst et al. (2016), Davis et al. (1987)) allowing surface area and porosity to be determined. Relaxation measurements can be obtained between 1 - 15 minutes (Fairhurst et al. (2016), Davis et al. (1987)). Particulate suspensions are present in numerous industries including pigments, cosmetics, pharmaceuticals and foods, and frequently, these are at high volume fraction (Bux et al. (2015)). Particle surface area is an important consideration, as an increase in the concentration of colloidal particles in a suspension results in a larger total surface area

available, thus increasing the potential for surface reactions with the surrounding environment.

The total surface area of solid particles is often determined for dry powders by Brunauer-Emmett-Teller (BET), whereby, nitrogen gas molecules physically adsorb onto a particles surface in layers (Lowell and Shields (1991), Sing (1989)). Critically, BET is not capable of determining the total particle surface area for particles in solid-liquid (S-L) dispersions (Davis et al. (1987)) and is considered to be somewhat time-consuming thus reducing its versatility. For example, some samples require extensive degas times, up to 24 hours and moreover, BET is dependent on the temperature and de-gas conditions used to obtain measurement reproducibility (Sing (2001)).

Mercury porosimetry and gravimetric analysis are alternative techniques for the measurement of surface area, however, they also require dry powders (Lowell et al. (2004)). The drying of wet suspensions frequently lead to aggregation and agglomeration (Bowen and Carry (2002)), resulting in surface area measurements that are unreliable and misrepresentative of the particles surface area in a S-L dispersion. Thus, it would be of significant advantage to measure the surface area of particles in a S-L dispersion accurately. Furthermore, such a technique could be used as an online monitoring tool to produce TiO₂ pigment.

2.3.2 Surface area determination and porosity

Despite Nuclear magnetic resonance (NMR) being a commonly used technique for the identification of unknown compounds, the use of proton relaxation rates to determine surface area is not often observed in the literature. This section focuses on a literature review based on relaxometry to determine surface area and a discussion on the successes and uncertainties that have arisen. Although the quantity of available publications is limited, research based on relaxometry to determine particle surface area is interestingly spread across a large time period, with initial measurements made by Davis et al. (1987), up to more recently published work by Fairhurst et al. (2016).

Davis et al. (1987), explored the use of solvent NMR to determine surface area and compared their findings to BET data. Three different amorphous fumed silica powders were studied, these samples all had negligible internal porosity and therefore only a single exponential relaxation rate was observed, compared to a possible biexponential relaxation indicating water in pores. If the NMR relaxation rates are in good agreement with BET surface area data it can be expected that a plot of $1/T_1$ vs the product of the surface area

(measured by BET) with solid concentration (SAC) would yield a straight line. This plot should result in the y intercept correlating to the systems bulk measurement where no solids are present. Figure 2-32, shows an excellent agreement to this theory, where the extrapolation of fumed silica powders at SAC equal to zero gives rise to the bulk water value.

Davis et al. (1987) also investigate the relaxation rates of three controlled pore glass samples which equally showed a good agreement with NMR theory. Although they showed that NMR was in good agreement with BET data, the study focused on samples of large specific surface area, where all samples were greater than $77.5 \text{ m}^2/\text{g}$, the ability to measure samples of low surface area accurately has not been shown here. Further, the system studied is not representative of commonly encountered highly concentrated industrial slurries which often contain mixtures of particles, inorganic contaminants, and surfactants.

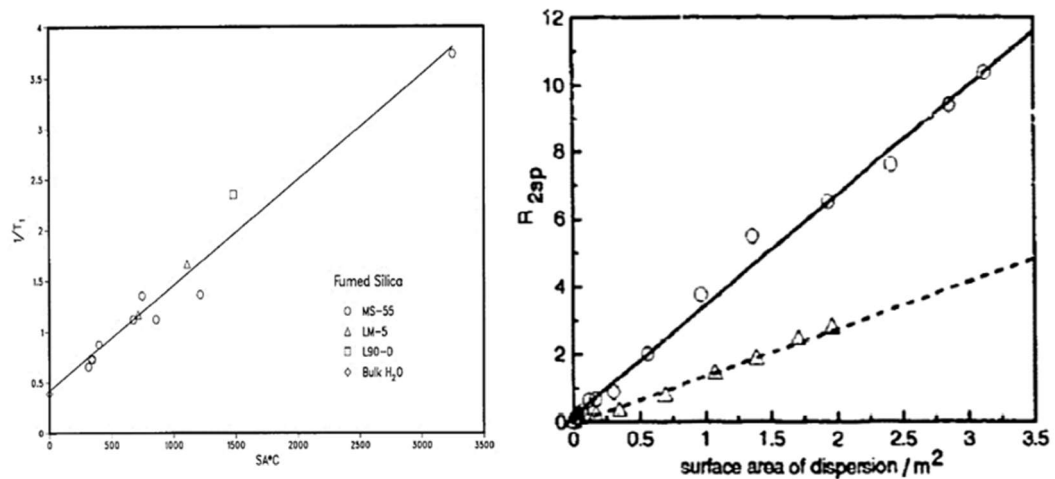


Figure 2-32: Relaxation rates for various fumed silica powders, Davis et al. (1987) (left) and Cosgrove et al. (1992) relaxation rate enhancement of alumina (circle) and polystyrene latex (triangle) both in water, as a function of particle surface area (right).

Cosgrove et al. (1992) studied relative relaxation enhancements for alumina (surface charge density $0.42 \mu\text{Ccm}^{-2}$) and polystyrene latex ($1.6 \mu\text{Ccm}^{-2}$). They showed the time bound water spends at the surface of a particle is not entirely determined by the surface charge of the particle (Figure 2-32). In the case of alumina despite a lower surface charge compared to polystyrene latex a greater relative enhancement is observed, thus indicating

the faster relaxation of bound water at the alumina surface. Alumina containing surface hydroxyl groups causes the motional restriction of water through specific interactions.

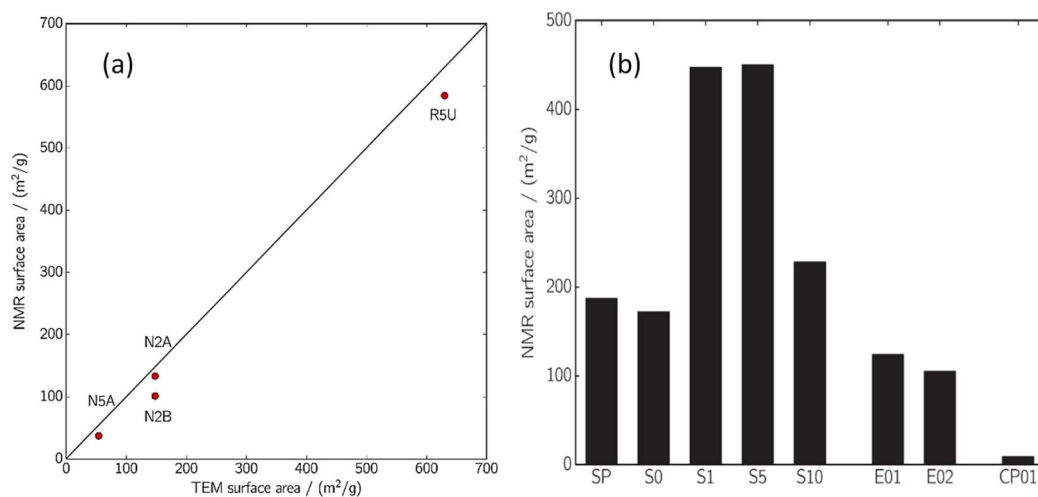


Figure 2-33: (a) Fairhurst et al. (2016), nanocarbon blacks with vary primary particle sizes dispersed in tetrahydrofuran with surface area calculated from T_2 relaxation data compared to TEM surface area (b) Fairhurst et al. (2016) investigated the use of solvent NMR to understand changes in surface area for milled samples, using constant mechanical energy. Samples denoted ‘S’ were 2% w/w graphene nanoplatelet dispersions, S0, S1, S5 and S10 have added dispersant 0, 1, 5 and 10% content as a fraction of total solids. SP a bought milled sample 20% w/w with 0% surfactant. E01 and E02 are nanographite dispersed in ethanol and processed differently for milling.

More recently, Fairhurst et al. (2016), investigated dispersion and formulation behaviour of nanostructured carbon materials including graphene oxide, nanographite and porous graphene using NMR relaxometry. Figure 2-33 (a) shows good agreement between the NMR and TEM surface area data, however, for all nanostructured carbons the NMR results are lower than the comparative TEM data, this suggested there is some degree of particle aggregation of the nanomaterial when dispersed in tetrahydrofuran. Nanocarbon materials N2A and N2B both had a primary particle size of 20 nm determined through TEM analysis, the NMR results elucidate to different internal structures and varying degrees of particle aggregation. They also demonstrated the use of NMR to indicate particle aggregation and illustrate changes in surface area with different milling preparation methods (Figure 2-33 (b)). They propose that NMR could offer a practical advantage for the ability to monitor milling and comminution processes on-line, this would be advantageous as industrial slurries are often opaque and at high concentrations

where other particle characterisation techniques for example particle sizing through light scattering encounter problems.

Figure 2-33 (b) shows that solvent NMR might be useful in determining the optimum dispersant concentrations to add into a milling processes, here it is observed a decrease in the NMR surface area for sample S10, it is thought this is due to the excess of non-adsorbed polymer present leading to flocculation of the particles in the dispersion (Fairhurst et al. (2016)). Of further interest, Figure 2-33 (b), illustrates a change in the surface area between E01 and E02, (milled nanographite dispersed in ethanol), showing different milling preparation methods lead to an altered wetted surface area, detectable by NMR relaxometry. Although Fairhurst et al. (2016) have shown the NMR technique to be promising for gaining an understanding of changes in surface area during a milling process, this study does not consider industrially relevant milling conditions; for example, highly concentrated slurries and further samples were prepared ex-situ.

Zhang et al. (2017) were not able to obtain exact surface area values using relaxation NMR for surface modified silica in water or n-hexane despite measuring the surface area of silica nanoparticles by BET before and after hydroxylation. Zhang et al. (2017) did not further expand on the details as to why the surface area could not be determined using the results reported in Figure 2-34, in theory it should be possible and since three different sized silica samples were used (15, 30 and 50) at least one of these samples could have been used as a reference material to calculate the relaxation constant required to obtain NMR surface area values as described in section 3.1.

In water the R_{2sp} is greatest for the larger silica particles (50 nm) and R_{2sp} decreases for a decrease in particle size (i.e. increase in particle surface area) which contradicts the expected NMR theory that particles of larger surface area have faster relaxation times and larger R_{sp} as described in section 3.1. This might be due to aggregation of silica causing a reduction in R_{2sp} . For particles dispersed in n-hexane, the trend is opposite. 1) The R_{2sp} decreased with increasing particles size (i.e. lower surface area) in agreement with accepted NMR theory. 2) The hydroxylation caused a decrease in R_{2sp} . After hydroxylation the particles were less aggregated but surface OH groups occupy a large surface area reducing the surface area available for hexane leading to a reduction in R_{2sp} .

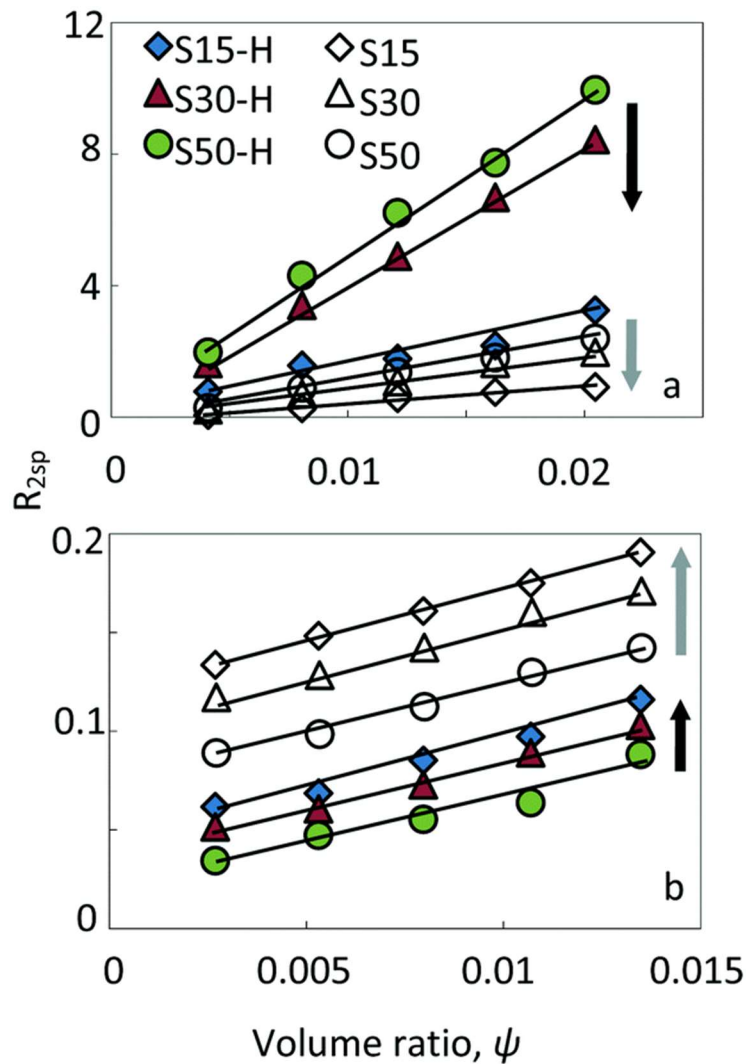


Figure 2-34: Zhang et al. (2017) R_{2sp} of differently sized original and hydroxylated silica in different solvents, namely, Milli-Q water (a) and n-hexane (b), as a function of the volume ratio between the particle and liquid (ψ) in each system. The arrow \uparrow suggests an enhanced surface area with decreased particle sizes and the arrow \downarrow suggests a reduced surface area with decreased particle sizes.

Thoma et al. (1993) investigated three different titania powders and one silica, two of the titania powders were aluminosilicate coated rutile, of pigment grade quality, and had a N_2 BET surface area of 13.6 and 24.5 m^2/g , and the third titania powder uncoated with a surface area of 8.3 m^2/g . Table 2-1 shows there is a concentration range over which the best NMR surface area results are obtained, at low concentrations the difference between the T_1 of the slurry and T_1 of the bulk is small which leads to inaccuracy in the measurement and further problems with suspension settling often occur. In contrast, deviations for highly concentrated slurries occur due to a decrease in signal to noise from the NMR signal due to reduction in the number of protons present in the system.

Table 2-1: Thoma et al. (1993), NMR static slurry particle surface area measurements for TiO₂ samples, aluminosilicate coated rutile R900 and 902dd, and uncoated 101dd. An additional silica measurement was made F2849 for material comparison. The materials were prepared at various weight concentrations and compared to classical BET surface area measurements (all values in m²/g).

Sample	F2849	101dd	R900	902dd
Dry-N ₂ /BET	3.1	8.3	13.6	24.5
Dry-Particle size	1.2 ¹	1.9 ¹	4.7 ²	2.2 ¹
20 wt%	*	*	20.0	*
33 wt%	*	7.5	12.9	18.5
40 wt%	*	8.0	11.9	24.2
50 wt%	4.1	9.4	10.9	23.7
60 wt%	3.5	9.9	13.7	22.7
70 wt%	3.5	3.2	13.2	33.7
80 wt%	4.1	***	***	***

*****Weight loading too high for slurry handling. *Sample settling.**

Relaxation NMR measurements are useful to determine the specific surface area of porous cement materials (Barberon et al. (2003)) and study the effects of water reducing agents on sealing materials in cement (Li et al. (2012)). Chen et al. (2013), Chen et al. (2015) have correlated relaxation NMR studies to determine the surface area of highly porous metal-organic frameworks to BET and Langmuir surface area measurements. However, there is limited literature available demonstrating the potential of NMR relaxation for on-line surface area measurements of concentrated slurries, which is of interest to this studentship.

Thoma et al. (1993) discuss the theoretical possibility of determining agglomerate sizes by altering relaxation times. As previously described, porous particles have three different solvent environments, this can be related to three different relaxation environments for an agglomerate which include: 1) surface water, 2) intra-bulk fluid within the agglomerate and 3) inter bulk fluid surrounding the agglomerate. For a small agglomerate with a slow

relaxation time, diffusion will occur between these phases and a single relaxation time will be observed. In contrast a large agglomerate with a fast relaxation time (high surface area) two or more relaxation times may be observed. They proposed that effective agglomerate size could be determined through varying the relaxation time using field strength or temperature and studying the changes in surface area. Despite Thoma et al. (1993) promoting this discussion in 1993, little research in in this area has been undertaken, as this “online” type of research was in advance of the times, however, technology in this area has since moved on dramatically, thus providing a significant opportunity for research within this field.

Relaxation NMR has also been used extensively to probe particle internal structure; for example, in geophysical well logging to estimate hydrocarbon-reservoir properties which include rock porosity, pore-size distribution, and permeability (Grunewald and Knight (2009)), while several studies have been conducted on the use of relaxation rates to examine porosity (Terenzi et al. (2015), Li et al. (2015), Gallegos et al. (1988), Gallegos et al. (1987)). A common technique to understand pore size is to use NMR cryoporometry, which utilizes melting point depression and relates this to the pore size through a melting point depression constant, however, this requires calibration with samples of known pore size distribution (Strange et al. (2003)).

Strange et al. (2003) used T_2 relaxometry in conjunction with the NMR pore theory stated in section 3.3, for sol-gel silica samples by estimating the surface relaxivity constant using gas adsorption measurements, (giving S/V). They observed variations in relaxation rates for similar porous sol-gel silica samples determined through alternative adsorption techniques. However, this should not be of any surprise seeing as relaxation NMR is surface dependent, and any impurities which dissolve into the surrounding liquid media have a profound effect on the relaxation rate obtained. It is important to be aware that all these studies require validation using an alternative technique to obtain the relaxivity constant.

2.3.3 Specific ion effects

Despite the number of previous studies, in wide research areas, there are still significant questions related to the application of NMR relaxometry for the measurement of colloidal surface areas, which has so far limited its wider use. In particular, is the influence of electrolyte conditions on the surface relaxation of solvent molecules, and whether specific ion effects from bound counterion monolayers may enhance or reduce the relaxation rate?

Flood et al. (2006) studied the relative relaxation enhancement (R_{sp}) of four salts (NaCl, MgCl₂, CaCl₂ and LaCl₃) in water at two different concentrations 2.5 and 5 mM, finding an enhancement in the R_{sp} between 0.15 and 3.0. However, these enhancements could not be correlated to the valency of the salt but were great enough to justify a calibration when studying silica and polymers in the presence of these salts. They observed the addition of these salts to increasing concentrations of silica (0-10 wt%) (Figure 2-35), and found that the addition of salt led to a regular increase in the magnitude of R_{sp} which was dependent on the concentration and valency of the salt, although no mechanism was proposed.

They suggested the addition of salt increases the silica-solvent affinity, in other words, there is an increase in the strength of binding of water at the silica surface as a function of ionic strength. At times this may be counterintuitive to relaxation NMR theory, which expresses that a larger surface area leads to a greater R_{sp} enhancement, and the addition of electrolyte can lead to coagulation of samples and thus a reduction in surface area. Further to this, it was proposed that the valency of the salt has the most dramatic effect on the relaxation rate constant (K_a), once again no mechanism has been proposed. This result is of great importance, as it indicates the ability to manipulate the K_a value for single particle systems, this could prove useful when probing internal and external structures of TiO₂.

Although, Flood et al. (2006) were the first to conduct a valency and concentration study on the effects of salts to silica measured through NMR relaxation, since 2006 there has been little progression within this area. It may perhaps be that previous research undertaken in this area has not been entirely thought about in terms of the implications which arise from specific ion interactions, and the impact this can have upon the vast areas in which surface area measurements can be applied. Supplementary to this, Flood et al. (2006) experienced difficulties with flocculation problems, which led to phase

separation of salt-silica systems over time. This phase separation was found to lead to two observations in T_2 values for each phase which did not fit the trends of the stable samples; this was particularly difficult for the LaCl_3 samples and was subsequently neglected for the latter experiments involving polymer-salt systems. Conte (2015) recently studied, the effects of ions on water structures using a low-field T_1 NMR relaxometry approach, more specifically using fast field cycling (FFC) NMR. Where FFC allows the frequency of the field to be varied from low kHz to 40 MHz, Conte (2015) observed an increase in the concentration of KCl from 0-3 mol L^{-1} , significantly decreases the relaxation rate R_1 .

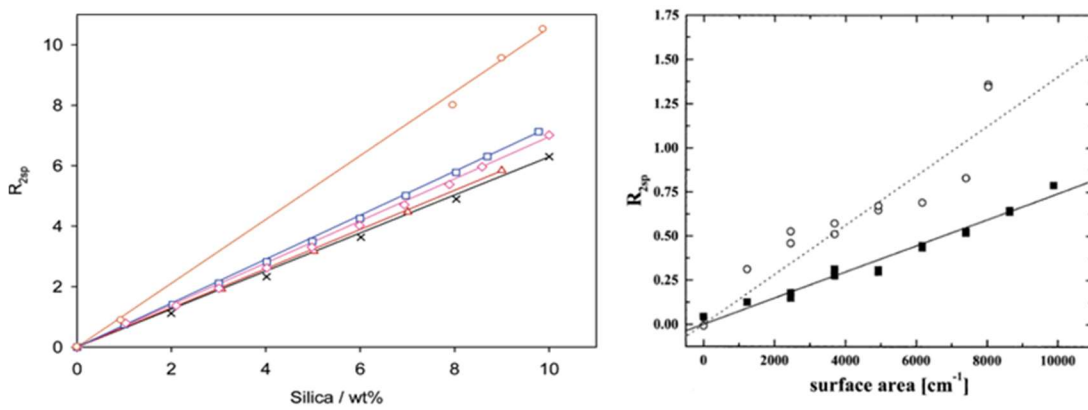


Figure 2-35: R_{sp} against silica concentration in the presence of salts: (x) No salt, (Δ) 1.25 mM MgCl_2 , (\square) 5 mM MgCl_2 , (\diamond) 5 mM CaCl_2 , and (\circ) 5 mM LaCl_3 by Flood et al. (2006) (left). NMR relaxation study of negatively charged sulphate-stabilised polystyrene latex nanoparticles (466 nm) in the presence of 0.25 M NaCl (open) and in water (closed) by Schwarz and Schönhoff (2002) (right).

Schwarz and Schönhoff (2002) carried out an NMR relaxation study on negatively charged sulphate-stabilised polystyrene latex nanoparticles (466 nm) in the presence of 0.25 M NaCl (Figure 2-35). They found the specific relaxation rate enhancement (R_{sp}) scaled linearly with the increase in concentration of polystyrene latex particles in the presence of H_2O and 0.25 M NaCl. They also reported an increase in the slope of the R_{sp}/ψ_p , in the presence of 0.25 M NaCl, and attribute the increase in this gradient to sodium ions forming a screening layer around the negatively charged polystyrene latex particles. This causes an increase in the immobilised water compared to the unscreened charges. Where the term immobilisation is referred to as increasing the amount of bound water to the particle surface, or, a reduction in the dynamics of the bound water, both of which cannot be separated from the NMR measurement (Schwarz and Schönhoff

(2002)). Katika et al. (2014) observed an effective increase in the surface area of chalk when saturated with divalent salts and measured with NMR relaxation. More specifically, they observed that chalk saturated with Mg-rich brines caused a shift in T_2 (spin-spin relaxation) to faster relaxation rates. However, it was concluded this result was due to precipitation within the pore space leading to an increase in the specific surface of the pore space, rather than specific ion effects.

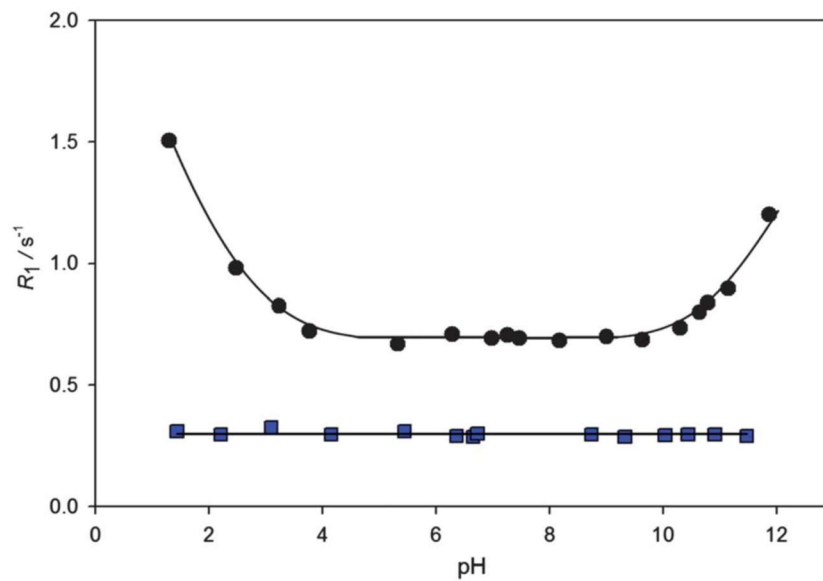


Figure 2-36: Van der Beek et al. (1991) spin-lattice relaxation rates of silica (circle) at 5.15 w/w% with varying pH and pure water (square) (Cooper et al. (2013(a))).

Van der Beek et al. (1991) investigated the influence of pH on the relaxation rate of silica and water dispersions (Figure 2-36), they found that at high and low pH extremes the relaxation rate dramatically increases for the silica dispersions. This response was not found for the pure water sample, in fact complete independence in the relaxation rate was observed regardless of pH. They suggest this enhancement observed for the silica dispersions is a result of an increased rate of proton exchange, occurring with water and OH groups at the surface of silica.

Further still, Van der Beek et al. (1991) suggest the partial dissolution of silica above pH 12 could lead to enhancements in relaxation due to paramagnetic impurities. It is important to note that they failed to highlight the change in particle charge across this pH range studied, although the surface charge of silica is well documented, being negatively

charged, the magnitude of this charge may indeed effect the relative relaxation enhancement observed. This pH effect would cause the determination of particle surface area complicated which is neglected by the theory (later described).

Specific ion effects clearly make the interpretation of NMR relaxometry significantly more complicated, and at worse mitigate the application of the technique. Despite literature reporting these specific ion effects, the influence of particle zeta potential charge and magnitude, and related influence of agglomeration have not previously been observed. Additionally, the increase in the magnitude of the R_{sp}/Ψ_p gradient may be correlated to the magnitude of the particle surface charge. These studies are of importance as titanium dioxide is produced in the presence of caustics and various metal ions, these ions could have a profound effect on an NMR signal used to determine particle surface area. Moreover, this effect is most likely concentration and valency dependent, thus it is of great significance to understand how ions effect the NMR relaxation signal, if this technique is to be utilised to monitor industrial suspensions changes in surface area.

2.3.4 Frequency

Surface enhanced relaxation is dependent on proton frequency, fluid temperature and surface chemistry (Glaves et al. (1988)). As previously conversed, Thoma et al. (1993) proposed agglomerate size could be determined through varying the relaxation time using field strength or temperature and studying the changes in surface area, thus it is important to understand the effect of frequency on relaxation measurements. As previously discussed, Davis et al. (1987), explored the use of solvent NMR to determine surface area and compared their findings to BET data, continuing from this study, Glaves et al. (1988) evaluated fluid and frequency effects. Figure 2-37, shows that both frequency measurements pass through the bulk T_1 measurement at each respective frequency and there is no deviation from linearity, however comparison of the gradients illustrates that relaxation is enhanced at lower frequencies (Glaves et al. (1988)). Therefore, for surface area analysis the lowest frequency should be used, though there is a balance due to a reduction in the signal to noise ratio of protons (Glaves et al. (1988)).

When motions are fast relaxation rates are not dependent on the measurement frequency, in contrast for slow molecular dynamics relaxation rates become frequency dependent (Steiner et al. (2011)). Fast field cycling (FFC) NMR is a rare technique where the frequency is varied from low MHz (40 MHz) to low kHz (Noack (1986)), with a limited number of instruments in a handful of laboratories (Lurie et al. (2010)), the compact

spectrometer and fast experimental times makes the technique ideal for a potential online process control tool. FFC can be used to study ^1H spin-lattice relaxation at a variety of frequencies, allowing the study of motional processes which occur at different timescales possible (Kruk et al. (2012)). The technique is sensitive to geometrically restricted environments, for example water in pores, because water molecules are orientated by a particle surface which is dependent on surface structure, NMR relaxation can probe surface topology (Anoardo et al. (2001)). Hence, this technique could be useful in probing interconnected particles in complex agglomerates.

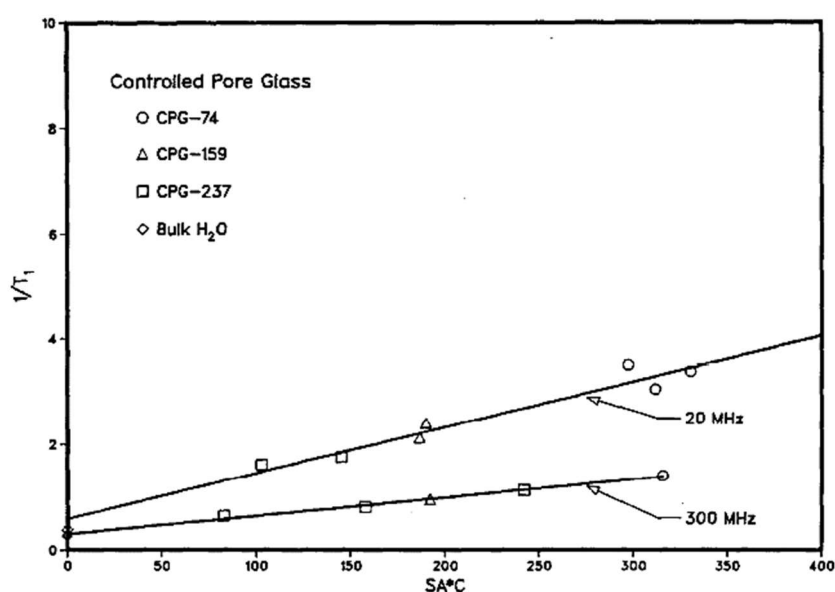


Figure 2-37: Variation of T_1 with surface area, concentration and frequency for water with controlled pore glass samples by Glaves et al. (1988).

2.3.5 Probing polymers, surfactants and surface chemistry

The use of relaxometry to probe colloidal suspensions, often in the presence of polymers, has received significant interest and an in-depth review has been conducted by Cooper et al. (2013(a)). More specifically, some examples include the investigation of; polymers in aqueous solution and gels (Shapiro (2011), Spěvák (2009)), polymer melts entanglement and surfactant polymer interactions (Pettersson et al. (2004), Gao et al. (1990)). The understanding of these bound solvent sites with polymers, appears to be well understood through relaxometry studies, this could provide additional understanding for milling

processes which also use polyphosphate dispersants and sometimes polymer coatings. Although there is a vast body of literature regarding the adsorption of polymers and surfactants probed using relaxation NMR (see review by Cooper et al. (2013(a))), no studies were found for the adsorption of polyphosphates onto colloidal particles. The following studies discussed have been picked to demonstrate how relaxation NMR can be used to probe adsorption isotherms, desorption events and competitive adsorption. Where possible the literature has been reviewed for similar particle systems encountered in this thesis, for example those that area alumina modified or Al containing clays.

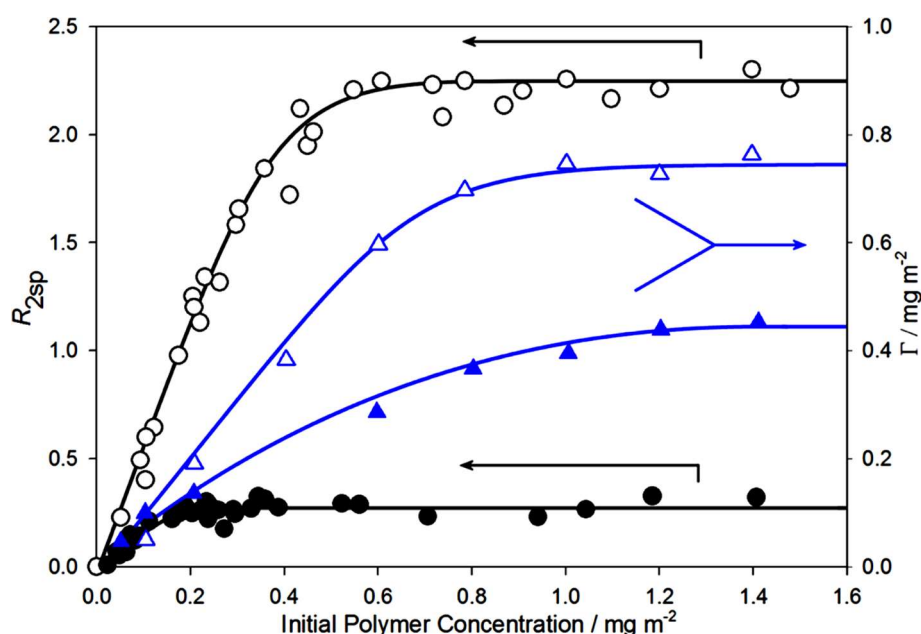


Figure 2-38: Adsorption isotherm of PVP onto colloidal silica (Δ) and alumina-modified silica (\blacktriangle) by Cooper et al. (2012). Pseudoisotherm generated from NMR data for silica (\circ) and alumina-modified silica (\bullet). The R_{2sp} is the measured R_2 scaled to an equivalent sample of bare particle to remove the effect of increasing surface area.

The effect of surfactants and electrolytes on polymer layer adsorption onto the surface of silica has been studied in detail using relaxation NMR (Flood et al. (2006), Flood et al. (2008), Flood et al. (2007b), Flood et al. (2007a)), and plots of the specific relaxation rate enhancement (R_{sp}) against increasing particle concentrations have been compared to adsorption isotherms. Cooper et al. (2012) demonstrate how relaxation NMR can be useful in probing adsorption isotherms for PVP adsorbed onto silica and alumina modified silica shown in . They observed a plateau in the NMR data corresponding to

surface saturation of PVP, however, this is sharper and occurs at lower PVP concentration than observed with the conventional isotherm technique.

This is because NMR is only sensitive to the train layer of the adsorbed PVP compared to the whole layer (Cooper et al. (2012), Van der Beek et al. (1991)). shows that the alumina-modified silica has a much lower enhancement of relaxation rate after adsorption of PVP. This was thought to be from a combined effect of (1) aluminium nuclei causing relaxation rate enhancement through specific quadrupolar interactions effectively screening the effect of the adsorbed polymer and (2) a weaker interaction between the polymer and the Al modified surface Cooper et al. (2012). Cattoz et al. (2012) show that relaxation NMR can be used to probe desorption events. They showed a reduction in R_{2sp} with increasing surfactant concentration to PVP adsorbed silica particles. Similarly, the R_{2sp} reaches a plateau where the addition of surfactant causes no change in the R_{2sp} where no additional removal of PVP is found.

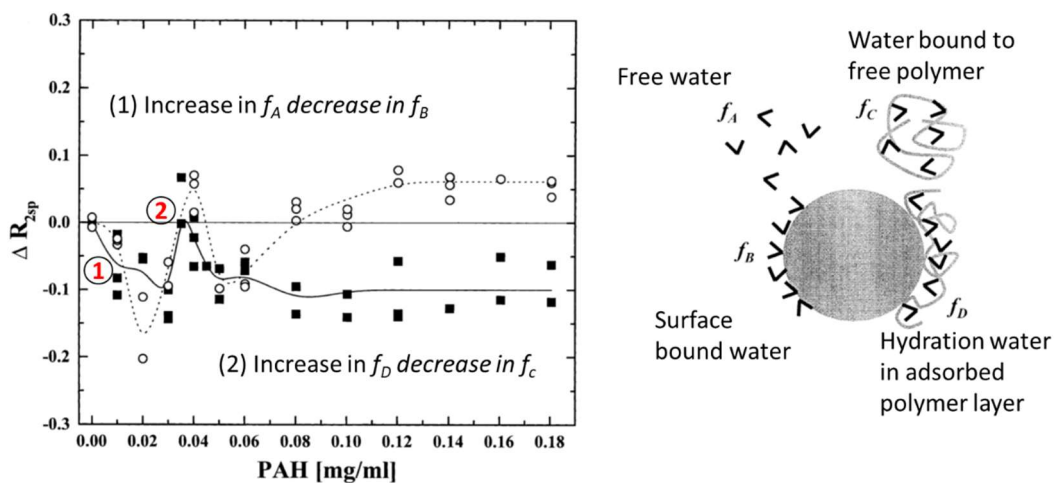


Figure 2-39: ΔR_{2sp} of the adsorption of a 1st layer to polystyrene latex particles. Filled symbols: PAH in H_2O , open symbols: PAH in 0.25 M NaCl. Reported by Schwarz and Schönhoff (2002).

The adsorption of poly-(allylamine hydrochloride) (PAH) onto polystyrene latex particles has been probed using relaxation NMR by Schwarz and Schönhoff (2002) and is shown in Figure 2-39. Figure 2-39 shows the relative relaxation enhancement (R_{2sp}) calculated from the T_2 relaxation data, here, the horizontal line ($R_{sp} = 0$) corresponds to a noninteracting system and deviation from this line is due to changes in water

immobilisation arising from polymer-particle interactions (Schwarz and Schönhoff (2002)). In water and salt, Schwarz and Schönhoff (2002) observed an initial decrease in R_{2sp} with increasing polymer concentration (point 1), followed by a maximum (point 2) and another decrease at higher PAH concentrations.

Schwarz and Schönhoff (2002) further detected a saturation in the zeta potential measurement to coincide with the plateau in R_{2sp} due to additional polymer not interacting with the particle surface and thus no further change in R_{2sp} is observed. In water, the plateau of R_{sp} is negative indicating a decrease in water mobility at the particle surface (Schwarz and Schönhoff (2002)). Schwarz and Schönhoff (2002) provide a detailed understanding relating to the shape of the R_{2sp} curves corresponding to contributions from water fractions at different sites (e.g. free water, water bound at particle surface, water bound to polymer in solution and hydration water in adsorbed polymer layer). Schwarz and Schönhoff (2002) clearly demonstrate the use of relaxation NMR to investigate complex multilayer adsorption processes.

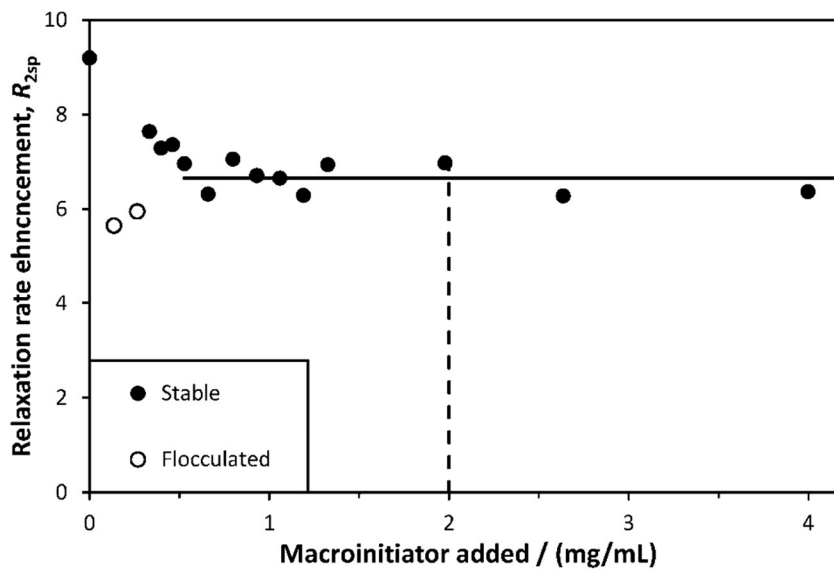


Figure 2-40: Specific relaxation rate enhancement (R_{2sp}) as a function of macroinitiator to particle ratio for 5 wt. % dispersions of 120 nm diameter silica in water Cheesman et al. (2013).

Cheesman et al. (2013) showed that the addition of a macroinitiator caused a decrease in the specific relaxation of silica particles (Figure 2-40). This is because water is displaced

from the silica surface due to adsorption of the macroinitiator and the new interaction between the macroinitiator and water interface has lower specific surface relaxivity. Typically increases in relaxation rates enhancements are observed for the adsorption of water-soluble polymers onto silica (Van der Beek et al. (1991), Cattoz et al. (2012)) due to an increase in surface bound water, however, as previously conversed Schwarz and Schönhoff (2002) showed fluctuations in R_{2sp} with minima and maxima recorded after the addition of polyelectrolyte onto polystyrene latex particles. The large scatter in data observed at low macroinitiator concentrations (Figure 2-40) is characteristic of an unstable colloidal system, at low concentrations (<0.3 mg/mL) charge patch flocculation occurs due to incomplete surface coverage (Cheesman et al. (2013)), here flocculation causes a reduction in surface area and observed is a reduced R_{2sp} . Cheesman et al. (2013) reported that the plateau in R_{2sp} corresponds to the saturation of the macroinitiator train layer at the silica surface and further addition of macroinitiator has no effect on the relaxation rate as the surface bound water is not further influenced.

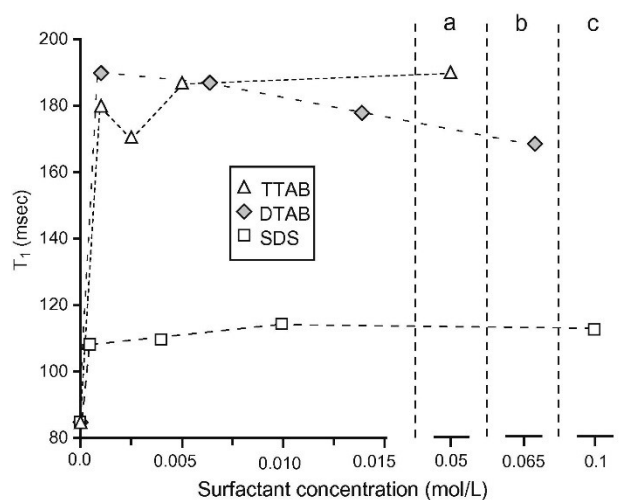


Figure 2-41: Surfactant concentration (prior to adsorption on kaolin) versus water T_1 values for solutions of the three surfactants SDS, TTAB, and DTAB adsorbed on unwashed kaolin by Totland et al. (2011).

Totland et al. (2011) compared the adsorption of three different surfactants onto kaolinite using relaxation NMR (Figure 2-41). They observed an initial increase in the T_1 relaxation values of water for all three surfactants studied. An increase in T_1 implies that the water/surfaces interactions are reduced. This is most likely due to the influence of Al in

kaolinite, causing relaxation rate enhancement through specific quadrupolar interactions prior to surfactant adsorption. Both sodium dodecyl sulfate (SDS) and tetradecyl trimethyl ammonium bromide (TTAB) reached a T_1 plateau at the CMC and further addition of surfactant caused no change in T_1 values. Whilst a reduction in T_1 is observed for dodecyl trimethyl ammonium bromide (DTAB) at higher concentrations due to desorption caused possibly by greater interactions of DTAB molecules in solution rather than DTAB at the surface of kaolinite (Totland et al. (2011)). Furthermore, Totland et al. (2011) suggested that the increased T_1 values for TTAB and DTAB was due to these surfactants adsorbing to a greater extent than SDS.

Furthermore, NMR relaxation has provided useful insight into competitive adsorption processes (Cooper et al. (2013(b)), Nelson et al. (2002)). Nelson et al. (2002) compared the relaxation enhancement of polyvinylpyrrolidone (PVP) and poly(ethylene oxide) (PEO) in silica dispersions and investigated these as mixed polymer systems. They found that the enhancement was different for the two polymers and the gradient of the R_{sp} plot against silica concentration highlighted information regarding the bound layer polymer conformation, where a transition point was observed indicating that PVP had displaced preadsorbed PEO (Figure 2-42) (Nelson et al. (2002)).

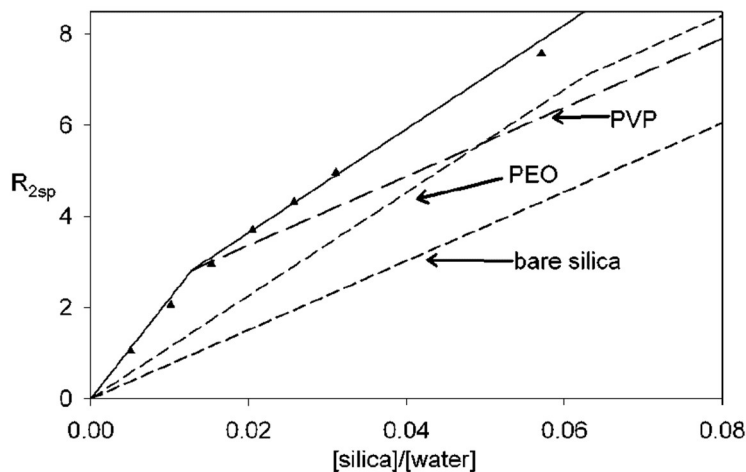


Figure 2-42: Nelson et al. (2002), show the displacement of preadsorbed PEO on silica particles by PVP.

2.4 Summary

Through this literature review it has been demonstrated that the milling of TiO₂ aggregates is rather complex, with phase transformations often occurring and the appearance of particle fines for extended milling times. These studies become particularly important to understand for the monitoring of surface area during milling when using relaxation NMR. This is because the technique is sensitive to not only surface area changes which are likely to be extremely large for the particle fines but further surface chemistry changes. As the technique is sensitive to surface chemistry changes it is important that the crystal phase of the milled material supplied by Venator is comprehensively characterised using an array of techniques to understand if any changes occur during milling. Further to this TEM analysis will be required on the milled material supplied by Venator to confirm changes in aggregate size and if particle fracturing occurs.

Polyphosphates are often used during the manufacturing process to disperse the pigment particles during milling which occurs at high solid concentrations. It has become apparent that the adsorption density of polyphosphates onto pigment particles is complex, with both chemisorption and physisorption occurring, not only are the adsorption isotherms onto clay particles influenced by changes in adsorption time but also pH (Connor and McQuillan (1999), Farrokhpay et al. (2010), Farrokhpay et al. (2012), Michelmore et al. (2000)). More concerning are the studies that indicate hydrolysis of polyphosphates under extreme pH conditions, temperature and in the presence of metal ions (Thilo (1965), Rulliere et al. (2012), Cini and Ball (2014), Rashchi and Finch (2000)). However, there appears to be limited research (Ma (2012), Farrokhpay et al. (2012), Andreola et al. (2006)) regarding the stability of polyphosphates following adsorption onto clay or mineral surface and ultimately if changes in the dispersion properties occur. Further to this there is no literature regarding the stability of polyphosphates during milling.

Therefore, several questions remain such as the influence of milling time and conditions on polyphosphate adsorption density and stability? It remains unclear if dispersant chemistry is likely to change as a result in milling and this is an important question to understand in relation to the use of relaxation NMR which can be used to detect both chemical and particle size changes. If simultaneous changes in particle size and surface chemistry occur during milling is one effect more dominant and is it possible to separate the effects observed during relaxation NMR monitoring?

Nuclear magnetic resonance (NMR) is commonly used for the identification of unknown compounds, however the use of relaxation NMR to determine surface area for aqueous environments is not often observed in the literature. Thoma et al. (1993) investigated the surface area of titania (aluminosilicate coated rutile) and silica powders, they found a good agreement between BET and NMR measurements across a range of particle concentrations and similar results for pore glass samples were reported by Davis et al. (1987). However, both studies by Thoma et al. (1993) and Davis et al. (1987) were undertaken using ideal samples which is often not representative of commonly encountered highly concentrated industrial slurries which often contain mixtures of particles, inorganic contaminants, and dispersants. Furthermore, questions remain regarding the sensitivity of the technique for probing small differences in surface area to imply changes in aggregate size during milling, which has not previously been demonstrated in the literature.

It has become apparent that Alumina surface hydroxyl groups cause the motional restriction of water through specific interactions leading to relative relaxation enhancements for alumina (Cosgrove et al. (1992)). Thus, it is not known what effect aluminium dopants will have on the relaxation rate of milled samples and if it is possible to mitigate the enhancement to allow for surface area determination. Further still, if alumina surface concentrations are found to vary with milling time along with potential dispersant hydrolysis and surface area changes, the interpretation of NMR results could become significantly challenging.

Literature has shown that specific ion effects clearly make the interpretation of NMR relaxometry more complicated (observed previously were enhancements in relaxation rates), and at worse mitigate the application of the technique. The influence of particle surface charge and magnitude, and related influence of agglomeration have not previously been studied simultaneous to changes in relaxation data in the presence of electrolytes. These studies are of importance as titanium dioxide is produced in the presence of caustics and various metal ions. Literature suggests that this effect is most likely to be concentration and valency dependent which warrants further investigation if this technique is to be utilised to monitor industrial suspensions changes in surface area.

2.5 Research objectives

- To understand how solvent relaxometry data compares to classical particle and crystal size characterisation techniques. This data will be compared to Brauner-

Teller-Emmett (BET theory which uses N₂ adsorption to calculate surface area). The surface area data will be converted into particle size and comparisons made with dynamic light scattering (DLS). To initially understand the technique, particles of different surface chemistry will be investigated such as silica, commercial titania and calcite.

- To study a new online sensor which can differentiate between changes in particle size for complex agglomerates, this technique should have the capability of early size control during the milling stage. Milled samples will be obtained from Venator's chloride manufacturing process, these samples will be extracted at various time intervals and characterised using solvent NMR relaxometry to measure the particle surface area (SA). To use the online sensor to generate surface area milling curves which could be used to derive particle size changes relevant to those generated during the TiO₂ milling process. Furthermore, to explore the advantages and limitations of using a low frequency desktop NMR machine.
- To study a sensor capable of achieving size data, for a highly concentrated slurry in the presence of inorganic contaminants. Solvent relaxation will be investigated using a 13 MHz (low frequency) desktop spectrometer which has a static measurement and a flow cassette capable of online measurements. Experiments will be performed using the static measurement set-up at different particle concentrations to understand the limitation of particle concentration. The surface area measurement will be studied in the presence of inorganic containments, for example inorganic salts.
- To understand if changes occur for the aluminium surface concentration or dispersant chemistry during milling and to probe these changes through surface charge and elemental composition techniques such as energy dispersive X-ray spectroscopy (EDS) and X-ray fluorescence (XRF). To relate any observable changes to relaxation NMR results.
- To investigate the strength of the polyphosphate interaction by measuring the elemental composition of the dispersant before and after centrifugal washing by XRF and X-ray photoelectron spectroscopy (XPS). To further understand the influence of milling time, temperature and ions found in hard water on the strength and adsorbed quantities of polyphosphate by XPS.

Table 2-2 Summary of parameters effecting NMR relaxation signal.

<i>Parameter and literature observations</i>	Potential influence on NMR results for the system under investigation
<p><i>Milling time or increase in particle surface area. Agglomerate and/or aggregate breakage.</i> Solvent relaxation NMR has previously been used to measure particle specific surface area (Fairhurst et al. (2016), Thoma et al. (1993), Davis et al. (1987), Glaves et al. (1988)).</p>	<p>An increase in the milling time of TiO₂ particles should lead to the breakage of aggregates. This would lead to an increase in specific surface area of the powder. As the water bound at a particles surface relaxes faster than the bulk, an increase in the average relaxation rate would be observed as milling time is increased. This would translate to an increase in the relative relaxation rate (R_{sp}), if only the surface area changes as a function of milling time and no change in the surface chemistry is observed.</p>
<p><i>Dispersant addition.</i> Solvent relaxation NMR has been used to study the adsorption of polymers and dispersants onto particles and shows changes in the relaxation rate of bound water at the particle interface (Cooper et al. (2012), Cooper et al. (2013(b)), Flood et al. (2006), Flood et al. (2008), Flood et al. (2007b), Nelson et al. (2002), Van der Beek et al. (1991), Fairhurst et al. (2016), Flood et al. (2007a), Cosgrove et al. (1992), Cooper et al. (2013(a))).</p>	<p>An increase in the concentration of SHMP in the presence of TiO₂ may lead to an increase in the relative relaxation rate, however the Al surface sites could lead to enhancement and in this case addition of a dispersant or polymer could lead to a reduction in R_{sp}.</p>
<p><i>Dispersant structural changes.</i> Structural changes in dispersants/polymers induced by milling have not been reported with solvent relaxation NMR previously.</p>	<p>It is not known what the specific effect on the relaxation rate would be if structural changes occurred for SHMP with milling time. If the SHMP chain becomes hydrolysed and bound water approaches that of the alumina-doped TiO₂ surface there may be an increase in the relaxation rate of the system due to the presence of alumina causing an enhancement in the relaxation rate.</p>

<i>Parameter</i> and literature observations	Potential influence on NMR results for the system under investigation
<p><i>Removal of dispersant.</i> Cooper et al. (2012) studied the competitive adsorption of poly(vinylpyrrolidone) (PVP) onto silica and alumina-modified silica particles. They reported that when PVP was initially adsorbed onto the alumina-modified particles, after the addition of silica particles, the presence of PVP was only observed on SiO₂ at equilibrium. In this case the PVP was removed from the alumina-modified particles. Nelson et al. (2002) studied the displacement of poly(ethylene oxide) (PEO) on silica particles by the adsorption of PVP and observed a transition point in the relative relaxation rate (R_{sp}).</p>	<p>Removal of the dispersant from a particle surface should lead to a decrease in the relative relaxation rate (R_{sp}) back to that of the “pure” particle system. However, for the alumina-modified TiO₂ system the bound water layer at the surface of particle is enhanced due to the presence of alumina and thus the relaxation rate of the “pure particle system” may be greater than the average relaxation rate probed when the dispersant is attached to the surface. Thus, the opposite trend would be observed, an increase in the relative relaxation rate of the “pure” particle system.</p>
<p><i>Alumina.</i> Cosgrove et al. (1992) studied relative relaxation rates for alumina. They showed that the time bound water spends at the surface of a particle is not entirely determined by the surface charge of the particle. They showed that alumina had a faster relaxation rate than polystyrene latex, indicating a faster relaxation of bound water at the alumina particle surface due to surface hydroxyl groups which causes the motional restriction of water through specific interactions.</p>	<p>An increase in the content of aluminium at the alumina doped TiO₂ particle surface, may cause an increase in the relaxation rate of bound water at the particle surface. If the alumina concentration at the surface increases as a function of milling time the increase in relaxation rate from surface area alone may be disproportional.</p>

Chapter 3 Relaxation NMR theory and method

The content of this Chapter relates to the NMR theory and experimental method used in Chapters 4, 5 and 6.

3.1 Relaxation NMR theory

This section explains the well-known theory, often taught at undergraduate level behind obtaining NMR proton relaxation rates and how these parameters can be measured. Following on from this is a detailed theory section describing how these measurements can be used to obtain surface area data and further still understand particle porosity.

Electrons have an associated spin and in an atom these spins can be paired to result in an atom containing no overall spin, however, for a ^1H atom this is not possible. There are three rules to determine the net spin of a nucleus (Hore (2015)):

- 1 The number of neutrons and protons are both even the atom will have no overall spin (Hore (2015)).
- 2 The number of neutrons plus the number of protons is odd results in a half integer spin (e.g. $\frac{1}{2}$) (Hore (2015)).
- 3 Both the number of neutrons and protons are odd the nucleus will have integer spin (e.g. 1, 2) (Hore (2015)).

The overall spin (\mathbf{I}) is important as the theory of nuclear magnetic resonance is based upon a physical phenomenon, where the nuclear magnetic moment of atomic nuclei interact in an externally applied magnetic field (\mathbf{B}), applied in the Z direction (Hore (2015)). When a field is applied these energy levels split (Figure 3-1) resulting in a magnetic quantum number (m) and the transition energy (ΔE) between these levels, given by Eq. (3-1) (Hore (2015)). Here, the fundamental nuclear constant is denoted γ (the gyromagnetic ratio) and \hbar is the reduced form of the Planck constant (Hore (2015)).

$$\Delta E = \gamma \hbar B \quad (3-1)$$

$$\frac{N_\beta}{N_\alpha} = e^{\frac{-\Delta E}{k_B T}} \quad (3-2)$$

The Boltzmann distribution shown in Eq. (3-2), (the population ratio N_{β}/N_{α}), describes the population of the energy levels for a nucleus in a magnetic field, resulting in the lower energy level containing more nuclei than the higher level. This population ratio is determined by thermodynamics, where, T , is the temperature and k_b the Boltzmann constant (Hore (2015)). A radiofrequency pulse (RF) causes the excitement of nuclei from a lower energy level to a higher one, when the frequency of the radiation is equal to the Larmor frequency determined by the transition energy (Hore (2015)). Termination of the RF pulse causes the spins to return to their equilibrium position and this process is called NMR relaxation (Hore (2015)).

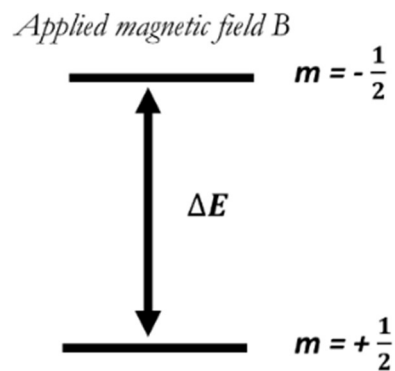


Figure 3-1: Energy levels for nucleus with spin number equal to $\frac{1}{2}$ (Hore (2015)).

A nucleus in the presence of a magnetic field will precess around the magnetic field on its axis of rotation (Figure 3-2) (Levitt (2001)). The frequency of the nuclei precessional orbit is equal to the Larmor frequency, (also equal to the transitional energy) (Levitt (2001)). When the nucleus adsorbs energy, the precessional angle will change and causes the magnetic moment to oppose the external applied field (Figure 3-2) (Levitt (2001)). The nuclei is then in a higher energy state e.g. spin $-\frac{1}{2}$ (Figure 3-1). Saturation occurs when the energy levels of the higher and lower states become equal, resulting in no further adsorption of electromagnetic radiation, however, nuclei can relax to return to their original lower state, this can occur via one of the relaxation mechanisms either spin-lattice (T_1) as shown by Figure 3-3 or spin-spin (T_2) relaxation as shown in Figure 3-5 (Levitt (2001)).

B applied magnetic field

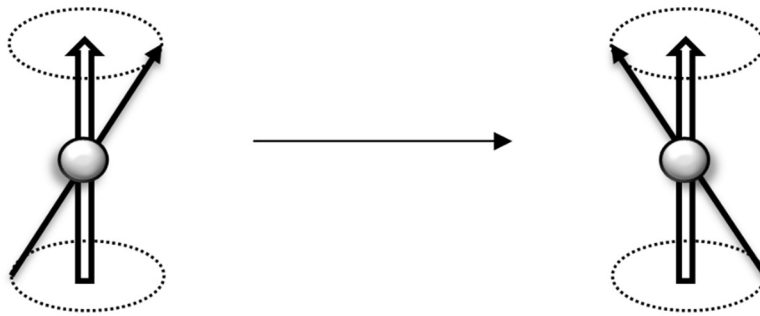


Figure 3-2: The adsorption of radiation by a nucleus in a magnetic field.

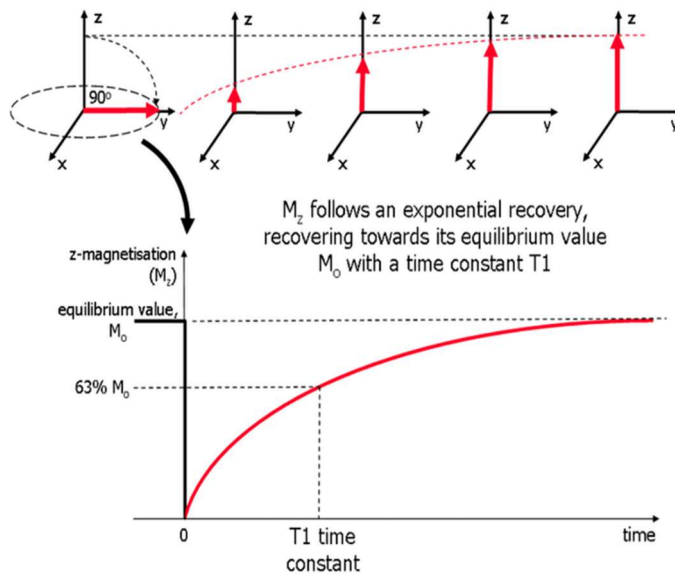


Figure 3-3: T_1 relaxation mechanism (Tadanki (2018)).

Spin-lattice or longitudinal relaxation occurs as a result of nuclei interacting with their surroundings, ultimately causing a change in the spin orientation back to equilibrium spin state, in the Z-axis (Levitt (2001), Cooper et al. (2013(a))). For spin $\frac{1}{2}$ nuclei this relaxation follows a first-order exponential, with a characteristic T_1 value (Figure 3-3), and this can be measured using an inversion recovery pulse sequence (Cooper et al. (2013(a))). For the inversion recovery sequence (Figure 3-4), a 180° radio frequency pulse is followed by a time (τ) (allowing T_1 relaxation mechanism of the spins to occur). After, a 90° pulse is applied causing the magnetization to rotate in the y-axis. The sequence is repeated for increasing correlation time values (τ), and a value of $5T_1$ is required between measurement repeats to ensure equilibrium is reached, resulting in longer experimental times than T_2

(Cooper et al. (2013(a))). More complicated multiple exponential decays of T_1 are seen when solvent molecules are not in fast exchange with each other, for example, water in a porous material (pore water) shows bi-exponential relaxation (Cooper et al. (2013(a))). The T_1 recovery curve is shown in Figure 3-3 (Levitt (2001)) and mathematically described by Eq. (3-3) (Cooper et al. (2013(a))). The characteristic T_1 time of a sample is achieved when 63 % of the longitudinal magnetisation is recovered.

$$M_z = M_o(1 - 2e^{-\frac{t}{T_1}}) \quad (3-3)$$

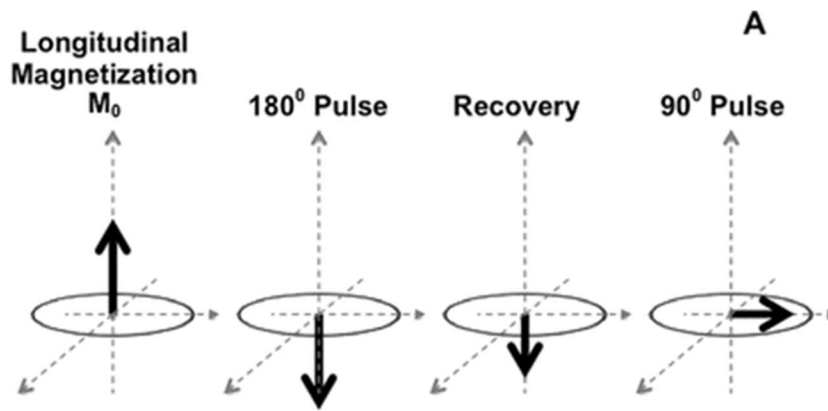


Figure 3-4: Illustration of the inversion recovery method by Currie et al. (2013).

The second process, spin-spin relaxation (T_2) also known as transverse relaxation occurs between neighbouring nuclei in the XY plane, and no interaction with the surrounding lattice occurs (Levitt (2001)). The T_2 recovery curve is shown in Figure 3-5 (Levitt (2001)) and mathematically described by Eq. (3-4) (Cooper et al. (2013(a))). T_2 relaxation is often measured using a Carr-Purcell-Meiboom-Gill (CPMG) pulse sequence (Cooper et al. (2013(a))). This method starts with a 90° pulse followed by a fixed wait time (τ) and a further 180° pulse and τ , after which this is repeated so that the magnetization amplitude of every second echo peak is measured to give the T_2 signal decay. A minimum delay time of $5T_1$ is required to avoid signal saturation. The characteristic T_2 time of a sample is achieved when 37 % of the transverse magnetisation is present.

$$M_{xy} = M_o(1 - e^{-\frac{t}{T_2}}) \quad (3-4)$$

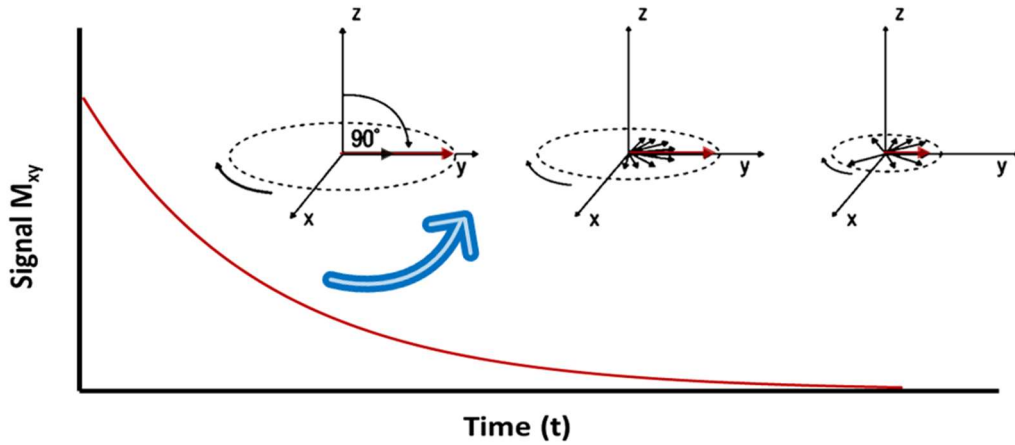


Figure 3-5: T_2 relaxation mechanism redrawn from Ridgway (2010).

3.2 NMR surface area theory

A dispersion constituting a single liquid and single particulate material is simplified to contain two liquid domains that have different relaxation rates (Gallegos et al. (1987), Barberon et al. (2003)), where a monolayer coverage of fluid on the particle surface is assumed. The first domain being the bulk liquid (R_b) which is far away from the particle surface and the second the bound solvent (R_s), which is the liquid molecules on the surface of the particle (Davis et al. (1987)).

The liquid bound at the particle surface has a relaxation time orders of magnitude shorter than the comparative bulk (2-3 seconds), as their motion becomes anisotropic and restricted, thus enhancing the relaxation rate (Cooper et al. (2013(b)), Fairhurst et al. (2016)). However, only a single average relaxation time is observed due to the fast interchange of the bulk and bound solvent (Cooper et al. (2013(b)), Fairhurst et al. (2016)).

The average relaxation rate (R_{av}) is weighted by the quantity of fluid in each domain, whereby the domains are additive as shown by Eq. (3-5) (Fairhurst et al. (2016)). Here, R_{av} , R_b and R_s (s^{-1}) are various solvent relaxation rates, detailed above, ψ_p is the particle to liquid volume ratio (dimensionless), S (m^2/g) is the total surface area per unit weight, L (m) is the surface layer thickness of the bound liquid, while ρ_p is the bulk particle density (g/m^3).

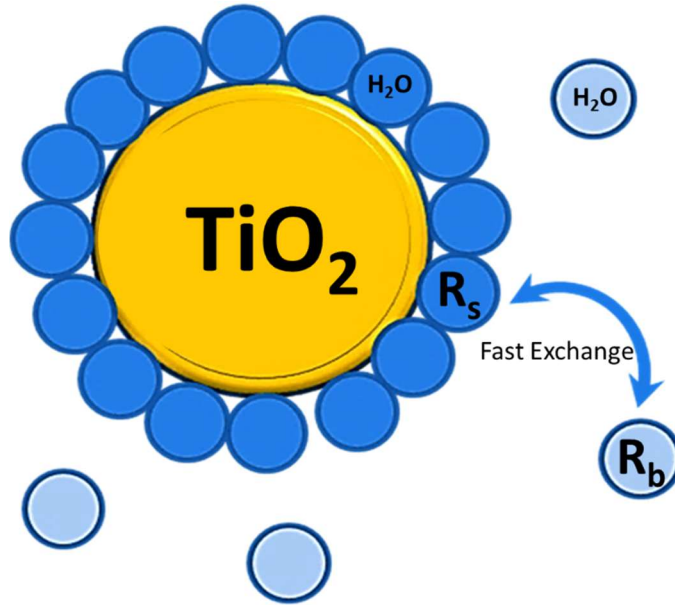


Figure 3-6: Exchange of bound (R_s) and bulk solvent (R_b), due to fast exchange only an average relaxation rate is measured by NMR (R_{av}).

$$R_{av} = \psi_p S L \rho_p (R_s - R_b) + R_b \quad (3-5)$$

The use of a standard reference material of a known surface area, allows a constant to be defined K_a , which for a given interface, can in principle be obtained for any material. This parameter is a surface specific relaxation constant ($\text{g}/\text{m}^2/\text{s}$), shown by Eq. (3-6), where, K_a is dependent on both particle type, associated surface chemistry and solvent (Fairhurst et al. (2016)). While, this dependency has limited the techniques use in some systems, nonetheless, it still provides a simple and rapid method to extract important information regarding changes in wetted surface area. Similar theory has previously been denoted for the online surface area measurements of concentrated slurries (Thoma et al. (1993)).

$$k_a = L \rho_b (R_s - R_b) \quad (3-6)$$

The particles' specific surface area for a given particle system is calculated by substituting Eq. (3-6) into Eq. (3-5) and rearranging, as shown by Eq. (3-7) (Fairhurst et al. (2016)). Here, R_{sp} is known as the specific relaxation enhancement (Eq. (3-8)) which is a dimensionless number (Cooper et al. (2013(a)), Cooper et al. (2013(b))).

$$S = \frac{R_{sp}R_b}{K_a\psi_p} \quad (3-7)$$

$$R_{sp} = \frac{R_{av}}{R_b} - 1 \quad (3-8)$$

Hence, the total surface area of particles in a suspension is calculated from the gradient of the R_{sp} plot as a function of particle volume ratio (ψ_p) (Fairhurst et al. (2016)). It is well accepted this theory holds true for a given particle-solvent system when:

- There is a fast exchange between the bulk and bound solvent and the NMR relaxation times are markedly different, where the bulk relaxation time is longer.
- A material with a high surface area should have a shorter relaxation time, as more fluid is bound to the surface.
- The particle systems are well dispersed and do not sediment during the relaxation measurement.
- Relaxation NMR is also dependent on temperature and frequency conditions and must, therefore, be kept constant throughout the measurement.

In reality, there are many potential factors that may affect R_s for different particle systems, or for the same particle systems in different surface environments. For example, the adsorption of surfactants and polymers has a big effect on R_s relaxation which is not captured by this equation. Other factors that can influence the rate of relaxation of surface bound water include, pH (Van der Beek et al. (1991)), paramagnetic species (Cooper et al. (2013(a))) and the presence of ^{27}Al (Cooper et al. (2012)). For, silica, pH extremes were found to enhance relaxation rates as observed by Van der Beek et al. (1991), whereas the relaxation rate for water was independent of pH. This enhancement for silica is due to proton exchange occurring at the particle surface between water and surface hydroxyl groups. Further, the dissolution of particles can result in relaxation rate enhancements, which for silica, this may occur above pH 12, and is a result of paramagnetic impurities entering into the bulk solution (Van der Beek et al. (1991)).

3.3 Expression of relaxation data to calculate porosity

Relaxation NMR is useful for the determination of internal structure, for example porosity. In the case of porous particles in water, three liquid domains exist, the first the

bulk which has a slow relaxation (R_b), the surface bound water (R_e) and finally liquid bound within the pores (pore water) (R_i) (Gallegos et al. (1988)). The pore fluid will have the fastest relaxation rate (R_i) as motion becomes more anisotropic, further to this a porous solid contains a variety of different pore sizes resulting in a T_2 distribution of pore water (Gallegos et al. (1988)). NMR relaxation is dependent on the pore throat diameter, pore volume and interfacial chemistry (Fairhurst et al. (2016)). A fast exchange model is assumed within the pore fluid, thus surface pore fluid has a fast relaxation time compared to the bulk pore fluid which has the same properties as the bulk liquid (no solids) (Gallegos et al. (1988), Krzyżak and Habina (2016), Fairhurst et al. (2016)). Therefore, in this case two separate magnetization decays are observed (Fairhurst et al. (2016)) as shown by Eq. (3-9), where M_t is the total magnetization and M_e and M_i are the magnetisation resulting from the bound surface water and pore water respectively (Fairhurst et al. (2016)).

$$M(t) = M_e \exp(-R_e t) + M_i \exp(-R_i t) \quad (3-9)$$

Subsequently, relaxation data might reveal a biexponential decay rather than a single exponential decay for the plot of magnetization against time (ms). From this biexponential decay it is possible to extract two relaxation times, one for the surface and one for the pore relaxation, these can be used to calculate surface area resulting from the two domains. The total observed spin-spin T_2 relaxation time ($T_{2(obs)}$) can be used to calculate the pore volume using the volume to surface ratio (V/S) (which is the effective pore radius) and a surface relaxivity constant (ρ) (m/ms) (Krzyżak and Habina (2016), Daigle et al. (2014)). The relaxation constant (ρ) can be calculated from mercury-injection capillary pressure experiments (Daigle et al. (2014)).

3.4 NMR Experiments Materials and Methods

Chapter specific material details used with the NMR can be found within each chapter. All NMR relaxation measurements were obtained using a portable bench-top device, the Acorn Area™, operating at 13 MHz and supplied by XiGo Nanotools. Prior to any operation, the instrument was thermally equilibrated for 24 hours, after which the resonance frequency was measured using a copper sulphate solution as received (Xigo Nanotools). A resonance frequency of approximately 13.07 MHz is regarded as adequate

for a measurement to proceed. A 90° -pulse length of $5.67 \mu\text{s}$, 180° -pulse length of $11.33 \mu\text{s}$ and a gain value of 10 dB were used for all relaxation measurements.

A T_1 experiment was planned according to the following procedure; an inversion-recovery sequence was measured with 11 points, averaging 4 scans with a recycle delay of 5 times the anticipated T_1 value. The 11 points on the magnetization vs time curve were planned based on 2^n , where n equals, the time spacing T (ms). Measurements along the curve started at a time T (ms) of one thousandths of the recycle delay, increasing with 2^n until reaching the final 11^{th} point. The anticipated T_1 value was initially approximated for each new particle dispersion or bulk liquid measurement, until the expected T_1 was within 20 % of the final T_1 measurement. Once the anticipated T_1 was within this range, three repeat measurements were performed and an average obtained. For example, an anticipated T_1 value of 1000 ms would give a recycled delay of 5000 ms and a planned inversion recovery sequence would range from $T/5$ (ms) to 5120 (ms).

A Carr–Purcell–Meiboom–Gill (CPMG) pulse sequence was used to measure the spin-spin T_2 relaxation. Typically, a series of four replicate scans were averaged to produce the CPMG trace, and the Xigo Nanotools software fitted the collected signal to a single exponential to extract the relaxation rate coefficient. A recycle delay of $5T_1$ between scans was used. An iterative process was initially used to determine an anticipated T_2 to within 20% of the “true value”. Three T_2 values were measured and averaged per sample and the associated standard deviation and standard error were calculated.

Chapter 4 Salt enhanced solvent relaxation and particle surface area determination via rapid spin-lattice NMR

The content of this Chapter has been published in Powder Technology, Volume 333, 2018, Pages 458-467, under the same title.

4.1 Introduction

Literature exists for the use of NMR to determine porosity (Terenzi et al. (2015), Li et al. (2015)) and polymer adsorption events (Cooper et al. (2013(a)), Cooper et al. (2013(b))), however, it is limited for surface area measurements (Thoma et al. (1993), Davis et al. (1987), Glaves et al. (1988)). Importantly, relaxation NMR not only probes changes in particle surface area but also the interfacial environment. While these few studies (Flood et al. (2006), Conte (2015), Schwarz and Schönhoff (2002), Katika et al. (2014), Van der Beek et al. (1991)) have indicated that electrolyte interactions generally result in an increase in relaxation rate, the underlying mechanism is still unclear. In addition, it is not known whether particle surface charge or magnitude may alter these effects. Importantly for application, there are also imperative questions as to what extent these effects may dominate or confound the use of these measurements for specific surface area analysis, greatly limiting the potential of NMR relaxation for on-line surface area measurements of concentrated slurries.

Despite the number of previous studies, in wide research areas, there are still significant questions related to the application of NMR relaxometry for the measurement of colloidal surface areas, which has so far limited its wider use. Understanding the limitations of the NMR technique is an integral question for this studentship, as the titanium dioxide manufacturing process contains a vast number of dopants to regulate particle size and control the crystal phase. Surplus to this, the TiO₂ milling processes contains added dispersants and electrolytes to aid the milling process by reducing aggregation. Further to this, NMR relaxometry could be a useful tool to determine external and internal particle properties of TiO₂ aggregates, as pore water relaxes faster than surface water which again relaxes faster than the bulk solvent. Hence, relaxation NMR could offer a greater understanding of aggregate breakage events whilst milling, which could allow for more efficient milling control.

To better understand these related phenomena, this chapter presents NMR relaxation measurements in various systems, with changes in both particle surface area and interfacial chemistry. Titanium dioxide, calcium carbonate and silica were selected, due to their likely differences in particle charge at neutral pH (Gustafsson et al. (2000), Somasundaran et al.

(1985), Wilhelm and Stephan (2006)). Additionally, their fine and cohesive nature, resulting in broad size distributions are representative of many commonly encountered industrial suspensions (Weir et al. (2012)). Systems with and without 1 M KCl were characterised, where the high salt concentration was thought to considerably enhance any potential ion effects, but also induce particle aggregation (and thus lower total surface area).

4.2 Materials and Methods

4.2.1 Materials

An initial NMR calibration was made using Ludox AS-40, 40 wt.% suspension standard (Sigma-Aldrich) which is denoted as *silica^a* throughout this chapter. Silica^a has a particle size 20-24 nm, and a specific surface area of 135 m²/g, as quoted by the supplier (Sigma-Aldrich). Silica^a was received suspended in distilled H₂O and an ammonium stabilising counterion. Dispersions were purified using an ion exchange resin Amberlite MB-150 (MP Biomedicals) to remove any residual electrolyte effects from the standard. Angstrom Sphere silica microspheres (Fiber Optic Center) were used and this silica is represented as *silica^b* from herein. Silica^b was supplied as a powder, where microspheres were stated as ~100 nm from the manufacturer. The density of both silica 'a' and 'b' was taken to be 2.2 g/cm³ (Hosokawa et al. (2007)). Pre-calcined (anatase) titanium dioxide (supplied by Venator Materials PLC) was also used, denoted *TiO₂^a*, as this material is known by the manufacturer to have a high surface area, due to reduced crystallinity of the anatase phase. The density of titanium dioxide, anatase, was taken as 3.79 g/cm³ (Braun et al. (1992)). Further measurements were conducted on another titanium dioxide (99.5% purity), obtained from Sigma-Aldrich and used without purification, denoted as *TiO₂^b*. TiO₂^b was previously used in the synthesis of Ti(SO₄)O nano-catalyst by Gardy et al. (2016) where the precursor was fully characterised in terms of crystal structure, particle size and BET surface area.

Calcium carbonate (in the calcite polymorphic form), calcite Omyacarb 2AZ (Omya) was also used in this study, due to its incorporation into many consumer products. The density of calcite was taken as 2.71 g/cm³, supplied by the manufacturer. Stock acid and base solutions were prepared to vary the pH of suspensions; hydrochloric acid (Sigma-Aldrich), reagent grade, 37 % was used to decrease the pH and potassium hydroxide pellets (Sigma-Aldrich) were used to increase the pH. Pure potassium chloride salt (Sigma-Aldrich) was used throughout to alter salt concentrations. Ethanol absolute was purchased from Fisher Scientific and used as received for transmission electron microscopy sample preparation.

4.2.2 Sonication

Prior to any analysis or characterisation, suspensions were dispersed using an ultrasonic bath (Clifton Sonic) for 30 minutes. Samples were further dispersed using an ultrasonic probe, Sonic Dismembrator (Fisher Scientific), at 30 % amplitude for 1 minute. All particle-salt measurements were also dispersed using this procedure and then left to mix for 24 hours on a carousel, to ensure the KCl had dissolved and allow time for any particle coagulation to occur.

4.2.3 Particle size and morphology

The particle size, morphology and surface structures were studied for TiO_2^a using a scanning electron microscope (SEM) SU8230 (Hitachi). Prior to SEM analysis, the TiO_2^a powder was placed onto an SEM stub and excess powder was removed by spraying with compressed air. TiO_2^a samples were coated before SEM analysis with a carbon coating of 10 nm using a Q150TE sputter coater (Quorum). SEM images were also obtained for calcite using EVO MA15 (Carl Zeiss). Calcite samples were prepared similarly to TiO_2^a , although, an iridium coating of 10 nm thickness was used. The particle size of two silica samples silica^a and silica^b were investigated using bright field transmission electron microscopy (TEM) FEI Tecnai F20-G2 FEGTEM operating at 200 kV. The silica^a suspension as supplied was pipetted directly onto a copper grid coated with holey carbon film and left to dry, and Silica^b was first suspended in ethanol with vigorous shaking before pipetting onto the grid. When conducting imaging, standard alignments were performed and samples were imaged across a wide magnification range, with numerous areas acquired. Thus, the images selected are representative of the samples analysed.

Particle size distributions were measured for calcite and TiO_2^a , using a Mastersizer 2000 (Malvern), with a standard operating procedure (SOP) of 10 runs, and a measurement taken after every 10 seconds, these 10 runs were then averaged to produce a single distribution. Silica^b particle size distributions were obtained using a Zetasizer Nano ZS (Malvern) with the instrument set to three measurements, each consisting of 15 cycles. The three measurements were then averaged to produce a single particle size distribution for silica^b with and without 1 M KCl.

The Mastersizer 2000 (Malvern) could not be used for TiO_2^a and calcite salt-particle size measurements, due to high shear in the cell, thought to break up coagulated particles. Instead, a Camsizer P4 dynamic image analyser (Retsch Technology), was employed to study the changes in particle size in the presence of the KCl electrolyte. Calcite and TiO_2^a suspensions were first prepared both at 1 vol. % in ultrapure water and 1 M KCl using a stock solution,

and suspensions were dispersed as previously stated. The Camsizer ultrasonic bath was switched off during these particle size measurements to reduce the shear in the cell and avoid breakage of any coagulated particles. A stock 10 mM KCl solution was used as the dispersant fluid in the attached Camsizer ultrasonic bath, and the circulation pump was set to 100 %. The Camsizer SOP was set to three measurements which was then averaged to produce a single distribution, with each run stopping after 80,000 images were analysed.

4.2.4 Settling measurements

A 12 channel Lumisizer Dispersion Analyser (LUM GmbH) was employed to investigate the sedimentation rate of the dispersions, and to further support particle coagulation and changes in particle size distributions. Calcite and TiO_2^{a} dispersions (1 vol.%) were prepared in ultrapure water and with 0.1 and 1 M KCl stock solutions. These suspensions were all dispersed as previously stated and then pipetted into a 10 mL polyamide sample cell PA 110-135XX (LUM GmbH). Settling test were carried out at 25 °C, using a transmission wavelength of 865 nm. The measurement SOP was set to 300 RPM, measuring 90 profiles with 10 second intervals. Each dispersion was run in duplicate and the results were averaged.

4.2.5 Surface charge

A Zetasizer Nano ZS (Malvern) was used to measure the zeta potentials of calcite, TiO_2^{a} and silica^b. Prior to analysis, a stock KCl solution was prepared at 0.1 mM in ultrapure deionised water. TiO_2^{a} , calcite and silica^b dispersions were prepared at a concentration of 1000 ppm each with the stock KCl electrolyte (0.1 mM). Further to this, stock base (KOH) and acid (HCl) solutions were prepared at 0.01, 0.1 and 1 M, to increase and decrease the pH of particle dispersions, respectively. For each surface charge measurement, one dispersion was made to vary with acid and another with base. All dispersions were kept mixing with a magnetic stirrer for approximately 10 minutes after altering the pH. The pH of suspensions were then measured using HI-208 Bench top pH meter (Hanna Instruments), before pipetting into DTS1070 folded capillary cells (Malvern). The zetasizer SOP was set for 3 measurements with a maximum of 100 profiles for each, the measurement automatically terminated when 10 stable profiles were sequentially collated. A total of 6 measurements were collected at each pH point on the zetapotential curve and averaged data was recorded with standard deviations.

4.2.6 Crystal structure

The x-ray powder diffraction patterns for TiO₂^a was obtained to investigate the nature of the crystalline phase, using a D8 X-ray Diffractometer (Bruker) and CuK α radiation source. The TiO₂^a sample was scanned from 2 θ angle 10° to 70° with a step size 0.0495° at 35 s per step.

4.2.7 Surface characterisation

The Brunauer–Emmett–Teller (BET) surface area and pore size measurements were obtained by the nitrogen adsorption-desorption method at 77.3 K using a TriStar 3000 (Micromeritics) surface analyser. TiO₂^a samples were degassed to remove any moisture and surface absorbed gases by using a vacuum oven at 120 °C for 24 h under a vacuum of 10 mmHg. The calcite samples were degassed under N₂ for 4 hours at 300 °C, and atmospheric pressure. Silica^b was degassed under vacuum oven at 100 °C for 17 hours overnight under a vacuum of 10 mmHg. The N₂ adsorption isotherms were used to calculate the BET parameters for both TiO₂^a and calcite; and desorption isotherms were used to calculate the average pore size by the Barrett-Joyner-Halenda (BJH) method.

4.2.8 Relaxation NMR measurements

The theory described in Section 3.4 has been used within this chapter with the exception for all NMR experiments. However, the author proposes a modification of Eq. (3-6) to allow for the surface area determination of multiple particle systems from the use of a single reference interface, as shown by Eq. (4-1). Here, K_a is the unknown materials specific surface relaxation constant (g/m²/ms), K_{ref} (g/m²/ms) is the calculated material specific relaxation constant of a standard reference material of known surface area. Here, ρ_b is the bulk particle density (g/m³) of the material of interest, and ρ_{ref} is the bulk particle density (g/m³) of the standard reference material.

$$K_a = \frac{K_{ref}\rho_b}{\rho_{ref}} \quad (4-1)$$

The replacement of Eq. (4-1) into Eq. (3-7), allows the determination of a particle's surface area. This theory requires that the following assumptions are met;

- The solvent remains constant and only a monolayer coverage of the bound solvent is assumed, thus both R_b and L are unchanged.

- Similar surface chemistries and conditions are required, and thus there must be negligible change in R_s .

Silica^a was used as a reference material. Prior to measuring the T_1 relaxation rates, dispersions were made in ultrapure water at 30, 20, 10 and 1 wt. %. These suspensions were left to stir with a magnetic stirrer bar for 24 hours with an ion exchange resin, the ion exchange resin was then removed by Buchner filtration. Silica^b dispersions were prepared at 1.1, 2.4, 3.3 and 5.0 wt. % in ultrapure water, and 1.0, 2.4, 3.3 and 5.0 wt.% with 1 M KCl. TiO₂^a dispersions were prepared at 10,15, 20 and 25 wt.% in ultrapure water and 10, 20 and 30 wt.% in 1 M KCl. TiO₂^b dispersions were used at 5 and 10 wt.% in ultrapure water. Similarly, calcite suspensions were prepared at 15, 20, 35, 40, 45 and 50 wt. % without salt and 44, 37 and 13 wt.% with 1 M KCl. All suspensions were dispersed according to the protocol described in the previous section before T_1 relaxation measurements were obtained.

4.3 Results and Discussion

4.3.1 Particle characterisation

Scanning electron microscopy (SEM) images were obtained for TiO₂^a and calcite as shown in Figure 4-1. SEM images of calcite (Figure 4-1 (a)) display the faceted nature of the particles, which is important to note as particle size measurements assume sphericity. In some cases, nanocrystallites were found to be agglomerated onto larger particles (Figure 4-1 (a) inset). Figure 4-1 (b) (inset) demonstrates the highly aggregated nature of TiO₂^a, with individual crystallites in the order of ~20-100 nm. TiO₂^a crystallites are fused together to form larger particles and a representative cluster is presented in (Figure 4-1 (b)). These TiO₂^a clusters ranged in Feret diameter between 1-3 μm .

The zeta potential recorded in background electrolyte is shown for TiO₂^a, calcite and silica in Figure 4-2. The pH_{iep} for TiO₂^a was ~6 and in good agreement with previous literature (Gustafsson et al. (2000)). Figure 4-2 also shows calcite to be positively charged, but unstable, fluctuating around 0-10 mV almost across the pH range studied. It is also noted that the partial solubility of calcite leads to a bi-carbonate ion formation, which caused an increase in measured neutral pH to pH 8-9 (still within the region of positive charge). These values are also consistent with literature, where Somasundaran et al. (1985) reported a pH_{iep} for calcite at approximately pH 10.5, with a positive trend and characteristic S-shape curve from pH 7.0-10.5. Silica^b was negatively charged across the entire pH range studied, approaching the pH_{iep}

towards pH 2, and in concurrence with silica literature values ranging from pH_{iep} 1-2 (Wilhelm and Stephan (2006)).

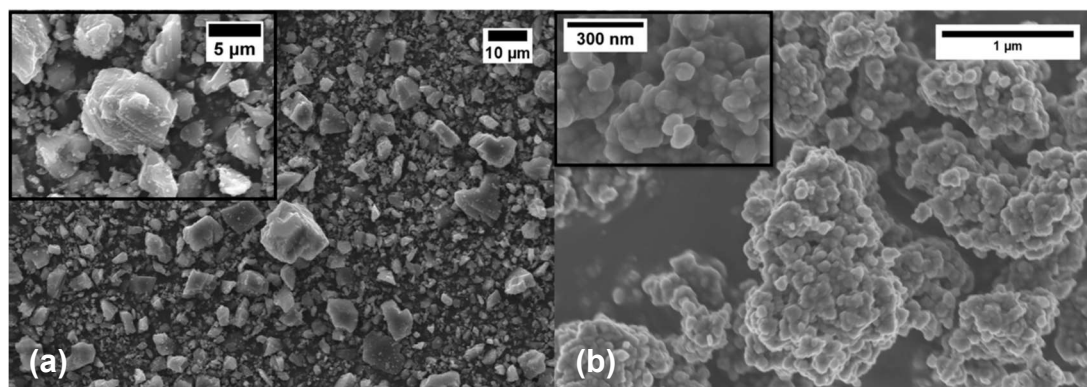


Figure 4-1: SEM images of (a) calcite, scale bar $10\ \mu\text{m}$ and inset scale bar $5\ \mu\text{m}$. SEM images of (b) titanium dioxide (TiO_2^{a}) scale bar $1\ \mu\text{m}$ and inset scale bar $300\ \text{nm}$.

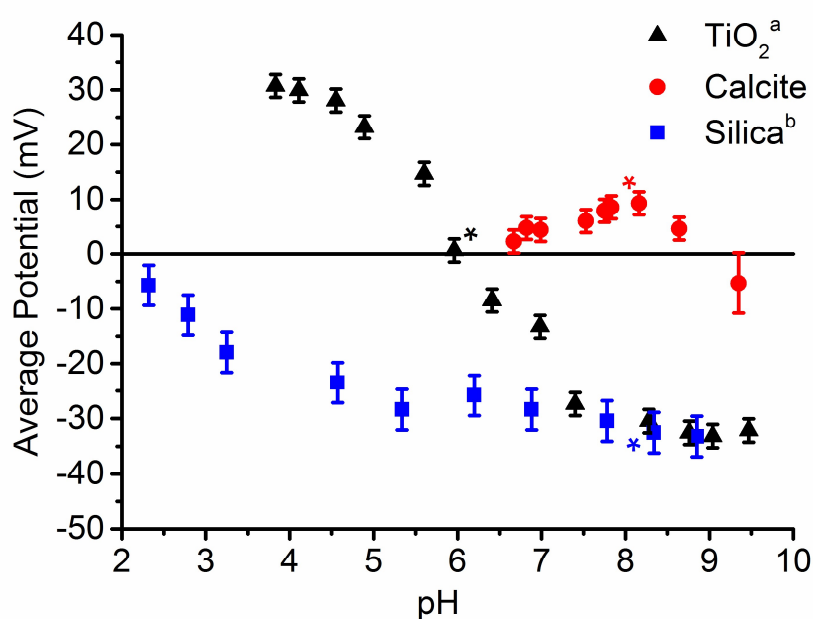


Figure 4-2: Zeta potentials for TiO_2^{a} (triangle), calcite (circle), and silica^b (square) in background electrolyte ($1 \times 10^{-4}\ \text{M}\ \text{KCl}$). The pH of each dispersion for NMR measurements are indicated by coloured asterisks (*). The standard deviation is shown as the error associated with the zeta potential over 6 measurements, for each particle system only the largest standard deviation recorded is shown. Excluding the value for calcite at $\sim\text{pH}\ 9.5$ due to the extremely disproportionate error and thus it has been indicated.

Figure 4-3, shows the particle size distribution (PSD) for TiO_2^a and calcite, where, it is observed TiO_2^a has a monomodal distribution, with a measured D_{50} of $1.63 \mu\text{m}$, which is in accordance with the observed clusters from SEM analysis (Figure 4-1). Calcite was found to have a slightly broader bimodal distribution and a D_{50} of $3.24 \mu\text{m}$. The effect of 1 M KCl on the PSD for TiO_2^a and calcite, measured with the Camsizer, is presented in Figure 4-4. As this data relies on image collection rather than Mie theory, the limit of the detection is $\sim 1 \mu\text{m}$, thus the distributions in Figure 4-4 are not directly comparative to those in Figure 4-3.

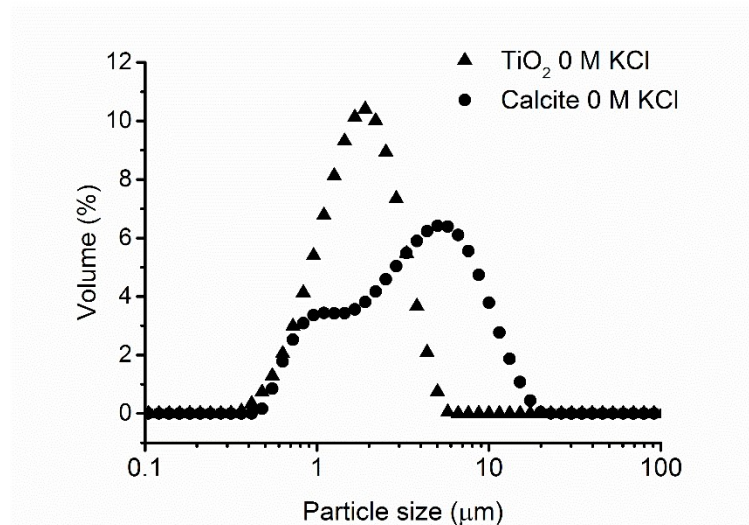


Figure 4-3: Particle size distributions from laser diffraction for sonicated calcite (circle), and TiO_2^a (triangle) dispersions without salt.

However, it is evident in Figure 4-4 (a) that the addition of 1 M KCl to TiO_2^a shows little change in the PSD, with only a small increase in volume % (3 %) is observed around $10 \mu\text{m}$, suggesting perhaps some slight coagulation of smaller particles. More apparent, is the increase in particle size for calcite in the presence of 1 M KCl, demonstrated by the growth of the peak height for particles of $\sim 100 \mu\text{m}$ in size. It is noted that there is evidence for calcite aggregation without salt, with a distinct aggregate peak also at $\sim 100 \mu\text{m}$, which was not observed from the Mastersizer data in Figure 4-3.

This difference is most likely due to a reduction in the level of the dispersion technique inside the measurement cell of the Camsizer (Figure 4-4) compared to the Mastersizer (Figure 4-3), this suggests for calcite the camsizer does not disperse as well. Bux et al. (2015) observed a similar phenomenon in titania PSD, dependent on dispersion mechanism. Although calcite shows a net positive surface charge (Figure 4-2), this has a relatively small magnitude, and

therefore it can be expected that some level of aggregation may take place regardless, although it is clear the majority of calcite particles in 0 M KCl are well dispersed.

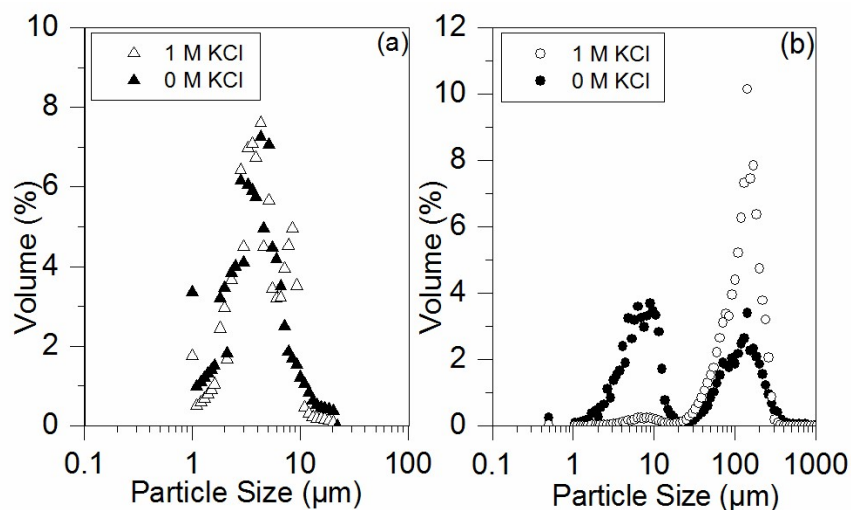


Figure 4-4: Particle size distribution from dynamic image analysis (a) TiO₂^a (triangle), and (b) calcite (circle), both in the presence of 0 M KCl (closed) and 1 M KCl (open).

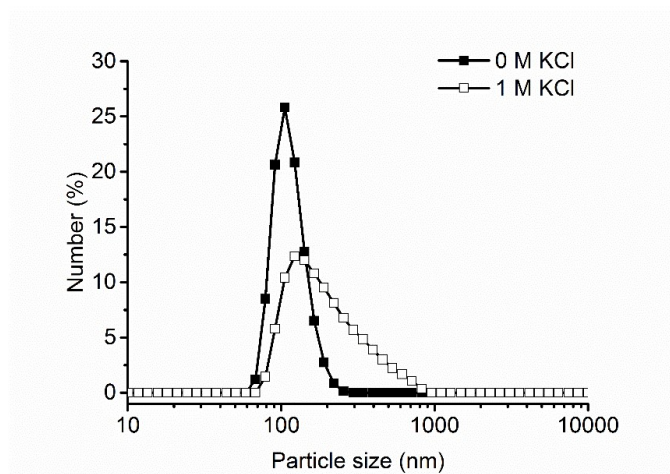


Figure 4-5: Dynamic light scattering particle size distribution for silica^b particles after 24 hours of mixing on carousel at 1 wt%, in the presence of 0 M KCl (closed) and 1 M KCl (open).

The change in silica^b PSD in the presence of 1 M KCl and without electrolyte was also investigated, as observed in Figure 4-5. The particle-water dispersion has a narrow monomodal size distribution with a D₅₀ of 110 nm (polydispersity index (PDI) 0.024), which increases to a D₅₀ of 171 nm (PDI 0.264) in 1 M KCl and a much broader distribution, thus illustrating the

coagulation of silica^b in the presence of the 1 M KCl electrolyte. TEM images of silica^b are shown in Figure 4-6 and show the spherical nature of these particles with little change in polydispersity which is in agreement with the zeta sizer results.

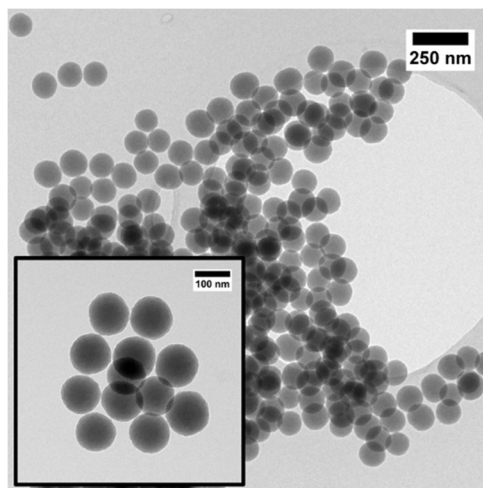


Figure 4-6: TEM images of silica^b nanoparticles, scale bar 250 nm and inset scale bar 100 nm.

Suspension settling rates under centrifugation were also used to elucidate changes in particle aggregation for TiO_2^a and calcite, with the addition of KCl electrolyte. Here, Figure 4-7 represents changes in dispersion height measured over time for titania and calcite systems in the Lumisizer. Average settling rates were approximated from the linear regime of the settling profiles in Figure 4-7. It can be observed from Figure 4-7 that there is little to no change in the settling time for TiO_2^a when in the presence of either 0.1 M or 1 M KCl, demonstrating that the titania is similarly aggregated regardless of solvent conditions. In contrast, both the 0.1 M and 1.0 M KCl calcite dispersions settled to a compacted bed in approximately 100 s, whereas the 0 M KCl calcite dispersion reached an analogous bed height in 900 s. While such an order of magnitude increase in settling rate, correlates to a 3-4 times increase in particle size (if related to the Stokes terminal settling equation) in reality this comparison is only qualitative and probably underestimates the aggregation in salt significantly. The reason is that, at 1 vol % all dispersions are likely within hindered settling zone conditions, where coagulation may significantly enhance hindered settling effects (Johnson et al. (2016)).

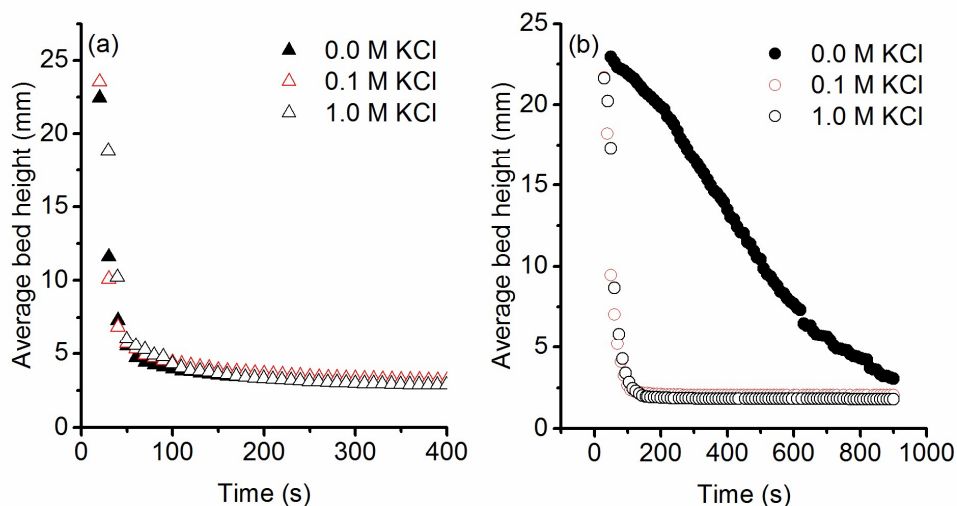


Figure 4-7: Average Lumisizer interface versus time measurements at 300 rpm for 1 vol% dispersions undergoing sedimentation, of TiO_2^a (a) and calcite (b) in 0 M (black closed), 0.1 M (red open) and 1 M (black open) KCl.

Ludox silica particles (silica^a) were used for the NMR calibration, which had a known surface area, quoted from the manufacturer as $135 \text{ m}^2/\text{g}$ and 20 - 24 nm in size (Sigma-Aldrich). The quoted surface area is in agreement with the calculated surface area ($124 \text{ m}^2/\text{g}$), if a spherical shape is assumed, with an average particle size of 22 nm. Transmission electron microscopy (TEM) images Figure 4-8 show the silica^a to be spheroidal, but with slightly irregular shapes and thus the larger quoted surface area is consistent with their morphologies.

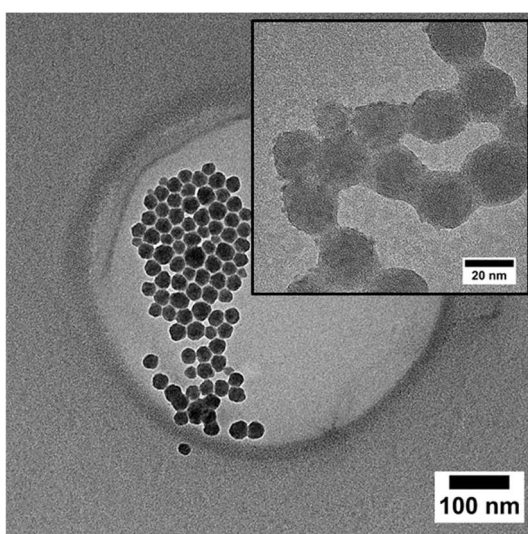


Figure 4-8: TEM images of Ludox AS-40 silica^a nanoparticles, scale bar 100 nm and inset silica^a scale bar 20 nm.

4.3.2 NMR relaxation calibration

As previously conversed Ludox silica particles (silica^a) were used for the NMR calibration, which had a known surface area, quoted from the manufacturer as 135 m²/g and 20 - 24 nm in size (Sigma-Aldrich). Figure 4-9 presents the measured T₁ relaxation rates of these silica dispersions, for various concentrations <20 vol. %. An increase in the concentration of silica^a was found to cause a decrease in the average relaxation time (as shown in Figure 4-9 (a)). This result is expected, since the liquid bound at the particle surface relaxes faster than the comparative bulk, and a higher concentration of particles leads to a larger total surface area and hence an increase in the fraction bound water. Thus, overall the relaxation time shortens as particle concentration is increased.

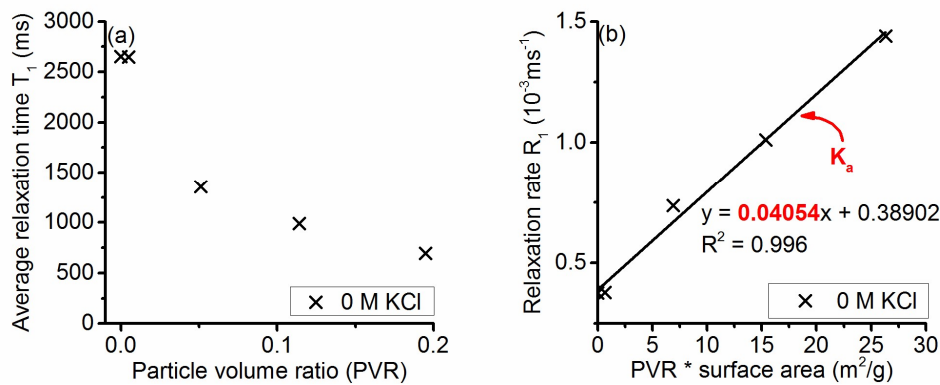


Figure 4-9: Calibration measurements for silica^a (Ludox standard) particles (a) relaxation time vs particle volume ratio and (b) average relaxation rates with the product of increasing particle volume ratio and known silica^a surface area (137 m²/g).

Figure 4-9 (b) displays the R_1 relaxation rate against the product of increasing particle volume ratio and known surface area of silica^a. Eq. (3-7) indicates that this relationship should yield a straight line trend, with a gradient proportional to K_a (the specific surface relaxation constant) which is dependent on both solvent and solid (Davis et al. (1987), Glaves et al. (1988)).

The K_a value extracted from the average slope for silica^a was $4.05 \times 10^{-5} \text{g}/\text{m}^2/\text{ms}$. A relaxation time of 2652.1 ms was measured for bulk H₂O, (no solids present), equating to a relaxation rate of $0.377 \times 10^{-3} \text{ms}^{-1}$. Further, theory states the y-intercept of the relaxation rate versus the product of the particle volume ratio and surface area, should yield $1/R_b$, where R_b is the relaxation rate of the bulk liquid (Davis et al. (1987), Glaves et al. (1988)).

Figure 4-9 (b), has a y-intercept of $0.389 \times 10^{-3} \text{ ms}^{-1}$, and comparing this result to the bulk relaxation rate measured for H_2O , suggests the error on this calibration measurement is around 3 %. Graves et al. (1988) state that relaxation measurements are reproducible within approximately 1% and to study low surface areas, the difference between R_b and R_s must be significant compared to the accuracy of the measurement. From herein, the specific surface relaxation constant determined for silica^a ($4.05 \times 10^{-5} \text{ g/m}^2/\text{ms}$), denoted K_{ref} in Eq. (4-1), was used to calculate the unknown specific surface relaxation constants K_a (Eq. (3-7)) for TiO_2^a , calcite and silica^b.

4.3.3 Enhancement of specific solvent relaxation in high electrolyte conditions

Relaxation NMR could prove to be a useful measurement when determining surface areas in the presence of surface modifiers, for example dispersive electrolytes or polymers. As previously discussed within the introduction, relaxation measurements can become significantly more complicated at interpreting in the presence of electrolytes, due to counterion effects. Here, 1 M KCl electrolyte was used to observe changes in relaxation, as a result of particle coagulation and competing counterion effects.

The NMR relaxation time was measured with increasing particle concentration for TiO_2^a , calcite and silica^b, and the relative relaxation enhancement R_{sp} was calculated using Eq. (3-8). The relaxation time was measured for bulk 1 M KCl (R_b) without any solids present, which gave a value of 2907 ms (shown in Figure 4-10 (a)). The R_b of bulk water was measured as approximately 2652 ms (shown in Figure 4-9 (a) and Figure 4-10 (a)). Figure 4-10 (c) and Figure 4-11 show the relative relaxation enhancement (R_{sp}) as a function of particle to volume ratio (Ψ_p) for TiO_2^a , calcite and silica^b respectively. It is expected from NMR relaxation theory that an increase in particle concentration results in a decrease in the relaxation time, equating to an increase in the R_{sp} , which is observed for both Figure 4-10 (c) and Figure 4-11. As aforementioned, this is because water at the particle surface has a faster relaxation time than water further away in the bulk, as the particle concentration increases, more surface becomes available, and thus a faster relaxation time is observed.

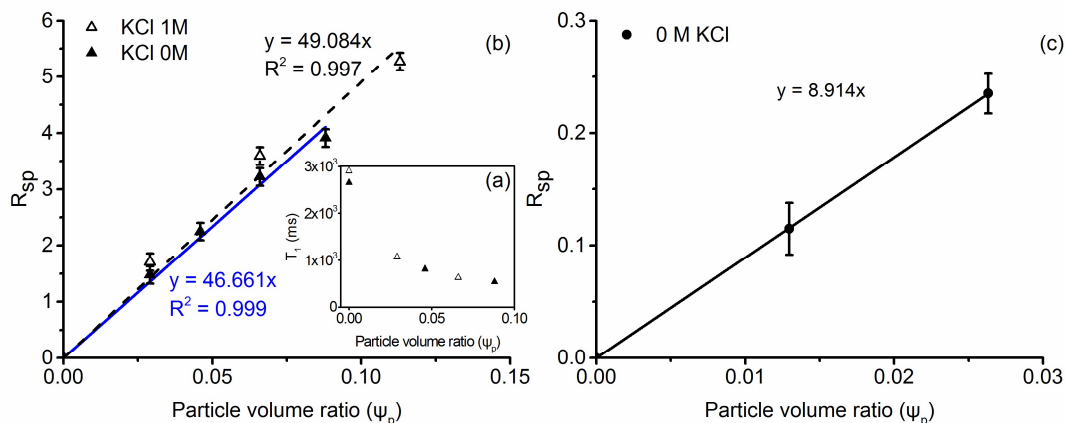


Figure 4-10: (a) shows average relaxation times for TiO_2^a with increasing particle concentration. (b) Relative relaxation rate enhancement (R_{sp}) for TiO_2^a with increasing particle concentration in 0 M KCl (closed triangle) and 1 M KCl (open triangle). The maximum standard deviation observed has been plotted as the error for both the 0 and 1 M salt measurements. (c) TiO_2^b relative relaxation rate enhancement in 0 M KCl with associated standard deviations shown as the error.

Comparing the R_b of the salt solution to R_b of pure water gives a relative relaxation enhancement (R_{sp}) of 0.1 for the solution only, similar to relative enhancements previously observed in the literature by Flood et al. (2006). This enhancement of 0.1 R_{sp} was enough to warrant a calibration of R_b to equal that of the salt solution rather than pure water, for the calculated R_{sp} for all particle-salt dispersions. Hence, both Figure 4-10 (c) and Figure 4-11 show the R_{sp} of particle dispersions with and without salt going through the origin of the R_{sp} versus Ψ_p plots. Table 4-1 summarises the measured K_a values (from the water systems), as well as the gradient values of the R_{sp}/Ψ_p relationships with and without 1 M KCl. The enhancement ratio in electrolyte conditions (comparing both R_{sp}/Ψ_p gradients) is also shown. It should be noted that Figure 4-10 (c) shows the relaxation NMR data for the TiO_2^b dispersions in water only, (this data will be discussed in section 4.3.4, in relation to surface area measurements).

It is evident that the electrolyte has a negligible effect on the relaxation times measured in TiO_2^a , compared to the water dispersions, as shown by Figure 4-10. Here, the gradient of the R_{sp}/Ψ_p values with and without electrolyte has a calculated enhancement ratio of 1.05. As previously demonstrated by particle size and settling measurements, TiO_2^a remains highly aggregated irrespective of solvent conditions. Thus, there is assumed to be no significant change in surface area for the high salt system, and it is possible to probe relaxation purely based on counterion effects. Therefore, it would appear these results are counter to enhancements in silica and polystyrene latex systems found previously (Flood et al. (2006),

Schwarz and Schönhoff (2002)). The TiO_2^a particle dispersions for the NMR measurements had a recorded pH of 6.1 and the zeta potential measurements shown in Figure 4-2 clearly indicated the TiO_2^a was around its isoelectric point (IEP). Hence, there should be no significant counterion layer around the particles, suggesting interaction between the particle surface and attracted ions may be critical to relaxation measurements, rather than simply electrolyte concentration.

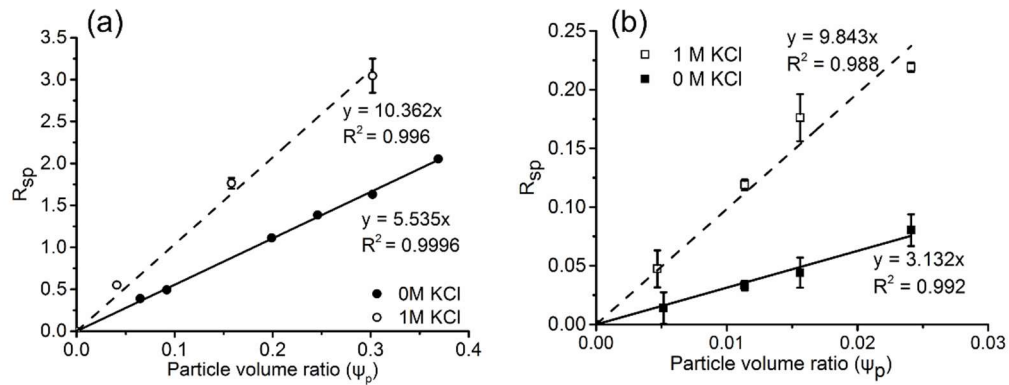


Figure 4-11: Relative relaxation rate enhancement (R_{sp}) for (a) calcite and (b) 100 nm silica with increasing particle concentration in 0 M KCl (closed circle) and 1 M KCl (opencircle). The associated standard deviation of R_{sp} is shown as the error for each particle concentration.

Table 4-1: Summary of NMR constants, gradients of the R_{sp}/Ψ_p plots with and without KCl, where the ratio of this change in gradient has been calculated, and ratio of the gradient between salt and no salt.

Material	Density (g/cm^3)	K_a specific surface relaxation constant ($\text{g}/\text{m}^2/\text{ms}$)	Gradient 0 M KCl R_{sp}/Ψ_p	Gradient 1 M KCl R_{sp}/Ψ_p	Ratio
Silica ^a	2.2	4.05×10^{-5}	n/a	n/a	n/a
TiO_2^a	3.79	6.98×10^{-5}	46.661	49.084	1.05
TiO_2^b	3.9	7.18×10^{-5}	8.917	n/a	n/a
Calcite	2.71	4.99×10^{-5}	5.535	10.362	1.87
Silica ^b	2.2	4.05×10^{-5}	3.132	9.843	3.14

Particle size, zeta potential and settling measurements have shown both calcite and silica^b to be coagulated in the presence of 1 M KCl; hence, a decrease in surface area would be expected, leading to a decrease in the R_{sp}/Ψ_p gradient. In contrast to this, both calcite and silica^b particle-salt dispersions were found to have a considerable increase in R_{sp} compared to particle-water dispersions (Figure 4-11). The R_{sp}/Ψ_p enhancement ratio is given in Table 4-1. For calcite, this ratio was found to be almost twice that of the corresponding particle-water gradient, while for silica^b it was over three times greater.

The pH of the calcite dispersions during the NMR experiments was measured to be at \sim pH 8, and the zeta potential measurements (Figure 4-2) illustrate that dispersions will be positively charged, as the calcite IEP is approximately pH 9. Therefore, a screening counterion layer of negatively charged chloride ions, will form around the positively charged calcite surface. For silica^b, dispersions were used at a pH of \sim 8. Thus, conversely, the silica will be strongly negatively charged (Figure 4-2) and a positive screening layer of potassium ions will form around the surface. Thus, the author proposes that the increase in the R_{sp} observed for calcite and silica (Figure 4-11) is due to this counterion effect, resulting in an increased relaxation rate for the bound water (R_b). This stipulation is further supported by the absence of the increase in R_{sp} for titania-salt dispersions (Figure 4-10), which is at the IEP, as discussed. It is interestingly noted also, that as high salt conditions were used, the diffuse electric double layer is assumed to be negligible. Nevertheless, as surface relaxation is assumed to occur from monolayer molecules, it is likely that the inner Helmholtz plane only influences behaviour. While similar relative enhancements for particle-salt dispersions have been reported in the literature and such specific ion effect have been proposed (Flood et al. (2006), Schwarz and Schönhoff (2002)), the influence of particle zeta potential charge and magnitude, and related influence of agglomeration have not previously been observed.

Additionally, the author suggests that the increase in the magnitude of the R_{sp}/Ψ_p gradient for silica^b compared to calcite may be due to the increased magnitude of the surface charge of the silica (Figure 4-2). However, this conclusion is difficult to state for certain, due to the confounding impact of aggregation, which would be expected to reduce the total surface area and thus the R_{sp} . Indeed, enhancement from the counterion effect alone may be expected to be even greater than measured in these systems, as the overall relaxation rate will be partially reduced from the lower particle surface area in high salt conditions.

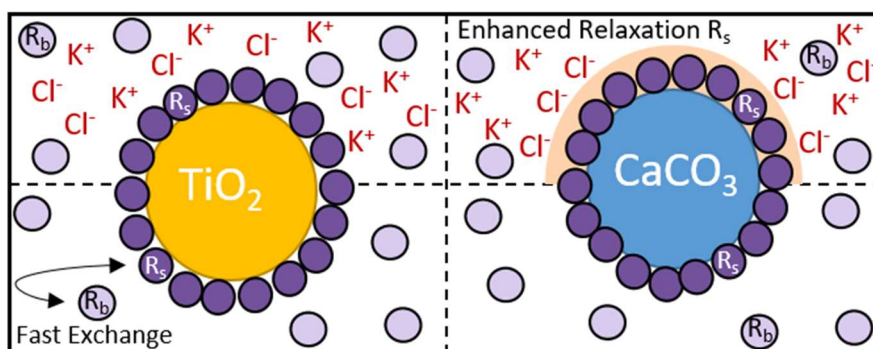


Figure 4-12: Schematic to show the difference in relaxation times for TiO_2 and Calcite in water and high electrolyte concentration.

4.3.4 Comparison of BET and NMR surface area determination

The relative relaxation enhancement (R_{sp}) for particle-water dispersions (Figure 4-10 and Figure 4-11) were used to determine the specific surface area of the two different titania samples, calcite and silica^b (using Eq. (3-7)) and compared to BET measurements. These surface area values are compared in Table 4-2. The R_{sp} of particle-salt dispersions were not used to calculate surface area due to the competing counterion effects previously outlined.

Table 4-2: Comparison of the calculated NMR surface area (SA), BET and calculated spherical surface area obtained from the particle size distribution for silica^b, TiO_2^a , TiO_2^b and calcite. * TiO_2^b BET surface area measurements were performed by Gardy et al. (2016) alongside **TEM particle size analysis.

Material	BET surface area (m^2/g)	Calculated spherical surface area [based on D_{50}] (μm) (m^2/g)	Calculated NMR surface area (m^2/g)
Silica ^a	n/a	124 [0.022]	n/a
Silica ^b	11.74 ± 0.05	27.3 [0.110]	29.9 ± 1.4
TiO_2^a	262.64 ± 1.95	0.971 [1.631]	252.8 ± 6.4
TiO_2^b	48.64*	69.9 [0.022]**	47.0 ± 0.1
Calcite	2.38 ± 0.01	0.648 [3.418]	41.8 ± 0.3

The specific surface relaxation constant previously determined for silica^a ($4.05 \times 10^{-5} \text{ g}/\text{m}^2/\text{ms}$), denoted K_{ref} was used to calculate K_a for silica^b, TiO_2^a , TiO_2^b and calcite and using respective particle densities. Table 4-2 also shows the calculated particle surface area, assuming spherical

particle shapes, and the previously recorded particle D_{50} values. The BET nitrogen adsorption-desorption isotherms are shown for TiO_2^a , calcite and silica^b, in the Appendix 1: Supplementary information to Chapter 4 section, Figures A1-1 to A1-3, alongside the pore size distributions and total pore volumes.

For silica^b (Table 4-2) the BET surface area was $\sim 12 \text{ m}^2/\text{g}$ compared to the NMR surface area $\sim 30 \text{ m}^2/\text{g}$, the smaller surface area obtained from the BET is most likely due to the agglomerated nature of silica^b, thus leading to several particle contact points where nitrogen adsorption cannot occur, hence causing the underestimation of the true surface area of silica^b in a dispersion. However, silica^b NMR surface area is in good agreement with the calculated spherical surface area (Table 4-2, $\sim 28 \text{ m}^2/\text{g}$), where, Figure 4-6 shows the TEM images of silica^b is monodispersed and uniformly spherical. Here, the value of using relaxation NMR is clearly highlighted, where BET otherwise failed, for determining surface area accurately for small colloidal particles where the surface chemistry remains unchanged compared to the reference material.

Comparison of the TiO_2^a specific surface area data highlighted in Table 4-2, shows that there is excellent agreement between the NMR SA ($\sim 253 \text{ m}^2/\text{g}$) and the BET SA ($\sim 263 \text{ m}^2/\text{g}$). This result is significant, as it provides evidence of the ability to measure particle SA for solid-liquid dispersions, in this case, where there is a change in surface potential yet surface chemistry remains similar as both the systems studied are oxides. It is important to note that the spherical estimates for the SA calculation of TiO_2^a is misleading, giving a surface area of $\sim 1 \text{ m}^2/\text{g}$. The very large SA of TiO_2^a would equate more to the nanocrystallites (20-100 nm), observed from SEM analysis (Figure 4-1) and not the measured D_{50} , which is agglomerated TiO_2^a .

Further to these results, TiO_2^b NMR SA ($47 \text{ m}^2/\text{g}$) is also in good agreement with the BET SA ($49 \text{ m}^2/\text{g}$), obtained from Gardy et al. (2016), as shown in Table 4-2. It appears both TiO_2 samples are within 4% of the corresponding BET measurements, which is significant, as sample conditioning requires a fraction of the time, without reducing the reproducibility and accuracy of the NMR measurements. Hence, it has been shown that a single calibration k_a can be used for different particle systems of similar chemistries, despite the fact that the surface charges were considerably different between the titania and silica^a standard. These results are consistent with findings from Van der Beek et al. (1991), who investigated the influence of pH on the relaxation rate of silica and water dispersions. Despite changes in the surface charge of silica across a broad pH range the relaxation rate remained largely unchanged, at least in low electrolyte conditions. However, they did observe differences under extreme pH conditions,

indicating relaxation enhancements as a result of, fast proton exchange and partial dissolution of silica.

Uncertainty in the phase purity and crystallinity of the TiO_2^a used was speculated, due to the very high surface area results obtained. For this reason, XRD analysis was conducted on the commercial sample (as seen in Appendix 1: Supplementary information to Chapter 4 section, Figures A1-4). Commercial titania of high surface areas are typically around $50 \text{ m}^2/\text{g}$ (Degussa p-25) (Yasir et al. (2001)), however, Wei et al. (2013) reported the syntheses of high purity phase pure anatase TiO_2 with a BET surface area of $186 \text{ m}^2/\text{g}$. The XRD patterns for TiO_2^a was measured and indexed using JCPDS-ICDD and confirmed the anatase phase (04-013-5313, TiO_2) (Aldon et al. (2006)). Line broadening can be observed in the XRD spectra and is most likely due to the poor crystallinity. Additionally, literature has shown BET trends for amorphous TiO_2 typically have higher surface areas than crystalline counterparts, with values usually greater than $250 \text{ m}^2/\text{g}$ (Froschl et al. (2012)).

The calculation of calcite surface area using relaxation NMR (Table 4-2, $\sim 42 \text{ m}^2/\text{g}$) was not found to be in good agreement with the BET results ($\sim 2 \text{ m}^2/\text{g}$), which leads to the uncertainty of the true surface area for either measurements. A recent study by Agnihotri et al. (1999) showed the influence of surface modifiers on the structure of precipitated calcium carbonate. Here, they recorded Linwood carbonate (having a 97% composition wt. % of calcium carbonate) to have a BET surface area of $1.9 \text{ m}^2/\text{g}$ for a D_{50} particle size of $6 \mu\text{m}$. This result is of a similar value for a comparable D_{50} , thus giving confidence in the BET surface area results obtained for calcite in this study. Further, the calculated calcite surface area (Table 4-2 $\sim 0.6 \text{ m}^2/\text{g}$) using the calcite D_{50} equivalent spherical diameter is of a similar magnitude to the BET SA ($\sim 2 \text{ m}^2/\text{g}$). The calculated value for calcite marginally underestimates the SA compared to BET, likely from calcite being more faceted (Figure 4-1). Therefore, there is some uncertainty in the much larger surface area estimate obtained for calcite using relaxation NMR.

However, it should not necessarily be expected that the surface area of the two measurement techniques will always give the same values, as the BET measurement requires a dry powder, and in contrast, relaxometry measures the wetted particle surface area. SEM images of calcite (Figure 4-1), show agglomeration of nanocrystallites onto the surface of larger particles ($\sim 250 \text{ nm}$). If these nanocrystallites are better dispersed during the NMR measurement, these smaller fines would dominate the measurement. As the water bound to the surface relaxes faster than the bulk, this would lead to a larger surface area observed for the NMR measurement compared to the BET. Although, N_2 can diffuse into primary particles of aggregates during

the BET measurement, bound nanocrystallites onto the primary particles' surface could lead to a reduction in the surface area measured by BET.

The aforementioned study by Agnihotri et al. (1999) reported surface areas for precipitated calcium carbonate of 17 m²/g obtained without the presence of surface modifiers, which increased to values between 40-60 m²/g in the presence of a surface modifier Dispex. Here, it is clearly shown the better dispersed the calcium carbonate, the larger the surface area (although, results were all obtained from BET measurements). Hence, the difference in the surface area results could be merely down to calcite nanocrystallites being well dispersed during the NMR measurements, however, these would need to be in the order of ~50 nm to equate for a spherical equivalent surface area of 42 m²/g.

Adding further complexity to the system, the solubility of the calcite could also lead to some degree of re-precipitation back onto the calcite surface, which again may increase the surface area detected for the NMR compared to the BET. Potential re-precipitation mechanisms would be consistent with previous explanations for enhanced surface areas calculated from NMR by Katika et al. (2014) in brine enriched chalk rocks.

A more plausible explanation to the large NMR surface area might be due to the partial solubility of calcium carbonate in water (0.013 g/L at 25°C) Aylward ((2008)), which may perhaps lead to an increase in the relaxation rate due to an increase in electrolyte concentration, leading to enhancements from counterion effects previously discussed. Thus, overall leading to an over estimation of the NMR surface area for calcite. More generally, the interfacial chemistry of the calcite is not similar enough to silica to allow for this reference material to be used, and thus the assumptions of Eq. (3-5 are no longer valid as the water bound at the particle interface (R_s) is significantly changed.

4.4 Summary

Electrolyte effects on relaxation NMR were investigated for a range of particle systems of differing particle charge. TiO₂^a was found to be unaffected by solvent conditions, remaining highly aggregated, and a negligible effect on the relaxation rate enhancement (R_{sp}) was observed under electrolyte conditions. It was concluded that due to the neutral particle charge during relaxation measurements no significant counterion screening layer was formed, and hence no additional relaxation enhancement was observed. In complete contrast, both calcite and silica^b, showed substantial enhancements in the R_{sp} in the presence of the KCl electrolyte. This was attributed to a counterion effect inducing a screening layer around both calcite and

silica (although oppositely charged), which increased the R_{sp} as a result of the enhancement in the particle-solvent affinity. Additionally, an increase in the magnitude of the R_{sp}/Ψ_p gradient for silica^b compared to calcite was noted. It was suggested this could be caused by the increased magnitude of the surface charge for silica^b, although further work is required for a more comprehensive understanding of this phenomena.

Relaxation NMR was used to successfully calculate the surface area of two titanium dioxide samples for highly concentrated suspensions, where there was excellent agreement between the NMR and BET surface area measurements. Further, relaxation NMR was also used effectively to calculate the surface area of silica^b, where BET otherwise failed. However, although the successes of solvent relaxation to calculate specific surface area were demonstrated, there was uncertainty in measurements of calcite surface area. The surface area calculated for calcite by NMR was far larger than by BET, which the author proposes is most likely due to both better dispersion of nanocrystallites in the liquid state, and partial solubility of calcite in water. Importantly, these results highlight that while the use solvent relaxation to study particle surface area offers faster experimental times and greater compatibility compared to conventional techniques, counterion effects make the interpretation of NMR relaxation rates significantly more complicated than theory suggests in many cases.

Chapter 5 Characterisation of polyphosphate dispersant interactions with aluminium-doped titania nanoparticles during milling

The content of this Chapter has been published in the Journal of Colloid and Interface Science, Volume 548, 2019, Pages 110-122, under the same title.

5.1 Introduction

Currently, TiO₂ pigments are manufactured in a continuous process with concentrations up to 600 g/L, and the particle size can be monitored using dynamic light scattering (DLS) (Schärftl (2007)). Concentrated slurries exhibit multiple scattering; which leads to significant errors in the measured sizes and cannot be accounted for by most of the commonly available DLS devices (Allouni et al. (2009)). Thus, to monitor the size of TiO₂ particles by DLS during a production process, aliquots must be sampled and diluted to concentrations where no multiple scattering occurs. Not only is this time consuming, but samples may be misrepresentative of the bulk system if an insignificant amount of statistics is collected on the dilute system or if particle aggregation/agglomeration occurs.

Studying industrially relevant processes is often not straight-forward, as the dispersions are commonly highly concentrated, opaque and may contain a variety of inorganic contaminants. However, nuclear magnetic resonance (NMR) relaxometry can be used to determine particle specific surface area, even for highly concentrated slurries (Fairhurst et al. (2016)), as previously demonstrated in Chapter 4. Relaxation NMR is an ideal candidate for an online process control tool, and could, for instance, offer the possibility of continuously monitoring particle surface area during milling. However, there are some uncertainties as to what extent the polyphosphate dispersant will have on the relaxation signal, and furthermore the influence of surface alumina concentration and other contaminants on relaxation rates.

Although efforts have been made to understand the influence of dispersants on slurry rheology during milling (see review by He et al. (2004)), there appears to be limited published research studying polyphosphates. Wang and Forssberg (1995) studied the interactions of sodium hexametaphosphate (SHMP) with dolomite in a stirred bead mill. They found that the use of SHMP, compared to organic dispersants, led to particles of a larger mean size and lower surface area. However, to the authors knowledge, the influence of milling time on the structure and density of polyphosphate dispersants on

the surface of titania pigment particles has not yet been explored, nor has there been any published research relating to the strength of the interactions through centrifugal washing.

Therefore, this chapter presents the characterisation of industrially produced alumina-doped TiO₂ pigment particles milled for different periods of time in the presence of a polyphosphate salt. This chapter aims to understand how milling affects the aggregate size and morphology of alumina-doped rutile pigment particles through particle size characterisation by TEM, X-ray disc centrifugation (XDC) and DLS. This chapter further aims to understand how the surface density and structure of the polyphosphate salt change with milling time. The stability of the polyphosphate layer against centrifugal washing is investigated by studying changes in the zeta potential and phosphorus content using XRF. Additionally, the use of NMR relaxometry has been explored as a novel technique to understand changes in surface area in real time during the milling process and understand the influence of the polyphosphate-alumina interactions on relaxation times.

5.2 Materials and Methods

Unmilled and milled titanium dioxide pigment samples were supplied by Venator. Sodium hexametaphosphate (Univar), known by the trade name Calgon, and abbreviated as SHMP throughout this manuscript, was added prior to the milling process to control titania dispersion properties. Stock acid and base solutions were prepared to vary the pH of suspensions, where hydrochloric acid (Sigma-Aldrich, reagent grade, 37%) was used to decrease the pH and potassium hydroxide pellets (Sigma-Aldrich) were used to increase the pH. Pure potassium chloride salt (Sigma-Aldrich) was used as background electrolyte for surface charge analysis. Ethanol absolute was purchased from Fisher Scientific and used as received for TEM sample preparation.

The industrially produced pigment samples were firstly adjusted to pH 10-10.5 with NaOH and sodium hexametaphosphate (SHMP) was added prior to milling at 0.14% w/w as P₂O₅ on TiO₂. Suspensions were milled at concentrations of 400 g/L in a stirred wet mill using a rotor speed of 12,000 RPM. The milling media used was grade 8 ballotini with a mean size of 500 µm. Aliquots of TiO₂ were removed after 1, 2, 4, 8, 16 and 32 minutes of milling and dried in an oven at 105 °C.

The so-obtained dried titania powder was heavily agglomerated due to capillary forces, and in order to handle the samples for dispersion characterisation, they were gently crushed using a mortar and pestle for 5 minutes. All suspensions were made in milli-Q water and dispersed using an ultrasonic bath (Clifton Sonic) for 30 minutes, unless otherwise stated. Samples were then further dispersed using an ultrasonic probe, a Sonic Dismembrator (Fisher Scientific), at 20% amplitude for 1 minute using a 6 mm horn tip. Some of the milled samples were washed post-milling in an attempt to remove poorly adsorbed SHMP, and these are stated as *washed* herein. For these samples, 2.5 wt.% dispersions were prepared in ultrapure water and centrifuged using a Heraeus Megafuge 16R Centrifuge (Thermo Scientific). Two wash cycles were performed. The first one was carried out at 6,000 RPM for 20 minutes, after which the supernatant was removed and conductivity measured using a Seven2Go S3 (Mettler Toledo). The concentration of the centrifuged samples were adjusted back to 2.5 wt.% using ultrapure water and washed for the second time at 8,000 RPM for 20 minutes. Once again the supernatant was removed, conductivity was measured, and the washed particles were re-dispersed to 2.2 wt.%.

5.2.1 Transmission electron microscopy (TEM)

Samples of TiO₂ milled for 1 and 32 minutes were prepared for TEM by suspending in ethanol and vigorously shaking, before a drop of the dispersion was placed onto a copper grid coated with a holey carbon film (Agar Scientific Ltd.) and left to dry. TEM analysis was used to investigate primary particle size and crystal structure on FEI Tecnai F20 FEGTEM operating at 200 kV. Bright field TEM was used to investigate particle size and morphology with images collected on a Gatan Orius CCD. Particle size analysis was conducted using Image J (Schneider et al. (2012)) by measuring the Feret diameter of primary particles. High magnification TEM images were used to obtain distances between atomic planes using a fast Fourier transform (FFT) function, from which d-spacings were then measured.

The dispersion state of TiO₂ nanoparticles after 32 minutes of milling was further investigated by dispersing in water and using the plunge-freeze and vacuum dry method, as previously described by Hondow et al. (2012). Briefly, this involved rapidly freezing a blotted 3.5 µL droplet onto continuous carbon coated TEM grids which had been plasma cleaned (1020 Fischione) for 10 seconds. The droplet was blotted using an FEI Vitrobot, with prior conditions set to 100% relative humidity and 21°C in the chamber. After a wait time of 10 seconds, the droplet was blotted once for 4 seconds. The blotted droplet was

rapidly plunged into liquid ethane, stored in liquid nitrogen, then transferred into a vacuum desiccator and allowed to sublime.

Energy dispersive X-ray spectroscopy (EDS) was used as elemental analysis for TiO₂ before after milling for 32 minutes (plunge-frozen and vacuum dried) to check for potential bead contamination from milling media, and to confirm the presence of the polyphosphate species on the alumina-doped pigment surface. EDS was performed using the SuperX (4 detector) system on the FEI Titan³ G2 operated at 300 kV. High angle annular dark field (HAADF) scanning TEM (STEM) images were recorded using a probe current of ~450 pA, with analysis performed using the Bruker Esprit (v1.9) software.

5.2.2 X-ray diffraction (XRD)

Titanium dioxide samples were analysed after 1 and 32 minute milling. The X-ray powder diffraction patterns were obtained to investigate the nature of the crystalline phase and calculate the crystallite sizes, using a D8 X-ray Diffractometer (Bruker) and CuK α radiation source. The titanium dioxide samples were prepared as powders and deposited onto a silicon holder. The samples were scanned from 2θ angle 10° to 70° with a step size 0.0490° at 304 ms per step. The obtained pattern was matched against anatase (Horn (1972)) and rutile (Okrusch (2003)) crystal structures, which were also used to index the d-spacing measured from TEM analysis.

Crystallite size, L (Å), was obtained using the Scherrer equation (Patterson (1939)) Eq. (5-1), where B is the line broadening in the XRD peak at the full width half maximum intensity (FWHM) after subtracting instrumental line broadening (radians). Here, the line broadening of the instrument was taken as 0.06°, and the FWHM was obtained by fitting a Gaussian distribution to the two most intense peaks observed in the XRD patterns. K is a dimensionless shape factor; a value of 0.89 was used as this relates to spherical particles (Patterson (1939)). $\frac{\lambda}{2}$ is the Bragg angle (radians) which was obtained from the peak position at the FWHM, and λ the wavelength of the incident x-rays taken as 1.5406 Å for the CuK α radiation source.

$$B = \frac{K\lambda}{L \cos \frac{\lambda}{2}} \quad (5-1)$$

5.2.3 Zeta potential characterisation

A Zetasizer Nano ZS (Malvern Instruments) was used to measure the zeta potential of the unmilled and milled dispersions as previously described in Chapter 4. Dispersions of TiO₂ in 0.1 mM KCl background electrolyte were prepared at 100 ppm.

5.2.4 Dynamic light scattering (DLS)

Titanium dioxide suspensions were prepared from the milled powder at 2 wt.% in ultrapure deionised water and dispersed, 25 µL aliquots were sampled and diluted in 20 mL of ultrapure deionised water and re-dispersed, before diluting by ten. The dispersions were filtered using 0.80 µm surfactant-free cellulose acetate filters (26 mm Minisart® Syringe filters; Sartorius), unless otherwise stated. This sample preparation was also used for TiO₂ milled for 1, 16 and 32 minutes after centrifugal washing. The DLS measurements were performed at 25 °C also using a Zetasizer Nano ZS (Malvern Instruments, 173° backscattering angle and 633 nm laser excitation wavelength). For each suspension, thirty 30 second measurements were carried out.

For all the investigated milled suspensions, the collected intensity auto-correlation data exhibited two relaxation modes. The fit of the data performed by the commercial Zetasizer code did not properly account for the second, longer, relaxation mode (as seen in Appendix 2: Supplementary information to Chapter 5 section, Figures A2-1). The intensity auto-correlation data were thus fitted in MatLab with a sum of two stretched exponentials (Eq. A2-1) using the Levenberg-Marquardt algorithm. An example of such a fit is provided in Figure A2-1 (b). It is worth noting that the few measurements for which the intensity auto-correlation data had an intercept higher than 1 were excluded from the data set, while the remaining intensity auto-correlation data were normalised to an intercept of 1. Assuming that the investigated relaxation mode is diffusive (see a more detailed explanation in Section 5.3.2 and in Appendix 2), corresponding hydrodynamic diameters D_H were calculated using Eq. A2-2 to A2-5.

Care must be exercised when characterising TiO₂ suspensions with light scattering as they can exhibit multiple scattering because of the TiO₂ high scattering index (*i.e.* 2.410). Multiple scattering leads to significant errors in size measurements if it is not accounted for and can be avoided by diluting TiO₂ suspensions. To determine the optimum TiO₂ concentration at which DLS measurements should be performed (Schärfl (2007), Allouni et al. (2009)), dilution trials were attempted. The results are shown and discussed in the Appendix 2: Supplementary information to Chapter 5 section, Figures A2-3, where the

influence of filtration is also discussed. The concentration corresponding to the dilution described at the beginning of this section (*i.e.* $\sim 2.5 \times 10^{-3}$ wt.%) was found to be optimal. To confirm that this concentration was appropriate, a few additional measurements were performed using a light scattering device equipped with a '3D mode' (instrument details provided in Appendix 2), which allows to correct for multiple scattering (Schärfl (2007)). There was no significant difference between the data collected with the '3D mode' (data not shown) and those collected with the standard '2D mode', thus confirming that the selected TiO₂ concentration allowed DLS measurements to be performed in absence of multiple scattering.

There was a concern that the amount of energy brought into the system during sonication could break the aggregates that may be present in the TiO₂ milled samples. Hence, DLS measurements were also performed on samples prepared using a lower energy intensive dispersion method (compared to sonication). The results are displayed in Figure A2-4 and show that sonication does not break the aggregates that may be present in solution, but successfully breaks the agglomerates formed when the TiO₂ milled particles are dried. These experiments are discussed in detail in the Appendix 2: Supplementary information to Chapter 5. The characterisation of the unmilled TiO₂ sample is detailed in the Appendix 2: Supplementary information to Chapter 5, Figure A2-5 and Table A2-1.

5.2.5 X-ray disc centrifugation (XDC)

Milled slurries obtained at $\sim 400 \text{ gL}^{-1}$ were diluted to $\sim 40 \text{ gL}^{-1}$ and the titanium dioxide particle size was determined by X-ray disc centrifugation using a BI-XDC Particle Size Analyzer (Brookhaven), run at a disc speed of 1,200 rpm for 40 min.

5.2.6 Brunauer–Emmett–Teller (BET)

Brunauer–Emmett–Teller (BET) surface area and pore size measurements were obtained for milled titanium dioxide samples using the method previously described in Chapter 4. TiO₂ samples were degassed to remove moisture using a vacuum oven at 120°C for 24 h under a vacuum of 10 mmHg. To determine the reproducibility of the results, two TiO₂ samples (1 and 2 minute milled) measurements were repeated using the same experimental conditions. No significant difference was observed for the 1 minute milled sample (a 0.02% variation) or the 2 minute milled sample (a 0.16 % variation), with repeated results within the experimental error.

5.2.7 NMR relaxometry

Suspensions were prepared at 2.5 wt.% in deionised water as previously described. The specific surface area (S) of milled titanium dioxide samples were calculated using the theory discussed in Chapter 4 and Fairhurst et al. (2016). The average relaxation time (T_{av}) of the TiO₂ dispersions were used to calculate the average relaxation rate (R_{av}) of the dispersion. The solvent (deionised water) relaxation time was measured (T_b) and converted into a solvent relaxation rate (R_b). A relaxation rate enhancement (R_{sp}) was calculated for the milled TiO₂ dispersions, (see Eq. (3-8)), using both R_{av} and R_b .

The R_{sp} was plotted against the particle volume ratio (ψ_p) and the gradient of the line of best fit obtained. The specific relaxation constant (K_a) for milled TiO₂ was calculated by equating the surface area to that obtained from the BET measurement for the 8 minute milled sample, giving a K_a of 3.93×10^{-4} g/m²/ms. Washed TiO₂ samples were also characterised with this procedure, but at a concentration of 2.2 wt.% (due to sample loss during the washing procedure). In order to compare R_{sp} values to those of the 2.5 wt.% unwashed samples, the T₁ relaxation rate was measured and converted into R_{sp} , and the equivalent R_{sp} value for a corresponding 2.5 wt.% slurry was back calculated from the R_{sp}/ψ_p gradient.

5.2.8 X-ray fluorescence (XRF)

Washed and unwashed TiO₂ dispersions at 2 wt.% were prepared. The dispersions were poured into plastic holders ensuring that there was enough volume to cover the surface of the cup. Cup holders (40 mm Spex Unicell) were covered with a polypropylene film to contain the sample before securing with the plastic ring counterpart, creating a taut smooth film on the surface of the sample cup. XRF measurements were performed in a helium atmosphere using a Rigaku Primus II WD XRF. The following settings were used; analysis: EZ scan, sample type: liquid, component type: metal and balance component: H₂O.

5.3 Results and Discussion

5.3.1 Microscopy, elemental characterisation and crystal structure

Transmission electron microscopy (TEM) images (Figure 5-1 and Figure 5-2) were obtained for TiO₂ particles in order to understand primary particle size and morphology changes within the two extreme milling times (after 1 minute and 32 minutes respectively).

It is noted that a large proportion of primary particles are rod shaped, while there is certainly some considerable variation in their shape factors. Jordan et al. (2016) analysed the self-assembly of rutile TiO_2 during initial stages of crystallization, where they reported elaborate structures of rutile TiO_2 , such as rutile fibre networks and twinning branched clusters. Although it should be emphasised that an alternative synthetic route is used for the samples in this study. Klein et al. (2011) stated that synthesis acidity is important in determining crystal morphology of rutile titania when produced by the precipitation method, and detailed structures including rods, broomlike agglomerates and cauliflower spherical agglomerates.

Clearly, the morphology of the nanoparticles depends on the conditions used, however observed in this study are spheres and rod shaped nanoparticles limited to TiO_2 produced in a flame reactor. It is assumed that the variation in shape-factors evidenced in Figure 5-1 and Figure 5-2 are likely from a distribution in growth rates, rather than differences in the underlying crystalline structure, which will be discussed in detail in the forthcoming section.

It should be noted that throughout this discussion the term ‘aggregate’ is referred to as an assembly of particles which are sufficiently strongly bound that they require bead milling to break the particle-particle bonds. This contrasts to the term ‘agglomerate’ which is referred to as a collection of aggregated particles which has formed upon drying, these are softer bound and as later discussed can be broken by sonicating the suspension.

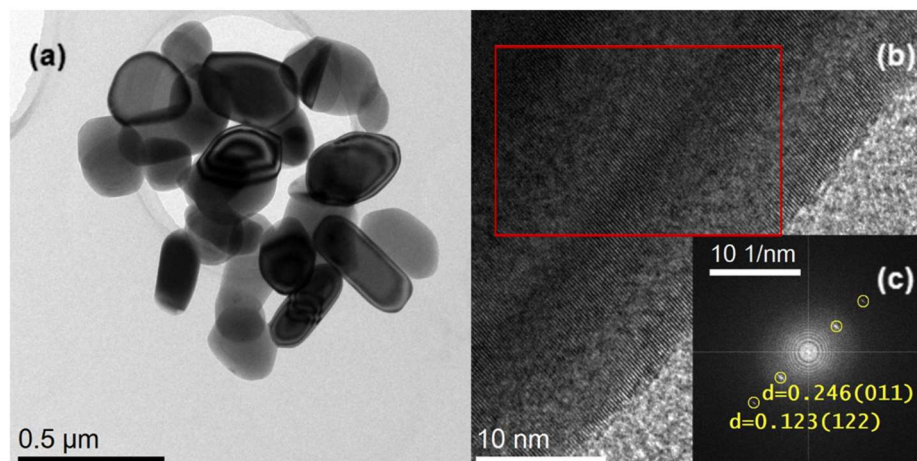


Figure 5-1: (a) TEM image of TiO_2 particles after milling for 1 minute. (b) High magnification image of a TiO_2 nanoparticle after 1 minute of milling to show the lattice fringes. (c) Fast Fourier transform (FFT) generated from the red square shown in (b), with measured d-spacings in nm and corresponding hkl planes shown referenced to the rutile crystal structure (Okrusch (2003)).

The average particle size was calculated using the Feret diameter of the TiO₂ primary particles, with over 100 particles measured for both the 1 and 32 minute milled samples, as given in the Appendix 2: Supplementary information to Chapter 5 section, Table A2-1. Little change is observed in the average primary particle size with increased milling time. A small number of aggregates (10) were analysed which had an average spherical diameter equivalent of ~1100 nm after 1 minute milling and 900 nm after 32 minutes milling. While it is expected that there may be some level of particle aggregation in TiO₂ slurries (Mandzy et al. (2005)), the observed aggregates could also have formed during sample drying on the TEM grid. Hence, the measured aggregate sizes are unlikely to be representative of the aggregates that may be present in the wet dispersions.

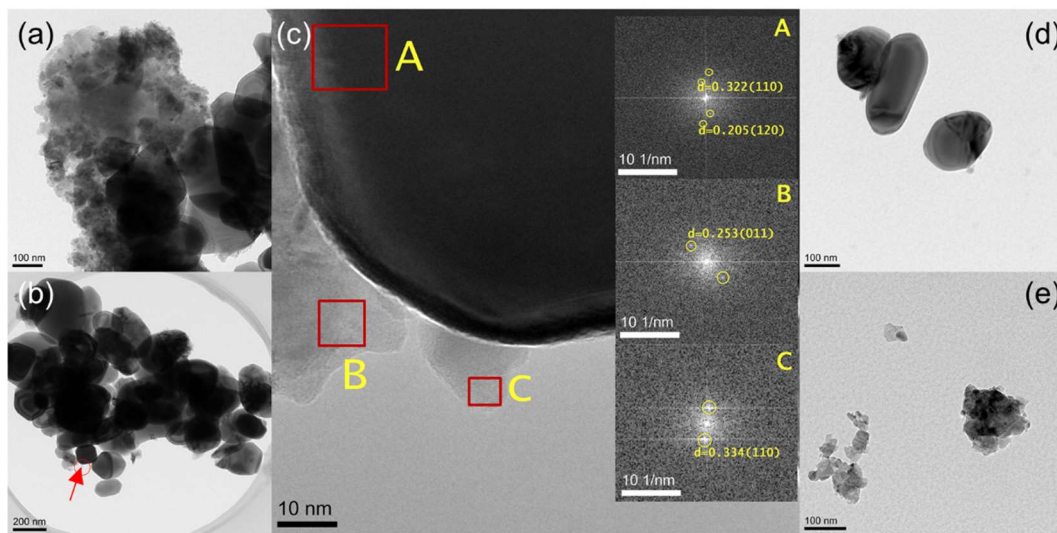


Figure 5-2: (a) & (b) TEM images of TiO₂ particles after milling for 32 minutes (particle fines electrostatically aggregated highlighted by the arrow in (b)). (c) High magnification TEM image at the point of the arrow in (b), with inset FFT taken from A, B and C sections indicated by the red box insets, with measured d-spacings and corresponding hkl planes shown (Okrusch (2003)). (d) & (e) TEM images indicating the dispersion state of TiO₂ after milling for 32 minutes, dispersed in water and prepared using the plunge-freeze method.

Critically, titania samples milled for 32 minutes showed evidence of particle fracturing (Figure 5-2), resulting in fines of ~20 nm, which appear to cluster together (Figure 5-2 (a)) and are also attached to larger particles (Figure 5-2 (c)), probably due to electrostatic attraction as stated by Sen et al. (2011). Sen et al. (2011), found particle fines in the order of 40 - 50 nm in size after high energy vibrational ball milling of anatase nanoparticles for 32 hours, where further milling for 100 hours caused disintegration of nanoparticles to

sizes of ~ 13 nm. They suggested that particle breakage is caused by critical stresses that generate plastic deformation. It has also been observed that high energy ball milling results in the formation of uncommon metastable TiO_2 -II phase.

Gajovic et al. (n.d) also showed that milling times of more than 10 hours for the anatase polymorph induced particle breakage towards 10 nm, while primary particles of larger sizes were still present Gajovic et al. (n.d). Therefore, it appears that for the current system, 32 minute milling supplies an excess milling energy, which not only is inefficient on time/energy costs, but negatively impacts the properties of the pigment particles, as the observed nanoparticle fines will lead to a reduction in the optical purity and whiteness. This is the first time, to the authors knowledge, that such breakage has been published for the harder rutile morphology (hardness scale anatase 5.5 – 6, compared to rutile 6 – 6.5) (Dana (1855)).

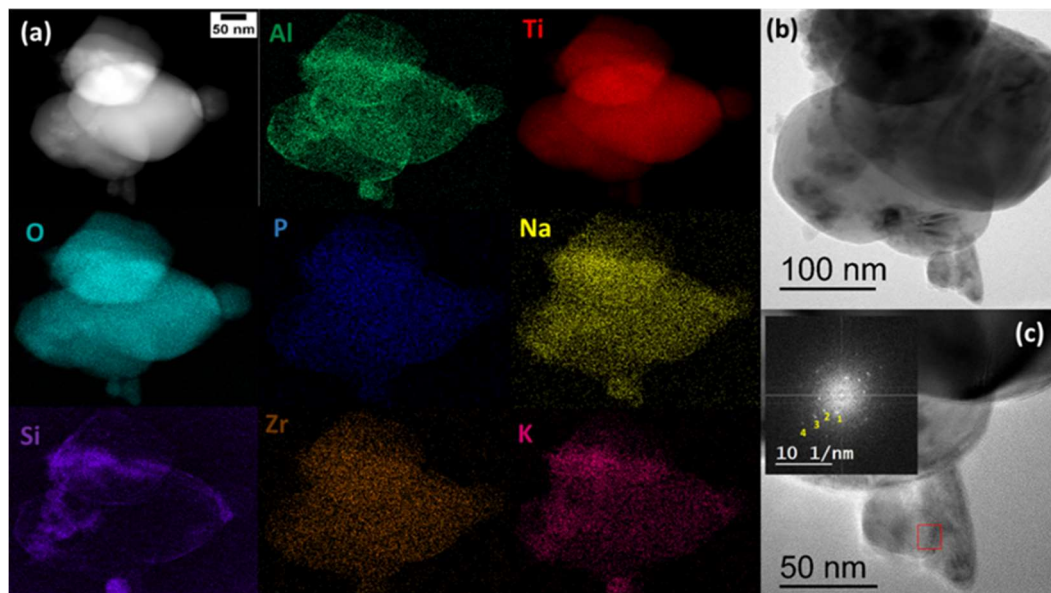


Figure 5-3: (a) STEM image of TiO_2 milled for 32 minutes with EDS maps showing spatial distribution of relative elements. (b) TEM image of the TiO_2 sample prepared using the plunge-freeze vacuum dry method and (c) higher magnification TEM image showing fractured fines with inset FFT from the square highlighted. d-spacings corresponding to hkl rutile crystalline phase (Okrusch (2003)) measured from inset FFT; $d_1 = 0.340$ nm (110), $d_2 = 0.248$ nm (011), $d_3 = 0.170$ nm (121), and $d_4 = 0.121$ nm (122).

The crystal structure of primary particles was investigated by analysis of lattice fringes in high magnification TEM images (Figure 5-1 (b)), and a fast Fourier transform (FFT) was generated to measure the d-spacing Figure 5-1 (c). The TiO_2 sample milled for 1 minute had primary particles of the rutile crystal phase, as observed by the d-spacing

corresponding to the (011) and the (122) planes of rutile (Okrusch (2003)), as shown in Figure 5-1 (c). Due to crystal phase transformations reported in the literature after milling anatase TiO₂ (Sen et al. (2011)), the crystal phase of the particle fines were also investigated for the 32 minute milled sample.

Figure 5-2 (c) shows three locations where the FFT was generated, either on the primary particle surface or on the fractured fines attached to the primary particle. The FFT generated from the primary particle (inset Figure 5-2 (c), point A) again indicates d-spacings corresponding to the rutile (110) and (120) planes (Okrusch (2003)), and the fractured fines (inset Figure 5-2 (c), points B and C) also have planes corresponding to the rutile (110) and (011) planes (Okrusch (2003)). The dispersion behaviour of fractured fines was investigated for the 32 minute milled TiO₂ sample, using the plunge-freeze and vacuum dry method described by Hondow et al. (2012), allowing a closer *in situ* assessment of aggregation unaffected by sample drying. The fractured fines appear to either attach to the primary particle surfaces (Figure 5-2 (d)) or cluster together (Figure 5-2 (e)), thus suggesting that the fractured fines are not well dispersed in the suspension, which may significantly impact on the overall optical properties of the bulk materials.

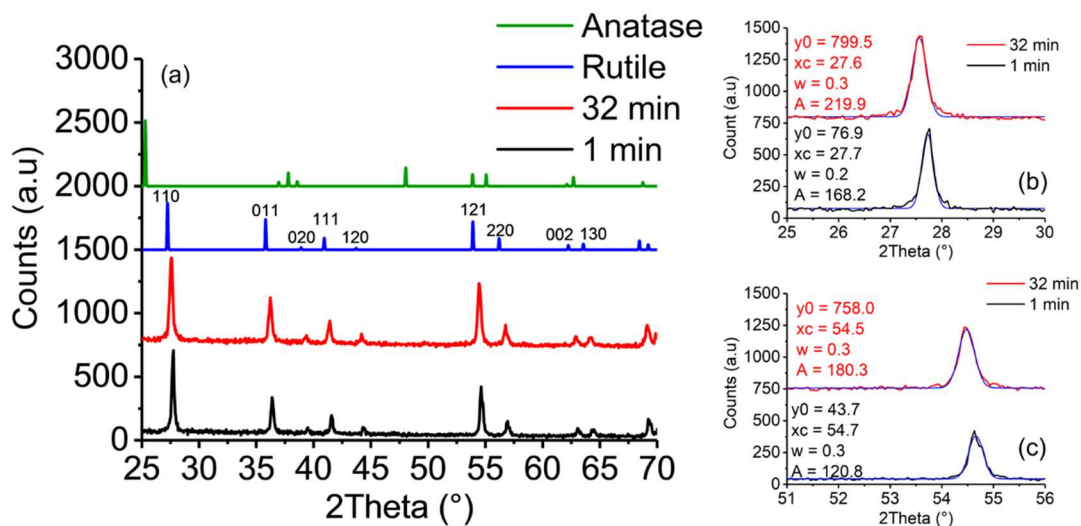


Figure 5-4: (a) X-ray diffraction (XRD) pattern of 1 (black) and 32 minute (red) milled TiO₂ samples compared to anatase (Horn (1972)) and rutile (Okrusch (2003)) crystal structures. (b) Expansion of (110) peak and (c) expansion of the (121) peak, both fitted to a Gaussian distribution with parameters y₀ (baseline count), X_c (central 2Theta), w (peak width) and A (count amplitude).

It was suspected that the ball milling media (glass ballotini) may contaminate the titania samples for extended milling times up to 32 minutes. Additionally, due to the industrial nature of the samples, other contaminants may also be present. Energy dispersive X-ray spectroscopy (EDS) was used as elemental analysis for the plunge-frozen 32 minute milled sample, as presented in Figure 5-3. It confirms the presence of silicon from the ballotini which is heterogeneously distributed across the particle. As the TiO₂ were milled in a slurry of sodium hexametaphosphate (SHMP), phosphorus and sodium are also evident, and appear to be evenly distributed on the surface.

Dopants are regularly added during the chloride process. For example, small quantities of AlCl₃ (between 0.01 to 10%, although 0.5 -2 % is more typical), are added to the reactor feed to control pigment aggregation and favour the rutile phase (Hartmann (1996), Braun et al. (1992), Wang et al. (2010)) and hence aluminium is also clearly evidenced on the particle surface. Finally, zirconia is also observed in Figure 5-3, which is a result of contamination from degradation of the impeller used in the mill. Figure 5-3 (b) shows a TEM of the particles from which the EDS was mapped. Here, observed fines are again attached to the larger primary particle surface. Figure 5-3 (c) shows the FFT generated from an area on the fines that also confirms the rutile crystal phase with the d-spacing and hkl planes (Okrusch (2003)). Additional EDS maps of the unmilled TiO₂ and 32 minute milled particles are displayed in Appendix 2 Figure A2-6 and A2-7, which also shows an even coverage of the elements associated with the presence of SHMP on the TiO₂ particles.

Table 5-1: Crystallite sizes calculated from Gaussian fitting of the (110) and (121) XRD peaks for 1 and 32 minutes milled TiO₂.

XRD Peak	110	110	121	121
Milling Time (min)	1	32	1	32
Position (°)	27.7	27.6	54.7	54.5
FWHM (°)	0.2	0.3	0.3	0.3
Crystallite size (nm)	48	36	39	35

Figure 5-4 (a) presents the XRD pattern of the TiO₂ samples after milling for 1 minute and 32 minutes. Peaks again matched the rutile powder diffraction pattern (Okrusch

(2003)), where no additional peaks were observed in the XRD pattern for both TiO₂ samples, further confirming phase and sample purity, although line broadening and a small shift in the peaks are detected. The peak broadening in the XRD was used to determine crystallite size for the two samples. Therefore, the two most intense peaks in the XRD pattern, (110) and (121), were fitted to a Gaussian distribution, as shown in Figure 5-4 (b and c). Table 5-1 shows the full width half maximum (FWHM) obtained from the Gaussian fit and the calculated crystallite size using the Scherrer equation (Eq. (5-1)) (Patterson (1939)). The primary crystallite size marginally decreases with milling time from ~40 - 47 nm after milling for 1 minute to ~35 nm after milling for 32 minutes, and this decrease suggests that stresses within the crystal structure leads to a broadening of the peaks.

The (110) peak at $2\theta \approx 27^\circ$ for rutile relates to the crystallite size of the shortest dimension, and the (001) or (002) plane corresponds to the longest dimension (Egerton and Tooley (2014)). Length to width ratios of 2:1 are common for rutile crystals (Egerton and Tooley (2014)), which would give rise to crystallite lengths of ~100 nm. Although this is in closer agreement with the primary particle sizes obtained from TEM, there is still a large discrepancy in the average crystal size. However, there are critical differences between direct primary particle size determination from TEM and crystal size characterisation by XRD, where primary particle sizes can only be measured by XRD if lattice planes are perfectly orientated (Egerton and Tooley (2014)). Hence, underestimation of particle sizes by XRD can occur, while it is clear that individual particles observed in the TEM do represent primary particles. In conclusion, no change in the primary particle size was observed with increased milling time, however there may be changes in the aggregate size. Longer milling times were found to induce particle fracturing resulting in nanoparticle fines 10-20 nm in size, although despite this, no change in the crystal structure was observed.

5.3.2 Particulate surface charge and size changes through milling and washing

Zeta potential values for 1 and 32 minute milled alumina doped TiO₂ in the presence of SHMP are presented in Figure 5-5 (a). Figure 5-5 (b) shows the evolution of the pigment zeta potential with milling time at neutral pH, before and after centrifugal washing. The investigated TiO₂ was found to have an isoelectric point (iep) between pH 3 to 4.5. With an increase in milling time leading to a lower pH_{iep}. Taylor et al. (2003) previously reported a change in rutile iep with alumina doping, with pure rutile pH_{iep} at 4.9. This contrasts to

alumina doped rutile which they reported had a pH_{iep} in the range of 8-9, dependent on the surface concentration of alumina.

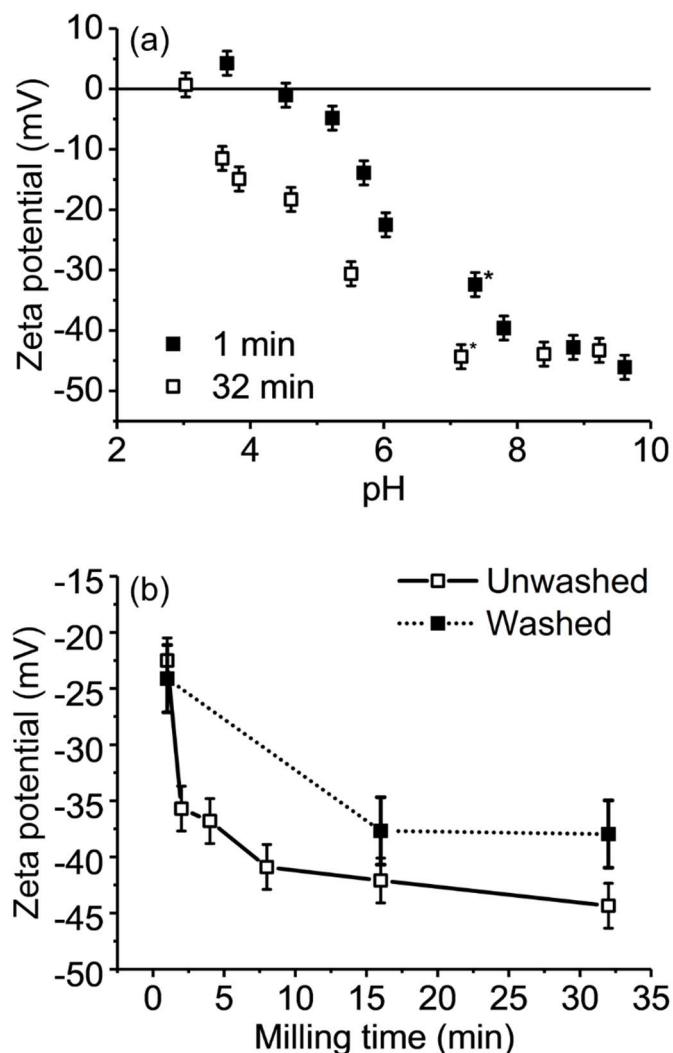


Figure 5-5: (a) Zeta potential of aluminium doped TiO_2 particles in the presence of sodium hexametaphosphate (SHMP) for 1 and 32 minutes of milling. The neutral pH is indicated by (*). (b) Change in the TiO_2 zeta potential with milling time at neutral pH before and after centrifugal washing. In both (a) and (b), error bars represent the maximum standard deviation.

The change in iep is due to the domination of aluminium hydroxide surface groups (Taylor et al. (2003)). However, while these values appear higher than those seen in Figure 5-5, Taylor et al. (2001), in other work, also reported the pH_{iep} of pigmentary titania to vary significantly with the addition of SHMP, which even at low concentrations had a strong effect on the surface chemistry. Indeed, they (Taylor et al. (2001)) showed that the zeta potential decreased with polyphosphate concentration, which was pronounced at

low pH (pH 4) and altered the reported pH_{iep} to between 3 and 5, dependent on the dispersant concentration, consistent with values reported in Figure 5-5. Further, Michelmore et al. (2000) have shown that increasing the concentration of phosphate and increasing the chain length of the linear polyphosphate decrease the magnitude of the zeta potential of titanium dioxide.

Figure 5-5 (a) therefore suggests that increasing milling time leads to the presence of more SHMP on the alumina-doped pigment surface. It is expected that milling will lead to an increase in agglomerate breakage, potentially leaving more alumina-rich surface sites exposed. Thus, any non or poorly adsorbed dispersant remaining in the aqueous phase may adsorb to these newly exposed sites, leading to a reduced (more negative) zeta potential at low pH, because of the high charge density of the SHMP. Above pH 8 however, the zeta potential values remain constant near -50 mV regardless of milling time, consistent with Taylor et al. (2001), and is indicative of the maximum potential magnitude of an adsorbed surface with SHMP.

Figure 5-6 shows the XRF phosphorus elemental analysis for both washed and unwashed TiO_2 samples milled for different times. It is important to note that the data has been first normalised to 100 % Ti content, then the relative change in phosphorus calculated by setting the 1 minute milled sample to 100% phosphorus content. The full elemental analysis obtained from XRF (which is also normalised to 100% Ti content) is given in Appendix 2 (Figure A2-8). There is a clear difference in phosphorus content for unwashed TiO_2 milled for 1 minute, compared to 16 and 32 minutes of milling where the phosphorus content is relatively unchanged.

Whilst more phosphorus is in the samples milled for longer time periods, the exact quantity of phosphorus on the surface of TiO_2 is unknown due to the semi-quantitative nature of the technique. However, this change in phosphorus content supports the previous hypothesis that more SHMP is present on the pigment surface when milling time is increased. It is important to note that we cannot be certain from the XRF results alone that phosphorus is on the surface of the pigment. However, as previously discussed in terms of the EDS analysis as shown in Figure 5-3, it is evident that phosphorus is spread over the particle surface rather than in the bulk solvent.

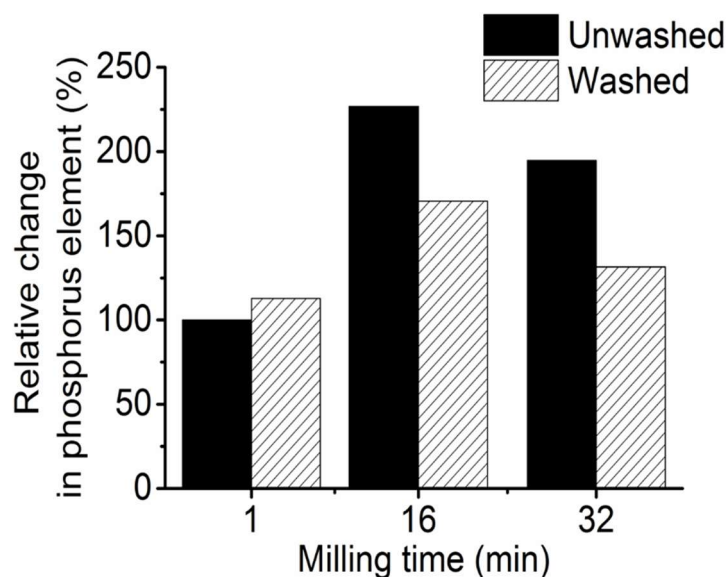


Figure 5-6: X-Ray fluorescence data showing the relative difference in phosphorus content for 1, 16 and 32 minute milled TiO_2 particles, before and after centrifugal washing. All XRF elemental data was first normalised by setting Ti mass% to 100%. The relative change in phosphorus content with milling time was calculated by setting the 1 minute milled sample to 100% phosphorus content.

Additionally, there are important differences between washed and unwashed samples. From the XRF data (Figure 5-6), washing does not induce a change in phosphorus content for the 1 minute milled sample, while it leads to a significant decrease in the phosphorus content for the 16 and 32 minute milled samples, inferring a partial loss of the SHMP dispersant for samples milled at longer times. These results are consistent with zeta potential changes presented in Figure 5-5 (b), where, again, washing does not induce any change in the zeta potential for the 1 minute milled sample, while it leads to a reduction in the magnitude of zeta potential for the 16 and 32 minute milled suspensions. Hence, it appears that whilst milling increases the surface density of the dispersant, the SHMP that is additionally adsorbed is more easily removed upon washing.

The interaction of SHMP and titania can be complex, with both chemisorption (considered irreversible) and electrostatic physisorption (considered reversible) are possible (Taylor et al. (2001)). It may be that the high energy of the mill induces some restructuring and increases physisorption of the dispersant which is more weakly bound. Farrokhpay et al. (2012) found that acidic pH, high calcium ion concentrations and elevated temperatures all decreased the ability of polyphosphate (Calgon T) to disperse titanium pigment particles of average primary particle size 230 nm. They concluded that the reduced dispersant performance, at least under high acid conditions and temperature,

was due to the hydrolysis of the polyphosphate chains, which was observed through infrared analysis. Furthermore, they reported that the reduction of the polyphosphate chain length from hydrolysis leads to a decrease in steric stabilisation, but the shorter chains still allowed electrostatic stabilisation to occur. Thus, we propose that mechanical activation at the pigment surface and high temperatures occurring during the milling process could either weaken the interaction between the adsorbed polyphosphate and the pigment surface, and/or cause the hydrolysis of the linear phosphate chains into shorter ones, thus allowing removal through centrifugal washing for the 16 and 32 minute milled samples.

Figure 5-7 presents the intensity auto-correlation data from DLS measurements of the 1 and 32 minute milled TiO₂ suspensions, with 30 measurements collected for each sample. For both samples, two relaxation modes are observed: (i) a relaxation mode characterised by a short relaxation time of $\sim 7 \times 10^{-4}$ s at 173° scattering angle, independent from the milling duration, and (ii) a relaxation mode characterised by a significantly longer relaxation time varying from one measurement to another. Owing to their relaxation times, the first and second relaxation modes are termed ‘fast’ and ‘slow’ relaxation modes, respectively. The fact that two relaxation modes are probed by DLS suggests that two populations of particles are present in the suspensions. The presence of two particle populations was already suggested by the TEM images, where primary particles and aggregates of primary particles were observed, though it could not be determined whether the aggregates were present in the TiO₂ suspensions or had formed during TEM sample preparation. It is worth noting that the DLS results do not rule out the formation of agglomerates during TEM sample preparation.

As discussed in Appendix 2, the intensity auto-correlation data could be described by the sum of two stretched exponentials (one for each relaxation mode; see Eq. (A2-1); thus allowing the determination of the relaxation times associated to each relaxation mode. The fact that the slow mode relaxation times vary from one measurement to another suggests that the slow relaxation mode is associated with large polydisperse ‘objects’, and may be assigned to aggregates. Due to the inter-measurement variability of the slow relaxation time, no further calculation was performed for the slow relaxation mode.

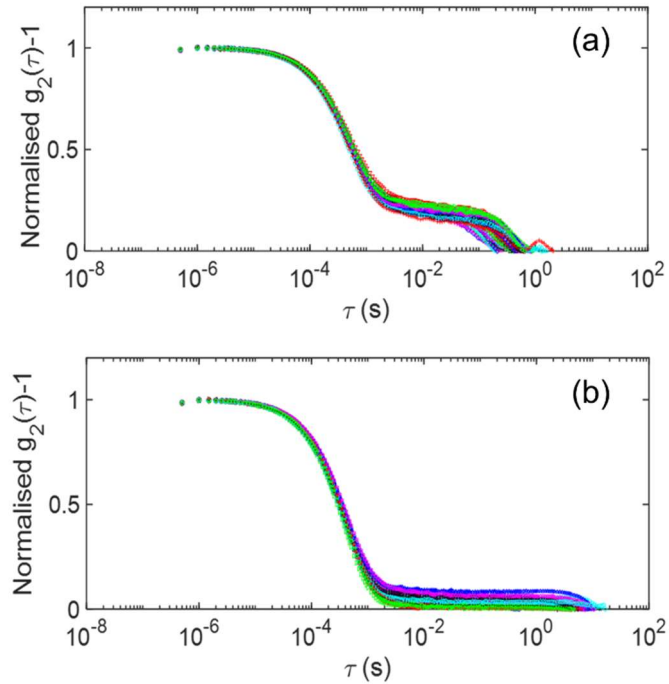


Figure 5-7: Intensity auto-correlation data from DLS measurements of TiO₂ suspensions prepared from 1 (a) and 32 (b) minute milled samples. Thirty 30 second measurements were performed for each sample, and each is represented by a different colour symbol.

The diffusive nature of the fast relaxation mode was confirmed with a light scattering device allowing DLS measurements to be performed at different scattering angles (see Appendix 2). Hence, the hydrodynamic diameter (D_H) associated with the fast relaxation mode could be calculated from the fast relaxation time using the Stokes-Einstein equation (see Eq. A2-4 and A2-5 in Appendix 2) and are shown in Figure 5-8. Figure 5-8 compares the particle diameters obtained from X-ray disc centrifugation, TEM and DLS measurements. The hydrodynamic diameters determined from DLS measurements compare very well to the primary particle sizes measured from TEM (with measured diameters of ~ 250 nm almost unchanged with milling time) thus suggesting that the fast relaxation mode probed by DLS can be assigned to the primary TiO₂ particles. Figure 5-8 also shows the ratio between the relative amplitudes of the fast and the slow modes (A_{fast} and A_{slow} , respectively) obtained by fitting the intensity auto-correlation data (see Eq. A2-1 in Appendix 2). A_{slow}/A_{fast} decreases with milling time, thus suggesting a decrease in the proportion of aggregates with milling time compared to the primary particles.

Particle size determination from XDC, based on terminal settling described by the Stokes law, can be used to probe a wider range of sizes (i.e. $\sim 0.01 - 50 \mu\text{m}$) than light scattering

(McFadyen and Fairhurst (1993)). XDC results shown in Figure 5-8 suggest an exponential-type decrease in particle or aggregate size with milling time. After 1 minute milling, the measured size is ~ 450 nm, which is assumed to be an average of the sizes of both primary particles and aggregates (considering that the primary particle size is ~ 250 nm, as determined from TEM images). As the milling time is increased, the number of aggregates in the dispersion decreases, and the average particle size determined by XDC decreases towards that expected of the primary particles (~ 250 nm). It is noted that, given the influences of particle shape (Shiels et al. (2018), Paul et al. (2017)) and aggregation (Johnson et al. (2016)) on sedimentation rate, XDC results must be taken with caution.

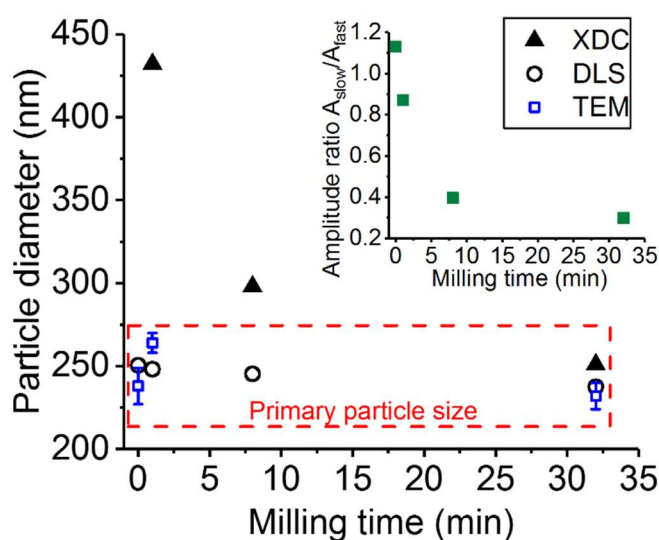


Figure 5-8: Particle diameter of unmilled and milled TiO_2 particles measured using dynamic light scattering (DLS). Also shown is the particle size measured by x-ray disc centrifugation (XDC) and transmission electron microscopy (TEM) with associated standard error. Additionally, given is the ratio A_s/A_f of fast and slow mode relative amplitudes (from DLS measurements) as a function of milling time (inset). It should be noted that the amplitude of the slow mode for the unmilled sample was calculated by $(A_2+A_3)/A_1$ where A_1 is the fast mode and A_2 and A_3 were the two additional slow modes present due to an increase in polydispersity.

The hydrodynamic diameters of the washed and unwashed milled TiO_2 samples were determined using DLS and can be found in the Appendix 2 (Table A2-2), alongside the values of the A_s/A_f ratios. The hydrodynamic diameter associated with the fast relaxation mode does not change upon washing; consistent with the fact that the size of the primary

particles is not expected to be affected by washing. For the 32 minute milled TiO₂ sample, the value of A_s/A_f is not affected by washing, suggesting also that the proportion of aggregates are not considerably affected by washing. Such an observation would be consistent with partial hydrolysis of the polyphosphate during milling, maintaining the electrostatic stability of the system after partial removal of poorly bonded phys-adsorbed dispersant with washing. Thus, the maintained layer is sufficient to continue to prevent primary particles from significant aggregation. Taylor et al. (2001) state the SHMP molecular weight to range between 1082 and 1286 Daltons which would be a sufficient length to induce steric stabilisation.

5.3.3 Surface area determination and NMR relaxometry of milled samples

Figure 5-9 presents the BET surface area plotted against the milling time. The specific surface area increases due to milling, from ~5.7 m²/g after 1 minute milling to 7.5 m²/g after 32 minute milling, corresponding to calculated spherical equivalent diameters of 248 nm to 188 nm, respectively (as shown on the right-hand axis). The equivalent sizes calculated from BET surface areas are in relatively good agreement with the sizes estimated from TEM and DLS. Measuring shear-dependent aggregates is complex and it is important to use a variety of techniques to characterise the system.

Gesenhues (1999) also monitored surface area of rutile TiO₂ using BET, observing an increase in surface area from 6 to 8 m²/g after 65 minutes milling. Other reported pigment TiO₂ surface areas are in the range of 8-9 m²/g by Taylor et al. (2001), 12 - 19 m²/g (Karakas and Çelik (2013), Allen et al. (2004)) and can be as high as 28 m²/g reported by Fazio et al. (2008). Mestl et al. (1995) milled molybdenum oxide and showed crystallite size to be fairly constant in the first hour of milling, with a small decrease in particle size and an increase in BET surface area, suggesting the breakage of agglomerates and larger particles. In the second phase of milling (milling times up to 600 minutes), the particle size drastically decreased, primary crystallites were broken down and amorphization occurred on their surface (Mestl et al. (1995)), all associated to an increase in the BET surface area. Thus, the results reported in Figure 5-9 suggest that the increase in the specific surface area comes from aggregate breakage.

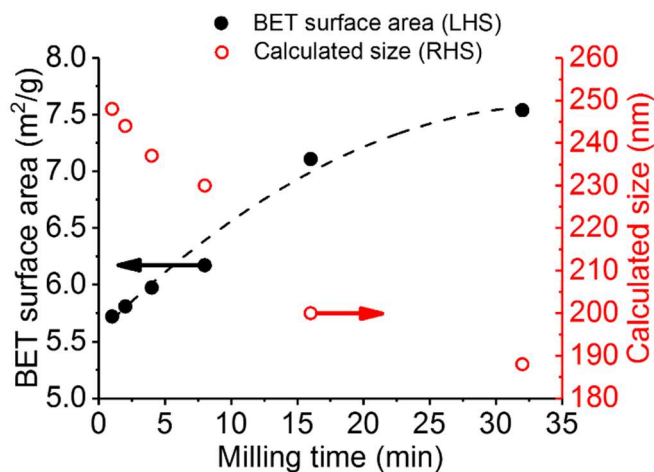


Figure 5-9: Brunauer–Emmett–Teller (BET) surface area for milled TiO₂ particles (left-hand side) with polynomial fit to guide the eye, and the calculated particle size based on a spherical shape (right-hand side) as a function of milling time.

The mean pore size obtained from BET measurements and the total pore volume (Appendix 2, Table A2-3) remain constant ranging from 16 nm to 19 nm, further suggesting that the change in surface area is largely accounted for by the decrease in aggregate sizes. Some of the increase in surface area may also be accounted for by the formation of the nanoparticulate fines, although, as they are adsorbed on the dried agglomerated samples, it is likely that their influence on surface areas changes is masked.

Changes in specific surface area, as measured by BET (in the dry state), were also compared to wet dispersion results from the NMR relaxometry measurements. Differences are observed in the NMR relaxation rate enhancement (R_{sp} ; in reference to water) for the alumina-doped pigment particles as the milling time is increased, as shown in Figure 5-10 (a) (for unwashed dispersions). It is well known that the liquid bound at a particle surface has a relaxation time orders of magnitude shorter than the comparative bulk (2-3 seconds) due to molecular motion becoming anisotropic and restricted at the surface, thus increasing the relaxation rate (Cooper et al. (2013(b)), Fairhurst et al. (2016)).

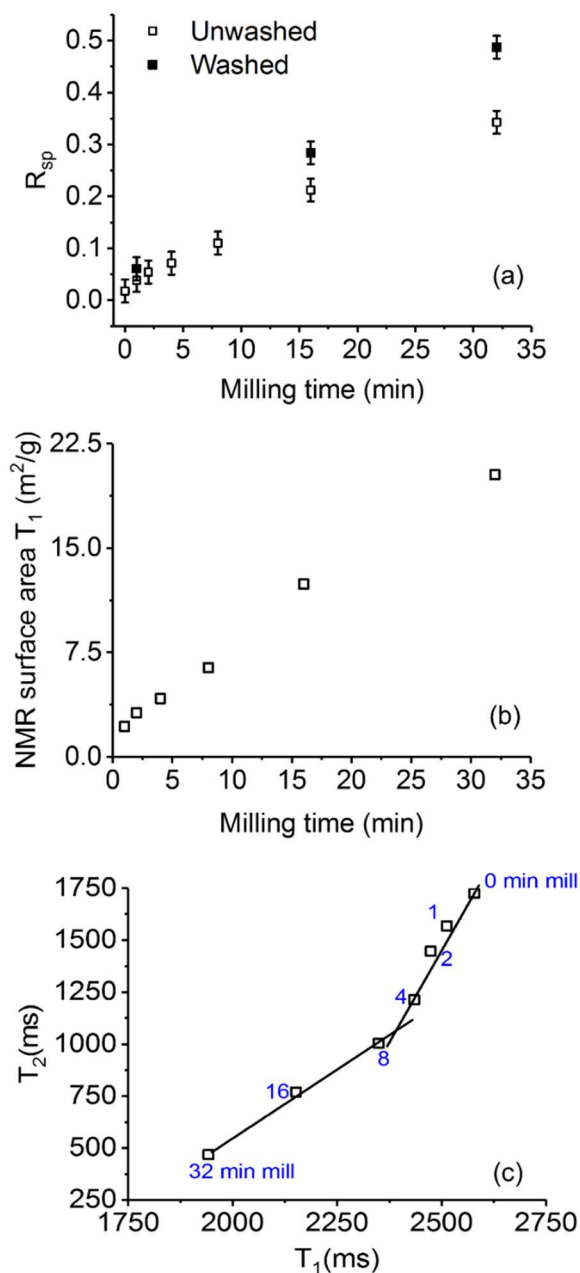


Figure 5-10: (a) T_1 relaxation rate enhancement (R_{sp}) for unmilled and milled TiO₂ particles compared to bulk water ($T_{1, \text{water}} \sim 2,600$ ms), with error bars representing the maximum standard deviation for washed and unwashed samples. (b) NMR surface area of unwashed samples calculated from T_1 and using the surface specific relaxation constants K_a ($g/m^2/ms$) derived from the 8-minute milled BET surface area. (c) NMR relaxation time measurements T_1 and T_2 for unwashed TiO₂ particles, with lines drawn across two regions to guide the eye.

Therefore, the increase in R_{sp} with respect to milling time also suggests an increase in surface area, which can be calculated from R_{sp} using a standard reference material of known surface area, as shown in Chapter 4. For dispersant-free suspensions of particles with identical surface chemistry, the relaxation rate scales linearly with increasing surface area (Cooper et al. (2013(b))). However, adsorption of a dispersant at the particle surface may also lead to an increase in the relaxation rate, from the decrease in the mobility of water at the particle surface (Cooper et al. (2013(b))).

Due to the complexities of correlating the interactions of the dispersant to a separate calibration system of known surface area, the BET surface area for the 8 minute milled samples was used to find K_a (the specific relaxation constant) allowing R_{sp} to be converted to particle surface area for the other milling times. The 8 minute milled sample was used as the reference system as it corresponds to the onset of the plateau observed in the zeta potential with increased milling time (Figure 5-5 (b)), consistent with an increase in concentration of SHMP at the particle surface. Therefore, it was thought that after 8 minutes of milling, the R_{sp} would be most significantly enhanced due to the contribution of SHMP at the particle surface rather than the increased surface area available from aggregate breakage. Thus, the K_a for milled TiO_2 was calculated and correlated to the surface area obtained from the BET measurement for the 8 minute milled sample, giving a K_a of $3.93 \times 10^{-4} \text{ g/m}^2/\text{ms}$.

Figure 5-10 (b) shows the calculated surface area as a function of milling time, which compares relatively well with the BET results (Figure 5-9) obtained at low milling times. However, at long milling times (16 and 32 minute milling) the calculated surface areas continue increasing significantly, rather than beginning to plateau (as observed with the BET data). The deviation observed in the NMR could be due to a number of factors. Importantly, BET measures the particle surface area as a dried powder, compared to NMR where surface area measurements are performed on the dispersed suspension. Therefore, it is likely that the surface area is smaller by BET due to the presence of agglomerates compared to NMR where these are broken during sonication (see Figure A2-4, Appendix 2).

However, it should be noted that the increase in surface area from agglomerate breakage is likely to be small and therefore alone cannot account for the differences. An additional explanation is the influence of the nanoparticle fines evidenced after long milling times from TEM, which at $\sim 20 \text{ nm}$ may contribute to much greater dispersion surface areas.

Whilst the effect of these nanoparticle fines would be masked in the dried powder BET, they would be more evident in dispersion conditions. Also, as it was evident from TEM that these fines largely adsorbed onto the primary particles, it is assumed that they would increase the surface area primarily through roughening of the primary particles surfaces. Nevertheless, given the magnitude of the changes in relaxation rate after 16 and 32 milling times, it is still difficult to attribute the differences to actual surface area increases alone.

To better understand relaxation changes with milling time, it was decided to consider both T_1 and T_2 relaxation measurements. Although both T_1 and T_2 can be used to determine particle surface area, using one or the other has both advantages and disadvantages (Fairhurst et al. (2016)). Whilst T_2 measurements are faster, which is advantageous if samples are not stable (for example, if sedimentation occurs), the relaxation time can become very small at high suspension concentrations, leading to potential measurement errors. Furthermore, T_2 is more sensitive to changes in available surface area, and to the presence of ferromagnetic or paramagnetic impurities. Due to the differences in sensitivity of T_1 and T_2 , it can be advantageous to measure both relaxation times, as shown in Figure 5-10 (c). Here, a clear inflection in the data arises between the 4 and 8 minute milled samples, correlated to the change in zeta potential for pigment samples (Figure 5-5 (b)), which plateaus after 8 minutes of milling, as previously conversed this is suggestive of monolayer SHMP coverage.

While it is evident that longer milling times lead to an increase in adsorption density of the SHMP, it was assumed that adsorption plateaus post 8 minutes, limiting further surface chemistry contributions (as discussed). However, given the potential for extended milling times to lead to hydrolysis or other structural changes of the dispersant because of the high energy milling conditions, we may have to consider the influence of the dispersant structure in addition to the influence of its density on NMR relaxation. It may be that hydrolysed SHMP has a greater influence on NMR surface relaxation than unmodified SHMP, although, due to the convoluted nature of the overall response, it is very difficult to further define the interactions between SHMP and the bound water.

After centrifugal washing, an increase in R_{sp} was observed, as shown in Figure 5-10 (a), where the increase is minimal and within the measurement error for the 1 minute milled sample, but this increase becomes significant with increased milling time. The first explanation is that the removed or hydrolysed polyphosphate (observed from the changes in zeta potential and phosphorus content determined using XRF), which occurs for

samples milled for longer periods of time, leads to an increase in exposed alumina surface sites. Aluminium (^{27}Al) is a quadrupolar nucleus and can cause enhancements in relaxation rates of bound solvent molecules at the colloid surface (Cooper et al. (2013(a))). However, if this was simply the case, one would expect the relaxation rate of the 1 minute milled sample (unwashed or washed) to show the largest enhancements, as these samples have the lowest phosphorus content according to XRF, and should therefore have more exposed Al surface sites.

For both the unwashed and washed samples milled for 16 and 32 minutes, the surface area increases, and the number of fines increases leading to a faster relaxation rate than the one of the washed or unwashed 1 minute milled samples. As previously stated, the ball mill energy might be altering the surface structure of the dispersant or exposing further Al sites, whilst some dispersant can be washed off, this is most likely weakly interacting salt that might not contribute to the large relaxation enhancements. The remaining chemisorbed polyphosphate salt may have an altered surface structure, and this, coupled with the increase in exposure of Al surface sites, may be the reason for the enhanced relaxation rates upon washing. While it is difficult to state for certain what changes in the dispersant structure are occurring without additional surface analysis and this is an area of ongoing investigation, the degradation of an ammonium salt of poly(methacrylic acid) used during wet ball milling of alumina has previously been reported (Chartier et al. (1996)).

5.4 Summary

The effect of milling time on the interaction between aluminium doped titania pigment particles and polyphosphate (SHMP) dispersant has been studied using multiple characterisation techniques. TEM highlighted the presence of ~ 20 nm titania fractured fines in samples milled for 32 minutes, that were found to have d-spacings correlating to a rutile crystal structure, implying that milling did not induce changes in crystal structure. The TiO_2 samples were found to have an isoelectric point (iep) in the range of pH 3 to 4.5, with an increase in milling time leading to a lower pH_{iep} . It was proposed that increasing milling time leads to the presence of more SHMP on the alumina-doped pigment surface, due to the breakage of agglomerates/aggregates.

DLS measurements probed two relaxation modes: (i) a mode characterised by a fast relaxation time, assigned to primary TiO_2 particles, and (ii) a mode characterised by longer relaxation times, subject to inter-measurement variability, and assigned to the aggregates

present in the suspensions. The hydrodynamic diameter associated with the primary TiO_2 particles did not change upon milling time, while the DLS data suggested that the proportion of aggregates in the suspensions decreased upon milling time.

Relaxation NMR data as a function of milling time showed a linear increase, and no plateau was detected, due to either the increase in surface area from fractured fines in samples milled for longer times, or due to the increase in SHMP concentration and/or dispersant restructuring at the surface of titania pigment particles; both leading to an overestimation of bulk surface area. It could be that hydrolysed SHMP has a greater influence on the NMR relaxation rate of bound water molecules leading to an enhancement in R_{sp} , which is difficult to state for certain without further surface/structural analysis. Importantly, this chapter demonstrates the difficulties of characterising shear-dependent milled aggregates and the need for multiple characterisation techniques, alongside the potential of NMR relaxometry as an online-process control tool for not only detecting changes in surface area but also surface chemistry.

Chapter 6 Degradation of polyphosphate dispersant interactions with aluminium-doped TiO₂ during high shear-milling

6.1 Introduction

The previous Chapter concluded that industrially milled Al doped TiO₂ samples with SHMP adsorbed resulted in particle fines of <20 nm after milling for 32 minutes. Furthermore, it was found that the polyphosphate (SHMP) content increased with an increase in milling time, as observed through changes in surface charge and elemental quantification techniques. It was possible to remove the polyphosphate through centrifugal washing, when the pigment samples were subjected to longer milling times, where a decrease in phosphorus content was observed and reduction in the surface charge (more positive). It was assumed that either additional SHMP adsorption or structural changes promoted with milling, resulted in a weakly bound SHMP layer that could be removed. However, chemisorbed dispersant was stable to repeated wash cycles. Consequently, the use of SHMP to disperse TiO₂ during the milling process, thus leads to several questions such as, to what extent milling time and temperature effect polyphosphate hydrolysis once adsorbed to the TiO₂ surface.

Despite the use of polyphosphates for industrial processing (Farrokhpay et al. (2012)) it is also known that aqueous polyphosphate solutions are not stable under several process conditions such as high temperature, acidic (pH) or basic (pH) and also in the presence of metal ions (Farrokhpay et al. (2012), Rulliere et al. (2012)). Smaller phosphates for example, orthophosphates can be formed by hydrolysis and these can have an impact on the dispersion properties of the system (Farrokhpay et al. (2012)). Since industrial milling waters usually contain some degree of soluble salts for example Ca²⁺ and milling can cause an increase in temperature to at least to a few tens of °C (Andreola et al. (2006)), the rate of hydrolysis and impact this may have on the dispersion properties of the pigment could be significant and has not extensively been investigated.

Andreola et al. (2006) studied SHMP adsorption and ageing on the rheological behaviour of kaolin dispersions with the effect of temperature and Ca²⁺ ions. They observed a sharp increase in the suspension's apparent viscosity after treatment at 60 °C, even for short ageing periods (10 hours). However, at 30 °C the change in the suspensions apparent viscosity were smaller and only accomplished after longer ageing times (50 hours). The

addition of Ca^{2+} ions to the suspension led to a significant increase in the apparent viscosity at 30 °C, even for short aging times. Andreola et al. (2006) suggest that these differences may be due to degradation hydrolysis of SHMP in solution.

Importantly the polyphosphate chain length has an impact upon steric stabilisation, with evidence suggesting that polyphosphates with phosphate units $n > 4$, have better dispersion properties than polyphosphates of shorter chain length (Feiler et al. (2000), Michelmore et al. (2000)). This is because steric stabilisation requires a proportion of the polyphosphate chain to extend into the solvent resulting in increased particle-particle repulsions and thus collisions are prohibited.

X-ray photoelectron spectroscopy (XPS) has previously been used to understand the adsorption behaviour of SHMP with mineral surfaces (Ni and Liu (2013), Zhang et al. (2019)). Zhang et al. (2019) investigated the P to Al atomic ratios before and after treating the kaolinite and diaspore (an aluminium oxide hydroxide mineral) surface with acid. The acid treated kaolinite led to a reduced adsorption capacity for SHMP, however acid treated diaspore adsorbed more SHMP than the untreated diaspore. Zhang et al. (2019) related these differences to changes the number of Al sites which they defined as unsaturated Al. An increase in unsaturated Al was observed after acid treatment of diaspore, thus allowing an increase in polyphosphate adsorption. Zhang et al. (2019) did not study the stability of the adsorbed SHMP-particle systems, nor did they investigate any changes in polyphosphate chain length. Ni and Liu (2013) also used XPS to investigate the adsorption behaviour of SHMP on pyrochlore and calcite.

Thus, this chapter examines the influence of milling time, temperature and calcium ions, upon polyphosphate (SHMP) degradation and dispersion efficiency when adsorbed onto Al doped TiO_2 . Industrially sourced aluminium-doped titanium dioxide nanoparticles (agglomerated reactor discharge) have been used in this study, which were extracted from the production process prior to SHMP adsorption. The SHMP was subsequently adsorbed under lab-scale controlled conditions. The degradation has been investigated through X-ray photoelectron spectroscopy (XPS) and the dispersion properties monitored indirectly through size and surface charge measurements. Additionally, the use of NMR relaxometry was used to investigate the influence of the polyphosphate-alumina interactions on relaxation times. In order to better understand how such a technique could be used as a process control tool for the online monitoring of TiO_2 particle size during processes such as milling.

6.2 Materials and Methods

6.2.1 Materials

Non-milled TiO₂ reactor discharge (RD) containing alumina burned into the crystal was supplied by Venator as a slurry and purified as described in section 6.2.2. This is industrial grade pigment titania that has been obtained prior to polyphosphate dosing. This material differs to the TiO₂ material used in Chapter 5 as those samples were obtained after dispersant dosing and milling. Sodium chloride (Sigma Aldrich) was used as the background electrolyte. Sodium hexametaphosphate, known by the trade name Calgon and abbreviated as SHMP throughout this thesis, was used to control the TiO₂ dispersion properties. The SHMP (Sigma Aldrich) had the chemical formula (NaPO₃)_n, chain length n=6 and a particle size of +200 mesh. 1 M HCl (Fisher Chemicals) and 1 M NaOH (Fisher Chemicals) was used to adjust the pH of slurries and stock solutions. In all instances dispersions and stock solutions were prepared using MilliQ water unless otherwise stated. Calcium chloride dihydrate (Sigma Aldrich) was used to replicate milling in hard water conditions.

6.2.2 Purification of TiO₂

The TiO₂ was washed three times in deionised water (5 L aliquots) to remove impurities. The suspension was left to sediment by gravity over two weeks before removing the supernatant. The TiO₂ was then dried in an oven at 100°C overnight.

6.2.3 Polyphosphate adsorption isotherm

100 ml of known concentration of SHMP was prepared at pH 4 in background electrolyte (0.001 M NaCl). After which, 0.1 g of Al doped TiO₂ (unmilled) was added with pH monitoring and continuous adjustment over one hour. The sample was then checked hourly for 4 hours and no significant drift in the sample pH was recorded. The sample was then left on the shakers overnight (12 hr) after which the pH was checked once again. The samples were then centrifuged, and the supernatant was removed and passed through a 0.22 µm syringe filter to remove any particles that remained. The supernatant was then analysed via ICP with a calibration made using SHMP in 0.001 M NaCl at pH 4. Samples were prepared using this method to obtain analogous pseudo-isotherms by relaxation NMR, with the exception that the samples were not centrifuged, and the supernatant was not removed. Instead aliquots (containing particles, adsorbed and unbound SHMP) were

removed after the samples were left on the shakers overnight and were measured using the method detailed in section 6.2.9.

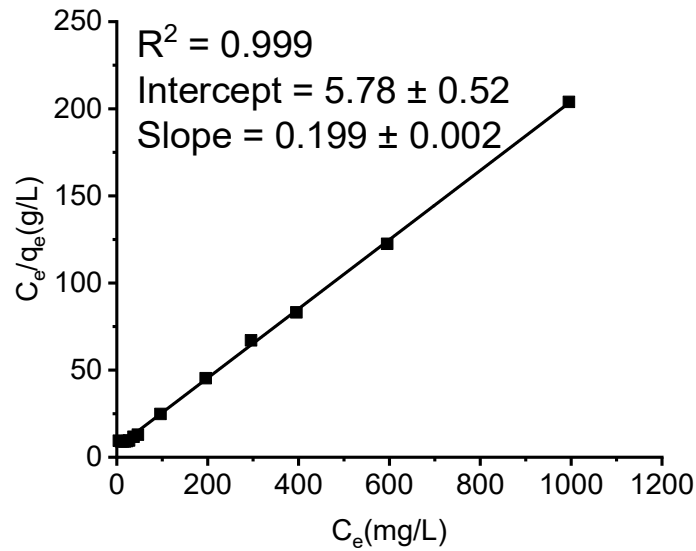


Figure 6-1: Linear plot of SHMP adsorption used to calculate the Langmuir isotherm parameters (at room temperature).

The Langmuir adsorption model was applied using the linear translation of the Langmuir equation (Langmuir (1918)) as shown by Eq. (6-1). Where, C_e is the adsorbate equilibrium concentration (mg/L), q_e is the amount of adsorbate in the adsorbent at equilibrium (mg/g), q_m the maximum adsorption capacity (mg/g) and b the Langmuir adsorption constant.

$$\frac{C_e}{q_e} = \frac{1}{q_m b} + \frac{C_e}{q_m} \quad (6-1)$$

The amount of SHMP adsorbed onto the adsorbent at equilibrium (q_e) was calculated using Eq. (6-2). Where C_0 is the initial concentration of SHMP in solution (mg/L), m is the mass of adsorbent (g) and V is the volume of SHMP solution (L). Here C_e is obtained from the ICP OES adsorption experiment.

$$q_e = (C_0 - C_e) \frac{V}{m} \quad (6-2)$$

Therefore, the linear plot of C_e/q_e vs. C_e , as shown in Figure 6-1, gives a slope of $1/q_m$ and intercept of $1/(q_m b)$, thus allowing the Langmuir adsorption constant (b) and maximum adsorption capacity to be calculated (q_m), as shown in

Table 6-1. These values were then used with the Linearized form of the Langmuir equation to calculate the theoretical amount of SHMP expected to adsorb for different initial concentrations of SHMP.

Table 6-1: Calculated parameters using the linearized form of the Langmuir equation and standard error shown.

Maximum adsorption q_m (mg/g)	5.03 ± 0.5
Langmuir constant (L/mg)	0.034 ± 0.002

6.2.4 Polyphosphate degradation experiments post-adsorption

55 ml of 1mM NaCl pH4 stock solution was added to 20 g of TiO₂ (dried) and mixed with a spatula until the large agglomerates disintegrated, after which the dispersion was mixed for 30 minutes with a magnetic stirrer and plate. A solution of SHMP was prepared by adding 1.4 g of SHMP to 15 ml of 1mM NaCl pH 4 stock solution. The addition of SHMP caused the pH of the background electrolyte to increase, thus, 1 M HCl was added dropwise to decrease the pH back to pH4. The SHMP solution was then vigorously shaken in order to dissolve the SHMP and added to the TiO₂ dispersion. The SHMP was left to adsorb for 1 hour onto TiO₂ with continuous stirring and the pH was monitored and adjusted back to pH4. Thus, the TiO₂ slurry was at 22 wt% and the total initial concentration of SHMP was at 20,000 ppm, which is in excess of the maximum adsorption capacity previously calculated.

The slurries were then processed either by milling, addition of calcium ions and/or heated, to understand the influence of processing conditions on the structure of SHMP attached to TiO₂. The effect of temperature on SHMP degradation was investigated by mixing the slurries continuously at 100 °C for 1 hour. Calcium ions were added in the form of calcium chloride dihydrate at an equivalent concentration of 500 mg/L (to mimic concentrations that could be expected in hard water) to the SHMP adsorbed TiO₂ slurry. The slurries were then left either at room temperature or 100 °C continuously stirring for 1 hour.

The remaining slurry was then washed by centrifugation on a Heraeus Megafuge 16R Centrifuge (Thermo Scientific). In order to remove any non-adsorbed SHMP which remained in the supernatant. Three wash cycles were performed, all in background electrolyte (pH4, 1 mM NaCl), at 10,000 RPM for 30 minutes. After the final wash cycle the supernatant was removed and the remaining suspensions were left to dry in a glass drying oven held at 50 °C for approximately one week. A non-milled TiO₂ sample with SHMP adsorbed was also left unwashed but dried in order to investigate if the washing procedure effected the SHMP structure, however, it should be noted that any non-adsorbed SHMP will then dry onto the particle surface.

6.2.5 Milling procedure

The TiO₂ slurry was milled at 22 wt% and the total initial concentration of SHMP was at 20,000 ppm. After adsorbing SHMP to the TiO₂ (as described in section 6.2.4), the milling beads (zirconia coated silica, 500 µm) were then added to the slurry to give a fill ratio of 0.8. The slurries were milled in a stainless-steel grinding chamber with a ceramic spindle which were fabricated to fit a Silverson L5M-A high shear mixer, allowing control over the stirrer speed. Initially, the mill was set to 100 rpm for 1 minute in order to fully coat the milling beads with the TiO₂ slurry. The rpm was then adjusted to 6,000 RPM and the slurries were milled for varied residence times (t = 2, 30 and 60 minutes). After the milling time elapsed the slurries were removed from the milling chamber and the grinding media was washed in copious amounts of deionised water and sieved between 350 and 560 µm mesh sieves, to remove any potential fragmented milling beads prior to reuse.

6.2.6 Zeta potential

A Zetasizer Nano ZS (Malvern Instruments) was used to measure the zeta potential of the dispersions as previously described in Chapter 4 section 4.2.5. Dispersions were

prepared at 100 ppm in 0.1 mM NaCl. Stock base (NaOH) and acid (HCl) solutions were prepared at 0.1 M, to increase and decrease the pH of the particle dispersions respectively.

6.2.7 Particle size

Particle size distributions were measured using a Mastersizer 2000 (Malvern) as described in Chapter 4 section 4.2.3. Concentrated TiO₂ dispersions with and without SHMP adsorbed were prepared at 15 wt.% in 1 mM NaCl at pH 9. A stock solution of 1 mM NaCl at pH 9 was also prepared in order to dilute the suspensions inside the Mastersizer shear cell. The pH was maintained to provide electrostatic stability and stop particle aggregation. The measurement procedure was repeated three times, taking a new sub sample of TiO₂ and these three measurements were averaged to create a single distribution.

6.2.8 Surface area by BET

Brunauer–Emmett–Teller (BET) surface area measurements were performed as previously described in Chapter 4 section 4.2.7. TiO₂ samples were degassed to remove moisture using a vacuum oven at 110°C for a minimum of 12 hours and maximum of 18 hours (no observed changes in mass occurred when leaving for longer periods), under a vacuum of 10 mmHg.

6.2.9 NMR relaxometry

Suspensions were prepared at 15 wt.% from the washed and dried powders at either pH 4, 7 or 9, adjusted dropwise with NaOH. Prior to analysis samples were dispersed in an ultrasonic bath for 30 minutes, followed by 2 mins on an ultrasonic probe at 30% amplitude. For surface area determination for TiO₂ without SHMP present the K_a was calculated using the BET surface area of the unmilled (0 min) TiO₂ sample. The K_a was then assumed to be constant with milling time as it was assumed that only the surface area changes with milling time and thus surface chemistry remains constant throughout.

6.2.10 X-ray photoelectron spectroscopy (XPS)

A Kratos Axis Ultra DLD system was used to collect XPS spectra using monochromatic Al $K\alpha$ X-ray source operating at 150 W (10 mA x 15 kV). Data was collected with pass energies of 160 eV for survey spectra, and 40 eV for the high-resolution scans with step sizes of 1 eV and 0.1 eV respectively. The system was operated in the Hybrid mode, using a combination of magnetic immersion and electrostatic lenses and acquired over an area

approximately $300 \times 700 \mu\text{m}^2$. A magnetically confined charge compensation system was used to minimize charging of the sample surface, and all spectra were taken with a 90° take of angle. A base pressure of *ca.* 1×10^{-9} Torr was maintained during collection of the spectra. Data was analysed using CasaXPS (v2.3.21) after subtraction of a Shirley background and using modified Wagner sensitivity factors as supplied by the manufacturer. Note that due to the overlap of the Na(1s) core-level with a portion of the Auger signal, a model for this background signal was obtained from TiO_2 and fitted in addition to a Na(1s) component.

6.3 Results and Discussion

6.3.1 Adsorption of polyphosphate onto Al doped TiO_2

Zeta potential values for the unmilled Al doped TiO_2 are shown in Figure 6-2, and the isoelectric point (i.e.p) is at $\sim\text{pH } 6$ which is in good agreement with Gustafsson et al. (2000). The surface charge of the TiO_2 at pH 4 is approximately +30 mV whilst at pH 9 it is approximately -45 mV, which are consistent with Taylor et al. (2003), although their i.e.p values were shifted towards an alumina surface likely due to the particles having a higher Al surface coverage than the samples used herein.

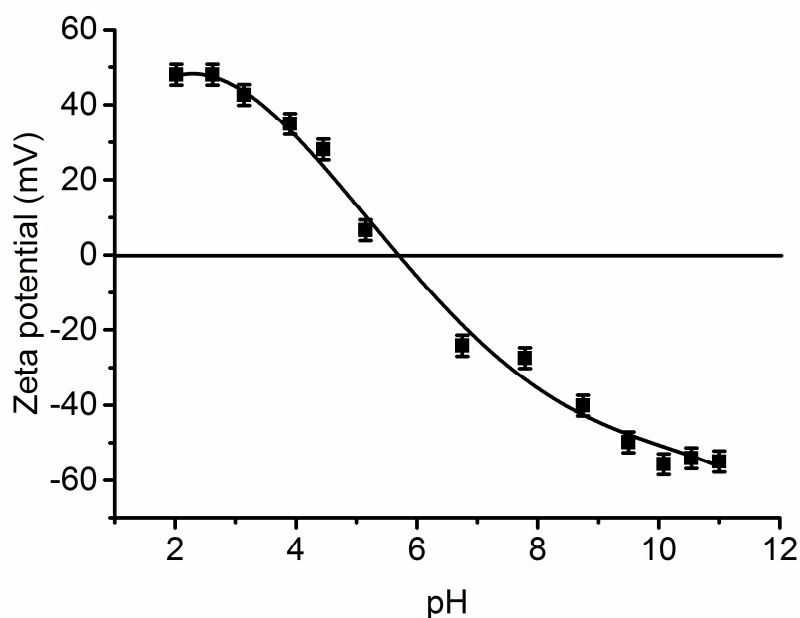


Figure 6-2: Zeta potential for unmilled Al doped TiO_2 in 1 mM NaCl background electrolyte.

SHMP is highly negatively charged, thus when the TiO_2 is at pH 4 it is likely that electrostatic adsorption will dominate between the negative phosphate groups and positive AlOH_2^+ and TiOH_2^+ sites at the particle surface. However, when the TiO_2 is at pH 9 the electrostatic interaction is repulsive. Despite this, literature has shown that polyphosphate adsorption still occurs (Michelmore et al. (2000), Taylor et al. (2001)), thus indicating that adsorption likely occurs via a chemisorption mechanism. At pH 9, the Al doped TiO_2 surface will be comprised of neutral AlOH groups, positive AlOH_2^+ and negative TiO^- . In this case electrostatic interactions between the particle and polyphosphate may occur with the AlOH_2^+ sites but are not favourable between the negative titanium hydroxide surface sites. However, chemisorption will occur through bidentate surface complexation leading to the formation of Al-O-P and Ti-O-P bonds (Taylor et al. (2001)).

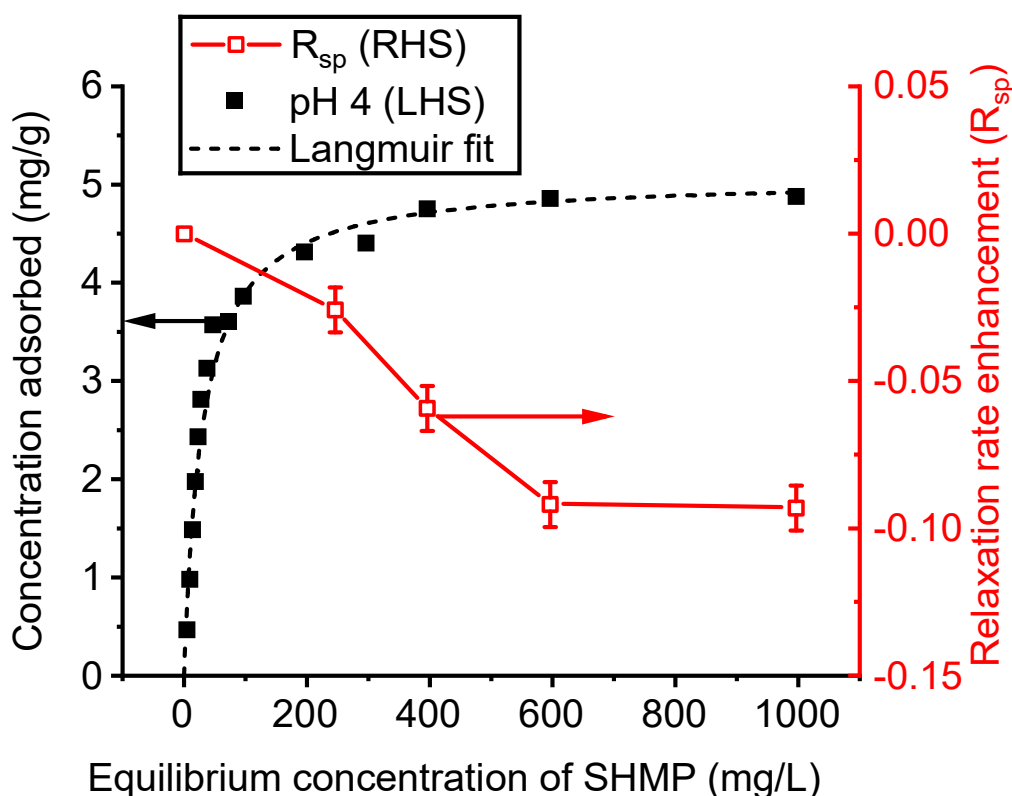


Figure 6-3: Adsorption isotherm of SHMP on unmilled Al doped TiO_2 at pH 4 in 1 mM NaCl by ICP-OES (black, closed). The black dashed line shows the Langmuir adsorption isotherm fit. Pseudo-isotherm (red, open) generated from the relaxation rate enhancement (R_{2sp}) calculated using the T_2 relaxation time. The R_{2sp} is scaled to an equivalent sample of the bare particle to remove the effect of the particle surface area with the maximum standard error plotted. The connecting line (red) is to guide the eye.

The adsorption isotherm of SHMP adsorbed onto Al doped TiO₂ at pH 4 in 1 mM NaCl are shown in Figure 6-3. The Langmuir adsorption model was applied using the Langmuir equation (Langmuir (1918)). It can be observed in Figure 6-3 that the concentration of adsorbed SHMP plateaus post 600 ppm equilibrium concentration, thus indicative of the maximum adsorption of SHMP to the unmilled TiO₂. Relaxation NMR is a technique that has previously been used to generate pseudo-isotherms (Cooper et al. (2012), Cooper et al. (2013(b)), Cooper et al. (2013(a))) and Figure 6-3 shows the pseudo-isotherm for the addition of SHMP onto unmilled Al doped TiO₂. The addition of SHMP caused a decrease in the specific relaxation rate enhancement, R_{2sp} compared to that of the pure particle surface.

The addition of a dispersant or polymer to a particle surface can cause an increase in R_{2sp} , due to the reduction in the rotational motion of surface bound water as shown by Cooper et al. (2013(a)). However, Cheesman et al. (2013), previously showed a decrease in the R_{2sp} for an increase in initial macroinitiator concentration to silica nanoparticles due to the displacement of water from the silica surface upon adsorption of the macroinitiator. Furthermore, reductions in R_{2sp} have been reported by Schwarz and Schönhoff (2002) for the addition of a polyelectrolyte to silica and was attributed to the replacement of surface bound water with polymer train segments. The adsorption of three different surfactants onto Kaolin clay (Al₂Si₂O₅(OH)₄) has previously been studied using relaxation NMR by Totland et al. (2011), where a decrease in the relaxation rate upon adsorption of surfactant was observed, due to the surfactant blocking water access to the paramagnetic surface.

It is important to note that the magnitude of change in R_{2sp} observed in this study is small (-0.1), which contrasts to Cheesman et al. (2013) where they reported R_{2sp} to decrease from ~9 down to 6 with an increase in macroinitiator concentration. Although relaxation rates cannot be directly compared for different particle systems, it is useful to understand the magnitude of changes in R_{2sp} reported for the adsorption of polymers and/or dispersants onto particle surface's. More similar changes in R_{2sp} (+/- 0.1 to 0.2) were reported by Schwarz and Schönhoff (2002) and values were also dependent on the presence of ions in the bulk solution. The reason such small changes in R_{2sp} were found here (Figure 6-3) is likely because the changes in SHMP adsorption at the particle surface are minimal (for the concentrations studied by NMR), as shown by the adsorption isotherm data.

Lower equilibrium concentrations of SHMP (<200 ppm) could not be used for the NMR study as settling problems were encountered. Although it would be useful to explore the changes in relaxation rates for lower SHMP surface coverage, this is not possible whilst settling occurs. Particles' settling during relaxation measurements lead to misrepresentative relaxation rates that are often faster than expected due to an increase in particle concentration within the measurement device. As discussed in Chapter 3 an increase in particle concentration causes an increase in the relaxation rate.

Figure 6-4 shows the change in the Al doped TiO₂ surface charge with an increase in SHMP concentration. The surface charge was at approximately -50 mV for equilibrium SHMP concentrations between 200-1000 ppm at pH 4. This is indicative of the maximum surface charge for SHMP coverage. At SHMP concentrations <100 ppm the zeta potential varies from -50 mV to +50 mV with a decrease in SHMP concentration, with +50 mV being the bare Al doped TiO₂ surface charge. The change in surface charge is likely a result of patchy surface coverage for low SHMP concentrations and ultimately this leads to particle aggregation and settling as shown in Figure 6-5.

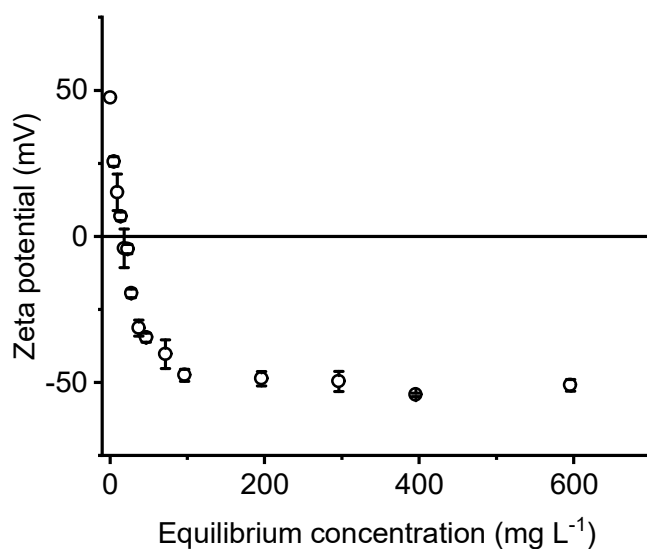


Figure 6-4: Al doped TiO₂ pigment particle surface charge with increasing polyphosphate (SHMP) concentration with the standard error shown.

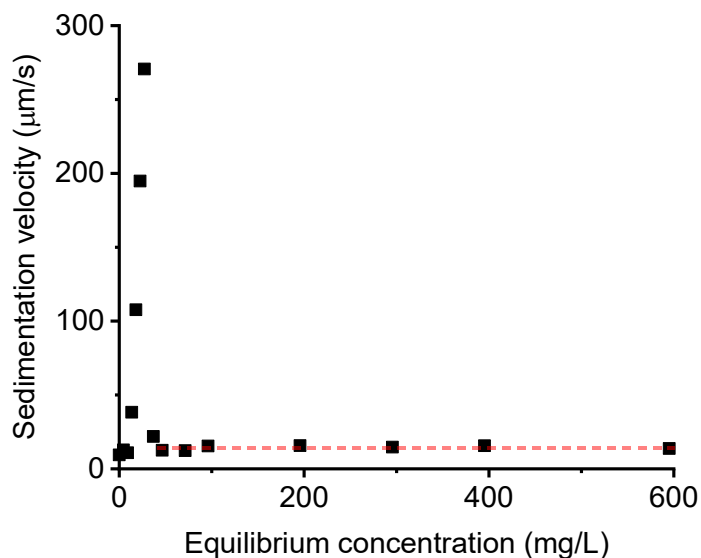


Figure 6-5: Al doped TiO₂ pigment particle sedimentation velocity (measured using the Lumisizer) with increasing polyphosphate (SHMP) concentration.

Nonetheless, the plateau of R_{2sp} observed in Figure 6-3 corresponds to the saturation of SHMP at the Al doped TiO₂ surface, occurring at an SHMP equilibrium concentration of 600 ppm, which is in agreement with the onset of the plateau for the adsorption isotherm. Above this SHMP equilibrium concentration (600 ppm), it can be concluded that further addition of SHMP to the bulk solution does not affect the adsorbed polyphosphate layer because solvent relaxation NMR is sensitive to the surface bound water at the SHMP-particle interface.

It is likely in the case of these experiments that the reduction R_{2sp} is induced due to the blocking of the Al-rich TiO₂ surface by SHMP extending into the solvent. Whereby Aluminium (²⁷Al) is a quadrupolar nucleus and can cause enhancements in relaxation rates of bound solvent molecules at the colloid surface (Cooper et al. (2013(a))). An increase in R_{1sp} was observed previously (Chapter 5, Figure 5-10 (a)) for pre-adsorbed SHMP onto Al doped TiO₂ pigment supplied milled by Venator, after particles were washed. The increase in R_{1sp} after washing was due to the removal of SHMP and exposure of the Al sites at the particle surface. This is therefore in agreement with the data reported in Figure 6-3 as the relaxation rate increases with a decrease in SHMP concentration as more surface Al sites are exposed.

6.3.2 Al doped TiO₂ surface area determination by BET and adsorption density comparison

Table 6-2 shows the maximum adsorbed quantity of polyphosphate onto Al doped TiO₂, which was calculated using the linear translation of the Langmuir equation (Langmuir (1918)), as shown by Eq. (5-1). The maximum adsorbed amount of polyphosphate was found to be 0.95 mg/m², this was almost twice the amount found by Taylor et al. (2001). The reason for the difference in adsorption behaviour is likely due to the difference in polyphosphate chain length. Here, SHMP has an average length n = 6, compared to the polyphosphate used by Taylor et al. (2001) which had a chain length n = 10-12.

It appears reasonable that the maximum adsorbed amount would half for a doubling in the chain length and this is in agreement with the literature (Michelmore et al. (2000)). Michelmore et al. (2000) investigated polyphosphate adsorption onto TiO₂ with varying polyphosphate chain length. They found that for n=4 the adsorption capacity reached 0.0002 mol/g compared to 0.0001 mol/g when the average chain length was n=10, therefore approximately doubling the adsorbed amount when the chain length is halved. This is because when the polyphosphates chain length increases, this results in more hindered packing around the particle surface and thus leads to lower adsorbed quantities.

Table 6-2: The maximum adsorbed amount of polyphosphate onto Al doped TiO₂ pigment using the Langmuir equation. Shown is a comparison of the maximum adsorbed quantity found by Taylor et al. (2001), with the differences in the experimental conditions highlighted.

Parameter	This experimental	Taylor et al. (2001)
Mass of particles (g)	0.1	10
BET surface area (m ² /g)	5.34	9.2
Polyphosphate chain length (n)	6	10-12
pH	4	4
Maximum amount of adsorbed polymer using Langmuir equation (mg/m ²)	0.95	0.56

Table 6-3: Comparison of BET surface area and size for (a) lab milled Al doped TiO₂ without polyphosphate after 30 minutes of milling. (b) milled Al doped TiO₂ with polyphosphate supplied by Venator (as characterised in Chapter 5).

Particle system	Milling time (min)	BET surface area (m ² /g)	Calculated spherical size (nm)
(a) Lab milled Al doped TiO ₂ no SHMP	30	8.16	174
(b) Venator milled Al doped TiO ₂ with SHMP	32	7.54	188

Table 6-3 shows a comparison of the BET surface area for milled Al doped TiO₂ with and without SHMP dispersant for similar milling times, it is interesting to note that the surface areas are very similar despite the use of dispersant, although the samples were obtained by different means of milling, for example, lab milled vs. industrially. However, the milling conditions for the lab mill were scaled accordingly and thus result in similar average primary particle size. With an increase in milling time there is an increase in surface area, after 60 minutes of milling the BET surface area reaches 9.60 m²/g. To ensure complete polyphosphate surface coverage values (equal to that of the 0 min milled sample), enough SHMP must remain in the aqueous phase during milling. As additional surfaces are formed the SHMP will adsorb onto these newly exposed surfaces. For these experiments where Al doped TiO₂ has been lab milled in the presence of SHMP, there is enough SHMP which remains in the supernatant to allow full coverage of the particles, see the Appendix 3: Supplementary information to Chapter 6, Sections A3.1 and A3.2 for further information.

The previous Chapter characterised industrially milled Al doped TiO₂ with SHMP adsorbed. Based on the adsorption isotherm shown in Figure 6-3, calculations have been made to understand if full coverage of SHMP occurs on an industrial scale, see Appendix 3: Supplementary information to Chapter 6 Sections A3.1 and A3.2 for more detail. To briefly summarise, Venator add 0.14 w/w% P₂O₅ on TiO₂, this would equate to a mass of 0.93g/L of SHMP. If milling occurs at pH 4, Venator do not add enough SHMP to the mill to ensure full particle coverage prior to milling, however, on an industrial scale SHMP is adsorbed at pH 9 to 11. The adsorption isotherm was not measured at pH 9 in this work, however others have adsorbed polyphosphates onto TiO₂ particles at pH 9 (Taylor et al. (2001), Michelmore et al. (2000)). Taylor et al. (2001) observed a three times

reduction in the maximum adsorbed polyphosphate concentration at pH 9 compared to pH 4, for a polyphosphate chain length $n=10-12$.

Using the assumption that three times less polyphosphate adsorbs at pH 9, Ventaor have enough SHMP in the mill to cover particles before milling. However, there is not enough to cover particles up to milling times of 60 minutes, as there will not be enough SHMP in the equilibrium phase. This is based on the assumption that three times less polyphosphate adsorbs at pH 9 compared to pH 4, and in reality this could be lower, for example Michelmore et al. (2000) have shown a ten times reduction. It should be noted that on the industrial scale pigment particles are added to the dosing tank and the pH is increased to 11, it is likely that the adsorption density is even lower than assumed in these calculations. Secondly, the amount of time the pigment particles remain in the dosing tank is not known, and Castellini et al. (2005) have shown SHMP adsorption onto kaolinite to plateau after 100 minutes of adsorption. Thus, in the previous Chapter an increase in the polyphosphate density was observed with an increase in milling time likely because the adsorption had not reached equilibrium, and the additional milling time allowed for further adsorption.

6.3.3 Al doped TiO₂ surface area determination BET and NMR comparison

Prior to the adsorption of SHMP, the surface area was determined for unmilled and milled Al doped TiO₂ through BET and T₂ relaxation NMR, as shown in Figure 6-6 (a). It is important to note that the NMR surface area (SA) calculation requires the derivation of a material specific relaxation constant K_a , this was calculated using the BET surface area of the 0 minute sample ($K_a = 0.01296 \text{ g/m}^2/\text{ms}$). After 60 minutes of milling TiO₂, the NMR SA was $\sim 11.7 \text{ m}^2/\text{g} \pm 0.7 \text{ m}^2/\text{g}$ equating to a particle size of $121 \text{ nm} \pm 7 \text{ nm}$. The BET surface area was $9.6 \text{ m}^2/\text{g} \pm 0.24 \text{ m}^2/\text{g}$ correlating to a primary particle size of $148 \text{ nm} \pm 4 \text{ nm}$. Austin (2019) show the change in particle size with increased milling time of TiO₂ without SHMP. They showed that after 60 minutes of milling the particle sizes recorded were D₁₀ ($0.158 \mu\text{m}$), D₅₀ ($0.279 \mu\text{m}$) and D₉₀ ($0.482 \mu\text{m}$). Relaxation NMR SA measurements are more sensitive to particles of smaller size as they occupy the largest wetted surface area. The change in the surface area (ΔSA) between NMR and BET measurements are shown in Figure 6-6 (b), the ΔSA steadily increases until about 15 minutes of milling and then appears to plateau. Interestingly, Austin (2019) have shown the particle size of milled Al doped TiO₂ to follow an exponential decay (Figure 6-6 (b) inset) which plateaus post 15 minutes of milling which seems to be analogous to ΔSA .

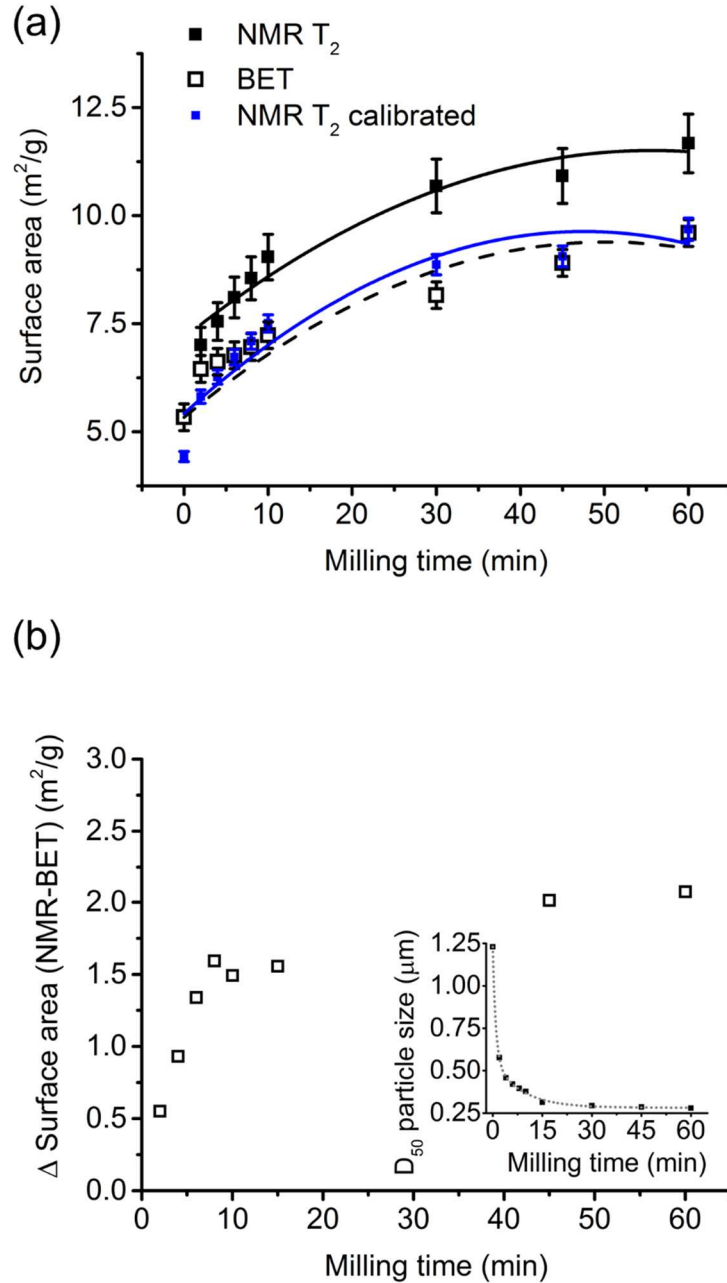


Figure 6-6: (a) Surface area for Al doped TiO_2 reactor discharge with milling measured by BET and T_2 relaxation NMR. NMR surface areas were calculated using the surface specific relaxation constant K_a ($\text{g}/\text{m}^2/\text{ms}$) derived from the 0-min milled BET surface area (black squares) and average K_a value taking into account each BET surface area (blue squares). The maximum error on the BET measurement is shown and the NMR error was calculated using the minimum and maximum K_a obtained from the minimum and maximum BET surface area at 0 minute milling. Polynomial fits are shown to guide the eye. (b) Shows the change in surface area between the two techniques as a function of milling time when the NMR is not calibrated. Inset is the D_{50} particle size with milling time (Austin (2019)).

Changes in particle size alone cannot account for such differences in the NMR SA measurements, and it should be noted that the NMR technique is sensitive to changes in available surface area but also surface chemistry. It has been assumed that changes in surface chemistry are minimal with milling time, however, Austin (2019) report changes in surface alumina concentration with an increase in milling time, which again seems to stabilise around post 15 minutes milling.

As previously discussed, Aluminium (^{27}Al) causes an enhancement in the relaxation rate of bound solvent molecules at the colloid surface and thus small changes in the surface concentration of Al are likely to have a significant impact on the calculated K_a for Al doped TiO_2 . Thus, the K_a is expected to vary for Al doped TiO_2 for each milling time measured. Therefore, an average K_a should be calculated by using the BET surface area for each milled sample. This gives a corrected K_a ($K_a = 0.01296 \text{ g/m}^2/\text{ms}$) and can be used to re-calculate the NMR surface area as shown in Figure 6-6 (a) (blue symbols). After this correction, the NMR and BET are in agreement, within the measurement error. This illustrates that relaxation NMR can be used to determine particle surface area for Al doped TiO_2 with milling, despite changes in surface alumina concentrations.

6.3.4 Al doped TiO_2 polyphosphate degradation after milling - probed by XPS

XPS has been used to probe the influence of milling time on SHMP adsorption and degradation, to gain a more detailed understanding of the bonding that occurs at the particle surface. The survey spectra for unmilled TiO_2 with SHMP adsorbed, and the reference spectra of SHMP and TiO_2 , are shown in Appendix 3: Supplementary information to Chapter 6 Figure A3-1. The main signals in the spectrum were Ti, O, P, Al, Na and C, arising from either the particle surface Al doped TiO_2 , polyphosphate SHMP or bonding between the particle and dispersant in the form of Al-O-P or Ti-O-P bonds.

Figure 6-7 shows the elemental quantification obtained by XPS for the milled samples, observed is a decrease in the P_{2p} concentration with an increase in milling, which suggests a decrease in the concentration of polyphosphate at the particle surface. Also shown in Figure 6-7 is a decrease in the P_{2p} concentration for the un-milled TiO_2 after centrifugal washing thus indicating that any physisorbed polyphosphate or weakly bound SHMP can be removed through washing, at least after SHMP adsorption at pH 4. As Figure 6-7 shows that P is still present after washing it suggests that a proportion of the SHMP is also bound strongly by chemisorption at pH 4, thus it could be expected that the TiO_2

remains stable even after washing so long as the surface charge remains repulsive and not patchy.

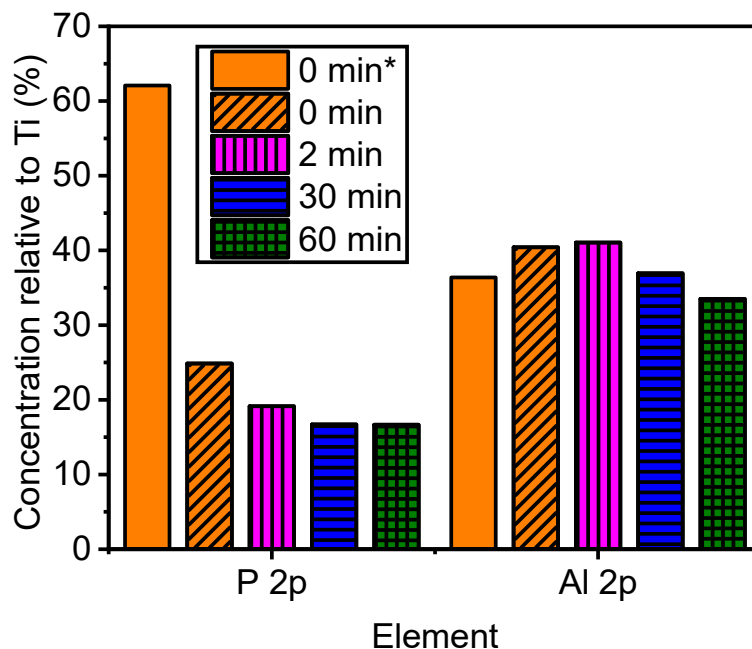


Figure 6-7: Elemental quantification of milled samples (washed) and un-milled (washed and un-washed*) obtained from XPS analysis, shown as a relative concentration to Ti (%) (Ti = 100 %) for the P_{2p} and Al_{2p} compositions.

Table 6-4: Al concentration (%) determined by XPS for milling Al doped titania pigment in the presence of SHMP.

Milling time (min)	Concentration of Al %
0	5.3
2	4.6
30	5.0
60	3.7
Average (4.7)	

Previously in Chapter 5, the change in surface Al concentration was discussed with milling. When no SHMP was present Austin (2019) observed a shift in the pH_{iep} for Aluminium doped titania pigment nanoparticles from pH ~6 without milling to pH ~8

(more similar to the pH_{iep} expected for an alumina surface) after 60 minutes of milling. It is important to note that the particles were milled using identical experimental conditions with the exception that SHMP was present. Table 6-4 shows the surface Al concentration measured by XPS with milling after SHMP is adsorbed to the particle surface. The results shown in Table 6-4 are not in agreement with those reported by Austin (2019) who found surface Al concentrations varied from $\sim 5.7\%$ (at 0 min milling) to $\sim 9.5\%$ (after 60 minutes of milling). The differences reported for these two studies may be due to the lubricative effect of SHMP during milling reducing the shear between particle surfaces and thus no apparent changes in Al concentration are observed, however further experimentation is required to support this theory.

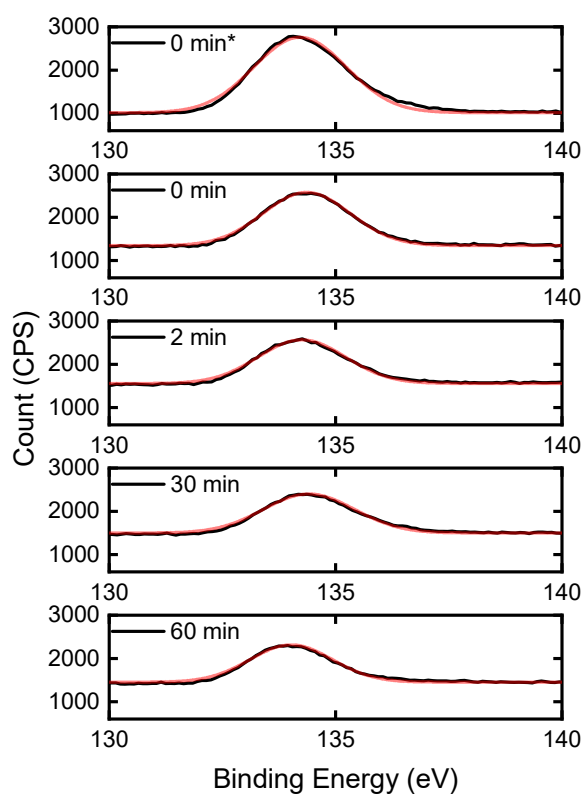


Figure 6-8: P_{2p} band for milled samples (washed) and un-milled (washed and unwashed*), fitted to a gaussian distribution shown in red.

Figure 6-8 shows the P_{2p} band for milled TiO_2 samples with adsorbed SHMP at pH 4, which has been fitted to a gaussian distribution with the peak width (FWHM) and peak positions shown in Table 6-5. The fitted P_{2p} peak width shows little to no change within the experimental error, with an increase in milling time from 0 to 60 minutes. The full

width at half maximum (FWHM) in XPS can be a useful indicator of chemical state changes but also physical influences. For example, broadening of the FWHM can be caused by a change in the number of chemical bonds contributing to the peak shape, or a change in the sample condition, due to X-ray damage or charging across the surface (Fairley et al. (2009)). Also observed in Figure 6-8 is a small shift in the binding energy of the P_{2p} band from 0 minutes of milling 134.5 eV (un-washed 134.1 eV) to 60 minutes 134.0 eV. Literature has shown the P_{2p} for pure SHMP was 134.1 V and SHMP treated calcite was 133.9 eV, both in agreement with the results observed for this study (Ni and Liu (2013)). Literature 2_{p3/2} binding energy values for phosphorus species are shown in Table 6-6, here it can be observed that the smaller phosphate species have lower binding energies.

Table 6-5: P_{2p} band fitted peak width (FWHM) and position as a function of milling time for washed and un-washed* TiO₂.

Milling time (min)	FWHM	Position
0*	2.35 ± 0.16	134.06 ± 0.01
0	2.21 ± 0.25	134.46 ± 0.02
2	2.21 ± 0.35	134.26 ± 0.03
30	2.32 ± 0.32	134.17 ± 0.02
60	2.15 ± 0.31	133.95 ± 0.02
Average	2.26 ± 0.28	-

Simon et al. (2007) previously reported the XPS spectrum for iron-sodium phosphate bead glasses and observed a shift in the P_{2p} peak to lower binding energies. They attributed this shift to an increase in the electron density around the phosphorus atom in the presence of iron oxide, suggesting that there were fewer P=O bonds due to the formation of linkages such as, P-O-Fe or Fe-O-Fe. Similarly, Majjane et al. (2014) observed a shift in the P_{2p} photoelectron peaks to lower binding energy due to the formation of P-O-V or V-O-V bonds via the breakage of P=O.

Thus, in the case for this work, a shift towards lower binding energy for the 60 minute milled sample could indicate the presence of smaller phosphate species. Although, if all polyphosphate chains were hydrolysed it could be expected that a greater difference in

the binding energy would be observed (compared to the 0.5 eV shown in Figure 6-8). Furthermore, the change in binding energy is also within the standard deviation previously reported for polyphosphate compounds as shown in Table 6-6. Therefore, it is important to quantify other chemical changes that may be observed in the survey scan, arising from a change in polyphosphate structure, before drawing such robust conclusions.

Table 6-6: P $2_{p3/2}$ binding energy values reported in the literature for different phosphate compounds (Moulder and Chastain (1992), Naumkin et al. (2000)).

Compound	Binding energy (eV)	Standard deviation (eV)
$(\text{PO}_4)^{3-}$ phosphate	133.2	0.7
$(\text{P}_2\text{O}_7)^{4-}$ pyrophosphate	133.2	0.6
P_2O_5	135.3	0.2
P_4O_{10}	135.6	0.1

The O1s spectra for the unmilled Al doped TiO_2 was used as a reference and is shown in Figure 6-9 (a). The O1s XPS signals were curve-fitted using assignments for rutile oxygen and hydroxyl groups arising from both titania and alumina. The fitted rutile oxygen component was found at 529.5 eV with a FWHM of 1.26, in agreement with previous literature for Al doped TiO_2 studies (Morris et al. (1999), Shvab et al. (2017), Barrère et al. (2003)). The hydroxide component at 531.6 eV with a FWHM of 2.54 was in close agreement with literature for Al-OH species (Morris et al. (1999), Zhang et al. (2019)) and Ti-OH species (Morris et al. (1999), Erdem et al. (2001), Barrère et al. (2003)). The O1s signal for SHMP without particles present is shown in Figure 6-9 (b), this has been fitted with three components. These components are the O1s arising from P=O and P-O-P bonds within the SHMP chain (531.3 eV, FWHM 1.45) in good agreement with literature (Cui et al. (2016)) and two Na Auger peaks at 533.0 eV and 536.3 eV.

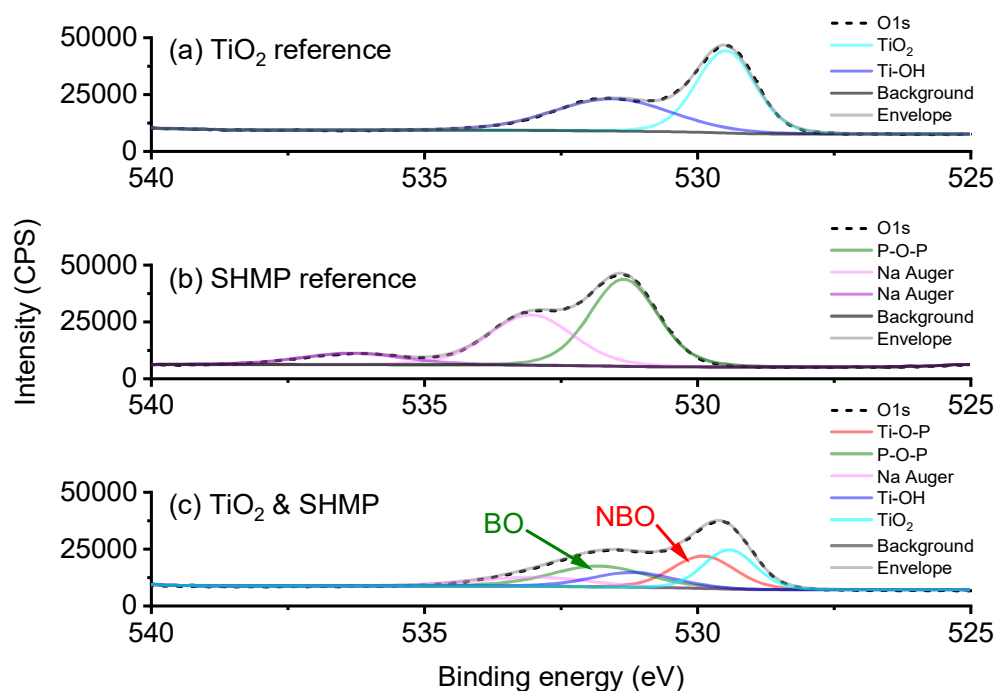


Figure 6-9: O1s peak with fitted components for (a) Al doped TiO₂ (unmilled), (b) SHMP and (c) Al doped TiO₂ unmilled with adsorbed SHMP.

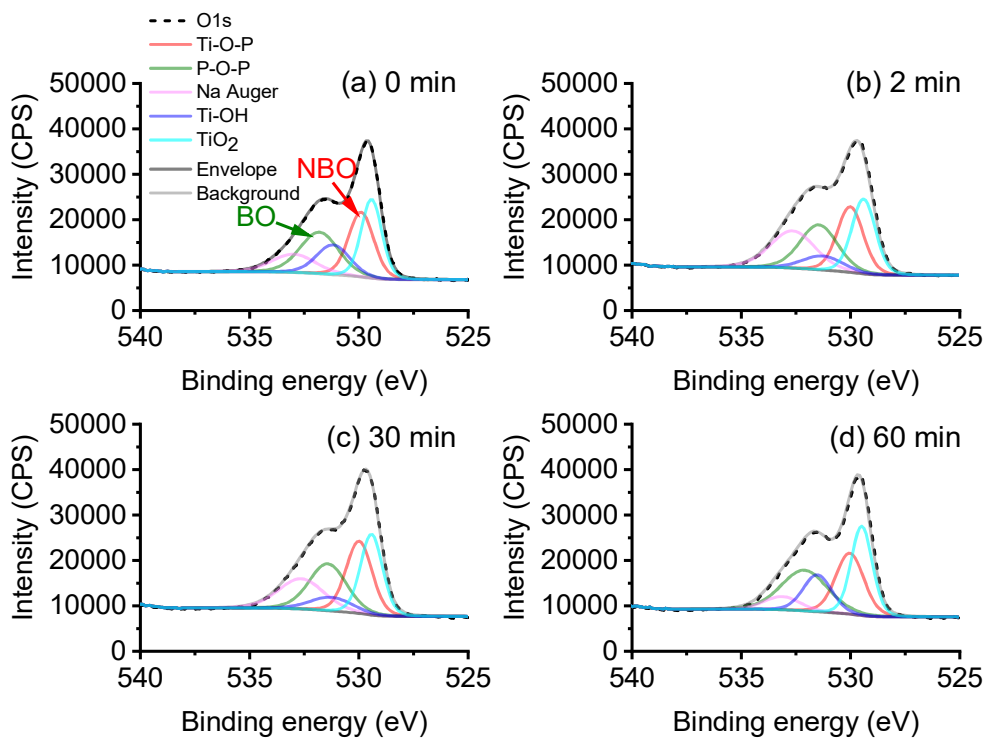


Figure 6-10: O1s peak with fitted components bridging oxygen (BO) and non-bridging oxygen (NBO) for Al doped TiO₂ with adsorbed SHMP after milling for (a) 0 min, (b) 2 min, (c) 30 min and (d) 60 min.

XPS analysis of phosphate glasses was first reported in the 1970s, several studies state that the O 1s signal can be fitted to two different components (Crobu et al. (2012)). The first component which resides at a higher binding energy consists of bridging P-O-P oxygen atoms, often denoted as BO (bridging oxygen). The second component is a mixture of terminal oxygen atoms (P = O and P-O-M) often called non-bridging oxygen (NBO) which is found at a lower binding energy (Crobu et al. (2012), Brow (2000), Crobu et al. (2010)). The latter (NBO peak) can be fitted to a single distribution, since the chemical shift between the P = O and P-O-M signals is small (Crobu et al. (2012)).

Table 6-7: O1s components for the bridging oxygen (BO) (P-O-P bonds) and the non-bridging oxygen (NBO) (Ti-O-P and P=O bonds) as a function of milling time. Shown is the BO and NBO O1s peak position (eV), the difference between these peaks is shown as $\Delta E_{(BO-NBO)}$ and the intensity ratio of BO/NBO.

Milling time (min)	BO O1s (eV)	NBO O1s (eV)	ΔE (eV)	FWHM BO O1s	FWHM NBO O1s	Intensity ratio O1s BO/NBO (CPS)
0*	531.66	530.07	1.59	1.58	1.08	1.13
0	531.79	529.88	1.91	2.07	1.36	0.80
2	531.40	529.97	1.43	2.03	1.41	0.82
30	531.41	529.97	1.44	2.02	1.40	0.79
60	532.07	529.99	2.08	2.50	1.52	0.83

However, for the samples analysed herein the O1s peak has been fitted to five components (Figure 6-10 (c)) consisting of Na Auger peak (due to the presence of Na in SHMP), NBO peak and BO peak. It is assumed that although the P-O-M peak would consist of M = Ti and Al in varying amounts, the shift in the signal is expected to be small and thus has been neglected. Also present in the sample will be TiO₂, (previous studies have fitted the O1s peak with BO, NBO and metal oxide peak (Crobu et al. (2010)) and TiOH from unbound SHMP sites, these have been fitted using the components which were found in the reference spectrum of Al doped TiO₂. Previous literature has shown that it is possible to distinguish polyphosphate chain length in XPS by calculating the ratio of the BO and NBO peaks used for fitting the O1s peak (Crobu et al. (2012), Brow (2000), Crobu et al. (2010)). Thus, the intensity ratio between BO and NBO was calculated for

Al doped TiO₂ with adsorbed SHMP for different milling times and the values can be found in Table 6-7.

In the present work, the O1s signal NBO fitted component was found to vary between milled samples from 529.9- 530.0 eV and the BO component was 531.4-532.1 eV. The BO component found in this work agrees well with the binding energy of SHMP adsorption onto kaolinite (Zhang et al. (2019)). To gain an insight into the influence of milling time on the position of the BO peak, the distance between the NBO and BO was calculated (ΔE). This value varied for the milled samples between 1.4-2.1 eV with no clear trend with respect to milling time. Previous work by Crobu et al. (2012), has shown that the ZnO content influenced the BO peak for different polyphosphate chain lengths, the value of zinc pyrophosphate was 1.43 eV and for zinc metaphosphate 1.67 eV.

The intensity ratio BO/NBO calculated in this work is unaffected by milling time. Despite other studies using this as an indicator of chain length, it has not been a useful tool for this study to probe hydrolysis. This could be due to the complexity of the system studied here compared to the relatively pure model system studied by Crobu et al. (2012). Quantification of the BO/NBO ratio can also be affected by the presence of contaminants (Crobu et al. (2012)). Contamination was previously studied for the Al doped TiO₂ system, where a variety of elements on the particles surface were detected by energy dispersive X-ray spectroscopy, as previously discussed in Chapter 5. Nonetheless, a significant increase in the BO FWHM is observed for the 60 minute milled sample, suggesting that more chemical environments are present. This is consistent with the theory that extended milling times induces hydrolysis and results in the removal of a proportion of the polyphosphate after washing.

A few studies, (Sherwood (2002), Gaskell et al. (2004)), have shown that the valence band region in XPS can be used to indicate different phosphate compounds and their oxides, compared to the information that can be identified by the core levels. The valence band could not be utilised in these studies due to the low resolution of the survey scan. To support the hypothesis that hydrolysis of SHMP occurs with increased milling times, the valence band should be investigated in future work and the adsorption of smaller phosphate chains to Al doped TiO₂ (with and without milling). The XPS regions for P_{2p} and O_{1s} should be investigated for these other systems, to observe if any changes occur for the BO/NBO ratio or binding energy of the BO and NBO components.

6.3.5 Al doped TiO₂ polyphosphate degradation after exposure to Ca²⁺ and heat treatment - probed by XPS

Since industrial milling waters usually contain some degree of soluble salts, for example Ca²⁺, and milling can cause an increase in temperature to a few tens of °C (Andreola et al. (2006)), the rate of hydrolysis of SHMP and impact this may have on the dispersion properties of the pigment could be significant. Therefore, CaCl₂ has been added to ultrapure water to simulate these soluble ions and SHMP was adsorbed onto Al doped TiO₂ at room temperature and 100°C.

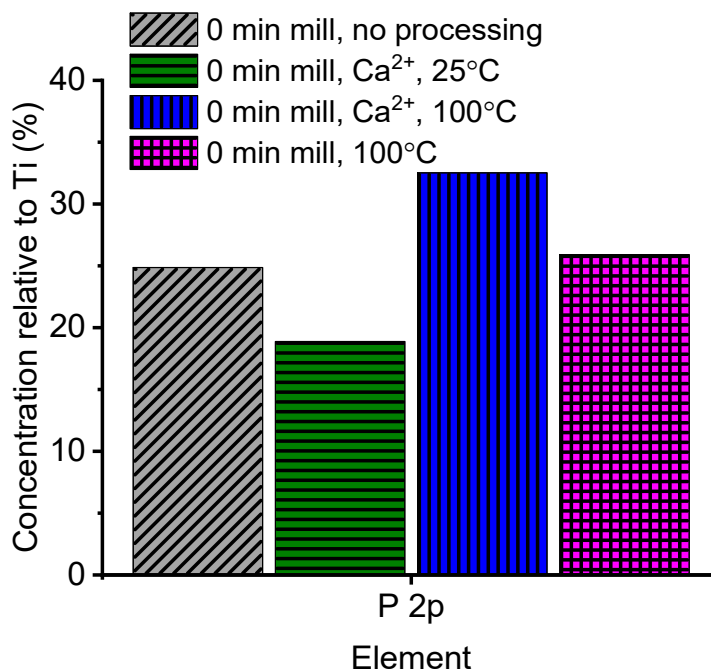


Figure 6-11: Elemental quantification from XPS data, shown as a relative concentration to Ti (%) for 0 min milled Al doped TiO₂ with adsorbed SHMP (grey) which has been subjected to different processing conditions after SHMP adsorption, Ca²⁺ at room temperature (green), Ca²⁺ at 100°C (blue) and 100°C (pink).

Figure 6-11 shows the relative quantities of P element found from analysis of the P_{2p} band in the XPS spectra, after the TiO₂ was treated with Ca²⁺ and/or elevated temperature. It is important to note for these experiments the influence of milling time was not investigated in-order to reduce any polyphosphate hydrolysis which can occur due to milling alone, thus the SHMP was adsorbed to unmilled Al doped TiO₂. Figure 6-11 shows the P_{2p} quantification for SHMP adsorbed to unmilled Al doped TiO₂ without any

processing. There is an increase in P_{2p} content for the adsorption of SHMP in the presence of Ca^{2+} at 100°C, however, at room temperature there is an apparent decrease in P_{2p} concentration, suggesting less SHMP adsorption onto the particle surface. It was thought that the increase in SHMP adsorption was due to the higher temperature alone, however, Figure 6-11 shows that at 100°C without Ca^{2+} no change in the P_{2p} content is detected.

To understand why there is a decrease in P_{2p} concentration with Ca^{2+} at room temperature and the contrary observed at higher temperature, several theories have been hypothesised:

- (i) Literature has previously stated that aqueous polyphosphates are susceptible to hydrolysis in the presence of Ca^{2+} ions (Andreola et al. (2006), Thilo (1965), Rulliere et al. (2012)). Hydrolysis of SHMP could result in lower concentrations adsorbed onto the particle surface (at least at room temperature). It might be that hydrolysed SHMP can adsorb back onto the particle surface leading to an increase in the phosphorus content and this may be a time/temperature driven event.
- (ii) Temperature alone at least for short experimental times <1 hour does not induce extensive hydrolysis of SHMP on the particle surface, if any. Andreola et al. (2006) adsorbed SHMP onto kaolinite and report that the apparent viscosity and yield stress increases with ageing and was more pronounced at 60°C. They suggest this could be due to a change in the adsorption of SHMP onto the particle surface, however a decrease in the adsorption ability of SHMP onto kaolinite at higher temperatures has been reported Castellini et al. (2005). Andreola et al. (2006) observed small changes in apparent viscosity of SHMP adsorbed onto kaolinite after 2 hours for distilled water at 30°C, distilled water at 60°C and Ca^{2+} at 30°C. After 5 hours the changes in apparent viscosity of the suspensions become more obvious and after 40 hours result in extremely different apparent viscosities.
- (iii) The Ca^{2+} can bind with at least two SHMP molecules and act as a bridge creating two SHMP layers at the particle surface. The formation of this phosphate “net” could be a time/temperature driven event. In this case an observed increase in SHMP content at the particle surface would be expected. Such networks have previously been postulated by Tan et al. (2016) for the adsorption of SHMP onto cement particles in the presence of Ca^{2+} and polycarboxylate superplasticizer.

- (iv) It is known that Ca^{2+} can form a strong soluble complex with SHMP (thermodynamic stability constant $K=10^{6.9}$) (Andreola et al. (2006), Kura et al. (1974), Farrokhpay et al. (2012)), if this occurs it may reduce the amount of SHMP available to be adsorbed onto the surface of TiO_2 . Therefore, it could be expected that the concentration of adsorbed SHMP decreases, hence a reduction in P_{2p} would be expected in the XPS. At higher temperature this thermodynamic stability is overcome and thus the same trends are not evident at higher temperature. However, this theory alone cannot account for the increase in P_{2p} concentration observed at 100°C with Ca^{2+} .
- (v) Alternatively, it could be that Ca^{2+} ions screen the negative charge of the polyphosphate causing a change in the packing density of SHMP at the particle surface, however this can only occur once the thermodynamic stability constant between SHMP and Ca^{2+} is overcome, otherwise complexation occurs first.

To investigate the above hypotheses further the changes the P_{2p} and Ca_{2p} bands were analysed, the peak position and FWHM are shown in Table 6-8. The average P_{2p} peak FWHM measured across all milled SHMP adsorbed TiO_2 samples, as previously conversed was 2.26 ± 0.28 . The P_{2p} values shown in Table 6-8 are all in agreement with this value. There is a slight shift in the peak position to lower binding energy when samples were heated to 100°C both with and without Ca^{2+} , which may be an indicator for hydrolysis and/or other structural changes of the polyphosphate backbone, however it is difficult to state for certain with such small changes occurring.

To exclude any degree of polyphosphate hydrolysis, the $\text{O}1s$ peak was fitted with an NBO and BO component as previously shown in Figure 6-10, these fits can be found in the Appendix 3: Supplementary information to Chapter 6 Figure A3-3. The intensity ratio between BO and NBO was calculated for Al doped TiO_2 with adsorbed SHMP, for the different processing conditions and the values can be found in Table 6-9. Table 6-9 shows a shift in the binding energy for all processed samples to lower binding energy for the BO peak and higher binding energy for the NBO peak, when compared to the unconditioned sample. However, these changes are small and likely within the error of the fitted components, thus it is reasonable to say that no significant changes are observed, and the values are comparable to those in Table 6-7. This suggests that hydrolysis does not occur for these samples under the time constraints used.

Table 6-8: XPS P2p and Ca2p bands peak position and FWHM shown for 0 min milled TiO₂ with different processing conditions. Also shown is the quantification (%) relative to the Ti element.

Sample conditioning	Peak	FWHM	Position (eV)	Quantification (%)
No processing	P _{2p}	2.21	134.46	24.9
[Ca ²⁺] at room temp.	P _{2p}	2.36	134.44	18.9
[Ca ²⁺] at 100°C	P _{2p}	2.34	134.20	32.5
100°C	P _{2p}	2.03	134.11	25.9
[Ca ²⁺] at room temp.	Ca _{2p}	0.42	348.16	0.5
[Ca ²⁺] at 100°C	Ca _{2p}	2.07	347.40	4.3

As previously conversed, Andreola et al. (2006), observed small changes in apparent viscosity of SHMP adsorbed onto kaolinite when influenced by Ca²⁺ and higher temperatures. However, the effects observed were minimal for suspensions investigated after 2 hours of treatment. Therefore, it is likely that some hydrolysis could be occurring for the samples studied here, although, it is likely to be minimal since the suspensions were only treated for 1 hour (Castellini et al. (2005)). Therefore, theories (i) and (ii) previously discussed can be excluded. Further experimentation is required to see the influence of time on the degree of hydrolysis and the effect this can have on dispersion performance, although it is important to note, that industrial milling times have been replicated in this study and typically do not exceed 60 minutes.

Table 6-8 shows almost a ten times increase in the concentration of the Ca_{2p} peak for Al doped TiO₂ treated with Ca²⁺ at 100°C, compared to at room temperature. Also observed, is a shift towards a lower binding energy for the Ca_{2p} peak from 348.16 eV to 347.40 eV, with an increase in suspension processing temperature. It is difficult to separate the metal carbonate peak in O1s spectra compared to the P-O and P=O bonds observed in SHMP due to the overlap of regions in the XPS spectra. The Ca_{2p} peak for different calcium compounds is as follows, CaCl₂ 348.0 eV (Demri and Muster (1995), Moulder and Chastain (1992)), CaO species 346.6 – 347.2 eV (Demri and Muster (1995), Moulder and Chastain (1992)) and for CaHPO₄ 347.0 – 347.4 eV (Demri and Muster (1995)). Based on the XPS binding energy for Ca²⁺ it appears the Ca_{2p} peak for TiO₂ treated at room temperature to be in better agreement with CaCl₂ reported binding energies (Demri and

Muster (1995), Moulder and Chastain (1992)), however, when treated at 100°C the Ca_{2p} binding energy is more similar to that found for calcium phosphate (Demri and Muster (1995)) complexes rather than CaO species (Demri and Muster (1995), Moulder and Chastain (1992)). Therefore, this suggests that the formation of an SHMP network linked by Ca-O bonds appears to be unlikely, despite Tan et al. (2016) previously reporting the formation of the SHMP network after adsorption at room temperature (although a different particle system was studied).

Table 6-9: O1s components for the bridging oxygen (BO) (P-O-P bonds) and the non-bridging oxygen (NBO) (Ti-O-P and P=O bonds) for 0 min milled TiO₂ with different processing conditions. Shown is the BO and NBO O1s peak position (eV) and the difference between these peaks is shown as $\Delta E_{(BO-NBO)}$ and the intensity ratio of BO/NBO.

Sample conditioning	BO O1s (eV)	NBO O1s (eV)	ΔE (eV)	FWHM BO O1s	FWHM NBO O1s	Intensity ratio BO/NBO (CPS)
No conditioning	531.79	529.88	1.91	2.07	1.36	0.80
[Ca ²⁺] at room temp.	531.51	530.02	1.49	2.02	1.41	0.85
[Ca ²⁺] at 100°C	531.64	530.03	1.61	2.03	1.37	0.88
100°C	531.63	530.01	1.62	1.65	1.44	0.90

Thus, it is proposed that the difference in phosphate adsorption under the influence of Ca²⁺ and different temperatures is due to a combination of events occurring within the system, which are discussed in points (iv) and (v). To further clarify, at room temperature SHMP forms a stable soluble complex with Ca²⁺ ions (Andreola et al. (2006), Kura et al. (1974), Farrokhpay et al. (2012)), resulting in a lower concentration of SHMP in the aqueous phase. This leads to a decrease in SHMP adsorption as the SHMP-Ca²⁺ complex is removed by centrifugation prior to XPS analysis, hence, a reduced concentration of phosphorus is observed by XPS. However, at 100°C, there is enough energy in the system to break the stable SHMP-Ca²⁺ complex, allowing Ca²⁺ ions to screen the negative charge on the SHMP backbone after chemisorption onto the Al doped TiO₂ surface. This most likely causes a change in the packing density of SHMP, allowing further adsorption, as this calcium phosphate interaction is likely to be very strong it is more stable to

centrifugation and hence an increase in calcium and phosphorus content is observed by XPS. It is worth mentioning that it is likely that this is an equilibrium process that is driven faster by the increase in temperature. However, further adsorption studies are required to validate this hypothesis, for example, with temperature and calcium ions varied alongside time. Further to these studies, the architectural characterisation of the SHMP-particle surface could be explored by atomic force microscopy (Biggs and Mulvaney (1996)).

6.3.6 Dispersion stability

Figure 6-12 (a) shows the zeta potential value as a function of pH after SHMP adsorption onto Al doped TiO₂. At all pH values studied, the pigment zeta potential in the presence of polyphosphate has become increasingly more negative, when compared to the surface charge of the bare pigment (Figure 6-2) (Taylor et al. (2001), Andreola et al. (2006)). For example, at pH 4 the pigment surface charge is approximately +30 mV and after SHMP adsorption at pH 4 is ~-50 mV, prior to centrifugal washing. After centrifugal washing, the zeta potential becomes less negative, suggesting the removal of polyphosphate. This is because at pH 4, SHMP is adsorbed by physisorption and chemisorption (Taylor et al. (2001)). The zeta potential remains negative after washing due to the remaining SHMP being chemisorbed through Ti-O-P bidentate complexation (Taylor et al. (2001)) and any remnants of electrostatically attracted SHMP. From the zeta potential measurements, it appears that TiO₂ dried powders can be dispersed back to their original state, as the surface charge is unchanged, across the entire pH range studied.

Chapter 5, showed that washing the industrially supplied SHMP coated pigment particles, caused a reduction in the zeta potential (i.e. it became more positive). The reduction in surface charge was only found for particles that were milled for long periods of time, for example, no change was seen for short milling times (1 minute) compared to longer milling times (16 and 32 minutes). As previously suggested, it was only possible to wash off SHMP from the longer milled samples due to the presence of extra physisorbed SHMP, as the samples had longer to reach equilibrium coverage in the mill. Therefore, a reduction in the surface charge upon washing observed in Figure 6-12 (a) only partially agrees with these previous findings. The most plausible explanation for the removal of polyphosphate from the unmilled sample, is due to the concentration of SHMP (in excess) and enough time was allowed for the samples to reach equilibrium coverage. Therefore, physisorbed SHMP can be removed from the 0 min sample.

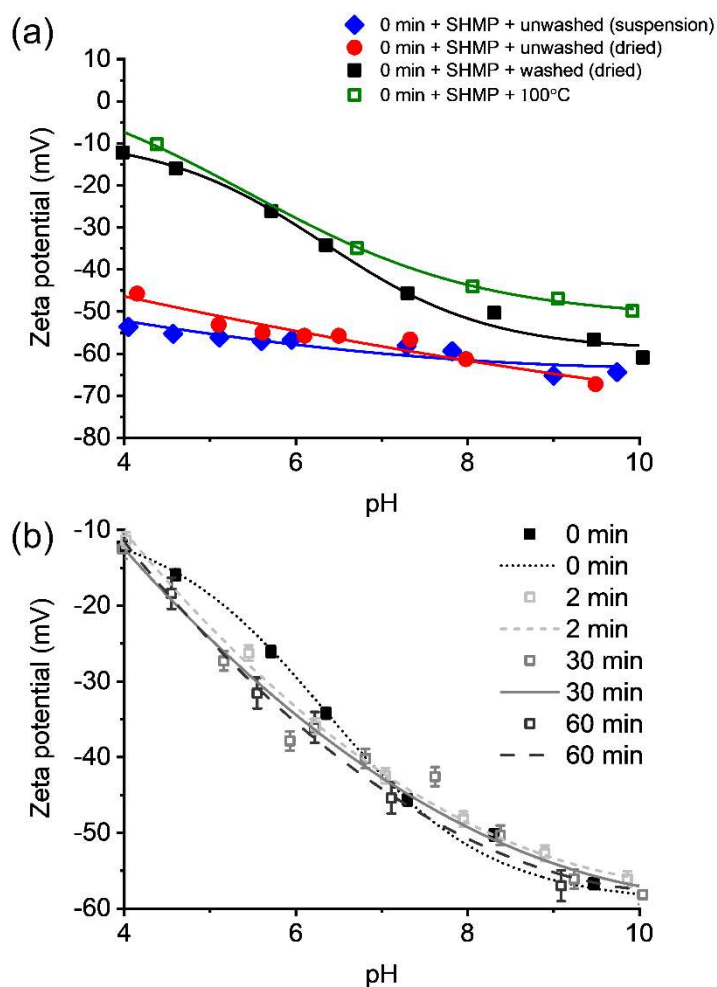


Figure 6-12: Surface charge of SHMP adsorbed onto Al doped TiO₂ under different processing conditions. (a) Surface charge with and without centrifugal washing and drying. (b) Surface charge as a function of milling time. The error bars show the largest standard error measured for each milled sample across the pH range studied.

Figure 6-12 (b) shows the zeta potential for washed and dried pigment after adsorption of SHMP, for different milling times. The isoelectric point (i.e.p) for milled samples was at \sim pH 3, this is in agreement for polyphosphate adsorption to Al doped TiO₂ surfaces reported by Taylor et al. (2001). There appears to be minimal changes in the zeta potential with milling time, which contrasts with the previous work discussed in Chapter 5, where the surface charge became more negative with an increase in milling time. Here, it is observed a shift towards lower zeta potential values with milling, but these are much less pronounced. The difference arises from the fact that only partial dispersant adsorption occurs in the industrial process, due to the fast dispersant mixing and pH increase used

to adsorb SHMP industrially, as discussed in detail in Appendix 3: Supplementary information to Chapter 6 Section A3.1. Therefore, as milling occurs with the industrial samples, more free dispersant exists in the supernatant, which can adsorb and alter the pH of the surface, thus much larger difference in surface charge can be observed.

The influence of grinding for dispersants adsorbed onto kaolin pigment has been studied by Zhao et al. (2013). They showed for SHMP pre-adsorption after grinding a decrease in the zeta potential, from -44 mV prior to grinding to -31 mV after grinding for 30 minutes, despite a reduction in the surface charge there was still a significant reduction in particle size recorded for grinding, this is likely because even after grinding the zeta potential remained highly negative. Closer inspection of the methods used by Zhao et al. (2013) do not show the grinding equipment used, for example milling rpm, further to this it appears dispersants were added to kaolin and heated to 98°C for 3 hours to reach an adsorption equilibrium. Samples were then dried and analysed or subjected to grinding prior to analysis. Therefore, it is unknown whether the decrease in the zeta potential is caused by (i) the effect of grinding or (ii) the effect of temperature or both combined, further to this there is no indication on the validity of results with the exclusion of experimental errors. Figure 6-12 (b) does not show such large differences in surface charge, despite XPS experiments indicating SHMP hydrolysis, this is most likely because enough SHMP remains on the surface regardless of hydrolysis due to the excess of the dispersant in the supernatant and long mixing times allowed for complete adsorption. Furthermore, surface charge measurements are an indirect technique to measure changes in dispersant density, thus to make such broad statements for such small changes in zeta potential would be naive.

Figure 6-13 shows particle size measurements for SHMP adsorbed onto TiO₂ with and without milling. For unmilled TiO₂ without SHMP a bimodal population of particles is present within the suspension. The adsorption of SHMP causes a shift in the population to a broad monomodal distribution. This is due to the highly negative charge of SHMP at pH 9 (-50 mV) causing particle electrostatic repulsion and also due to the chain length (n=6) allowing for some degree of steric stabilisation to occur (Taylor et al. (2001)). The influence of milling time on the particle size (with SHMP adsorbed) is shown in Figure 6-13. For all milled samples a reduction in particle size is observed, due to breakage of agglomerates towards the primary particle size. However, for samples milled for 30- and 60-minutes a small amount of particle aggregation is also observed with aggregates between 10 – 100 µm. This could be because longer milling times causes some degree of

hydrolysis of SHMP, as previously observed by XPS and potentially this may lead to the aggregation of a small number of particles due to a reduction in steric stabilisation.

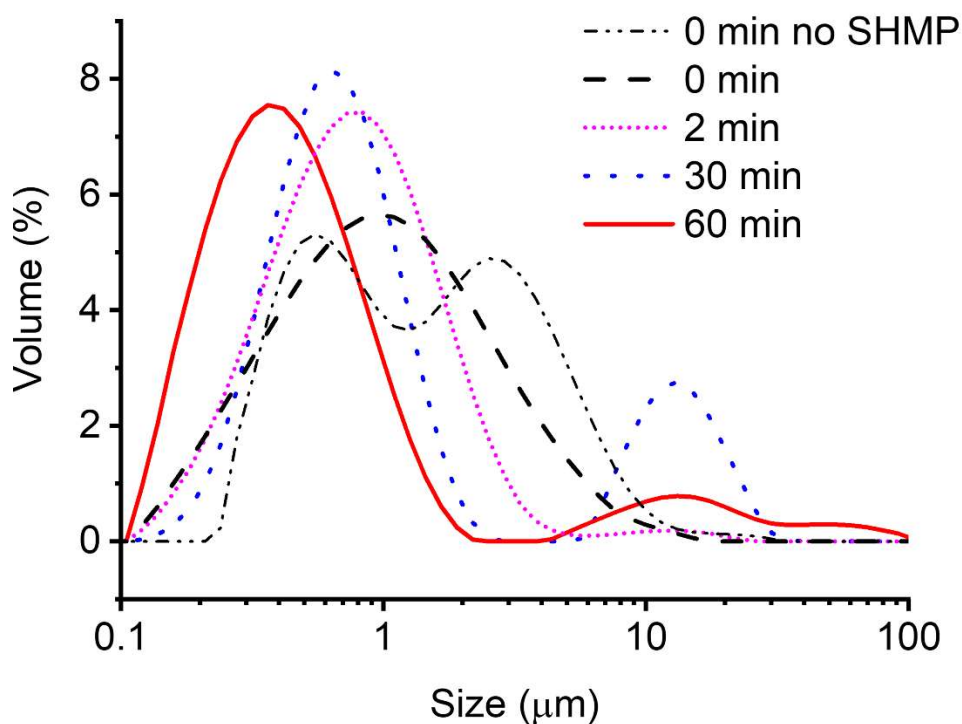


Figure 6-13: Size of Al doped TiO₂ with SHMP adsorbed as a function of milling time after dispersing at pH 9. Also shown is an unmilled sample without SHMP.

Chapter 5 showed that particle fines of ~10-20 nm were observed for samples milled for 32 minutes, these fines were either attached to primary particles or aggregated together. As previously conversed, the milling conditions used for this study were designed to mimic the industrial scale mill (from which samples were analysed in Chapter 5) and Table 6-3 shows the BET surface area measurements are in agreement for similar milling times. Thus, it would be reasonable to expect that for samples milled for 30 and 60 minutes to contain some fragmented particles. These fractured particles would have an extremely large surface area and tend to agglomerate. Consequently, it could be a combination of these small fines and SHMP hydrolysis leading to some degree of particle agglomeration, however, to confirm this further TEM studies would be required.

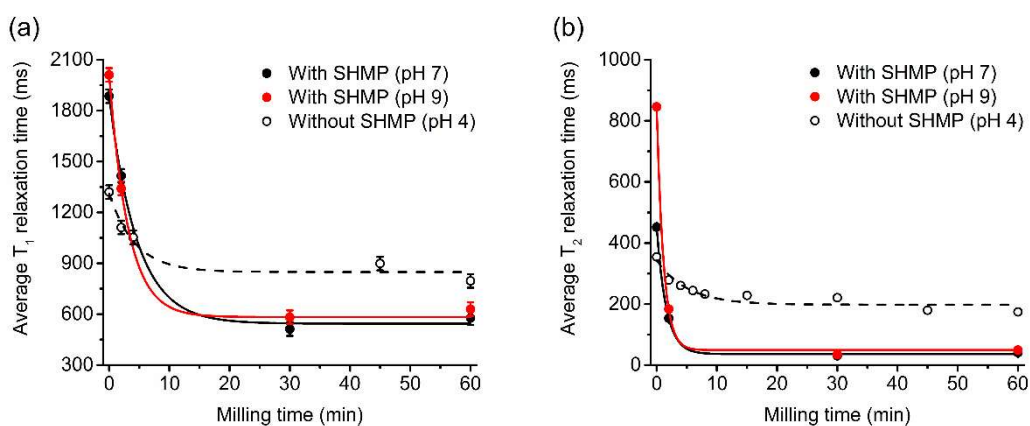


Figure 6-14: Relaxation NMR (a) T₁ and (b) T₂ for Al doped TiO₂ particles with SHMP and without under different pH conditions. The error bars show the maximum standard error recorded under the different pH conditions.

T₁ and T₂ relaxation measurements were performed for unmilled and milled Al doped TiO₂ both with and without SHMP adsorbed, shown in Figure 6-14. For short milling times, <5 minutes, the relaxation time is faster for the bare particle surface, this is due to aluminium present on the particle surface. Aluminium (²⁷Al) is a quadrupolar nucleus and can cause enhancements in relaxation rates of bound solvent molecules at the colloid surface (Totland et al. (2011), Cooper et al. (2013(a))). As previously conversed in section 6.2.3, the adsorption of SHMP onto unmilled TiO₂ (t = 0 minutes) resulted in longer relaxation times than the bare surface, as SHMP extends into the solvent and surface bound water molecules are blocked from the Al-rich TiO₂ surface. Totland et al. (2011), observed a decrease in the relaxation rate after adsorption of a surfactant to Kaolin clay, due to the surfactant blocking water access to the paramagnetic surface. Therefore, at low milling times in the presence of SHMP, it is not surprising that the adsorption of SHMP leads to an increase in the relaxation time, due to the blocking of Al sites at the particle surface. Furthermore, these findings agree with the previous Chapter (Chapter 5), which showed industrially adsorbed SHMP onto TiO₂ could be removed by centrifugal washing and caused an increase in the R_{sp} (relaxation rate enhancement), and this was attributed to the exposure of Al surface sites.

During pigment production TiO₂ is subjected to a range of chemical surface treatments, as well as, milling and drying operations, to give a range of products with particular properties for various end use applications (McNulty (2008)). Relaxation rates have previously been shown to vary with changes in pH by Van der Beek et al. (1991). They observed enhancements in the relaxation rate for silica in extreme pH conditions,

however, the relaxation rate remained constant over the pH range of 4-10. Furthermore, a few studies have previously shown, that the presence of electrolyte in particle systems measured by relaxation NMR, can lead to relaxation enhancements (Flood et al. (2006), Schwarz and Schönhoff (2002), Katika et al. (2014)). This phenomenon was further investigated in Chapter 4, where particles of different surface charge (calcite, TiO₂ and silica) were dispersed in high electrolyte conditions (1 M salt). It was found that particle coagulation had occurred (for systems not at their i.e.p), and thus a reduction in surface area and relaxation rates should be expected, however, relaxation rate enhancements were observed. Chapter 4 concluded that the increase in relaxation rates in high electrolyte conditions, was attributed to a counterion effect inducing a screening layer around both calcite and silica (although oppositely charged), which increased the NMR relaxation rate, as a result of the enhancement in the particle-solvent affinity.

Therefore, importantly for the application of relaxation NMR in an industrial manufacturing process, the influence of pH has been investigated and is shown in Figure 6-14. No change in the relaxation time was observed for SHMP adsorbed pigment particles from pH 7 to pH 9, this is because the surface charge remains negative around -45 mV to -60 mV (Figure 6-12 (b)) respective of pH, thus the particles have good charge stabilisation. Furthermore, the background electrolyte concentration is extremely low (1 mM NaCl) and thus enhancements are not observed, in agreement with previous literature (Flood et al. (2006)). However, at pH 4, the SHMP adsorbed TiO₂ particles were near their i.e.p. (Figure 6-12) which lead to particle aggregation and settling, ultimately resulting in misrepresentative relaxation rates.

Finally, Figure 6-14, for both T₁ and T₂ shows a cross-over in the relaxation times, where for longer milling times (> 5 minutes) the bare particle surface has a longer relaxation time than the SHMP adsorbed particle surface. It is not known exactly why this is the case and it is most likely due to a combination of factors. (i) Some of the changes may be from differences in surface area changes with milling times for particles with/without SHMP. With the decrease in relaxation time for SHMP being attributed to a greater surface area increase compared to without SHMP. (ii) XPS has shown a reduction in the SHMP coverage with an increase in milling time, it is thought this is due to polyphosphate degradation either leading to complete or partial removal of SHMP from the surface. Chapter 5, showed that for particles with adsorbed SHMP, washing led to an enhancement in the relaxation rate. This was attributed to hydrolysed SHMP having a greater interaction with bound water and further still the removal of SHMP allowing Al

sites to become exposed, both causing relaxation rate enhancement. The results in Figure 6-14 are consistent with these changes. The structure and/or density of SHMP at longer milling times clearly varies and this coupled with exposure of Al surface sites causes faster relaxation times. Polyphosphates of varying chain length should be adsorbed onto TiO₂ pigment particles and the influence of milling on relaxation time changes investigated. Correlation of these results with surface area measurements from BET may help to further decouple the results observed in Figure 6-14, which is important if the NMR technique is to be used as an online control tool.

6.4 Summary

Adsorption isotherms of SHMP onto Al doped TiO₂ reactor discharge at pH 4 in 1 mM NaCl were performed. The concentration of adsorbed SHMP plateaus post 600 ppm equilibrium concentration, thus indicative of the maximum adsorption of SHMP. Relaxation NMR was used to generate a pseudo-isotherm and the addition of SHMP caused a decrease in the specific relaxation rate enhancement, R_{2sp} compared to that of the pure particle surface. This was due to the blocking of the Al-rich TiO₂ surface by SHMP extending into the solvent, despite this a plateau in R_{2sp} still coincided with that of the ICP adsorption isotherm.

Relaxation NMR was used successfully to calculate the specific surface area of milled Al doped TiO₂ prior to SHMP adsorption and were in excellent agreement with BET surface area measurements. However, a calibration of the particle-solvent specific relaxation constant was first required due to the presence of aluminium at the particle surface, which was otherwise found to cause enhancements in the relaxation signal. Nonetheless, the usefulness of the technique for an online monitoring tool during milling has been clearly indicated.

A decrease in the P_{2p} concentration with increasing milling time was observed after XPS analysis. The XPS O_{1s} regions were fitted with five components to investigate changes in the polyphosphate chain length with milling. These components consisted of TiO₂, TiOH, P-O-P (P=O were treated alike to P-O-P due to the small shift in binding energy) and an Na Auger peak. No change in the BO/NBO ratio was found, despite broadening of the BO peak indicated by an increase in the FWHM suggesting some degree of hydrolysis for the 60 minute milled sample.

Changes in the zeta potential could not be resolved for the milled TiO₂ sample, even though a decrease in polyphosphate concentration was observed. This is since zeta potential measurements are only an average of the particle surface charges within the entire system and not necessarily sensitive to localised changes unless experienced by all particles. Despite no observable changes in the zeta potential, particle aggregation was still detected for samples milled for 30 and 60 minutes, where the concentration of surface adsorbed polyphosphate were previously found to decrease. This coupled with the XPS results suggests that extended milling times cause some degree of hydrolysis and/or removal of polyphosphate chains.

An attempt was made to replicate industrial milling waters by the addition of Ca²⁺ ions in the form of CaCl₂, additionally samples were also heated to 100°C to mimic bulk temperature increases that may be present within the mill. Two contradicting results were found; (i) Ca²⁺ at room temperature was found to cause a decrease in the polyphosphate concentration by XPS analysis. It was hypothesised this was due to the strong complexation formed by SHMP and Ca²⁺, resulting in lower concentrations of SHMP available for adsorption. (ii) addition of Ca²⁺ at 100°C was found to cause an increase in polyphosphate concentration from XPS analysis. It is thought that the increased temperature results in enough energy to break the strong SHMP Ca²⁺ complex. This then allows free Ca²⁺ to screen the negative polyphosphate backbone, which results in an increase in surface density of SHMP at the particle. Particle size measurements showed that when the surface SHMP concentration was lower, particle aggregation occurred and when SHMP concentration was higher, the particle size was reduced, in comparison to the un-treated SHMP adsorbed 0 min milled sample.

Further work is required to completely understand the changes reported herein, for example it is suggested that additional isotherms are obtained by using ICP, relaxation NMR and a quartz crystal microbalance, for the addition of Ca²⁺ with changes in adsorption temperature. Furthermore, the adsorption of smaller polyphosphates should be studied with milling and analysed by XPS.

Chapter 7 Conclusions and future perspectives

The aim of this thesis was to investigate the use of relaxation NMR to probe changes in the particle size of agglomerated pigment grade TiO_2 during milling and relate these results to ex-situ characterisation techniques. A further aim of this thesis was to understand if any there were any surface chemistry changes (e.g. aluminium or dispersant concentrations) that occurred when milling TiO_2 pigment and the influence this might have on NMR relaxation. The key findings are reported in this Chapter, alongside suggestions for further investigations to complement this work.

In Chapter 4, Ludox colloidal silica was used as a standard reference material for relaxation NMR measurements and a set of calibration measurements were performed at various particle concentrations. The solvent specific relaxation constant (K_a) was derived for the Ludox colloidal silica and was used to calculate the surface area of titanium dioxide, silica and calcite powders. The relaxation rate enhancement (R_{sp}) was calculated across a wide concentration range for all particle systems studied (up to 50 wt.% for calcite), even at high particle concentrations the spread of the relaxation data was small (with linear fits R^2 values close to 0.99). The main challenge encountered when dealing with the concentrated slurries was insuring that they were homogenous and furthermore the physical act of pipetting these slurries into the NMR tubes (5mm diameter), which becomes significantly more challenging at high particle loading.

Nonetheless, relaxation NMR was used to determine the surface area of two TiO_2 powders and the results correlated well with the BET surface area (TiO_2^a anatase type 263 m^2/g (BET) and 253 m^2/g (NMR), TiO_2^b 49 m^2/g (BET) and 47 m^2/g (NMR)). Furthermore, relaxation NMR was used to calculate the surface area of silica^b from the standard Ludox reference material. The silica^b surface area measurements correlated well with the calculated spherical surface area based on the average particle size from DLS and TEM showed the monodispersed spherical nature of these particles.

Although the use of relaxation NMR to calculate the particle surface area of TiO_2 and silica was demonstrated, there was some uncertainty in the measurement obtained for calcite. The surface area calculated for calcite by NMR was far larger than by BET, which the author proposes is most likely due to both better dispersion of nanocrystallites in the liquid state, partial solubility of calcite in water and the huge change in the surface chemistry of calcite compared to the silica standard reference material. Further, experimentation is required to demonstrate the use of relaxation NMR for carbonated

materials by using a standard reference material with more similar surface chemistry, for example, magnesium carbonate.

Chapter 4 also showed the effect that electrolytes can have on relaxation data, which ultimately lead to an overestimation of particle surface area when the particle conditions allowed for relaxation rate enhancement. The addition of 1 M KCl to TiO_2^a caused little changes in the particle size, with TiO_2^a remaining highly aggregated. Similarly, there were no obvious changes in the settling behaviour of TiO_2^a with electrolyte. Furthermore, the addition of electrolyte to TiO_2^a did not cause any significant changes in the average relaxation rate measured. It was concluded that due to the neutral particle charge during relaxation measurements, no significant counterion screening layer was formed, and hence no additional relaxation enhancement was observed.

In complete contrast, both calcite and silica^b, showed substantial enhancements in the R_{sp} in the presence of the KCl electrolyte. This was counterintuitive as particle size measurements and settling data showed the particles' were coagulated, which would lead to a reduction in surface area and therefore a reduction in R_{sp} would be expected. It was concluded that a counterion effect, inducing a screening layer around both calcite and silica (although oppositely charged), caused an increase the R_{sp} as a result of the enhancement in the particle-solvent affinity at the particle surface. Additionally, an increase in the magnitude of the R_{sp}/Ψ_p gradient for silica^b compared to calcite was noted. It was suggested this could be caused by the increased magnitude of the surface charge for silica^b, although further work is required for a more comprehensive understanding of this phenomena.

Importantly, the results reported in Chapter 4, highlight that while the use of solvent relaxation to study particle surface area offers faster experimental times and greater compatibility compared to conventional techniques, counterion effects make the interpretation of NMR relaxation rates significantly more complicated than theory suggests. This could be problematic for the TiO_2 production process, which will contain some degree of soluble salts that will interact with the bound water layer when TiO_2 is milled (e.g. not at its i.e.p). While similar relative enhancements for particle-salt dispersions have been reported in the literature (for low electrolyte concentrations) and such specific ion effect have been proposed (Flood et al. (2006), Schwarz and Schönhoff (2002)), the influence of particle zeta potential charge and magnitude, and related influence of agglomeration have not previously been observed. Furthermore, it is possible

to account for such enhancements if the particle surface area is not simultaneously changing. Further experimentation is required to understand the influence of particle surface charge, electrolyte concentration, and salt valency on relaxation NMR results, particularly at high salt concentrations where coagulation is induced.

Chapter 5, characterised titania pigment particles (supplied by Venator) taken from the industrial milling process at various residence times. These samples were heavily agglomerated aluminium doped TiO_2 particles, which also contained a polyphosphate dispersant, called sodium hexametaphosphate (SHMP). The effect of milling time on the interaction between aluminium doped titania pigment particles and polyphosphate (SHMP) dispersant was studied using multiple ex-situ characterisation techniques.

DLS measurements probed two relaxation modes: (i) a mode characterised by a fast relaxation time, assigned to primary TiO_2 particles, and (ii) a mode characterised by longer relaxation times, subject to inter-measurement variability, and assigned to the aggregates present in the suspensions. The hydrodynamic diameter associated with the primary TiO_2 particles did not change upon milling time and there was excellent agreement with the TEM primary particle size. The DLS showed a reduction in the second mode with milling, suggesting that the proportion of aggregates in the suspensions decreased with increased milling time.

TEM highlighted the presence of ~ 20 nm titania fractured fines in samples milled for 32 minutes, these fines were not observed in the pigment samples milled for 1 minute. It is not known at what residence times fractured particles are formed, since only the two milling extreme times were analysed by TEM, and a further microscopy investigation is required to pin point this exact time. However, in contrast to the literature, particle fines were found to have d-spacing correlating to the rutile crystal structure and thus milling did not induce changes in crystal structure.

The pigment TiO_2 samples were found to have an isoelectric point (iep) in the range of pH 3 to 4.5, with an increase in milling time leading to a lower pH_{iep} . The presence of SHMP was confirmed through elemental analysis using energy-dispersive X-ray spectroscopy and X-ray fluorescence (XRF). The XRF data showed that the relative phosphorus content had increased for the 16 and 32 minute milled samples, to levels nearly twice that of the 1 minute milled sample. It was proposed that longer milling times lead to the presence of more SHMP on the alumina-doped pigment surface, potentially due to the breakage of agglomerates/aggregates and continued adsorption of SHMP as

the particles are milled for a longer time, (i.e. insufficient time has been allowed during the industrial process for complete SHMP surface coverage of TiO_2 to occur). After centrifugal washing a decrease in the phosphate concentration was observed by XRF and the zeta potential became more positively charged. Centrifugal washing showed that the polyphosphate could be removed from the particle surface, however, this was only applicable to the longer milled samples (16 and 32 minutes). Thus, it was proposed that additionally adsorbed SHMP for the longer milled samples was weakly bound as it could be removed indicating physisorption.

Due to the presence of aluminium dopant on the surface of the pigment particles, the relaxation constant K_a derived in Chapter 4 for TiO_2 (which previously showed excellent agreement for the NMR surface area with BET) could not be used. This was due to aluminium causing a relaxation rate enhancement at the particle surface. Instead, K_a was derived using the 8 minute milled sample and correlating the NMR data to the BET surface area. This mid-ranged milling time was used to calibrate the sample, due to the observed plateau in the zeta potential, which was thought to limit any contributions from dispersant chemistry changes.

Despite this calibration, the relaxation NMR data as a function of milling time showed a linear increase, and no plateau was detected which contrasted to the BET results. Furthermore, the NMR and BET results did not agree at longer milling times. This was due to either the increase in surface area from fractured fines in samples milled for longer times, or due to the increase in SHMP concentration and/or dispersant restructuring at the surface of titana pigment particles; both leading to an overestimation of bulk surface area. Literature has previously shown that aqueous polyphosphates are not stable under acidic pH and high temperature, therefore there was a concern over potential hydrolysis occurring during milling. It could be that hydrolysed SHMP has a greater influence on the NMR relaxation rate of bound water molecules leading to an enhancement in R_{sp} , which is difficult to state for certain without further surface/structural analysis.

After centrifugal washing there was an increase in the relative relaxation enhancement for the samples which were milled for longer, this coincided with the XRF results which demonstrated polyphosphate removal. This increase could be due to either dispersant restructuring at the surface of titana pigment particles or the exposure of aluminium sites at the particle surface leading to NMR enhancements.

Chapter 6 used XPS to investigate the degradation of SHMP adsorbed onto aluminium doped TiO₂ pigment with milling. Firstly, dispersant (SHMP) free unmilled pigment was obtained from Venator and high shear milled at lab scale. Relaxation NMR was used to calculate the surface area of the aggregates with milling time and the results were correlated to BET and size measurements. After calibrating K_a to consider the aluminium rich surface there was excellent agreement with the BET results, however prior to this the NMR surface area was higher. Furthermore, the difference between the surface area measurements (NMR – BET) rapidly increased in the first 10 minutes of milling, this coincided with surface aluminium concentrations increasing which was reported by Austin (2019). Thus, the importance of averaging the K_a to obtain a representative value with changes in milling time was highlighted and the usefulness of the technique for an online monitoring tool during milling has been clearly indicated.

Relaxation NMR was used to generate a pseudo-isotherm of SHMP adsorbed onto Al doped TiO₂. The addition of SHMP caused a decrease in the specific relaxation rate enhancement, R_{2sp} compared to that of the pure particle surface. This was due to the blocking of the Al-rich TiO₂ surface by SHMP extending into the solvent, despite this a plateau in R_{2sp} still coincided with that of the ICP adsorption isotherm. These results show a decrease in R_{2sp} with increased surface coverage are in agreement with the conclusions from Chapter 5, which showed an increase in relaxation rate as polyphosphate was removed from the particle surface.

A decrease in the P_{2p} concentration with increasing milling time was observed after XPS analysis. Interestingly, this differs to the results in Chapter 5, which showed an increase in polyphosphate with increased milling time. The reason for this difference, is due to the time allowed for adsorption to occur (complete surface coverage) for the lab milled samples, compared to the commercially obtained milled samples. Despite no observable changes in the zeta potential, particle aggregation was still detected for samples milled for 30 and 60 minutes, where the concentration of surface adsorbed polyphosphate were previously found to decrease. This coupled with the XPS results suggests that extended milling times cause some degree of hydrolysis and/or removal of polyphosphate chains.

Industrial milling waters were replicated by the addition of Ca²⁺ ions in the form of CaCl₂, additionally samples were also heated to 100°C to mimic bulk temperature increases that may be present within the mill. Two contradicting results were found; (i) Ca²⁺ at room temperature was found to cause a decrease in the polyphosphate by XPS analysis, it was

hypothesised this was due to the strong complexation formed by SHMP and Ca^{2+} resulting in lower concentrations of SHMP available for adsorption. (ii) addition of Ca^{2+} at 100°C was found to cause an increase in polyphosphate concentration from XPS analysis, it is thought that the increased temperature results in enough energy to break the strong SHMP Ca^{2+} complex. This then allows free Ca^{2+} to screen the negative polyphosphate backbone, which results in an increase in surface density of SHMP at the particle. Further work is required to completely understand these XPS results, for example it is suggested that additional isotherms are obtained by using ICP, relaxation NMR and a quartz crystal microbalance, for the addition of Ca^{2+} with changes in adsorption temperature. Furthermore, the adsorption of smaller polyphosphates should be studied with milling and analysed by XPS and relaxation NMR. This would allow a catalogue of relaxation constants (K_a) to be determined, ultimately leading to a more accurate understanding of particle size when milling.

Overall, this thesis demonstrates the difficulties of characterising shear-dependent milled aggregates and the need for multiple characterisation techniques. However, the potential of NMR relaxometry as an online-process control tool for not only detecting changes in surface area but also surface chemistry has been shown. Ongoing research is required as discussed within this chapter to understand the complex surface chemistry changes observed for the samples studied in this thesis. Ultimately, still required is an industrial testing phase at Venator on specific commercial operations, to allow analysis and potential feedback control of the particle formation reactor and connected milling units. Furthermore, this novel NMR sensor could be compared to other techniques being developed for the at-line monitoring of particle size either commercially or at Leeds; such as acoustic backscatter/transmission and focused beam reflectance measurement (FBRM) systems.

References

2002. Whiter than white: options for the compounder. *Plastics, Additives and Compounding*, 4, 18-21. [https://doi.org/10.1016/S1464-391X\(02\)80150-7](https://doi.org/10.1016/S1464-391X(02)80150-7).
2014. Global and China Titanium Dioxide Industry Report, 2014-2017. Research In China. <https://www.prnewswire.com/news-releases/global-and-china-titanium-dioxide-industry-report-2014-2017-300077141.html> [Accessed 10.10.2019]
- AGNIHOTRI, R., MAHULI, S. K., CHAUK, S. S. & FAN, L.-S. 1999. Influence of Surface Modifiers on the Structure of Precipitated Calcium Carbonate. *Industrial & Engineering Chemistry Research*, 38, 2283-2291.
- AKHTAR, K., PRATSINIS, S., & MASTRANGELO, S. 1994. Vapor phase synthesis of Al-doped titania powders. *Journal of Materials Research*, 5, 1241-1249.
- AKHTAR, M. K., XIONG, Y. & PRATSINIS, S. E. 1991. Vapor synthesis of titania powder by titanium tetrachloride oxidation. *AIChE Journal*, 37, 1561-1570.
- ALDON, L., KUBIAK, P., PICARD, A., JUMAS, J. C. & OLIVIER-FOURCADE, J. 2006. Size Particle Effects on Lithium Insertion into Sn-doped TiO₂ Anatase. *Chemistry of Materials*, 18, 1401-1406.
- ALLEN, N. S., EDGE, M., ORTEGA, A., SANDOVAL, G., LIAUW, C. M., VERRAN, J., STRATTON, J. & MCINTYRE, R. B. 2004. Degradation and stabilisation of polymers and coatings: nano versus pigmentary titania particles. *Polymer Degradation and Stability*, 85, 927-946.
- ALLOUNI, Z. E., CIMPAN, M. R., HØL, P. J., SKODVIN, T. & GJERDET, N. R. 2009. Agglomeration and sedimentation of TiO₂ nanoparticles in cell culture medium. *Colloids and Surfaces B: Biointerfaces*, 68, 83-87.
- ANDREOLA, F., CASTELLINI, E., FERREIRA, J. M. F., OLHERO, S. & ROMAGNOLI, M. 2006. Effect of sodium hexametaphosphate and ageing on the rheological behaviour of kaolin dispersions. *Applied Clay Science*, 31, 56-64.
- ANOARDO, E., GALLI, G. & FERRANTE, G. 2001. Fast-field-cycling NMR: Applications and instrumentation. *Applied Magnetic Resonance*, 20, 365-404.
- AUSTIN, D. 2019. Time and energy dependant surface properties of stirred wet milled alumina doped titanium dioxide. In preparation.
- AYLWARD, G. F., TRISTAN (2008). *SI Chemical Data Book* John Wiley & Sons Australia.
- BADAIRE, S., POULIN, P., MAUGEY, M. & ZAKRI, C. 2004. In Situ Measurements of Nanotube Dimensions in Suspensions by Depolarized Dynamic Light Scattering. *Langmuir*, 20, 10367-10370.
- BALÁŽ, P. 2008. High-Energy Milling. *Mechanochemistry in Nanoscience and Minerals Engineering*. Berlin, Heidelberg: Springer Berlin Heidelberg.
- BARBERON, F., KORB, J. P., PETIT, D., MORIN, V. & BERMEJO, E. 2003. What is the surface specific area of porous cement-based material? A nuclear magnetic relaxation dispersion approach. *Magnetic Resonance Imaging*, 21, 355-357.
- BARRÈRE, F., LEBUGLE, A., VAN BLITTERSWIJK, C. A., DE GROOT, K., LAYROLLE, P. & REY, C. 2003. Calcium phosphate interactions with titanium oxide and alumina substrates: an XPS study. *Journal of Materials Science: Materials in Medicine*, 14, 419-425.

- BECKER, M. & SCHWEDES, J. 1999. Comminution of ceramics in stirred media mills and wear of grinding beads. Extended version of the presentation at the 9th European Symposium on Comminution, September 8–10, 1998, Albi, France. *Powder Technology*, 105, 374-381.
- BÉGIN-COLIN, S., GIROT, T., LE CAËR, G. & MOCELLIN, A. 2000. Kinetics and Mechanisms of Phase Transformations Induced by Ball-Milling in Anatase TiO₂. *Journal of Solid State Chemistry*, 149, 41-48.
- BEHRA, J. S., MATTSSON, J., CAYRE, O. J., ROBLES, E. S. J., TANG, H. & HUNTER, T. N. 2019. Characterization of Sodium Carboxymethyl Cellulose Aqueous Solutions to Support Complex Product Formulation: A Rheology and Light Scattering Study. *ACS Applied Polymer Materials*, 1, 344-358.
- BEL FADHEL, H., FRANCES, C. & MAMOURIAN, A. 1999. Investigations on ultra-fine grinding of titanium dioxide in a stirred media mill. *Powder Technology*, 105, 362-373.
- BERNOTAT, S. & SCHÖNERT, K. 2000. Size Reduction. *Ullmann's Encyclopedia of Industrial Chemistry*.
- BERSTEIN, G. & G. N. R. 1965. Titanium dioxide pigments. Google Patents.
- BIGGS, S. & MULVANEY, P. 1996. Surfactant and Polymer Adsorption: Atomic Force Microscopy Measurements. *Surfactant Adsorption and Surface Solubilization*. American Chemical Society.
- BLÜMICH, B. & SINGH, K. 2018. Desktop NMR and Its Applications From Materials Science To Organic Chemistry. *Angewandte Chemie International Edition*, 57, 6996-7010.
- BOWEN, P. & CARRY, C. 2002. From powders to sintered pieces: forming, transformations and sintering of nanostructured ceramic oxides. *Powder Technology*, 128, 248-255.
- BRAUN, J. H., BAIDINS, A. & MARGANSKI, R. E. 1992. TiO₂ pigment technology: a review. *Progress in Organic Coatings*, 20, 105-138.
- BROW, R. K. 2000. Review: the structure of simple phosphate glasses. *Journal of Non-Crystalline Solids*, 263-264, 1-28.
- BUX, J., PEAKALL, J., BIGGS, S. & HUNTER, T. N. 2015. In situ characterisation of a concentrated colloidal titanium dioxide settling suspension and associated bed development: Application of an acoustic backscatter system. *Powder Technology*, 284, 530-540.
- CAPITANI, D., SOBOLEV, A. P., DI TULLIO, V., MANNINA, L. & PROIETTI, N. 2017. Portable NMR in food analysis. *Chemical and Biological Technologies in Agriculture*, 4, 17.
- CASTELLINI, E., BERTHOLD, C., MALFERRARI, D. & BERNINI, F. 2013. Sodium hexametaphosphate interaction with 2:1 clay minerals illite and montmorillonite. *Applied Clay Science*, 83-84, 162-170.
- CASTELLINI, E., LUSVARDI, G., MALAVASI, G. & MENABUE, L. 2005. Thermodynamic aspects of the adsorption of hexametaphosphate on kaolinite. *Journal of Colloid and Interface Science*, 292, 322-329.

- CATHERINE L. COOPER, T. C., JEROEN S. VAN DUIJNEVELDT, MARTIN MURRAY AND STUART W. PRESCOTT 2013. The use of solvent relaxation NMR to study colloidal suspensions. *Soft Matter*, 9, 7211.
- CATTOZ, B., COSGROVE, T., CROSSMAN, M. & PRESCOTT, S. W. 2012. Surfactant-Mediated Desorption of Polymer from the Nanoparticle Interface. *Langmuir*, 28, 2485-2492.
- CHARTIER, T., SOUCHARD, S., BAUMARD, J. F. & VESTEGHEM, H. 1996. Degradation of dispersant during milling. *Journal of the European Ceramic Society*, 16, 1283-1291.
- CHEESMAN, B. T., NEILSON, A. J. G., WILLOTT, J. D., WEBBER, G. B., EDMONDSON, S. & WANLESS, E. J. 2013. Effect of Colloidal Substrate Curvature on pH-Responsive Polyelectrolyte Brush Growth. *Langmuir*, 29, 6131-6140.
- CHEN, J. J., KONG, X., SUMIDA, K., MANUMPIL, M. A., LONG, J. R. & REIMER, J. A. 2013. Ex Situ NMR Relaxometry of Metal–Organic Frameworks for Rapid Surface-Area Screening. *Angewandte Chemie*, 125, 12265-12268.
- CHEN, J. J., MASON, J. A., BLOCH, E. D., GYGI, D., LONG, J. R. & REIMER, J. A. 2015. NMR relaxation and exchange in metal–organic frameworks for surface area screening. *Microporous and Mesoporous Materials*, 205, 65-69.
- CINI, N. & BALL, V. 2014. Polyphosphates as inorganic polyelectrolytes interacting with oppositely charged ions, polymers and deposited on surfaces: fundamentals and applications. *Advances in Colloid and Interface Science*, 209, 84-97.
- COLE, R. J. 1974. The Pigmentation of Paints. *Review of Progress in Coloration and Related Topics*, 5, 75-85.
- CONNOR, P. A. & MCQUILLAN, A. J. 1999. Phosphate Adsorption onto TiO₂ from Aqueous Solutions: An in Situ Internal Reflection Infrared Spectroscopic Study. *Langmuir*, 15, 2916-2921.
- CONTE, P. 2015. Effects of ions on water structure: a low-field ¹H T₁ NMR relaxometry approach. *Magnetic Resonance in Chemistry*, 53, 711-718.
- COOPER, C. L., COSGROVE, T., VAN DUIJNEVELDT, J. S., MURRAY, M. & PRESCOTT, S. W. 2012. Colloidal Particles in Competition for Stabilizer: A Solvent Relaxation NMR Study of Polymer Adsorption and Desorption. *Langmuir*, 28, 16588-16595.
- COOPER, C. L., COSGROVE, T., VAN DUIJNEVELDT, J. S., MURRAY, M. & PRESCOTT, S. W. 2013(a). The use of solvent relaxation NMR to study colloidal suspensions. *Soft Matter*, 9, 7211-7228.
- COOPER, C. L., COSGROVE, T., VAN DUIJNEVELDT, J. S., MURRAY, M. & PRESCOTT, S. W. 2013(b). Competition between Polymers for Adsorption on Silica: A Solvent Relaxation NMR and Small-Angle Neutron Scattering Study. *Langmuir*, 29, 12670-12678.
- CORPORATION, H. 2016. Annual report which provides a comprehensive overview of the company for the past year.
- COSGROVE, T., OBEY, T. M. & TAYLOR, M. 1992. Solvent relaxation NMR: bound fraction determination for sodium Poly(styrene sulphonate) at the solid/solution interface. *Colloids and Surfaces*, 64, 311-316.

- CROBU, M., ROSSI, A., MANGOLINI, F. & SPENCER, N. D. 2010. Tribochemistry of Bulk Zinc Metaphosphate Glasses. *Tribology Letters*, 39, 121-134.
- CROBU, M., ROSSI, A., MANGOLINI, F. & SPENCER, N. D. 2012. Chain-length-identification strategy in zinc polyphosphate glasses by means of XPS and ToF-SIMS. *Analytical and Bioanalytical Chemistry*, 403, 1415-1432.
- CROCE, P. S. & MOUSAVI, A. 2013. A sustainable sulfate process to produce TiO₂ pigments. *Environmental Chemistry Letters*, 11, 325-328.
- CUI, S., WAN, S., ZHU, Q., TIEU, A. K., ZHU, H., WANG, L. & COWIE, B. 2016. Tribochemical Behavior of Phosphate Compounds at an Elevated Temperature. *The Journal of Physical Chemistry C*, 120, 25742-25751.
- CURRIE, S., HOGGARD, N., CRAVEN, I. J., HADJIVASSILIOU, M. & WILKINSON, I. D. 2013. Understanding MRI: basic MR physics for physicians. *Postgraduate Medical Journal*, 89, 209.
- D. FAIRHURST, A. S. W. P. 2011. The use of nuclear magnetic resonance as an analytical tool in the characterisation of dispersion behaviour. *Spectroscopy Europe*, 23, 13-16.
- DAIGLE, H., THOMAS, B., ROWE, H. & NIETO, M. 2014. Nuclear magnetic resonance characterization of shallow marine sediments from the Nankai Trough, Integrated Ocean Drilling Program Expedition 333. *Journal of Geophysical Research: Solid Earth*, 119, 2631-2650.
- DANA, J. D. 1855. *Manual of Mineralogy*, Durrie & Peck.
- DAVIS, P. J., GALLEGOS, D. P. & SMITH, D. M. 1987. Rapid Surface Area Determination via NMR Spin-Lattice Relaxation Measurements. *Powder Technology*, 53, 39-47.
- DEMRI, B. & MUSTER, D. 1995. XPS study of some calcium compounds. *Journal of Materials Processing Technology*, 55, 311-314.
- DONG, X., SUN, Z., LIU, Y., JIANG, L. & ZHENG, S. 2018. Insights into effects and mechanism of pre-dispersant on surface morphologies of silica or alumina coated rutile TiO₂ particles. *Chemical Physics Letters*, 699, 55-63.
- DU, Y.-J., YANG, Y.-L., FAN, R.-D. & WANG, F. 2016. Effects of phosphate dispersants on the liquid limit, sediment volume and apparent viscosity of clayey soil/calcium-bentonite slurry wall backfills. *KSCCE Journal of Civil Engineering*, 20, 670-678.
- DUROUDIER, J.-P. 2016. 2 - Grinding Energy. In: DUROUDIER, J.-P. (ed.) *Size Reduction of Divided Solids*. Elsevier.
- EGERTON, T. A. & TOOLEY, I. R. 2014. Physical characterization of titanium dioxide nanoparticles. *International Journal of Cosmetic Science*, 36, 195-206.
- ERDEM, B., HUNSICKER, R. A., SIMMONS, G. W., SUDOL, E. D., DIMONIE, V. L. & EL-AASSER, M. S. 2001. XPS and FTIR Surface Characterization of TiO₂ Particles Used in Polymer Encapsulation. *Langmuir*, 17, 2664-2669.
- FAIRHURST, D., COSGROVE, T. & PRESCOTT, S. W. 2016. Relaxation NMR as a tool to study the dispersion and formulation behavior of nanostructured carbon materials. *Magnetic Resonance in Chemistry*, 54, 521-526.
- FAIRLEY, N., LTD, C. S. & STAFF, C. S. L. 2009. *CasaXPS Manual 2.3.15: Introduction to XPS and AES*, Casa Software, Limited.

- FARROKHPAY, S., MORRIS, G. E. & BRITCHER, L. G. 2012. Stability of sodium polyphosphate dispersants in mineral processing applications. *Minerals Engineering*, 39, 39-44.
- FARROKHPAY, S., MORRIS, G. E., FORNASIERO, D. & SELF, P. 2005. Influence of polymer functional group architecture on titania pigment dispersion. *Colloids and Surfaces A: Physicochemical and Engineering Aspects*, 253, 183-191.
- FARROKHPAY, S., MORRIS, G. E., FORNASIERO, D. & SELF, P. 2010. Stabilisation of titania pigment particles with anionic polymeric dispersants. *Powder Technology*, 202, 143-150.
- FAZIO, S., GUZMÁN, J., COLOMER, M. T., SALOMONI, A. & MORENO, R. 2008. Colloidal stability of nanosized titania aqueous suspensions. *Journal of the European Ceramic Society*, 28, 2171-2176.
- FEILER, A., JENKINS, P. & RALSTON, J. 2000. Metal oxide surfaces separated by aqueous solutions of linear polyphosphates: DLVO and non-DLVO interaction forces. *Physical Chemistry Chemical Physics*, 2, 5678-5683.
- FILIPPOU, D. & HUDON, G. 2009. Iron removal and recovery in the titanium dioxide feedstock and pigment industries. *JOM*, 61, 36.
- FLOOD, C., COSGROVE, T., ESPIDEL, Y., HOWELL, I. & REVELL, P. 2007a. Sodium Polyacrylate Adsorption onto Anionic and Cationic Silica in the Presence of Salts. *Langmuir*, 23, 6191-6197.
- FLOOD, C., COSGROVE, T., ESPIDEL, Y., HOWELL, I. & REVELL, P. 2008. Effects of Surfactants and Electrolytes on Adsorbed Layers and Particle Stability. *Langmuir*, 24, 7323-7328.
- FLOOD, C., COSGROVE, T., HOWELL, I. & REVELL, P. 2006. Effects of Electrolytes on Adsorbed Polymer Layers: Poly(ethylene oxide)–Silica System. *Langmuir*, 22, 6923-6930.
- FLOOD, C., COSGROVE, T., QIU, D., ESPIDEL, Y., HOWELL, I. & REVELL, P. 2007b. Influence of a Surfactant and Electrolytes on Adsorbed Polymer Layers. *Langmuir*, 23, 2408-2413.
- FROSCHL, T., HORMANN, U., KUBIAK, P., KUCEROVA, G., PFANZELT, M., WEISS, C. K., BEHM, R. J., HUSING, N., KAISER, U., LANDFESTER, K. & WOHLFAHRT-MEHRENS, M. 2012. High surface area crystalline titanium dioxide: potential and limits in electrochemical energy storage and catalysis. *Chemical Society Reviews*, 41, 5313-5360.
- GAJOVIC, A., FURIC, K. & MUSIC, S. Ball-Milling of TiO₂ and ZrO₂. *Rudjer Boskovic Institute, Bijenicka*, 54, 10000.
- GAJOVIĆ, A., STUBIČAR, M., IVANDA, M. & FURIĆ, K. 2001. Raman spectroscopy of ball-milled TiO₂. *Journal of Molecular Structure*, 563, 315-320.
- GALLEGOS, D. P., MUNN, K., SMITH, D. M. & STERMER, D. L. 1987. A NMR technique for the analysis of pore structure: Application to materials with well-defined pore structure. *Journal of Colloid and Interface Science*, 119, 127-140.
- GALLEGOS, D. P., SMITH, D. M. & BRINKER, C. J. 1988. An NMR technique for the analysis of pore structure: Application to mesopores and micropores. *Journal of Colloid and Interface Science*, 124, 186-198.

- GAO, Z., WASYLISHEN, R. E. & KWAK, J. C. T. 1990. NMR studies in surfactant and polymer-surfactant systems: Micelle formation of sodium ω -phenyldecanoate and interaction with poly(ethylene oxide). *Journal of Colloid and Interface Science*, 137, 137-146.
- GARDY, J., HASSANPOUR, A., LAI, X. & AHMED, M. H. 2016. Synthesis of Ti(SO₄)O solid acid nano-catalyst and its application for biodiesel production from used cooking oil. *Applied Catalysis A: General*, 527, 81-95.
- GASKELL, K. J., SMITH, M. M. & SHERWOOD, P. M. A. 2004. Valence band x-ray photoelectron spectroscopic studies of phosphorus oxides and phosphates. *Journal of Vacuum Science & Technology A*, 22, 1331-1336.
- GESENHUES, U. 1999. Substructure of titanium dioxide agglomerates from dry ball-milling experiments. *Journal of Nanoparticle Research*, 1, 223-234.
- GLAVES, C. L., DAVIS, P. J. & SMITH, D. M. 1988. Surface area determination via NMR: Fluid and frequency effects. *Powder Technology*, 54, 261-269.
- GORRASI, G. & SORRENTINO, A. 2015. Mechanical milling as a technology to produce structural and functional bio-nanocomposites. *Green Chemistry*, 17, 2610-2625.
- GRUBB, G. F. & BAKSHI, B. R. 2011. Life Cycle of Titanium Dioxide Nanoparticle Production. *Journal of Industrial Ecology*, 15, 81-95.
- GRUNEWALD, E. & KNIGHT, R. 2009. A laboratory study of NMR relaxation times and pore coupling in heterogeneous media. *Geophysics*, 74, E215-E221.
- GUSTAFSSON, J., MIKKOLA, P., JOKINEN, M. & ROSENHOLM, J. B. 2000. The influence of pH and NaCl on the zeta potential and rheology of anatase dispersions. *Colloids and Surfaces A: Physicochemical and Engineering Aspects*, 175, 349-359.
- HAN, Y., LIU, W., ZHOU, J. & CHEN, J. 2016. Interactions between kaolinite AlOH surface and sodium hexametaphosphate. *Applied Surface Science*, 387, 759-765.
- HARTMANN, A. 1996. Process for the use of rutile promoter and control additives in the manufacture of titanium dioxide by the chloride process. Google Patents.
- HE, M., WANG, Y. & FORSSBERG, E. 2004. Slurry rheology in wet ultrafine grinding of industrial minerals: a review. *Powder Technology*, 147, 94-112.
- HEIMANN, R. B. 2010. *Classic and Advanced Ceramics: From Fundamentals to Applications*. Wiley.
- HERKIMER, S. M. 1998. A process for manufacturing titanium dioxide pigment having a hydrous oxide coating using a media mill. Google Patents.
- HINLEY, J. J. & PORTER, D. M. 1976. *Pigments*. Google Patents.
- HONDOW, N., BRYDSON, R., WANG, P., HOLTON, M. D., BROWN, M. R., REES, P., SUMMERS, H. D. & BROWN, A. 2012. Quantitative characterization of nanoparticle agglomeration within biological media. *Journal of Nanoparticle Research*, 14, 977.
- HORE, P. 2015. *Nuclear Magnetic Resonance*, Oxford University Press.
- HORN, M. S., C. F.; MEAGHER, E. P. 1972. Refinement of the structure of anatase at several temperatures Sample: T = 25 C. *Zeitschrift fur Kristallographie*, 273-281.

- HOSOKAWA, M., NOGI, K., NAITO, M. & YOKOYAMA, T. 2007. *Nanoparticle Technology Handbook*, Elsevier Science.
- HOTTA, Y., YILMAZ, H., SHIRAI, T., OHOTA, K., SATO, K. & WATARI, K. 2008. State of the Dispersant and Particle Surface During Wet-Jet Milling for Preparation of a Stable Slurry. *Journal of the American Ceramic Society*, 91, 1095-1101.
- INKYO, M., TAHARA, T., IWAKI, T., ISKANDAR, F., HOGAN, C. J. & OKUYAMA, K. 2006. Experimental investigation of nanoparticle dispersion by beads milling with centrifugal bead separation. *Journal of Colloid and Interface Science*, 304, 535-540.
- JALILI, M. M., DAVOUDI, K., ZAFARMAND SEDIGH, E. & FARROKHPAY, S. 2016. Surface treatment of TiO₂ nanoparticles to improve dispersion in non-polar solvents. *Advanced Powder Technology*, 27, 2168-2174.
- JAYASUNDARA, C. T., YANG, R. Y., YU, A. B. & RUBENSTEIN, J. 2010. Effects of disc rotation speed and media loading on particle flow and grinding performance in a horizontal stirred mill. *International Journal of Mineral Processing*, 96, 27-35.
- JEON, S., THAJUDEEN, T. & HOGAN, C. J. 2015. Evaluation of nanoparticle aggregate morphology during wet milling. *Powder Technology*, 272, 75-84.
- JOHNSON, M., PEAKALL, J., FAIRWEATHER, M., BIGGS, S., HARBOTTLE, D. & HUNTER, T. N. 2016. Characterization of Multiple Hindered Settling Regimes in Aggregated Mineral Suspensions. *Industrial & Engineering Chemistry Research*, 55, 9983-9993.
- JORDAN, V., JAVORNIK, U., PLAVEC, J., PODGORNIK, A. & REČNIK, A. 2016. Self-assembly of multilevel branched rutile-type TiO₂ structures via oriented lateral and twin attachment. *Scientific Reports*, 6, 24216.
- KARAKAŞ, F. & ÇELİK, M. S. 2013. Mechanism of TiO₂ stabilization by low molecular weight NaPAA in reference to water-borne paint suspensions. *Colloids and Surfaces A: Physicochemical and Engineering Aspects*, 434, 185-193.
- KATIKA, K., ADASSI, M., ALAM, M. M. & FABRICIUS, I. L. 2014a. Changes in Specific Surface as observed by NMR, caused by saturation of Chalk with porewater bearing divalent Ions. *diffusion-fundamentals.org*, 22, 1-14.
- KIRTIL, E., CIKRIKCI, S., MCCARTHY, M. J. & OZTOP, M. H. 2017. Recent advances in time domain NMR & MRI sensors and their food applications. *Current Opinion in Food Science*, 17, 9-15.
- KLEIN, S. M., CHOI, J. H., PINE, D. J. & LANGE, F. F. 2011. Synthesis of rutile titania powders: Agglomeration, dissolution, and reprecipitation phenomena. *Journal of Materials Research*, 18, 1457-1464.
- KLIMPEL, R. R. 1999. The selection of wet grinding chemical additives based on slurry rheology control. To the memory of R.R. Klimpel. The organizers of the 9th European Symposium on Comminution would like to pay tribute to R.R. Klimpel who tragically died on November 4, 1998.1. *Powder Technology*, 105, 430-435.
- KRUK, D., HERRMANN, A. & RÖSSLER, E. A. 2012. Field-cycling NMR relaxometry of viscous liquids and polymers. *Progress in Nuclear Magnetic Resonance Spectroscopy*, 63, 33-64.

- KRZYŻAK, A. T. & HABINA, I. 2016. Low field ^1H NMR characterization of mesoporous silica MCM-41 and SBA-15 filled with different amount of water. *Microporous and Mesoporous Materials*, 231, 230-239.
- KURA, G., OHASHI, S. & KURA, S. 1974. Complex formation of cyclic phosphate anions with bivalent cations. *Journal of Inorganic and Nuclear Chemistry*, 36, 1605-1609.
- KWADE, A. 1999. Wet comminution in stirred media mills — research and its practical application. *Powder Technology*, 105, 14-20.
- KWAN, C. C., MIO, H., QI CHEN, Y., LONG DING, Y., SAITO, F., PAPADOPOULOS, D. G., CRAIG BENTHAM, A. & GHADIRI, M. 2005. Analysis of the milling rate of pharmaceutical powders using the Distinct Element Method (DEM). *Chemical Engineering Science*, 60, 1441-1448.
- LANGMUIR, I. 1918. The adsorption of gases on plane surfaces of glass, mica and platinum. *Journal of the American Chemical Society*, 40, 1361-1403.
- LEONG, Y.-K. & ONG, B.-C. 2015. Polyelectrolyte-mediated interparticle forces in aqueous suspensions: Molecular structure and surface forces relationship. *Chemical Engineering Research and Design*, 101, 44-55.
- LEVITT, M. H. 2001. *Spin Dynamics: Basics of Nuclear Magnetic Resonance*, Wiley.
- LI, X., LI, Y., CHEN, C., ZHAO, D., WANG, X., ZHAO, L., SHI, H., MA, G. & SU, Z. 2015. Pore size analysis from low field NMR spin–spin relaxation measurements of porous microspheres. *Journal of Porous Materials*, 22, 11-20.
- LI, X., LIN, B., ZHAI, C., NI, G. & LI, Z. 2012. Relaxation study of cement based grouting material using nuclear magnetic resonance. *International Journal of Mining Science and Technology*, 22, 821-824.
- LINDBERG, C., AKROYD, J. & KRAFT, M. 2017. Developing breakage models relating morphological data to the milling behaviour of flame synthesised titania particles. *Chemical Engineering Science*, 166, 53-65.
- LING, N. N. A., HABER, A., MAY, E. F., FRIDJONSSON, E. O. & JOHNS, M. L. 2017. By-line NMR emulsion droplet sizing. *Chemical Engineering Science*, 160, 362-369.
- LOWELL, S. & SHIELDS, J. E. 1991. Adsorption isotherms. *Powder Surface Area and Porosity*. Dordrecht: Springer Netherlands.
- LOWELL, S., SHIELDS, J. E., THOMAS, M. A. & THOMMES, M. 2004. Other Surface Area Methods. *Characterization of Porous Solids and Powders: Surface Area, Pore Size and Density*. Dordrecht: Springer Netherlands.
- LURIE, D. J., AIME, S., BARONI, S., BOOTH, N. A., BROCHE, L. M., CHOI, C.-H., DAVIES, G. R., ISMAIL, S., Ó HÓGÁIN, D. & PINE, K. J. 2010. Fast field-cycling magnetic resonance imaging. *Comptes Rendus Physique*, 11, 136-148.
- LYNCH, A. J. & ROWLAND, C. A. 2005. *The History of Grinding*, Society for Mining, Metallurgy, and Exploration.
- M. GARDON & GUILMANY, J. M. 2014. Milestones in Functional Titanium Dioxide Thermal Spray Coatings: A Review. *Journal of Thermal Spray Technology*, 23, 577-595.

- MA, M. 2012. The Dispersive Effect of Sodium Hexametaphosphate on Kaolinite in Saline Water. *Clays and Clay Minerals*, 60, 405-410.
- MAGRITEK. 2019. *Benchtop NMR products* [Online]. Available: <http://www.magritek.com/products/spinsolve/> [Accessed 03/10/2019].
- MAJJANE, A., CHAHINE, A., ET-TABIROU, M., ECHCHAHED, B., DO, T.-O. & BREEN, P. M. 2014. X-ray photoelectron spectroscopy (XPS) and FTIR studies of vanadium barium phosphate glasses. *Materials Chemistry and Physics*, 143, 779-787.
- MANDZY, N., GRULKE, E. & DRUFFEL, T. 2005. Breakage of TiO₂ agglomerates in electrostatically stabilized aqueous dispersions. *Powder Technology*, 160, 121-126.
- MANUEL JESÚS GÁZQUEZ, J. P. B., RAFAEL GARCIA-TENORIO, FEDERICO VACA 2014. A Review of the Production Cycle of Titanium Dioxide Pigment. *Materials Sciences and Applications*, 5, 441-458.
- MCCULLOUGH, J. F., VAN WAZER, J. R. & GRIFFITH, E. J. 1956. Structure and Properties of the Condensed Phosphates. XI. Hydrolytic Degradation of Graham's Salt. *Journal of the American Chemical Society*, 78, 4528-4533.
- MCFADYEN, P. & FAIRHURST, D. 1993. High-resolution particle size analysis from nanometres to microns. *Clay Minerals*, 28, 531-537.
- MCNULTY, G. S. 2008. *Production of titanium dioxide*, International Atomic Energy Agency (IAEA), IAEA.
- MEHDILO, A. & IRANNAJAD, M. 2012. Iron Removing From Titanium Slag For Synthetic Rutile Production. *Physicochemical Problems of Mineral Processing* 42, 425-439.
- MESTL, G., HERZOG, B., SCHLOEGL, R. & KNOEZINGER, H. 1995. Mechanically Activated MoO₃. 1. Particle Size, Crystallinity, and Morphology. *Langmuir*, 11, 3027-3034.
- MEYER, K., KERN, S., ZIENTEK, N., GUTHAUSEN, G. & MAIWALD, M. 2016. Process control with compact NMR. *TrAC Trends in Analytical Chemistry*, 83, 39-52.
- MICHELMORE, A., GONG, W., JENKINS, P. & RALSTON, J. 2000. The interaction of linear polyphosphates with titanium dioxide surfaces. *Physical Chemistry Chemical Physics*, 2, 2985-2992.
- MIKULÁŠEK, P., WAKEMAN, R. J. & MARCHANT, J. Q. 1997. The influence of pH and temperature on the rheology and stability of aqueous titanium dioxide dispersions. *Chemical Engineering Journal*, 67, 97-102.
- MITCHELL, J., GLADDEN, L. F., CHANDRASEKERA, T. C. & FORDHAM, E. J. 2014. Low-field permanent magnets for industrial process and quality control. *Progress in Nuclear Magnetic Resonance Spectroscopy*, 76, 1-60.
- MORRIS, G. E., SKINNER, W. A., SELF, P. G. & SMART, R. S. C. 1999. Surface chemistry and rheological behaviour of titania pigment suspensions. *Colloids and Surfaces A: Physicochemical and Engineering Aspects*, 155, 27-41.
- MOULDER, J. F. & CHASTAIN, J. 1992. *Handbook of X-ray Photoelectron Spectroscopy: A Reference Book of Standard Spectra for Identification and Interpretation of XPS Data*, Physical Electronics Division, Perkin-Elmer Corporation.

- NAUMKIN, A. V., KRAUT-VASS, A., GAARENSTROOM, S. W. & POWELL, C. J. 2000. NIST X-ray Photoelectron Spectroscopy Database, NIST Standard Reference Database Number 20, . In: TECHNOLOGY, N. I. O. S. A. (ed.). Gaithersburg MD.
- NELSON, A., JACK, K. S., COSGROVE, T. & KOZAK, D. 2002. NMR Solvent Relaxation in Studies of Multicomponent Polymer Adsorption. *Langmuir*, 18, 2750-2755.
- NI, X. & LIU, Q. 2013. Adsorption behaviour of sodium hexametaphosphate on pyrochlore and calcite. *Canadian Metallurgical Quarterly*, 52, 473-478.
- NICHOLS, G., BYARD, S., BLOXHAM, M. J., BOTTERILL, J., DAWSON, N. J., DENNIS, A., DIART, V., NORTH, N. C. & SHERWOOD, J. D. 2002. A review of the terms agglomerate and aggregate with a recommendation for nomenclature used in powder and particle characterization. *Journal of Pharmaceutical Sciences*, 91, 2103-2109.
- NIE, X., ZHUO, S., MAENG, G. & SOHLBERG, K. 2009. Doping of Polymorphs for Altered Optical and Photocatalytic Properties. *International Journal of Photoenergy*, 2009, 22.
- NIKA, V. 2018. TiO₂ Applications as a Function of Controlled Surface Treatment.
- NOACK, F. 1986. NMR field-cycling spectroscopy: principles and applications. *Progress in Nuclear Magnetic Resonance Spectroscopy*, 18, 171-276.
- OHENOJA, K., ILLIKAINEN, M. & NIINIMÄKI, J. 2013. Effect of operational parameters and stress energies on the particle size distribution of TiO₂ pigment in stirred media milling. *Powder Technology*, 234, 91-96.
- OKRUSCH, M. S., U.; HOCK, R.; BRUMMER, A.; THEISINGER, H.; BAIER, M. 2003. Intergrown niobian rutile phases with Sc- and W-rich ferrocolumbite: an electron-microprobe and Rietveld study. *American Mineralogist*, 986-995.
- PATTERSON, A. L. 1939. The Scherrer Formula for X-Ray Particle Size Determination. *Physical Review*, 56, 978-982.
- PAUL, N., BIGGS, S., SHIELS, J., HAMMOND, R., EDMONDSON, M., MAXWELL, L., HARBOTTLE, D. & HUNTER, T. 2017. Influence of shape and surface charge on the sedimentation of spheroidal, cubic and rectangular cuboid particles.
- PETTERSSON, E., TOPGAARD, D., STILBS, P. & SÖDERMAN, O. 2004. Surfactant/Nonionic Polymer Interaction. A NMR Diffusometry and NMR Electrophoretic Investigation. *Langmuir*, 20, 1138-1143.
- PILARSKA, A., LUKOSEK, M., SIWIŃSKA-STEFAŃSKA, K., PILARSKI, K. & JESIONOWSKI, T. 2014. Use of MgO to Promote the Oxyethylation Reaction of Lauryl Alcohol. *Polish Journal of Chemical Technology*, 16, 36-42.
- RASHCHI, F. & FINCH, J. A. 2000. Polyphosphates: A review their chemistry and application with particular reference to mineral processing. *Minerals Engineering*, 13, 1019-1035.
- REYES-CORONADO, D., RODRÍGUEZ-GATTORNO, G., ESPINOSA-PESQUEIRA, M. E., CAB, C., COSS, R. D. & OSKAM, G. 2008. Phase-pure TiO₂ nanoparticles: anatase, brookite and rutile. *Nanotechnology*, 19, 145605.

- RIDGWAY, J. 2010. Cardiovascular magnetic resonance physics for clinicians: Part I. *Journal of cardiovascular magnetic resonance : official journal of the Society for Cardiovascular Magnetic Resonance*, 12, 71.
- RIEGEL, S. D. & LESKOWITZ, G. M. 2016. Benchtop NMR spectrometers in academic teaching. *TrAC Trends in Analytical Chemistry*, 83, 27-38.
- RULLIERE, C., PERENES, L., SENOCQ, D., DODI, A. & MARCHESSEAU, S. 2012. Heat treatment effect on polyphosphate chain length in aqueous and calcium solutions. *Food Chemistry*, 134, 712-716.
- SALMAN, A. D., GHADIRI, M. & HOUNSLOW, M. 2007. *Particle Breakage*, Elsevier Science.
- SCHAERTL, W. & ROOS, C. 1999. Convection and thermodiffusion of colloidal gold tracers by laser light scattering. *Physical Review E*, 60, 2020-2028.
- SCHÄRTL, W. 2007. *Light Scattering from Polymer Solutions and Nanoparticle Dispersions*, Springer Berlin Heidelberg.
- SCHNEIDER, C. A., RASBAND, W. S. & ELICEIRI, K. W. 2012. NIH Image to ImageJ: 25 years of image analysis. *Nat Meth*, 9, 671-675.
- SCHWARZ, B. & SCHÖNHOFF, M. 2002. A ¹H NMR relaxation study of hydration water in polyelectrolyte mono and multilayers adsorbed to colloidal particles. *Colloids and Surfaces A: Physicochemical and Engineering Aspects*, 198-200, 293-304.
- SEHGAL, A. & SEERY, T. A. P. 1999. Anomalous Dynamic Light Scattering from Solutions of Light Absorbing Polymers. *Macromolecules*, 32, 7807-7814.
- SEN, S., RAM, M. L., ROY, S. & SARKAR, B. K. 2011. The structural transformation of anatase TiO₂ by high-energy vibrational ball milling. *Journal of Materials Research*, 14, 841-848.
- SEPELAK, V., BEGIN-COLIN, S. & LE CAER, G. 2012. Transformations in oxides induced by high-energy ball-milling. *Dalton Transactions*, 41, 11927-11948.
- SHAPIRO, Y. E. 2011. Structure and dynamics of hydrogels and organogels: An NMR spectroscopy approach. *Progress in Polymer Science*, 36, 1184-1253.
- SHERWOOD, P. M. A. 2002. Introduction to Studies of Phosphorus-Oxygen Compounds by XPS. *Surface Science Spectra*, 9, 62-66.
- SHIELS, J., HARBOTTLE, D. & HUNTER, T. N. 2018. Synthesis and Physical Property Characterisation of Spheroidal and Cuboidal Nuclear Waste Simulant Dispersions. *Materials*, 11, 1235.
- SHVAB, R., HRYHA, E. & NYBORG, L. 2017. Surface chemistry of the titanium powder studied by XPS using internal standard reference. *Powder Metallurgy*, 60, 42-48.
- SIGMA-ALDRICH. *Ludox Silica AS-40 Data Sheet* [Online]. Available: <http://www.sigmaaldrich.com/catalog/product/aldrich/420840?lang=en®ion=GB> [Accessed 22/05/2017].
- SILVA ELIPE, M. V. & MILBURN, R. R. 2016. Monitoring chemical reactions by low-field benchtop NMR at 45 MHz: pros and cons. *Magnetic Resonance in Chemistry*, 54, 437-443.

- SIMON, V., MURESAN, D., TAKÁCS, A. F., NEUMANN, M. & SIMON, S. 2007. Local order changes induced in calcium–sodium–phosphate glasses by transition metals. *Solid State Ionics*, 178, 221-225.
- SING, K. 2001. The use of nitrogen adsorption for the characterisation of porous materials. *Colloids and Surfaces A: Physicochemical and Engineering Aspects*, 187–188, 3-9.
- SING, K. S. W. 1989. 6th International Conference on Surface and Colloid Science The use of gas adsorption for the characterization of porous solids. *Colloids and Surfaces*, 38, 113-124.
- SOMASUNDARAN, P., AMANKONAH, J. O. & ANANTHAPADMABHAN, K. P. 1985. Mineral—solution equilibria in sparingly soluble mineral systems. *Colloids and Surfaces*, 15, 309-333.
- SPĚVÁČEK, J. 2009. NMR investigations of phase transition in aqueous polymer solutions and gels. *Current Opinion in Colloid & Interface Science*, 14, 184-191.
- STEINER, E., BOUGUET-BONNET, S., BLIN, J.-L. & CANET, D. 2011. Water Behavior in Mesoporous Materials As Studied by NMR Relaxometry. *The Journal of Physical Chemistry A*, 115, 9941-9946.
- STORY, P., GREEN, K. A. & HALKO, J. E. 1994. Titanium dioxide dispersibility. Google Patents.
- STRANGE, J. H., MITCHELL, J. & WEBBER, J. B. W. 2003. Pore surface exploration by NMR. *Magnetic Resonance Imaging*, 21, 221-226.
- SUTCLIFFE, S. 2/11/2016 2016. RE: Market research regarding Huntsman TiO₂ manufacturing process Market research regarding Huntsman TiO₂ manufacturing process.
- TADANKI, S. 2018. *Multiple Resonant Multiconductor Transmission line Resonator Design using Circulant Block Matrix Algebra*.
- TAN, H., ZOU, F., MA, B. & BAI, Y. 2016. *Effect of sodium hexametaphosphate and trisodium phosphate on dispersion of polycarboxylate superplasticizer*.
- TAYLOR, M. L., MORRIS, G. E. & SMART, R. S. C. 2001. Polyphosphate interaction with aluminium-doped titania pigment particles. *Colloids and Surfaces A: Physicochemical and Engineering Aspects*, 190, 285-294.
- TAYLOR, M. L., MORRIS, G. E. & SMART, R. S. C. 2003. Influence of aluminum doping on titania pigment structural and dispersion properties. *Journal of Colloid and Interface Science*, 262, 81-88.
- TELEKI, A., AKHTAR, M. K. & PRATSINIS, S. E. 2008. The quality of SiO₂-coatings on flame-made TiO₂-based nanoparticles. *Journal of Materials Chemistry*, 18, 3547-3555.
- TERENZI, C., CASIERI, C., DE LUCA, F., QUARESIMA, R., QUARTA, G. & TUDISCA, V. 2015. Firing-Induced Microstructural Properties of Quasi-Diamagnetic Carbonate-Based Porous Ceramics: a ¹H NMR Relaxation Correlation Study. *Applied Magnetic Resonance*, 46, 1159-1178.
- THILO, E. 1965. The Structural Chemistry of Condensed Inorganic Phosphates. *Angewandte Chemie International Edition in English*, 4, 1061-1071.
- THILO, E., EMELÉUS, H. J. & SHARPE, A. G. 1962. Condensed Phosphates and Arsenates. *Advances in Inorganic Chemistry and Radiochemistry*. Academic Press.

- THOMA, S. B., SMITH, D. M., BOUGHTON, J. & DAVIES, R. 1993. On-line Surface Area Measurement of Concentrated Slurries using low field spin-lattice relaxation NMR. *Particle & Particle Systems Characterization*, 10, 246-251.
- THYBO, A. K., ANDERSEN, H. J., KARLSSON, A. H., DØNSTRUP, S. & STØDKILDE-JØRGENSEN, H. 2003. Low-field NMR relaxation and NMR-imaging as tools in differentiation between potato sample and determination of dry matter content in potatoes. *LWT - Food Science and Technology*, 36, 315-322.
- TOTLAND, C., LEWIS, R. T. & NERDAL, W. 2011. ¹H NMR relaxation of water: A probe for surfactant adsorption on kaolin. *Journal of Colloid and Interface Science*, 363, 362-370.
- USAMI, A. 1999. Rigorous solutions of light scattering of neighboring TiO₂ particles in nanocrystalline films. *Solar Energy Materials and Solar Cells*, 59, 163-166.
- VALLAR, S., HOUIVET, D., EL FALLAH, J., KERVADEC, D. & HAUSSONNE, J. M. 1999. Oxide slurries stability and powders dispersion: optimization with zeta potential and rheological measurements. *Journal of the European Ceramic Society*, 19, 1017-1021.
- VAN DER BEEK, G. P., STUART, M. A. C. & COSGROVE, T. 1991. Polymer adsorption and desorption studies via proton NMR relaxation of the solvent. *Langmuir*, 7, 327-334.
- VAN DUYNHOVEN, J. P. M., MAILLET, B., SCHELL, J., TRONQUET, M., GOUDAPPEL, G.-J. W., TREZZA, E., BULBARELLO, A. & VAN DUSSCHOTEN, D. 2007. A rapid benchtop NMR method for determination of droplet size distributions in food emulsions. *European Journal of Lipid Science and Technology*, 109, 1095-1103.
- VELAMAKANNI, B. V. & FUERSTENAU, D. W. 1993. The effect of the adsorption of polymeric additives on the wet grinding of minerals 1. Mechanisms of suspension stabilization. *Powder Technology*, 75, 1-9.
- WACHTMAN, J. B. 2009. *Ceramic Manufacturing Council - Kilns and Firing*, Wiley.
- WANG, T.-H., NAVARRETE-LOPEZ, A. M., LI, S. & DIXON, D. A. 2010. Hydrolysis of TiCl₄, Initial Steps in the Production of TiO₂. *J. Phys. Chem. A*, 114, 7561-7570.
- WANG, Y. & FORSSBERG, E. 1995. Dispersants in Stirred Ball Mill Grinding. *KONA Powder and Particle Journal*, 13, 67-77.
- WEI, X., ZHU, G., FANG, J. & CHEN, J. 2013. Synthesis, Characterization, and Photocatalysis of Well-Dispersible Phase-Pure Anatase TiO₂ Nanoparticles. *International Journal of Photoenergy*, 2013, 6.
- WEIR, A., WESTERHOFF, P., FABRICIUS, L., HRISTOVSKI, K. & VON GOETZ, N. 2012. Titanium Dioxide Nanoparticles in Food and Personal Care Products. *Environmental Science & Technology*, 46, 2242-2250.
- WILHELM, P. & STEPHAN, D. 2006. On-line tracking of the coating of nanoscaled silica with titania nanoparticles via zeta-potential measurements. *Journal of Colloid and Interface Science*, 293, 88-92.
- WILLS, B. A. & FINCH, J. A. 2016. Chapter 5 - Comminution. In: WILLS, B. A. & FINCH, J. A. (eds.) *Wills' Mineral Processing Technology (Eighth Edition)*. Boston: Butterworth-Heinemann.
- XIGO. 2019. Available: <https://www.xigonanotools.com/area/> [Accessed 03/10/19].

- XIONG, X., WANG, Z., WU, F., LI, X. & GUO, H. 2013. Preparation of TiO₂ from ilmenite using sulfuric acid decomposition of the titania residue combined with separation of Fe³⁺ with EDTA during hydrolysis. *Advanced Powder Technology*, 24, 60-67.
- YANG, Y.-L., REDDY, K. R., DU, Y.-J. & FAN, R.-D. 2017. Sodium hexametaphosphate (SHMP)-amended calcium bentonite for slurry trench cutoff walls: workability and microstructure characteristics. *Canadian Geotechnical Journal*, 55, 528-537.
- YASIR, V. A., MOHANDAS, P. N. & YUSUFF, K. K. M. 2001. Preparation of high surface area TiO₂ (anatase) by thermal hydrolysis of titanyl sulphate solution. *International Journal of Inorganic Materials*, 3, 593-596.
- ZHANG, L. W., LI, H., CHEN, F. Y., ZHANG, D., WU, M., PAN, B. & XING, B. S. 2017. New insights provided by solvent relaxation NMR-measured surface area in liquids to explain phenolics sorption on silica nanoparticles. *Environmental Science: Nano*, 4, 577-584.
- ZHANG, N., EJTEMAEI, M., NGUYEN, A. V. & ZHOU, C. 2019. XPS analysis of the surface chemistry of sulfuric acid-treated kaolinite and diaspore minerals with flotation reagents. *Minerals Engineering*, 136, 1-7.
- ZHANG, W., ZHU, Z. & CHENG, C. Y. 2011. A literature review of titanium metallurgical processes. *Hydrometallurgy*, 108, 177-188.
- ZHAO, L., LIU, Y., WANG, L., ZHAO, H., CHEN, D., ZHONG, B., WANG, J. & QI, T. 2014a. Production of Rutile TiO₂ Pigment from Titanium Slag Obtained by Hydrochloric Acid Leaching of Vanadium-Bearing Titanomagnetite. *Industrial & Engineering Chemistry Research*, 53, 70-77.
- ZHAO, L., LIU, Y., WANG, L., ZHAO, H., CHEN, D., ZHONG, B., WANG, J. & QI, T. 2014b. Production of Rutile TiO₂ Pigment from Titanium Slag Obtained by Hydrochloric Acid Leaching of Vanadium-Bearing Titanomagnetite. *Industrial & Engineering Chemistry Research*, 53, 70-77.
- ZHAO, L. H., HE, L. & HE, B. H. 2013. Effect of Dispersants Pre-Adsorption and Grinding on Dispersion Performance of Kaolin Pigment. *Advanced Materials Research*, 748, 41-45.
- ZION 2016. Titanium Dioxide Market for Paints & Coatings, Plastic, Paper and Other Applications: Global Industry Perspective, Comprehensive Analysis, Size, Share, Growth, Segment, Trends and Forecast, 2014 – 2020.

Research bibliography

Scientific journal and conference papers

- Elliott, L. N., Bourne, R. A., Hassanpour, A., Edwards, J. L., Sutcliffe, S. & Hunter, T. N. 2018. Salt enhanced solvent relaxation and particle surface area determination via rapid spin-lattice NMR. *Powder Technology*, 333, 458-467.
- Elliott, L. N., Behra, J. S., Hondow, N., Bourne, R. A., Hassanpour, A., Edwards, J. L., Sutcliffe, S. & Hunter, T. N. 2019. Characterisation of polyphosphate coated aluminium-doped titania nanoparticles during milling. *Journal of Colloid and Interface Science*, 548, 110-122.
- Elliott, L. N., Bourne, R. A., Hassanpour, A., Edwards, J. L., Sutcliffe, S. & Hunter, T. N. 2019. Characterisation and degradation of polyphosphate dispersant interactions with aluminium-doped titania nanoparticles during milling. *16th European Symposium on Comminution & Classification (ESCC 2019), 2-4 September 2019, Leeds, UK*.
- Elliott, L. N., Austin, D., Bourne, R. A., Hassanpour, A., Edwards, J. L., Sutcliffe, S. & Hunter, T. N. Degradation of polyphosphate dispersant interactions with aluminium-doped TiO₂ during high shear-milling. In preparation.
- Elliott, L. N., Mushing E. & Hunter, T. N., Probing the interaction of lecithin dispersant with milled sugar and wafer particles using relaxation NMR. In preparation.

Oral and poster presentations associated with this thesis

- ‘Specific ion effects and particle surface area via NMR relaxometry’. International Colloid and Surface Science Symposium, July 2017, Manchester, oral presentation.
- ‘Monovalent salt effects on enhanced solvent NMR relaxation and particle surface area determination’. 16th Conference of the International Association of Colloid and Interface Scientists, Rotterdam, The Netherlands, May 2018, oral presentation.
- ‘Monovalent salt effects on enhanced solvent relaxation and particle surface area determination via. spin-lattice NMR relaxation measurements’, McBain Medal

Meeting 2018 - Making and breaking colloidal assemblies: using chemical, physical, and mechanical stimuli to control soft matter, December 2018, poster presentation.

- ‘Characterisation of polyphosphate dispersant interactions with aluminium-doped titania nanoparticles during milling’. The 9th biennial Australian Colloid and Interface Symposium, Hobart, February 2019, oral presentation.

Scholarships and grants associated with this thesis

- The Leeds for Life Conference Award of £500 was awarded in January 2019 allowing this work to be presented at the 9th biennial Australian Colloid and Interface Symposium, Hobart, February 2019.

Appendix 1 Supplementary information to Chapter 4

The following graphs are in support of the data presented and discussed in Chapter 4.

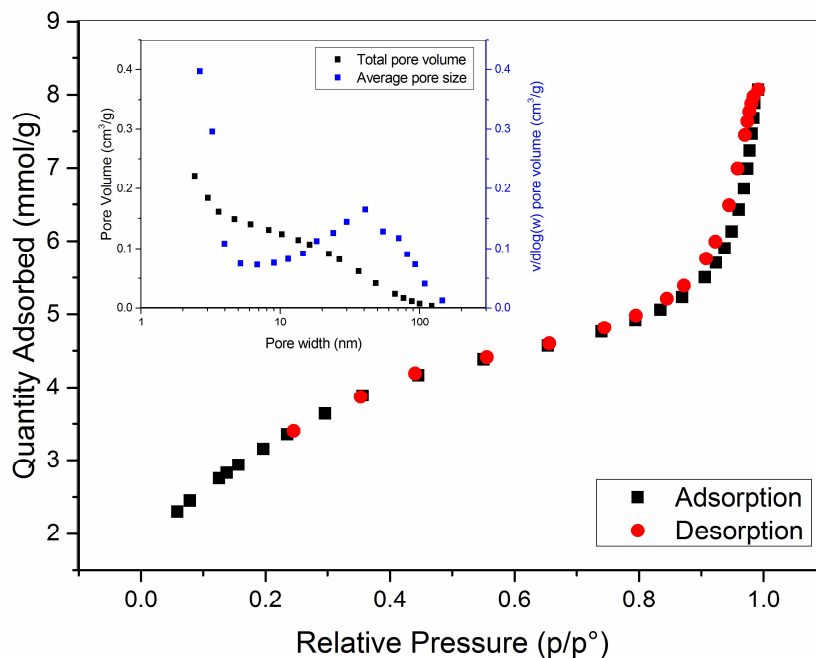


Figure A1- 1: N₂ adsorption-desorption isotherms and total pore volumes for TiO₂^a.

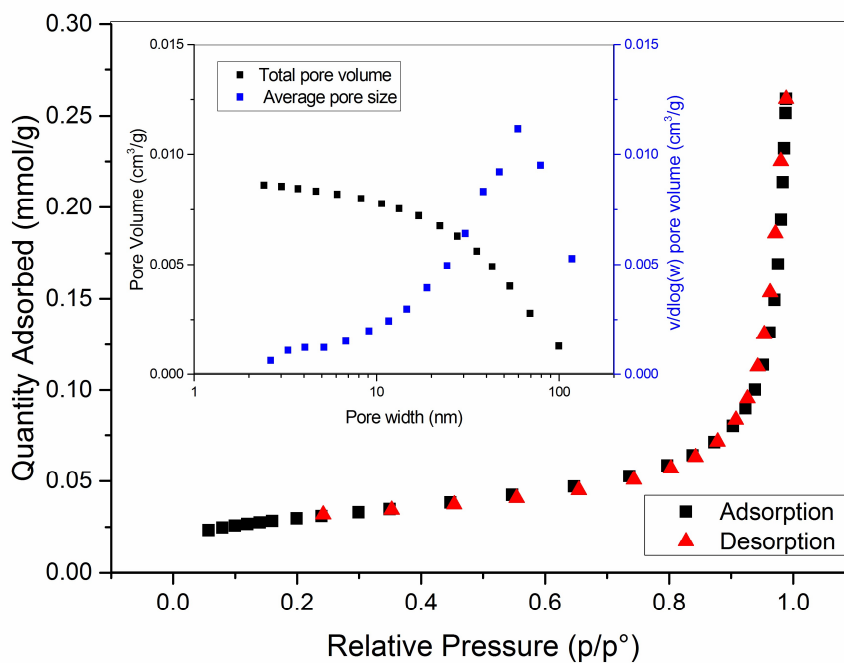


Figure A1- 2: N₂ adsorption-desorption isotherms and total pore volumes for calcite.

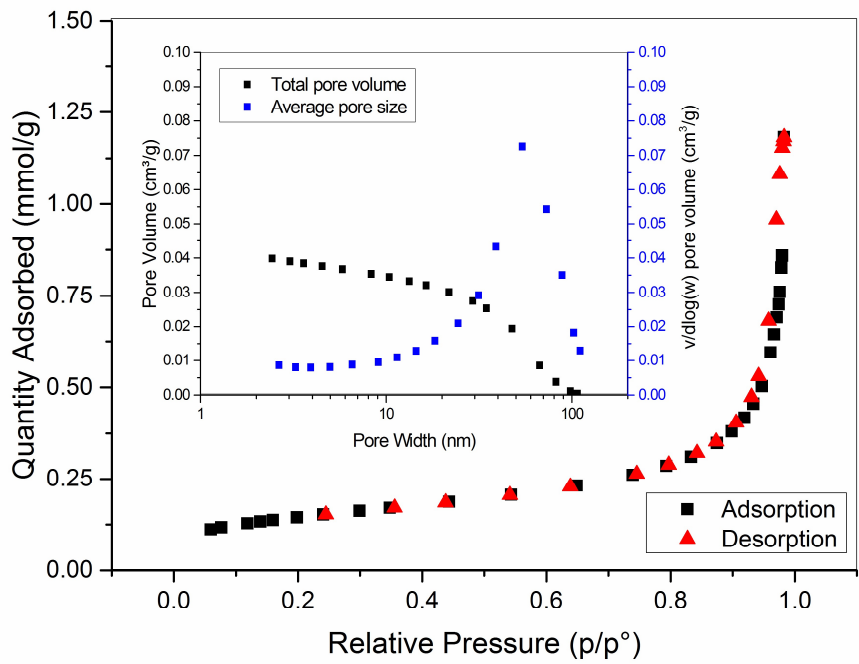


Figure A1- 3: N₂ adsorption isotherm for 100 nm silica^b.

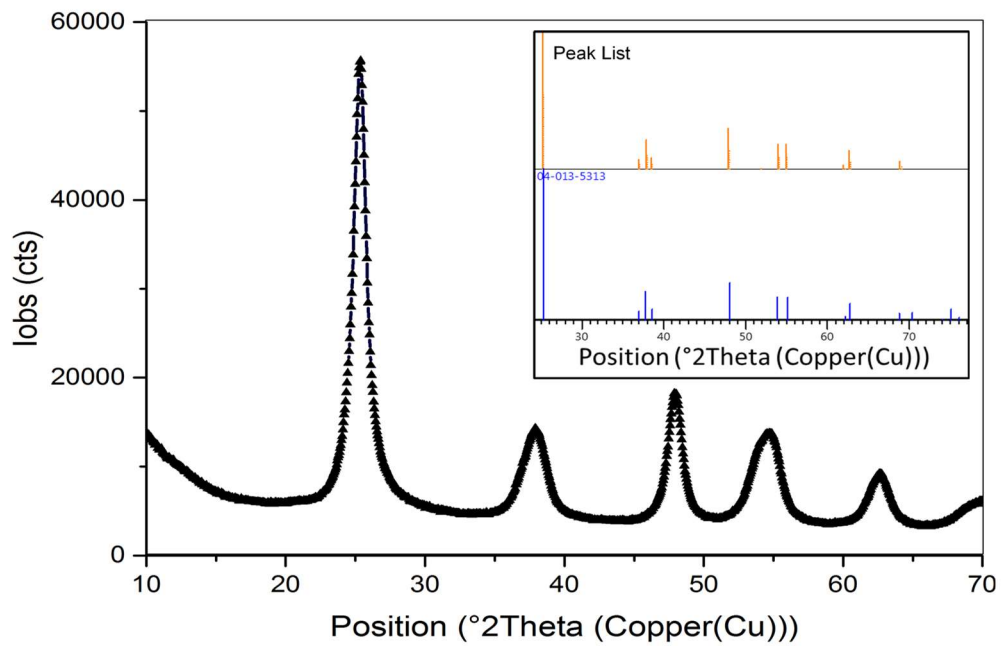


Figure A1- 4: Powder XRD profiles for TiO₂^a at room temperature.

Appendix 2 Supplementary information to Chapter 5

The following graphs and text are in support of the data presented and discussed in Chapter 5.

A2.1 Dynamic light scattering methodology

A2.1.1 Equations and fitting

Function used for fitting the intensity auto-correlation data:

$$g^{(2)}(\tau) - 1 = \left[A_f e^{-\left(\frac{\tau}{\tau_{e,1}}\right)^{\beta_1}} + A_s e^{-\left(\frac{\tau}{\tau_{e,2}}\right)^{\beta_2}} \right]^2 \quad (\text{A2- 1})$$

where f and s refer to the ‘fast’ and the ‘slow’ modes respectively, A_i is the relative amplitude of the mode i (compared to the other mode), β_i is the stretching coefficient of the mode i and $\tau_{e,i}$ is an effective relaxation time of the mode i .

Relationship between the average relaxation time τ_i of the mode i and $\tau_{e,i}$:

$$\tau_i = \frac{\tau_{e,i}}{\beta_i} \Gamma\left(\frac{1}{\beta_i}\right) \quad (\text{A2- 2})$$

Calculation of the scattering vector q :

$$q = \frac{4\pi n \sin\left(\frac{\theta}{2}\right)}{\lambda} \quad (\text{A2- 3})$$

where n is the refractive index of the suspension medium ($n_{water} = 1.33$), θ is the scattering angle and λ is the laser excitation wavelength.

Calculation of the diffusion coefficient D , assuming that the relaxation mode associated to the relaxation time τ is diffusive (*i.e.* that τ follows a q^2 -dependence):

$$D = \frac{1}{\tau q^2} \quad (\text{A2- 4})$$

Calculation of the hydrodynamic radius R_H :

$$R_H = \frac{kT}{6\pi\eta D} = \frac{D_H}{2} \quad (\text{A2- 5})$$

where k is the Boltzmann constant, T the temperature and η the viscosity of the suspension viscosity ($\eta_{water} = 0.89$ mPa.s at 25°C).

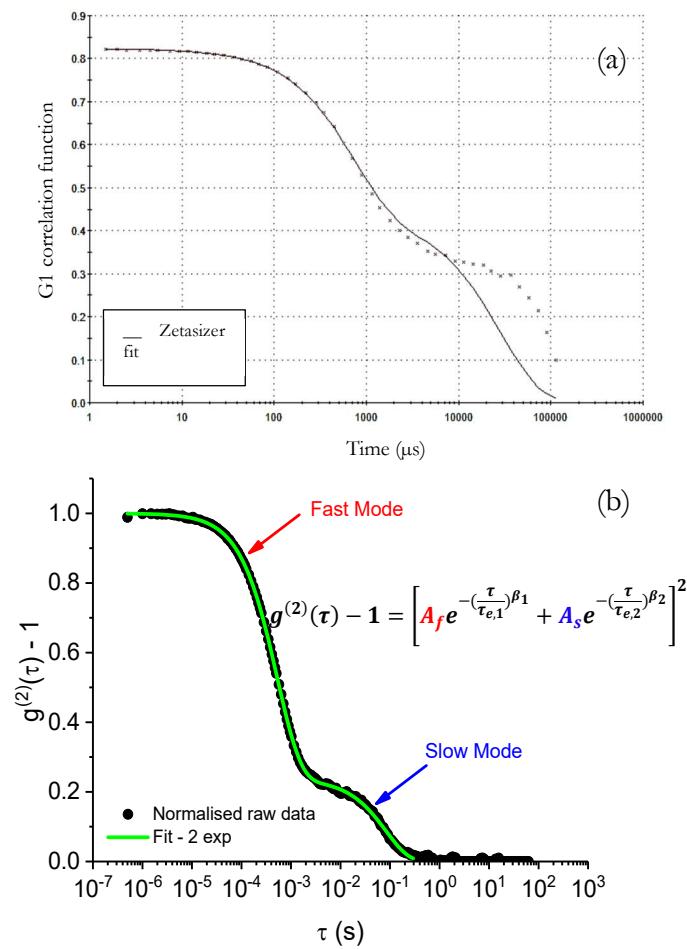


Figure A2- 1: (a) Example of the fitting performed automatically by the Zetasizer and (b) illustration of the fitting parameter performed in MatLab used to calculate R_H .

A2.1.2 Details about the light scattering device used to check for multiple scattering and to check the diffusive nature of the fast mode relaxation time

This instrument is a 3D LS spectrometer (LS Instruments, Switzerland) equipped with a Diode-Pumped Solid State (DPSS) laser ($\lambda = 660$ nm, maximum power: 100 mW; Cobolt FlamencoTM 100; Cobolt), an automated laser attenuator and two avalanche photodiode (APD) detectors. Both incident and detected lights were vertically polarised. ‘2D’ and ‘3D mode’ measurements were performed in pseudo-correlation mode and in modulated 3D cross-correlation mode, respectively.

A2.1.3 Checking the diffusive nature of the fast relaxation mode

DLS measurements were performed using a light scattering device able to perform measurements at different scattering angles. The intensity auto-correlation data obtained for a 1 minute milled TiO₂ suspension are shown in Figure A2- 2 (a). A single relaxation mode was observed at low scattering angles, while two relaxation modes can be observed at high scattering angles. It was initially assumed that the main relaxation mode corresponds to the fast relaxation mode probed by the Zetasizer (see section 5.3.2). The data were fitted using Eq. A2-2, with $A_s = 0$ for $\theta = 30\text{-}70^\circ$ as the second relaxation mode was absent. The so-obtained values of the effective relaxation time of the fast mode $\tau_{e,f}$ were used to calculate the average relaxation time τ_f using (A2- 2, whose reciprocal values were plotted against q^2 together with the value obtained from the Zetasizer measurements, and are shown in Figure A2- 2 (b). As seen from the Figure, the combined LS-Instrument-Zetasizer data can be described by a straight line going through the origin and corresponding to (A2- 4. Such a behaviour confirms that the investigated relaxation mode is diffusive, and that it corresponds to the fast relaxation mode probed by the Zetasizer.

As discussed in Chapter 5, the fast and the slow relaxation modes could be assigned to the primary TiO₂ particles and to aggregates, respectively. The fact that the second relaxation mode was not probed by the LS-Instrument device at low angles is surprising Schärfl (2007). Indeed, large objects usually scatter more at low angles compared to small objects, therefore the relative amplitude of the slow mode A_s was expected to increase as the scattering angle decreases (Schärfl (2007), Behra et al. (2019)). Usami (1999) showed that the scattering efficiency of TiO₂ clusters (whether agglomerates or aggregates) present in a nanocrystalline film decreased when the scattering angle decreased, and equalled that of isolated 275 nm diameter TiO₂ particles at a scattering angle of 100°. No

data were shown for lower scattering angles, but such a behaviour could explain the fact that the aggregates were not probed at low scattering angles.

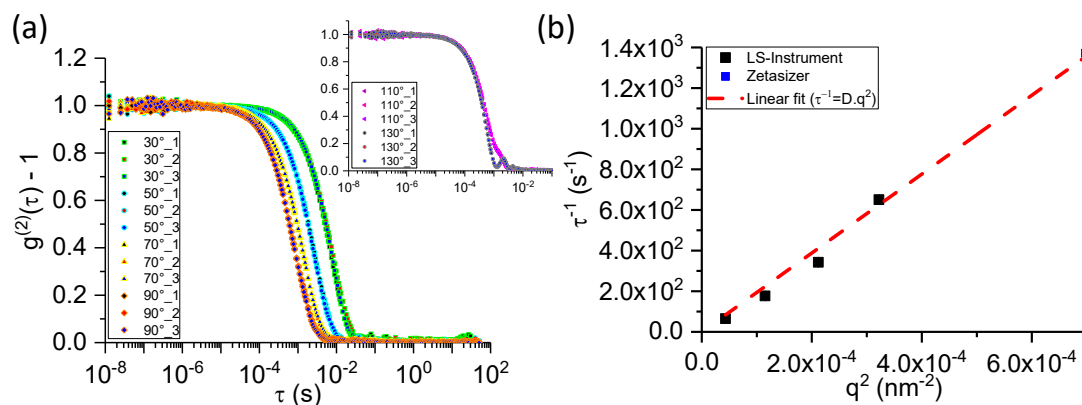


Figure A2- 2: Angular dependence of the DLS data collected on a 1 minute milled TiO₂ suspension. (a) Intensity auto-correlation data at different scattering angles obtained using the LS-Instrument device (see details in Section A2.1.2). Three 60 second measurements were performed for each angle. (b) Reciprocal of the fast mode relaxation time determined from the intensity auto-correlation data shown in the main part of (a) as a function of q^2 . Black and blue data points were collected using the LS-Instrument device and the Zetasizer, respectively. The dashed red line is a linear fit to the data, used to determine the diffusion coefficient D associated with the fast relaxation mode (see (A2- 4)).

As shown in the inset of Figure A2- 2 (a), at the two highest investigated scattering angles (*i.e.* $\theta = 110$ and 130°), not only is the slow relaxation mode present, but the intensity auto-correlation data oscillate. Such a behaviour was reported for samples containing two populations of scatterers that both absorb light and is thought to come from the local convection of the scatterers induced by a local increase of the sample temperature caused by light absorption (Sehgal and Seery (1999), Schaertl and Roos (1999), Badaire et al. (2004)). According to the absorption spectrum published by Reyes-Coronado et al. (2008), rutile absorbs a small fraction of light at the wavelength used for the experiments ($\lambda_{\text{laser}} = 660$ nm). Another hypothesis is that the high scattering efficiency of the TiO₂ clusters at high scattering angles (Usami (1999)) leads to a local heating of the sample and is responsible for the oscillations observed in the intensity auto-correlation data. Decreasing the laser power helped reduce the oscillations (data not shown) (Sehgal and Seery (1999), Schaertl and Roos (1999), Badaire et al. (2004)), but the oscillations could never be fully removed at 130° . This further illustrates the difficulty of performing light

scattering measurements on TiO_2 particle suspensions. The data collected at 110° and 130° scattering angles were not used to calculate the diffusion coefficient associated with the fast relaxation mode as the determination of the fast relaxation mode would have required another, more complex, approach (Sehgal and Seery (1999), Schaertl and Roos (1999)).

A2.1.4 Dilution, filtration and reproducibility trials

Figure A2- 3 shows the dilution trials performed with the LS-Instrument device to find the optimum sample concentration for DLS measurements. For all investigated dilution factors, the values of the hydrodynamic radius equal each other within the experimental error, suggesting that any of these concentrations would be suitable. When similar measurements were performed using the Zetasizer (data not shown), samples obtained after a dilution by 20 had a count rate below 200 kcps, which is the lower boundary recommended by the Zetasizer manufacturer for data collection. Hence, to avoid multiple scattering while being within the instrument optimal collection conditions, a dilution factor of 10 was selected for the study.

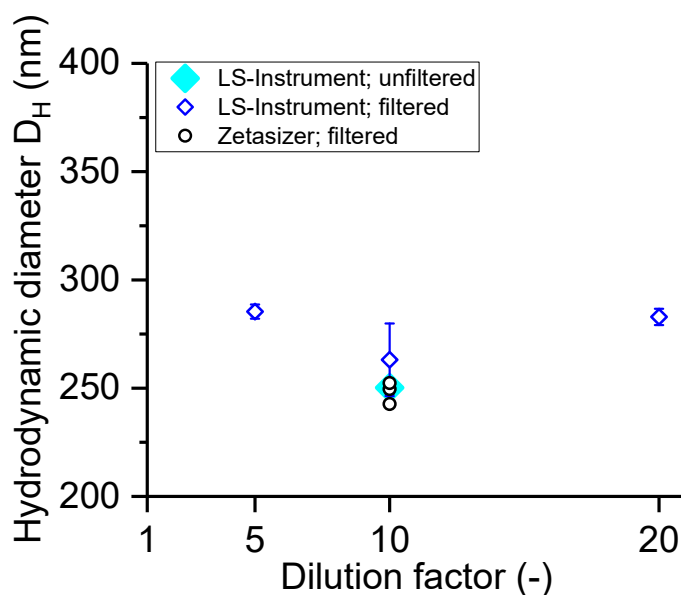


Figure A2- 3: Influence of filtration and dilution on the hydrodynamic diameter D_H for 1 minute milled TiO_2 studied with the LS-Instrument device. D_H values were calculated with Eq. (A2- 5) using the diffusion coefficient obtained from the method described in Section A2.1.3. Hydrodynamic diameters obtained from Zetasizer measurements are also shown for both comparison and reproducibility check purposes.

Filtration trials were performed using both 0.45 μm pore size nylon filters (non-sterile Fisherbrand[®] syringe filters) and 0.8 μm pore size surfactant-free cellulose acetate filters (26 mm Minisart[®] syringe filters). As seen in Figure A2- 3, the hydrodynamic radius calculated from both unfiltered and 0.8 μm filtered samples diluted by 10 are identical within the experimental error. It is worth noting, though, that for the unfiltered sample, the slow relaxation mode was present at all scattering angles, contrary to the 0.8 μm filtered sample for which it was only present at high scattering angles. Hence, filtration through 0.8 μm filters was efficient at removing some of the largest aggregates and helped to reduce the amplitude of the slow relaxation mode. The data collected after 0.45 μm filtration (data not shown) led to a count rate that was below the lower boundary recommended by the Zetasizer manufacturer. The 0.8 μm filters were thus selected for the rest of the study. Finally, the reproducibility of the data collected with the Zetasizer was checked on three samples obtained from the dilution by 10. As seen in Figure A2- 3, the values of the hydrodynamic radius are close to each other and agree with the ones obtained from the LS-Instrument device.

A2.1.5 Checking the method to disperse TiO_2 particles

There was a concern over breaking aggregates because of the amount of energy put into the system during sonication. Thus, DLS measurements were also performed on suspensions prepared using a less energy intensive dispersion method, as shown in Figure A2- 4. Milled TiO_2 suspensions were prepared at the previously selected concentration (see Section A2.1.4, where it also corresponds to the suspension diluted by 10), dispersing the suspensions with a rotating carousel for 10 minutes between each dilution. The suspension contained large visible aggregates/agglomerates that sedimented quickly. For DLS measurements, the upper fraction of the suspension, free from those large visible aggregates/agglomerates, was sampled. Furthermore, the suspensions were not filtered due to concern over larger agglomerates (though smaller than the ones which sedimented after sample preparation) present in the system. DLS measurements were performed with the Zetasizer according to the size measurement SOP described in Section 5.2.4 of Chapter 5.

As for the sonicated suspensions, the intensity auto-correlation data (data not shown) exhibited two relaxation modes. The inter-measurement variability was however more significant than for sonicated suspensions and is thought to come from the fact that carousel-dispersed suspensions contained a higher amount of larger and more

polydisperse ‘objects’ corresponding to both aggregates and agglomerates. It is worth noting that this higher inter-measurement variability is most unlikely to come from the absence of filtration as unfiltered sonicated suspensions did not exhibit such a high inter-measurement variability. Furthermore, a higher number of measurements had to be discarded from the data sets as the intercepts of the intensity auto-correlation data were higher than 1. Such high intercept values also confirm the presence of large objects in the suspensions.

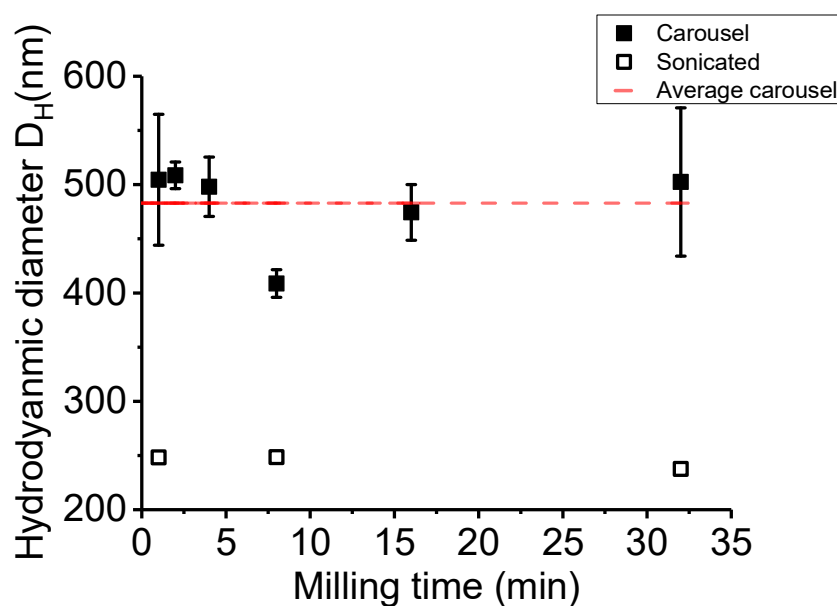


Figure A2- 4: Hydrodynamic diameter D_H for milled TiO_2 particles dispersed using the rotating carousel for 10 minutes (note that these samples have not been filtered) compared to TiO_2 particles dispersed by sonication.

The hydrodynamic diameter was calculated from the fast mode relaxation time and is shown in Figure A2- 4. The values obtained for the carousel-dispersed suspensions are significantly higher than those obtained for the sonicated suspensions and corresponding to the primary TiO_2 particles, showing that sonication breaks up the agglomerates formed from TiO_2 sample drying after milling. There is however little change in the hydrodynamic radius with milling time between carousel-dispersed suspensions, as well as between sonicated suspensions. As the energy input from sonication is not as high as the energy input from the high energy ball mill required to break aggregates, it only breaks up agglomerates, allowing DLS measurements to be more reproducible. Thus, in order to obtain consistent data with reduced experimental error, the sonication method was used

for all other DLS measurements. It is not expected to break aggregates but will break agglomerates induced from drying.

A2.2 Characterisation of unmilled TiO₂

The hydrodynamic diameter was also calculated for an unmilled TiO₂ sample. The sample was measured using the Zetasizer with the same conditions as previously described (0.8 μm filter, dilution by 10 and 30 minutes in sonic bath followed by 1 minute on the ultrasonic probe). Observed in the intensity auto-correlation data were three relaxation modes (Figure A2- 5), one fast and two slow modes, thus the data was fitted with an additional slow mode and hydrodynamic diameter calculated accordingly. The hydrodynamic diameter calculated using the fast mode was in agreement with the 1 and 32 minute milled primary particle size, and further still in agreement with the TEM data (see, Table A2- 1).

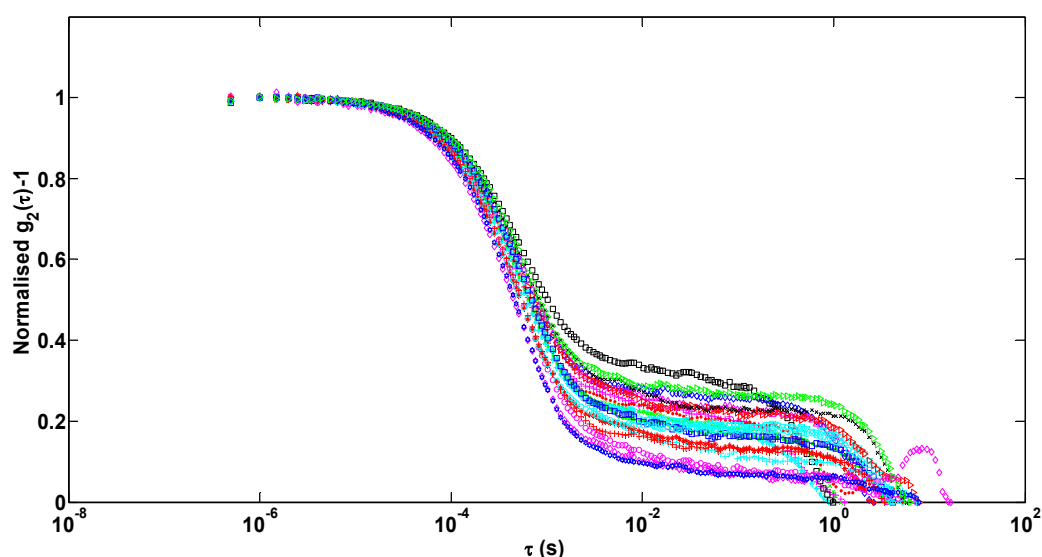


Figure A2- 5: Intensity auto-correlation data from DLS measurements of an unmilled TiO₂ suspension. Thirty 30 second measurements were performed for each sample, where each measurement is represented by a different colour symbol. Some data was rejected and not fitted as the auto-correlation function was greater than 1.

A2.3 Additional data related to TiO₂ particle size by TEM

Table A2- 1: TiO₂ particle size calculated from the Feret diameter of primary particles observed by TEM for unmilled and two milled samples.

Mill Time (min)	No. particles	Diameter (nm)	Standard error (nm)
0	70	238	11
1	238	264	6
32	109	232	8

A2.4 Additional EDS maps of TiO₂

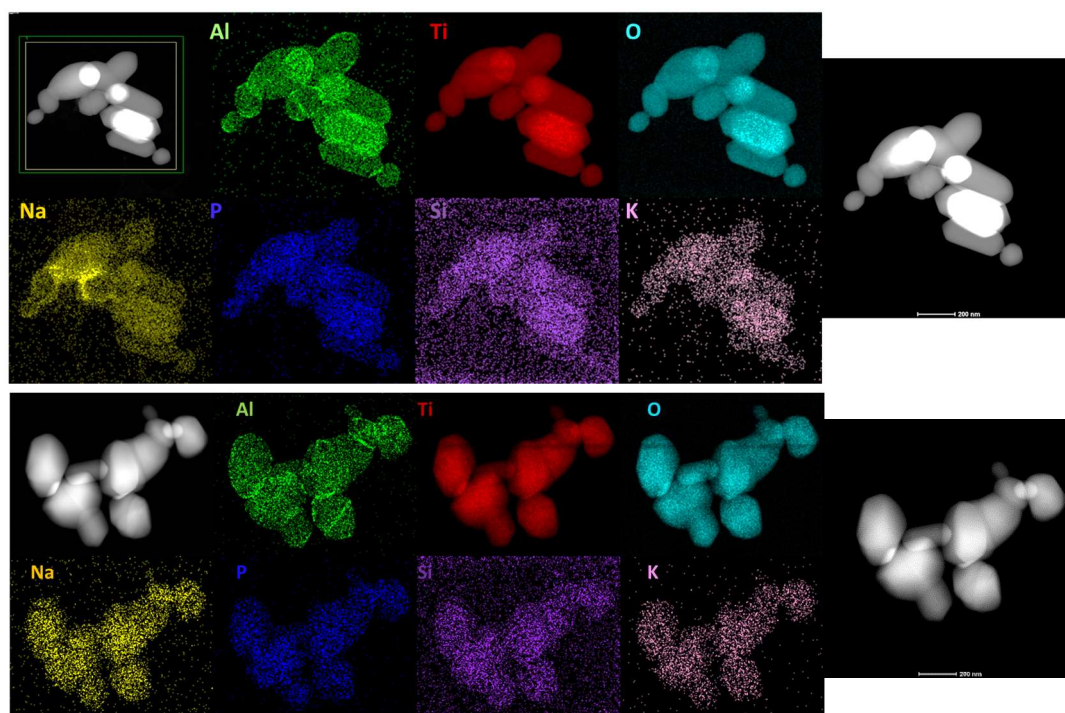


Figure A2- 6: STEM EDS maps showing the distribution of elements in alumina-doped TiO₂ before milling for two different aggregates. Scale bar 200 nm (shown on right hand side image)

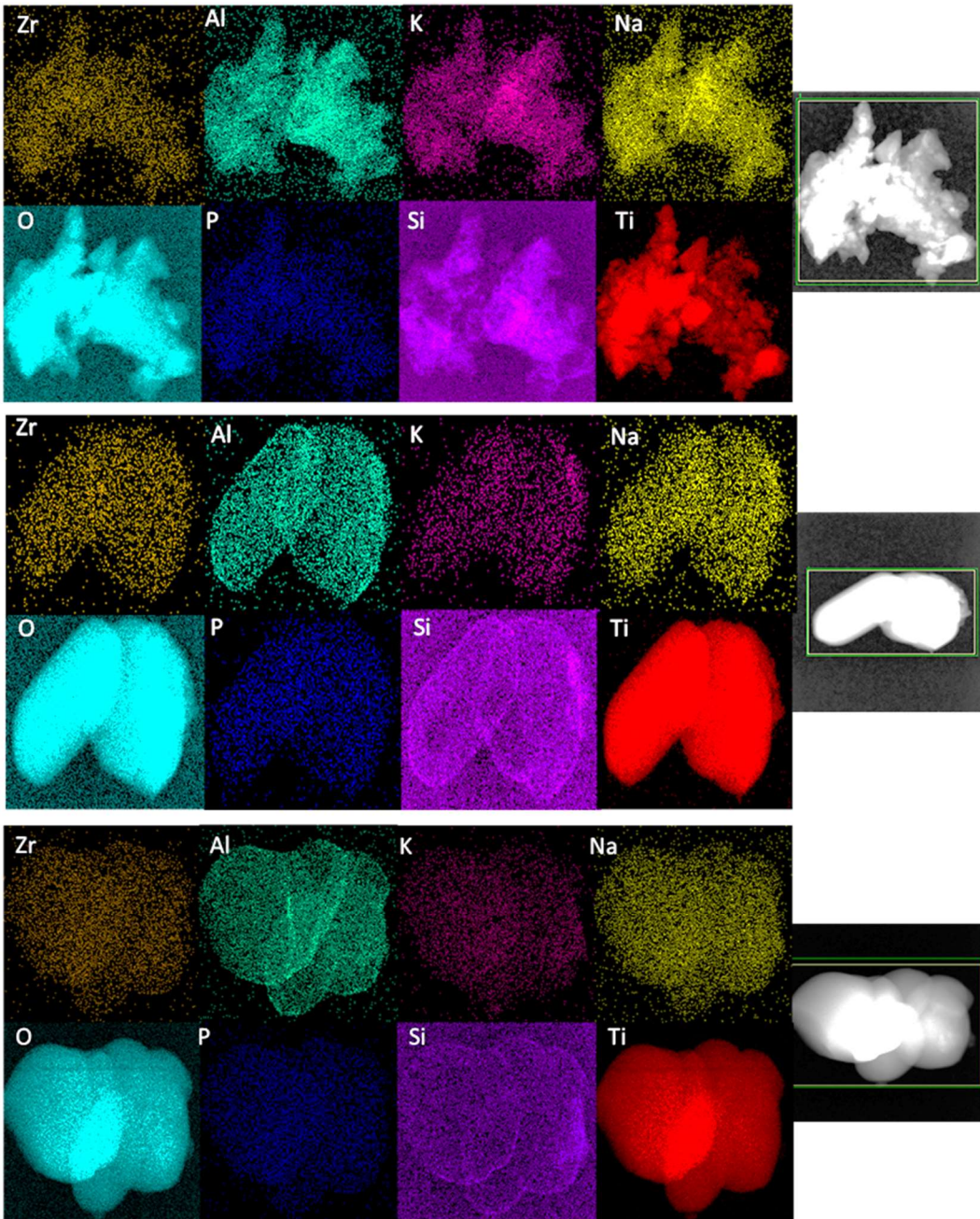


Figure A2- 7: STEM EDS maps showing the distribution of elements in alumina-doped TiO_2 after 32 minutes of milling.

A2.5 Additional data comparing washed and unwashed TiO₂ samples

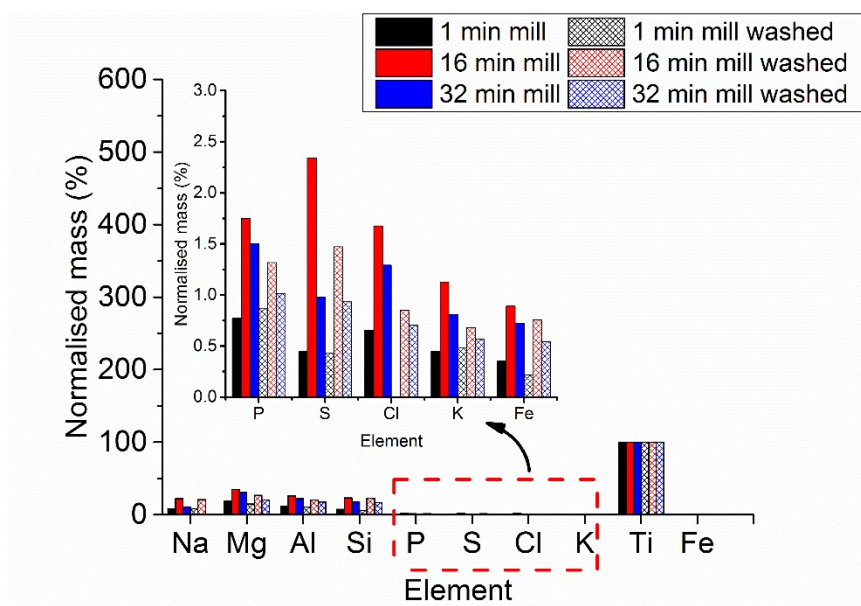


Figure A2- 8: Difference in elemental content for unwashed and washed milled TiO₂ particles obtained using X-ray fluorescence. The mass % has been normalised to the TiO₂ mass % which were set to 100%.

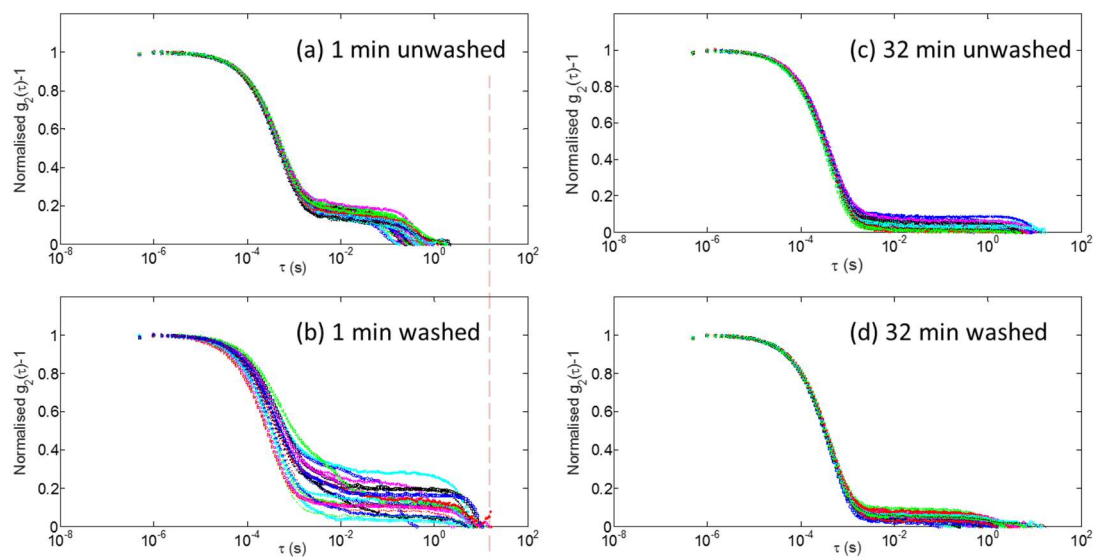


Figure A2- 9: DLS intensity auto-correlation data for (a) unwashed and (b) washed TiO₂ milled for 1 minute. Also shown are similar data for (c) unwashed and (d) washed TiO₂ milled for 32 minutes. The vertical red dashed line represents the highest relaxation time observed for the slow relaxation mode for the 1 minute unwashed sample shown in (a).

Table A2- 2: Hydrodynamic diameter D_H of milled TiO_2 samples determined from Zetasizer measurements for washed and unwashed samples. Also shown is the ratio of the relative amplitudes of the fast and the slow modes (A_s/A_f).

Milling time (min)	D_H (nm)		Average A_s/A_f	
	Unwashed	Washed	Unwashed	Washed
1	249 ± 3	244 ± 19	0.87 ± 0.02	0.77 ± 0.08
16	-	246 ± 2	-	0.37 ± 0.02
32	238 ± 3	229 ± 3	0.30 ± 0.02	0.33 ± 0.02

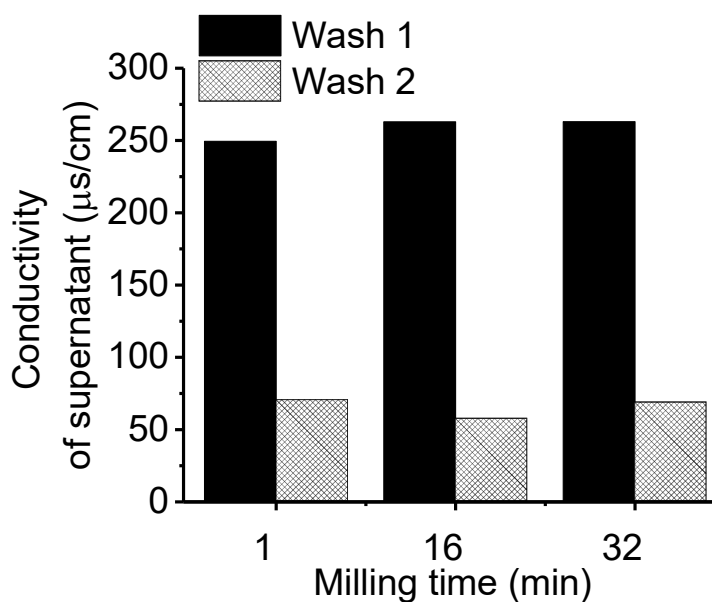


Figure A2- 10: Conductivity measurements of the supernatant taken off after the 1st and the 2nd wash cycles for TiO_2 samples milled for 1, 16 and 32 minutes.

Table A2- 3: Surface area, mean pore size and pore volume obtained from BET measurements for milled TiO₂ pigment particles.

Mill time (min)	*BET surface area (m ² /g)	**BJH mean pore size (nm)	**BJH total pore volume (cm ³ /g)
1	5.72	16.6	0.02
2	5.80	18.5	0.02
4	5.98	22.1	0.03
8	6.17	23.1	0.03
16	7.11	17.9	0.03
32	7.54	19.1	0.04

*Brunauer–Emmett–Teller (BET) and **Barrett-Joyner-Halenda (BJH) methods.

Appendix 3 Supplementary information to Chapter 6

The following graphs and text are in support of the data presented and discussed in Chapter 6.

A3.1 Lab milling SHMP coverage calculations

Is there enough SHMP in the lab milled system to cover particles before milling ($t = 0$ minutes), if equating to the adsorption isotherm at pH 4?

The lab milling used 20 g Al doped TiO₂ in 70 mL of background electrolyte.

Particle surface area 0 minutes by BET = 5.34 m²/g

Total particle area for adsorption = 20 g * 5.34 m²/g = 107 m²

Maximum adsorbed amount of polyphosphate at pH 4 was 0.95 mg/m² (using the linear translation of the Langmuir equation, see Table 6-2).

Amount of SHMP required to cover particles (g) = 107 m²* 0.95 mg/m² = 0.10 g

SHMP added to the mill = 1.4 g

SHMP in equilibrium = 1.4 g – 0.1 g = 1.3 g in 70 mL = Equivalent to ~18,600 mg/L which means there is enough SHMP in the equilibrium phase to ensure maximum SHMP coverage.

Is there enough SHMP in the lab milled system to cover particles before milling ($t = 60$ minutes), if equating to the adsorption isotherm at pH 4?

The lab milling used 20 g Al doped TiO₂ in 70 mL of background electrolyte.

Particle surface area 0 minutes by BET = 9.60 m²/g

Total particle area for adsorption = 20 g * 9.60 m²/g = 192 m²

Maximum adsorbed amount of polyphosphate at pH 4 was 0.95 mg/m² (using the linear translation of the Langmuir equation, see Table 6-2).

Amount of SHMP required to cover particles (g) = 192 m²* 0.95 mg/m² = 0.18 g

SHMP added to the mill = 1.4 g

SHMP in equilibrium = 1.40 g – 0.18 g = 1.22 g in 70 mL = Equivalent to ~17,400 mg/L which means there is enough SHMP in the equilibrium phase to ensure maximum SHMP coverage.

A3.2 Venator calculations for polyphosphate adsorption

Typical milling times = 0 – 60 minutes

Surface area by BET (milling time = 0 – 60 minutes) = $5.34 \text{ m}^2/\text{g} - 9.60 \text{ m}^2/\text{g}$

Typical milling concentrations = 400 – 600 g/L

Venator add 0.14 w/w % P_2O_5 on TiO_2 , therefore, assuming a milling concentration of 400 g/L, than 0.56 g P_2O_5 is required.

SHMP contains 60-70% P_2O_5 , therefore, the amount of SHMP added to the milling process is 0.93 g/L

Is there enough SHMP in the industrial system to cover particles before milling ($t = 0$ minutes), if equating to the adsorption isotherm at pH 4?

Assumption: calculations are based upon a 1 L volume and lower particle concentration of 400 g/L.

Particle area required to cover = $400 \text{ g} * 5.34 \text{ m}^2/\text{g} = 2136 \text{ m}^2$

Mass of SHMP required to cover particles = $2136 \text{ m}^2 * 0.95 \text{ mg}/\text{m}^2$ (maximum adsorbed amount of polyphosphate at pH 4, using the linear translation of the Langmuir equation, see Table 6-2) = 2029 mg = 2 g

Therefore, if milling at pH 4, Venator do not add enough SHMP to the milling process to insure full particle coverage further to this as the surface area increases with milling time, there will not be enough SHMP in the supernatant to provide particle coverage.

Is there enough SHMP in the industrial system to cover particles before milling ($t = 0$ minutes), if equating to the adsorption isotherm at pH 9?

The adsorption isotherm was not measured at pH 9 in this work, however others have adsorbed polyphosphates onto TiO_2 particles at pH 9 (Taylor et al. (2001), Michelmore et al. (2000)). Taylor et al. (2001) reported maximum polyphosphate adsorption quantities for chain length $n=10-12$ using the Langmuir equation at pH 4 was $0.56 \text{ mg}/\text{m}^2$ and at pH 9 $0.2 \text{ mg}/\text{m}^2$. Therefore, Taylor et al. (2001) observed a three times reduction in the maximum adsorbed polyphosphate concentration. This contrast to Michelmore et al. (2000), who observed a ten times reduction in polyphosphate adsorption at pH 9, compared to pH 4, for a polyphosphate chain length $n=4$.

Therefore, for the purpose of this calculation it will be assumed that a three times reduction in the maximum adsorbed quantity could be expected for SHMP at pH 9.

Assumption: calculations are based upon a 1 L volume and lower particle concentration of 400 g/L.

$$\text{Particle area required to cover} = 400 \text{ g} * 5.34 \text{ m}^2/\text{g} = 2136 \text{ m}^2$$

Mass of SHMP required to cover particles = $2136 \text{ m}^2 * 0.32 \text{ mg}/\text{m}^2$ (three times less than the maximum adsorbed amount of polyphosphate at pH 4, using the linear translation of the Langmuir equation, see Table 6-2) = 676 mg = 0.7 g

As the amount of SHMP added to the milling process is 0.93 g/L there is enough SHMP in the system to cover all particles prior to milling.

Does enough SHMP remain in the equilibrium phase to ensure this?

Equilibrium concentration g/L = $0.93 - 0.7 = 0.23 \text{ g}/\text{L} = 230 \text{ mg}/\text{L}$. This appears to be at the onset of the adsorption plateau, at least at pH 4, Taylor et al. (2001) show at pH 9 this onset of the plateau shifts to slightly higher concentrations but the change is small. Thus, it appears that Venator add enough SHMP to cover unmilled particles at pH 9.

Does enough SHMP remain in the equilibrium phase to account for the increase in surface area for particles milled for 60 minutes?

Assumption: calculations are based upon a 1 L volume and lower particle concentration of 400 g/L.

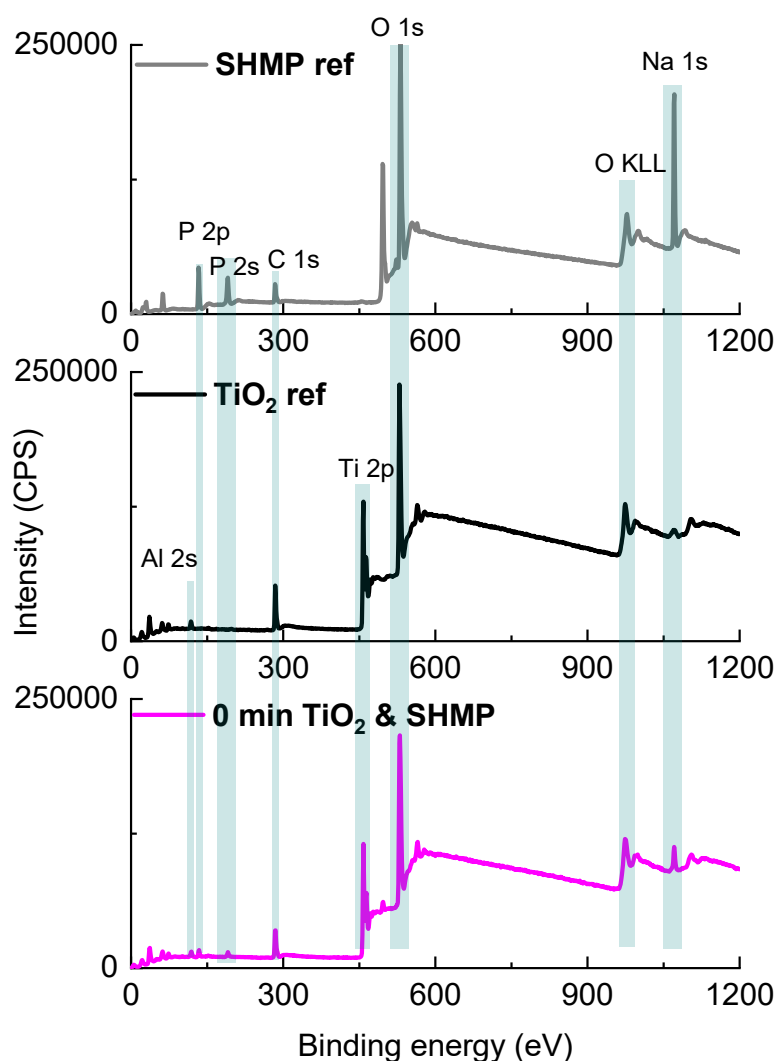
$$\text{Particle area required to cover} = 400 \text{ g} * 9.60 \text{ m}^2/\text{g} = 3840 \text{ m}^2$$

Mass of SHMP required to cover particles = $3840 \text{ m}^2 * 0.32 \text{ mg}/\text{m}^2$ (three times less than the maximum adsorbed amount of polyphosphate at pH 4, using the linear translation of the Langmuir equation, see Table 6-2) = 1229 mg = 1.2 g

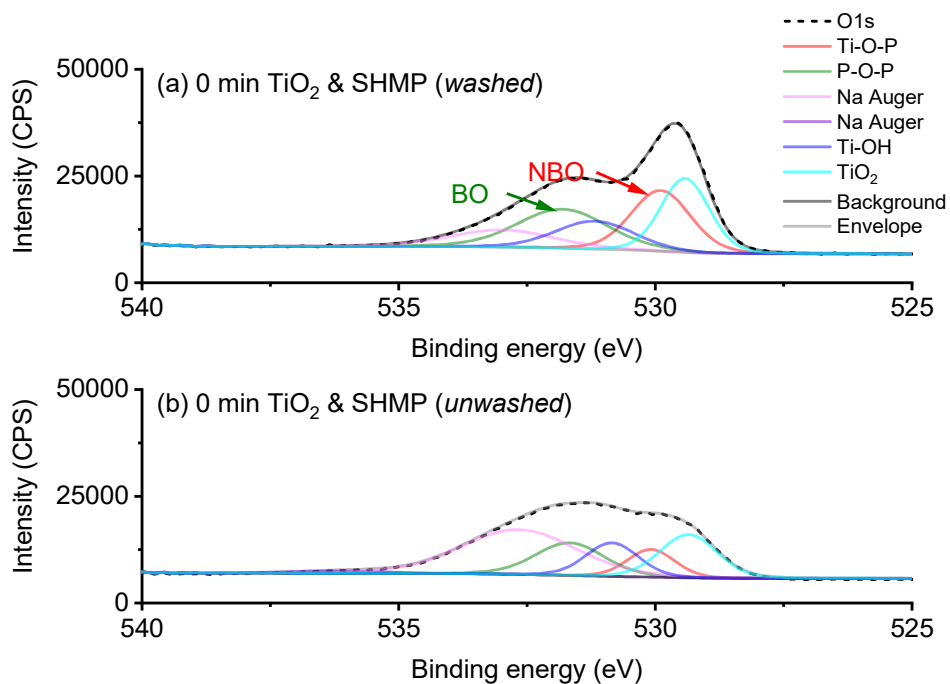
As the amount of SHMP added to the milling process is 0.93 g/L there is not enough SHMP available to cover the particle surface area once milled for 60 minutes. Firstly, it is important to remember that these calculations assumed that three times less polyphosphate adsorbs at pH 9 compared to pH 4 and this may not be the case, as Michelmore et al. (2000) have shown a ten times reduction. Therefore, if the reduction in polyphosphate adsorption occurs to this extent enough SHMP will remain in the equilibrium phase to cover the particle surface after 60 mins of milling.

It is important to note on the industrial scale, that the pigment particles are added to the dosing tank and the pH is increased to 11 whilst SHMP is adsorbed, so the adsorption density may even be much lower than assumed here. Furthermore, Castellini et al. (2005) have shown SHMP adsorption onto kaolinite to plateau after 100 minutes of adsorption. The time-dependent concentration of SHMP at different initial concentrations SHMP onto Al doped TiO₂ has not been studied, however, this would be useful in further aiding understanding of the industrial adsorption process.

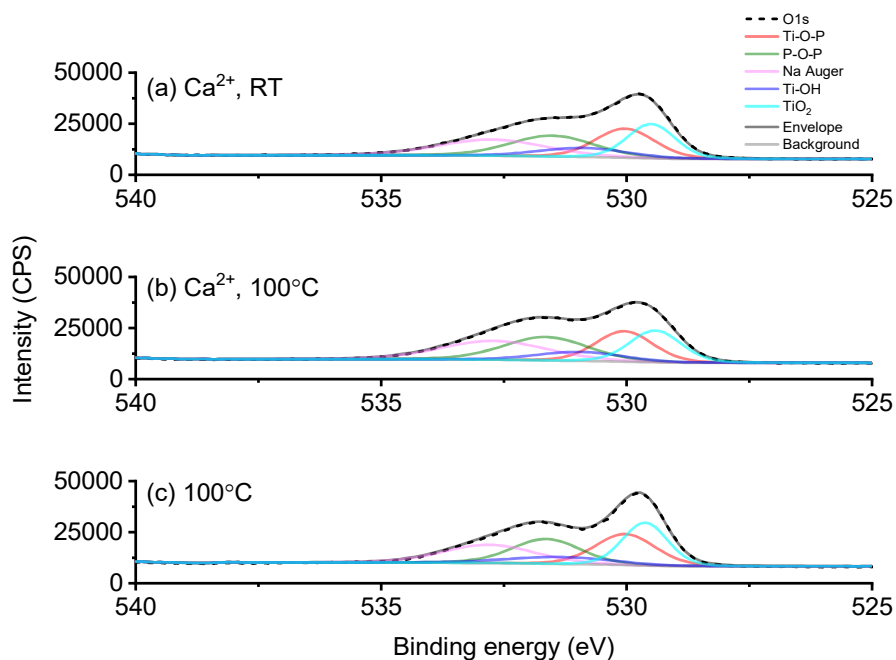
A3.3 XPS survey scans



A3- 1: XPS survey scans of SHMP reference, TiO₂ reference (no SHMP) and 0 min milled TiO₂ with SHMP adsorbed after washing.



A3- 2: XPS O1s peak for 0 min milled TiO_2 with adsorbed SHMP (a) washed and (b) unwashed. Shown are the bridging oxygen (BO) and non-bridging oxygen (NBO) components.



A3- 3: XPS O1s peak for 0 min milled TiO_2 with adsorbed SHMP (a) Ca^{2+} at room temperature (RT) (b) Ca^{2+} at 100 °C and (c) 100 °C. Shown are the bridging oxygen (BO) and non-bridging oxygen (NBO) components.